New Approaches to Weak Gravitational Lensing

A THESIS SUBMITTED TO THE UNIVERSITY OF MANCHESTER
FOR THE DEGREE OF DOCTOR OF PHILOSOPHY
IN THE FACULTY OF ENGINEERING AND PHYSICAL SCIENCES

2015

By
Lee Robert Whittaker
School of Physics and Astronomy

Contents

Abstract **12**

Declaration **13**

Copyright **14**

Acknowledgements **15**

The Author **16**

Supporting Publications 19

1 Introduction to cosmology **21**

1.1 Introducing the standard cosmological model 22

1.1.1 The Friedmann equations 25

1.1.2 Density parameters 27

1.2 Linear structure formation 30

1.3 Observational probes of cosmology 32

1.3.1 Cosmic microwave background (CMB) 32

1.3.2 Type Ia supernovae 34

1.3.3 Baryonic acoustic oscillations 35

1.3.4 Redshift-space distortions 36

1.3.5 Galaxy clusters 36

2 Weak gravitational lensing **39**

2.1 Lensing deflection angle 40

2.2 Linearized lensing formalism 43

2.3 Cosmic shear 45

2.4 The lensing power spectrum 46

2.5 Principles of galaxy shape estimation 49

2.6 Measuring the shapes of galaxies 52

2.6.1 Moments-based methods 53

2.6.2 Model-based methods 54

2.6.3 Lensing using galaxy orientations 55

2.7 Intrinsic alignments 58

3 Weak lensing using only galaxy position angles **63**

3.1 Introduction 64

3.2 Constructing angle-only shear estimators 65

3.2.1 Shear estimation using χ^2 minimization 69

3.2.2 Removal of noise bias 73

3.3 Measuring position angles 77

3.3.1 Using the angle-only method 80

3.3.2 A method for measuring the position angles 81

3.3.3 Debiasing angle-only shear estimates using simulations 84

3.3.4 A comparison of angle-only shear estimates with the KSB method 87

3.4 Impact of errors on $f\left(\left|\boldsymbol{\epsilon}^{\rm int}\right|\right)$ estimates 90

3.5 Tests on simulations 95

3.6 Demonstration on the CFHTLenS data 101

3.7 Conclusions 109

4 Demonstrating position angle-only shear estimators on the GREAT3 simulations **113**

4.1 Introduction 114

4.2 Measuring the position angles 115
4.2.1 The integrated light method 116
4.2.2 A moments-based method 116
4.2.3 Using `IM3SHAPE` 117
4.3 Application to the GREAT3 simulations 118
4.4 Results 129
4.5 Discussion 135

5 Separating weak lensing and intrinsic alignments using radio observations 139
5.1 Introduction 140
5.2 Methods and techniques 142
5.2.1 The Brown & Battye (BB) estimator 143
5.2.2 The corrected BB (CBB) estimator 148
5.2.3 Required galaxy numbers for the CBB estimator 153
5.3 Alternative approaches 155
5.3.1 Full angle-only estimator (FAO) 155
5.3.2 Hybrid method 161
5.4 Tests on simulations 164
5.5 Conclusions 172

6 Conclusion 175

A Deriving the $F_1(|\boldsymbol{g}|)$ function 181

B Including a variable σ_α 185

C Deriving the 3rd order estimator 187

D Residual bias in the iterative method 191

E Error on the first iteration 193

F Correcting the Brown & Battye estimator **197**

G Details of the FAO estimator **199**

References **202**

List of Tables

1.1 Planck 2015 best-fit cosmological parameters 30

3.1 Mean and standard deviation - equations (3.20) and (3.31) 76

4.1 Results from the tests on the GREAT3 simulations 134

5.1 Mean and standard deviation - BB and CBB estimators 149

5.2 Mean and standard deviation - FAO and hybrid estimators 157

5.3 Mean and fractional bias for the power spectra reconstructions 170

List of Figures

1 Large-scale structure from GADGET-2 20

1.1 Hubble's law 23
1.2 Evolution of the Universe 27
1.3 Planck 2015 power spectrum 33

2.1 Typical lens system 41
2.2 Constraints σ_8-Ω_m - DES SV 47
2.3 Two-point correlation functions - CFHTLenS 48
2.4 Example galaxy image 52
2.5 Illustration of the different angles 56
2.6 Mean cosine from Schneider & Seitz (1995) 56
2.7 The dependence of the mean cosine on the shear 57

3.1 $F_1\left(|\boldsymbol{g}|\right)$ function for the Rayleigh distribution 70
3.2 χ^2 of equation (3.20) 72
3.3 Residual bias of equations (3.22) and (3.23) 73
3.4 Best-fit estimates using equations (3.20) and (3.31) 77
3.5 Residual bias of equations (3.20) and (3.31)) 78
3.6 Simulated galaxy image 78
3.7 Integrated light distribution 82
3.8 Integrated light distribution as a function of galaxy orientation 83
3.9 Distribution of shear estimates - KSB and angle-only 87

3.10 Distribution of shear estimates - KSB and angle-only with one iteration 88
3.11 Recovered shear estimates as a function of input 89
3.12 $f\left(\left|\boldsymbol{\epsilon}^{\rm int}\right|\right)$ for the case of 5×10^4 galaxies 90
3.13 Fractional bias in the recovered $|\boldsymbol{g}|$ estimates 91
3.14 Absolute value of the fractional bias in equation (3.52) 92
3.15 Absolute fractional bias for 2×10^5 galaxies 94
3.16 Reconstruction of the distribution of dark matter in simulations 96
3.17 Fractional difference between $F_1\left(|\boldsymbol{g}|\right)$ and the 3rd order approximation 97
3.18 R.m.s. residuals from simulations 101
3.19 Mass reconstructions for the W1 field of the CFHTLenS 106
3.20 Mass reconstructions for the W2 field of the CFHTLenS 107
3.21 Mass reconstructions for the W3 field of the CFHTLenS 108
3.22 Mass reconstructions for the W4 field of the CFHTLenS 109
3.23 R.m.s residuals for the CFHTLenS 110

4.1 Reconstructed $f\left(\left|\boldsymbol{\epsilon}^{\rm int}\right|\right)$ from GREAT3 using `IM3SHAPE` 120
4.2 Distribution of position angles measured from field 2 of GREAT3 . . 121
4.3 Distributions of galaxy fluxes and $R_{\rm e}$ 123
4.4 Mean flux of the galaxies plotted as a function of mean $R_{\rm e}$ 123
4.5 Modified distributions of flux and $R_{\rm e}$ 125
4.6 Difference between recovered and input $\boldsymbol{g}$ - integrated light and moments 131
4.7 Difference between recovered and input $\boldsymbol{g}$ - `IM3SHAPE` 132
4.8 Multiplicative and additive biases for GREAT3 134

5.1 Residual bias in the BB estimator 146
5.2 Recovered shear and IA estimates for equations (5.20) and (5.22) . . . 150
5.3 Residual bias for the CBB estimator 151
5.4 Number of galaxies in the sample as a function of error on $\alpha^{\rm int}$ 154
5.5 Recovered shear and IA estimates for the FAO and hybrid estimators . 158
5.6 Residual bias in the FAO estimator 161

5.7 Residual bias in the hybrid estimator 164
5.8 Reconstructed power spectra for the BB and CBB estimators 168
5.9 Reconstructed power spectra for the FAO and hybrid estimators 169
5.10 Fractional errors of the power spectra reconstructions 171

The University of Manchester

ABSTRACT OF THESIS submitted by Lee Robert Whittaker
for the Degree of Doctor of Philosophy and entitled
"New Approaches to Weak Gravitational Lensing", September 2015.

This thesis is concerned with developing new methods for performing weak gravitational lensing with the aim of addressing specific systematic effects in weak lensing surveys.

The first of these effects is the multiplicative biases which arise as a result of isotropic smearing. This smearing may be due to atmospheric seeing or an instrumental PSF. Isotropic smearing circularizes a galaxy image and leads to a systematic underestimate of the modulus of the observed ellipticity. The orientation of the observed galaxy is, however, unaffected. We exploit this property by formulating a weak lensing shear estimator that requires measurements of galaxy position angles only, thereby avoiding the contribution from this systematic. We demonstrate the method on simulations and the CFHTLenS data by reconstructing convergence maps and comparing the results with the standard full ellipticity based approach. We show that the difference between the reconstructed maps for the two approaches is consistent with noise in all of the tests performed. We then apply the technique to the GREAT3 challenge data using three distinct methods to measure the position angles of the galaxies. For all three methods, we find that the position angle-only approach yields shear estimates with a performance comparable with current well established shape based techniques.

The second effect addressed arises from the intrinsic alignment of the source galaxies. This alignment mimics a shear signal, and hence biases estimates of the shear. To mitigate this effect, we develop three shear estimators that include polarization information from radio observations as a tracer of a galaxy's intrinsic orientation. In addition to the shear estimator, we also develop estimators for the intrinsic alignment signal. We test these estimators by successfully reconstructing the shear and intrinsic alignment auto and cross-power spectra across three overlapping redshift bins.

Declaration

No portion of the work referred to in this thesis has been submitted in support of an application for another degree or qualification of this or any other university or other institution of learning.

Copyright

Acknowledgements

I would like to express my sincere gratitude to my supervisors Professor Michael Brown and Professor Richard Battye. It has been both a pleasure and an honour to work with them, and their guidance and support has been invaluable throughout my PhD.

I am also grateful to the ERC for support through the award of an ERC Starting Independent Researcher Grant (EC FP7 grant number 280127).

The Author

The author was born in November 1979 in Warrington, England. He studied an MPhys in theoretical physics at the University of Manchester, England. He graduated in 2012 and began a PhD at the Jodrell Bank Centre for Astrophysics in the same year, for which this thesis is submitted.

To my wife and parents, who have made this possible through their support.

Supporting Publications

Part of the work presented in this thesis is contained in the following papers:

- Whittaker, L., Brown, M. L., and Battye R. A. 2014 "Weak lensing using only galaxy position angles" (MNRAS 445:1836-1857)[1]
- Whittaker, L., Brown, M. L., and Battye R. A. 2015 "A demonstration of position angle-only weak lensing shear estimators on the GREAT3 simulations" (arXiv:1505.08131 accepted by MNRAS)[2]
- Whittaker, L., Brown, M. L., and Battye R. A. 2015 "Separating weak lensing and intrinsic alignments using radio observations" (MNRAS 451:383-399)[3]

This work is entirely my own, except for Sections 3.5 and 5.4, which were done in collaboration with Michael L. Brown.

[1] Chapter 3
[2] Chapter 4
[3] Chapter 5

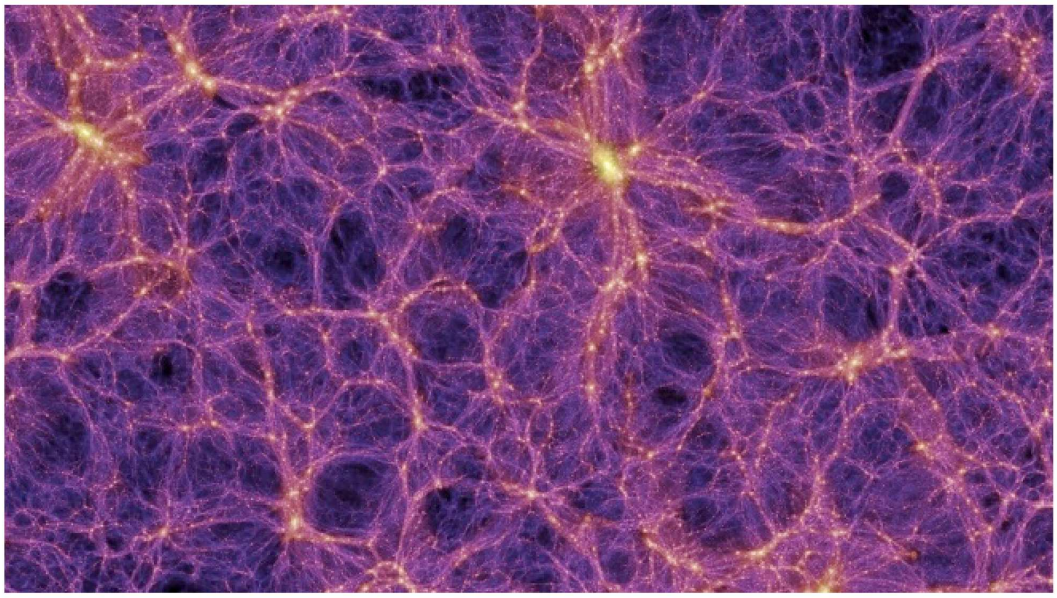

Figure 1: A simulation of the large-scale structure run with GADGET-2 (Springel 2005).

Chapter 1

Introduction to cosmology

Cosmology is the study of the evolution and large scale dynamics of the Universe. Modern scientific cosmology is a relatively young branch of astronomy. However, it can trace its roots to the days when our early ancestors first looked up at the stars and pondered on such questions as "how did it all begin?" For the majority of our recorded history, it was believed that humans occupied a special place in the Universe. The Ptolemaic model consisted of the Universe being centred on the Earth, with all of the heavenly bodies circling around us. In the 1500s, Copernicus proposed that it was, in fact, the Sun that was at the centre of the Universe, and that the Earth and other planets orbited the Sun.

Observations in the years that followed began to provide evidence that the stars were not uniformly distributed about the skies, as it was previously believed. In the late 1700s, William Herschel identified a disc like distribution of the stars (Herschel 1786) - the Milky Way - and placed our Solar System at the centre. It was Shapely, in the early 1900s, that showed the solar system was actually situated about two-thirds of the way out from the centre of the Milky Way. However, it was then the Milky Way that was placed at the centre of the Universe. In 1952, Baade finally confirmed that our place in the Universe is not special (Liddle 2003). Our galaxy is fairly typical - just one of around 100 billion galaxies in the observable Universe. The idea that our place in the Universe is not special now lies at the heart of modern cosmology.

In the wake of Einstein's general theory of relativity (1916), the assumption that the Universe is homogeneous and isotropic on large scales was invoked in an attempt to solve the Einstein field equations for the simplest possible large-scale mass distribution. This assumption of large scale ($>100\,\mathrm{Mpc}$) symmetry is known as the cosmological principle, and it has been verified by observations of the cosmic microwave background (CMB) (Penzias & Wilson 1965; Smoot et al. 1992; Wu et al. 1999) and the distribution of galaxies (Colless et al. 2001; Abazajian et al. 2003). From this assumption, the Robertson-Walker metric was developed and, from this metric, the Friedmann equations. These equations describe the expansion of a universe that obeys the cosmological principle within the framework of general relativity.

Cosmological models that obey the Robertson-Walker metric and the Friedmann equations are generally described as FRW models. The ΛCDM model is one example of an FRW model. ΛCDM provides a good description of many cosmological observations, such as the structure of the CMB and the accelerating expansion of the Universe. Within this model, the accelerated expansion of the Universe is deemed to be the result of dark energy. This energy has a constant density and is identified with the cosmological constant (Λ) that is present in the Einstein field equations. The model is also structured around the existence of cold dark matter (CDM). The presence of cold dark matter in the model explains many of the gravitational phenomena that are observed but cannot be explained by the existence of baryonic matter alone, such as the shape of the velocity curves of spiral galaxies (Rubin et al. 1980). Cosmological models, of which the ΛCDM model is but one, are constructed using a set of cosmological parameters. The precise determination of the cosmological parameters is one of the primary goals of modern cosmology.

1.1 Introducing the standard cosmological model

The roots of modern cosmology lie in general relativity. The Einstein field equations describe the relationship between the content of matter-energy in the Universe and the

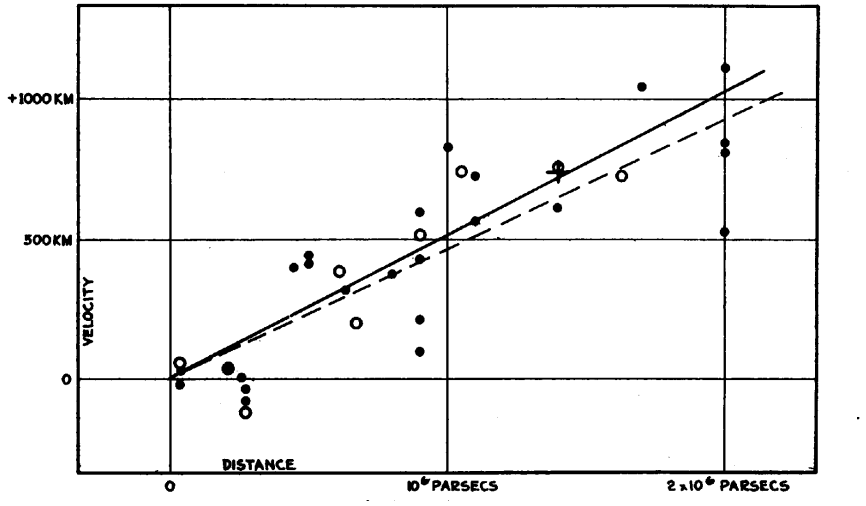

Figure 1.1: The relationship between galaxy recession velocity and distance to the galaxy, as originally presented by Hubble (1929). The black points and full line represent the linear relationship when considering galaxies as single objects. The open circles and dashed line represent the relationship when combining the galaxies into groups according to proximity in direction and distance. The cross is the mean velocity corresponding to the mean distance of 22 galaxies whose distance could not be measured individually.

curvature of spacetime. The field equations are

$$G_{\mu\nu} + \Lambda g_{\mu\nu} = \frac{8\pi G}{c^4} T_{\mu\nu}, \tag{1.1}$$

where $G_{\mu\nu}$ is the Einstein tensor, which describes the curvature of spacetime, and $g_{\mu\nu}$ is the metric tensor, which captures the geometrical causal structure of spacetime. $T_{\mu\nu}$ is the energy-momentum tensor and describes the energy density and momentum at a given point in spacetime. This tensor is the source of the spacetime curvature. The constant on the right-hand side of the field equations is determined by the requirement that Newton's law of gravitation is recovered in the weak field limit. The term $g_{\mu\nu}\Lambda$ does not effect the energy conservation law ($\nabla_\nu T^{\mu\nu} = 0$) and so can be added arbitrarily (see Hartle (2003) for a discussion). Historically, this term was originally added by Einstein to counter the effects of gravity with the aim of explaining a static Universe. This idea was dismissed when Edwin Hubble (Hubble 1929) discovered that the Universe is expanding.

Hubble showed that the recession velocity of a galaxy is approximately proportional to its distance from us, as shown in Figure 1.1. This relation can be expressed in terms of the recession velocity of a galaxy, v, the Hubble constant, H_0, and the proper distance to the galaxy, D, as

$$v = H_0 D. \tag{1.2}$$

The term H_0 has be to be measured by observation, and the first good estimate of H_0 was made by Sandage (1958) using observations of Cepheid variable stars. This value was found to be $\sim 75\,\mathrm{kms}^{-1}\mathrm{Mpc}^{-1}$. The value of H_0 found by the Planck Collaboration et al. (2015a) using Planck CMB temperature and lensing data is $H_0 = (67.8 \pm 0.9)\ \mathrm{kms}^{-1}\mathrm{Mpc}^{-1}$. If the expansion of the Universe is assumed to be independent of time, then H_0^{-1} provides an estimate of the age of the Universe. Given the Planck results, this age is $\sim$14.4 billion years. This is slightly older than the current accepted age, which is $\sim$13.8 billon years, as the expansion of the Universe is now known to be time-dependent.

From Hubble's discovery in 1929 until the 1990s, it was assumed that the cosmological constant is zero. However, the discovery by two independent groups - the High-Z Supernova Search Team (Riess et al. 1998) and the Supernova Cosmology project (Perlmutter et al. 1999) - that the expansion of the Universe is accelerating led to the current accepted hypothesis that the Universe consists of approximately 70% of an unknown form of energy - dark energy - which acts to oppose the force of gravity on large scales. The simplest form of dark energy is one that is constant in both space and time. This can be modelled by reintroducing the constant Λ to the field equations. There are other possible cosmological models which can explain the accelerated expansion, such as that of a dark energy for which the density is not constant but, instead, evolving with time.

1.1.1 The Friedmann equations

In order to use the Einstein equations to model the Universe, one must first assume a form for the metric. The usual assumption is that the Universe obeys the cosmological principle. In such a universe, the most general form of the spacetime metric, which is defined in terms of the metric tensor $g_{\mu\nu}$ and the infinitesimal comoving coordinate displacement $\mathrm{d}x^{\mu}$ (Peacock 1999), is

$$g_{\mu\nu}\mathrm{d}x^{\mu}\mathrm{d}x^{\nu} = \mathrm{d}s^2 = -\left(c\mathrm{d}t\right)^2 + a\left(t\right)\left[\mathrm{d}r^2 + f_K^2\left(\chi\right)\left(\mathrm{d}\theta^2 + \sin^2\theta\mathrm{d}\phi^2\right)\right], \tag{1.3}$$

where χ is the comoving radial coordinate and $\mathrm{d}s^2$ is the line element. This is known as the Robertson-Walker metric. Comoving coordinates factor out the expansion of the Universe so that the distance between two objects is unaffected by the expansion. This implies that the metric is free from the cross terms $\mathrm{d}t\mathrm{d}x^i$, where the postscript i denotes a spatial coordinate, and that the spatial part of the metric is scaled by a single function of time, $a\left(t\right)$, which is the scale factor and describes the spatial expansion. To preserve isotropy, this term must be a function of time only. The function $f_K\left(\chi\right)$ is the comoving angular diameter distance to coordinate χ. This function encapsulates the geometry of the Universe and is given for three distinct cases of three-dimensional space with curvature K:

$$f_K\left(\chi\right) = \begin{cases} K^{-\frac{1}{2}}\sin\left(K^{\frac{1}{2}}\chi\right) & \text{for } K > 0 \text{ (spherical)} \\ \chi & \text{for } K = 0 \text{ (flat)} \\ \left|K\right|^{-\frac{1}{2}}\sinh\left(\left|K\right|^{\frac{1}{2}}\chi\right) & \text{for } K < 0 \text{ (hyperbolic).} \end{cases} \tag{1.4}$$

The Robertson-Walker metric follows from the assumption of the cosmological principle. If we also assume that the Universe can be modelled as consisting of an isotropic and homogeneous fluid with density ρ and pressure p, the energy-momentum

tensor is a diagonal matrix, and we can write the equation of state as

$$p = \omega \rho c^2, \tag{1.5}$$

where ω is a dimensionless number which characterizes the relation. Assuming the perfect fluid model and the Robertson-Walker metric, there are only two independent solutions to the field equations. They are

$$\left(\frac{\dot{a}}{a}\right)^2 = \frac{8\pi G\rho}{3} + \frac{\Lambda c^2}{3} - \frac{Kc^2}{a^2}, \tag{1.6}$$

$$\frac{\ddot{a}}{a} = -\frac{4\pi G}{3}\left(\rho + \frac{3p}{c^2}\right) + \frac{\Lambda c^2}{3}. \tag{1.7}$$

These are the Friedmann equations. The first equation is given by the 00 component of the field equations and reveals a connection between the density of the Universe and its global geometry. The second equation comes from a combination of the trace of the field equations and the first equation. This is the acceleration equation, which implies that density and pressure decrease the rate of expansion. However, a positive cosmological constant can counter this effect and cause the rate of expansion to increase.

For a given a rate of expansion, $\dot{a}/a$, we can define the critical density, ρ_c, as the density which yields a flat Universe, $K = 0$. This is found to be

$$\rho_c = \frac{3H^2}{8\pi G}, \tag{1.8}$$

where we have defined the Hubble parameter as $H(t) \equiv \dot{a}/a$. From equation (1.8), we see that the critical density depends on H only. The Hubble constant, H_0, is defined as the value of the Hubble parameter at the present day epoch: $H_0 \equiv H\,(t = 0)$. We also parameterize the Hubble constant in terms of the dimensionless parameter h, such that

$$H_0 = 100h\,\mathrm{kms}^{-1}\mathrm{Mpc}^{-1}. \tag{1.9}$$

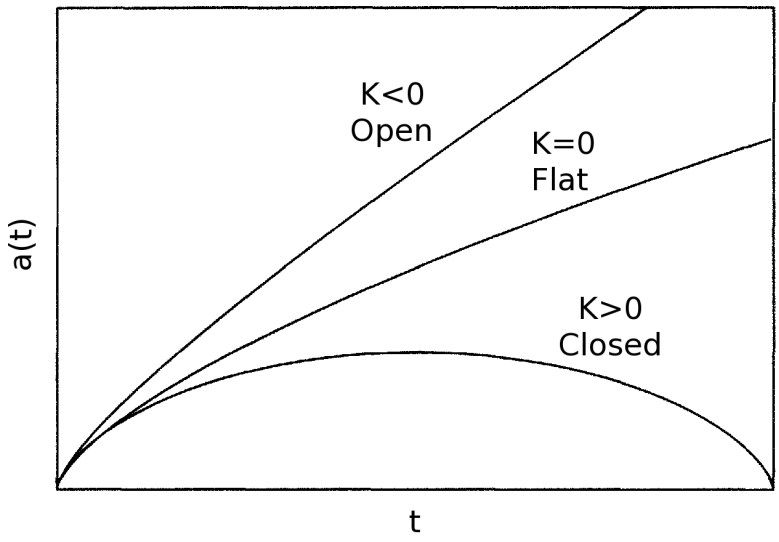

Figure 1.2: Three different possible evolutions of the Universe corresponding to the three different global geometries and ignoring the effects of dark energy. An open Universe continues to expand forever, with gravity negligibly reducing the expansion rate. The expansion rate of a flat Universe asymptotically approaches zero as $t \rightarrow \infty$. The expansion of a closed Universe is slowed by gravity and eventually stops. The Universe then contracts and ultimately collapses to a singularity called the big crunch.

If the Universe has a density greater than ρ_c, it has a spherical global geometry and is described as closed. If the density of the Universe is lower than ρ_c, the structure is hyperbolic and described as open. Figure 1.2 shows how the scale of the Universe evolves as a function of time for the three distinct cases of spatial curvature and assuming zero contribution from dark energy.

1.1.2 Density parameters

If we take the time derivative of equation (1.6) and substitute it into the acceleration equation, we can show that

$$\dot{\rho} = -3H\left(\rho + \frac{p}{c^2}\right). \tag{1.10}$$

This equation expresses the conservation of energy and is independent of the cosmological constant.

Using the equation of state (given in equation (1.5)) and the conservation of energy (equation (1.10)), we can solve the Friedmann equations for three distinct cases. A matter dominated universe exhibits zero pressure, corresponding to $\omega = 0$. A radiation dominated universe in thermal equilibrium has $\omega = 1/3$. A dark energy dominated universe corresponds to $\omega = -1$. For these three cases, the solutions to the Friedmann equations are

$$\begin{aligned} \rho_{\mathrm{m}} &= \rho_{\mathrm{m},0} a^{-3} & a(t) &\propto t^{\frac{2}{3}} & &\text{(matter dominated)}, \\ \rho_{\mathrm{r}} &= \rho_{\mathrm{r},0} a^{-4} & a(t) &\propto t^{\frac{1}{2}} & &\text{(radiation dominated)}, \\ \rho_{\Lambda} &= \rho_{\Lambda,0} & a(t) &\propto \exp(H_0 t) & &\text{(dark energy dominated)}, \end{aligned} \tag{1.11}$$

We can define the density parameter at the present epoch, Ω, as

$$\Omega = \frac{\rho_0}{\rho_{c,0}} = \frac{8\pi G \rho_0}{3H_0^2}, \tag{1.12}$$

If we assume that the Universe consists of matter, radiation, and dark energy with a constant density, we can define a density parameter for each constituent, x, as

$$\Omega_x = \frac{\rho_x(t=0)}{\rho_{c,0}} = \frac{8\pi G \rho_x(t=0)}{3H_0^2}, \tag{1.13}$$

where the dark energy density is

$$\rho_{\Lambda} = \frac{\Lambda c^2}{8\pi G}. \tag{1.14}$$

These three components now define the curvature density parameter, Ω_K, such that

$$\Omega_{\mathrm{m}} + \Omega_{\mathrm{r}} + \Omega_{\Lambda} + \Omega_K = 1, \tag{1.15}$$

with $\Omega_K = -(c/H_0)^2 K$, which has the opposite sign to the curvature, K.

Using the results of equation (1.11) and equations (1.13) and (1.15), we can write

equation (1.6) in terms of the density parameters and the Hubble parameter:

$$H(a) = H_0\sqrt{\Omega_{\rm m}a^{-3} + \Omega_{\rm r}a^{-4} + \Omega_\Lambda + \Omega_K a^{-2}}. \tag{1.16}$$

Since there is no strong physical motivation for modelling dark energy as a cosmological constant, we can assume the equation of state to be a function of the scale factor, $\omega = \omega(a)$. With this generalization, equation (1.16) is

$$H(a) = H_0\sqrt{\Omega_{\rm m}a^{-3} + \Omega_{\rm r}a^{-4} + \Omega_{\rm de}\exp\left(-3\int_1^a {\rm d}a'\frac{1+\omega(a')}{a'}\right) + \Omega_K a^{-2}}, \tag{1.17}$$

where $\Omega_{\rm de}$ is the density of dark energy at the present day epoch. In the absence of a well motivated model for dark energy, the equation of state is often parameterized by the first coefficient of a Taylor expansion as $w(a) = w_0 + w_1(1-a)$ (Chevallier & Polarski 2001; Linder 2003).

The simplest model that fits current observations is the six parameter ΛCDM model. In this model, it is assumed that $\Omega_K = 0$, $\omega = -1$, and the contribution of neutrino masses to the total density of the Universe is negligible. Assuming this model, equation (1.17) simplifies to

$$H(a) = H_0\sqrt{\Omega_{\rm m}a^{-3} + \Omega_{\rm r}a^{-4} + \Omega_\Lambda}. \tag{1.18}$$

Ignoring neutrino masses, the total matter density has a contribution from baryons, $\Omega_{\rm b}$, and cold dark matter, $\Omega_{\rm c}$. The ΛCDM model can then be described in terms of the physical baryon density, $\Omega_{\rm b}h^2$; the physical dark matter density, $\Omega_{\rm c}h^2$; the Hubble constant, H_0; the optical depth of reionization, τ; the power of the primordial curvature fluctuations at $k_0 = 0.05\,{\rm Mpc}^{-1}$, $A_{\rm s}$; and the scalar spectral index, $n_{\rm s}$. The current best-fitting values of these six parameters as measured by the Planck Collaboration et al. (2015a) are shown in Table 1.1.

One may express the RHS of equations (1.16) - (1.18) in terms of redshift. As photons travel to us from a distant event at the emitted time $t_{\rm emit}$, the frequency of the photon, ν, is decreased (or equivalently, the wavelength is increased) by the expansion

Parameter	TT,TE,EE+lowP+lensing+ext 68% limits
$\Omega_{\rm b}h^2$	0.02230 ± 0.00014
$\Omega_{\rm c}h^2$	0.1188 ± 0.0010
H_0	67.74 ± 0.46
τ	0.066 ± 0.012
$\ln(10^{10}A_{\rm s})$	3.064 ± 0.023
$n_{\rm s}$	0.9667 ± 0.0040

Table 1.1: The six cosmological parameters of the ΛCDM model measured by the Planck Collaboration et al. (2015a). These results combine Planck CMB power spectra with lensing reconstruction and external data (BAO+JLA+H_0). The external JLA data is a "joint light curve analysis" sample constructed using type Ia supernovae data from the Supernova Legacy Survey (SNLS) and the Sloan Digital Sky Survey SDSS.

of the Universe. This reduction in frequency is described by the redshift, z, and is given by

$$\frac{\nu_{\rm emit}}{\nu_0} \equiv 1 + z = \frac{a_0}{a\left(t_{\rm emit}\right)}, \tag{1.19}$$

where subscript 0 denotes $t = 0$. There are a number of methods currently used to determine an object's redshift. One method uses photometry, whereby one observes the object's brightness through various broad filters and looks for shifts in specific features, such as spectral breaks (Erben et al. 2013; Sánchez et al. 2014).

1.2 Linear structure formation

On scales $<100\,\mathrm{Mpc}$, the Universe is inhomogeneous and anisotropic. This is the regime of galaxies and galaxy clusters. The evolution of these structures is believed to have originated with tiny quantum fluctuations in the primordial inflationary cosmos. These fluctuations generated small-amplitude density inhomogeneities which produced the temperature fluctuations observed in the CMB. These inhomogeneities eventually evolved into the large-scale structure we observe today, such as dark matter filaments and galaxy halos.

In the early Universe, the small scale perturbations can be successfully studied using linear perturbation theory. The underlying theory of cosmological perturbations can be recovered from a linearized form of general relativity, though the derivation is somewhat involved. However, assuming a non-relativistic fluid, much of the required physics can be derived using a Newtonian approach (Peebles 1980; Peacock 1999).

Density fluctuations are parameterized by the density contrast

$$\delta\left(\mathbf{x},t\right)=\frac{\rho\left(\mathbf{x},t\right)-\bar{\rho}\left(t\right)}{\bar{\rho}\left(t\right)}, \tag{1.20}$$

where $\bar{\rho}\left(t\right)$ is the background density at time t and $\mathbf{x}$ is the comoving coordinate. For an ideal non-relativistic fluid, the fundamental equations governing fluid motion are the Euler equation, the continuity equation and the Poisson equation. We can linearize these equations in a comoving coordinate system to yield

$$\dot{\delta}=-\frac{1}{a}\boldsymbol{\nabla}\cdot\boldsymbol{v} \qquad \text{(continuity equation)}, \tag{1.21}$$

$$\dot{\boldsymbol{v}}+H\boldsymbol{v}=-\frac{\boldsymbol{\nabla}\delta p}{a\bar{\rho}}-\frac{1}{a}\boldsymbol{\nabla}\Phi \qquad \text{(Euler equation)}, \tag{1.22}$$

$$\nabla^{2}\Phi=4\pi Ga^{2}\bar{\rho}\delta \qquad \text{(Poisson equation)}, \tag{1.23}$$

where $\boldsymbol{v}$ is the peculiar velocity of the fluid and δp is a pressure perturbation about the background value. For the special case of a dark matter dominated universe, it can be shown that a combination of these three equations leads to the differential equation which describes the evolution of δ as

$$\ddot{\delta}+2H\dot{\delta}=4\pi G\bar{\rho}\delta. \tag{1.24}$$

Here the Hubble parameter represents the expansion of the universe and opposes gravitational collapse. This equation allows for growing modes of the form $\delta\propto t^{2/3}\propto a$, and hence, in the matter dominated era, the growth of dark matter density fluctuations is proportional to the scale factor. The presence of dark energy in the Universe

suppresses the growth of structure.

As the density contrast approaches unity, the fluid equations (equations (1.21) - (1.23)) can no longer be linearized when studying structure formation. In this case, one can trace the evolution of structure using N-body simulations. These simulations model the dark matter in a given volume as N point masses which interact through gravitational attraction. The evolution of structure can then be studied as the simulation advances through time. One example of such an N-body simulation is the publicly available GADGET-2 code introduced by Springel (2005).

1.3 Observational probes of cosmology

Cosmological probes provide a way of testing theoretical predictions and constraining cosmological models through observation. The primary focus of this thesis is weak gravitational lensing. Weak lensing probes the distribution of matter in the Universe and provides information about the late time evolution of structure. This probe is discussed in detail in the next chapter. However, weak lensing is but one of a number of probes available to present day cosmologists. Here we briefly discuss some of the alternative probes used in cosmology today.

1.3.1 Cosmic microwave background (CMB)

The early Universe ($\lesssim$380,000 after the big-bang) consisted of a hot plasma. In this period, the Universe was opaque as the photons interacted with electrons and baryons. As the Universe expanded, it cooled. At a temperature of about $3000\,\mathrm{K}$, electrons bound to protons and formed hydrogen atoms; this is known as recombination. With the electrons and protons bound in hydrogen atoms, the photons decoupled and their mean free path increased exponentially. These photons have traveled to us since decoupling and are observed at the present epoch as the CMB.

The CMB provides information about the Universe at a redshift of $z \approx 1100$. Due

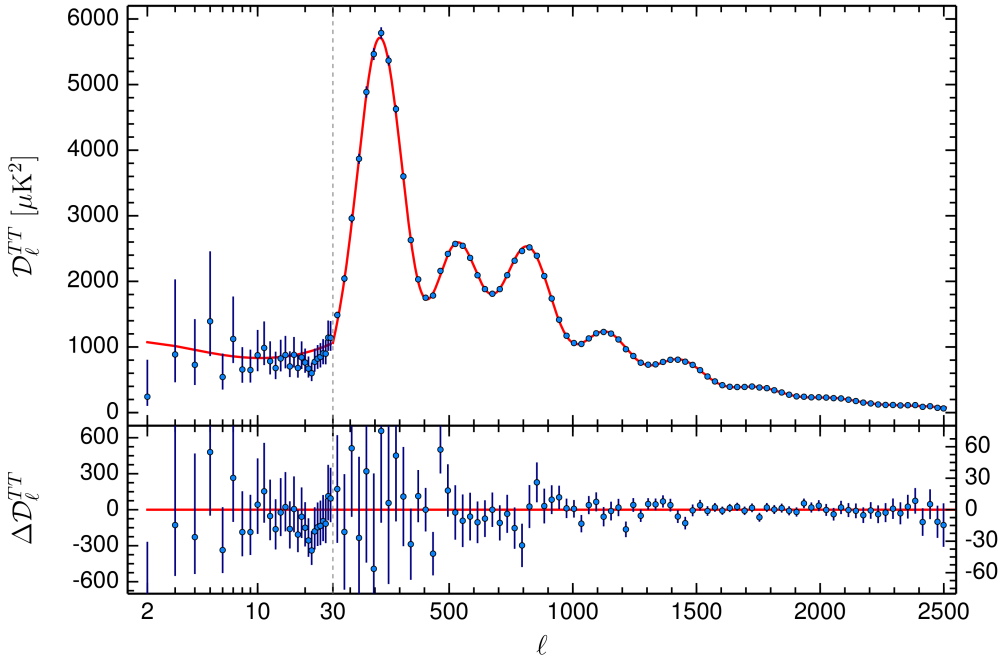

Figure 1.3: The top panel shows the Planck 2015 temperature power spectrum (Planck Collaboration et al. 2015a). The best-fit six parameter ΛCDM model is shown as the red curve. Residuals between the model and the data are shown in the bottom panel. The error bars are the 1σ uncertainties.

to the redshift of the CMB photons, the temperature of the CMB observed today is around $2.73\,\mathrm{K}$. However, at the time of recombination small density inhomogeneities produced anisotropies in the temperature. These anisotropies were first observed in 1992 by the COBE satellite (Smoot et al. 1992) and provide a snapshot of the Universe at the time of recombination.

The density fluctuations in the primordial Universe eventually seeded the growth of the large scale structure observed in the Universe today. Hence, by measuring the power spectrum of the temperature fluctuations in the CMB, we can place powerful constraints on cosmology. This method of constraining cosmology has been the primary focus of many space based, balloon based and ground based observations, such as those made by the Atacama Cosmology Telescope (ACT) (Dunkley et al. 2011), the South Pole Telescope (SPT) (Keisler et al. 2011) and the Wilkinson Microwave

Anisotropy Probe (WMAP) (Hinshaw et al. 2013). Figure 1.3 shows the temperature power spectrum measured by the Planck Collaboration et al. (2015a).

In addition to the temperature power spectrum, there is much interest in measuring the polarization properties of the CMB. It is understood that inflation in the early Universe would have generated gravitational waves which imprinted a characteristic B-mode signal in the CMB. Measuring this signal would therefore provide a means of constraining models of inflation. In 2014, BICEP2 claimed a detection of the sought after B-mode signal (Ade et al. 2014). However, later in 2014, a collaboration between the BICEP2 team and Planck showed that the B-mode detection made by BICEP2 is consistent with the signal expected from interstellar dust (Planck Collaboration et al. 2014).

1.3.2 Type Ia supernovae

Type Ia supernovae are thought to occur in binary systems where matter is accreted onto a white dwarf from a companion star. When the white dwarf reaches a critical mass of $\sim$1.44 solar masses, it explodes as a type Ia supernova. All type Ia supernovae exhibit a similar luminosity during their brightest phase and can therefore be used as a "standard candle" when estimating the relative distances of their host galaxies. As the light travels to us from the supernovae, it is also redshifted by the cosmic expansion. These two effects can be combined to provide a physical map of the expansion history of the Universe.

In 1998, observations of type Ia supernovae by two independent teams, the High-Z Supernova Search Team (Riess et al. 1998) and the Supernova Cosmology Project (Perlmutter et al. 1999), provided the unexpected observational evidence that the expansion of the Universe is accelerating. The Dark Energy Survey (DES) (The Dark Energy Survey Collaboration 2005) aims to use observations $\sim$2000 type Ia supernovae to further constrain the expansion history of the Universe

1.3.3 Baryonic acoustic oscillations

Baryonic acoustic oscillations (BAOs) provide a "standard ruler" which can also be used to constrain the expansion history. Overdensities in the primordial plasma of the early Universe gravitationally attracted matter inwards. As the matter collapsed towards the overdensity, photon-matter interactions created an outward pressure that countered the gravitational collapse and produced oscillations that traveled outward from the centre of the overdensity at just over half of the speed of light. This outward wave consisted of both baryons and photons. Dark matter interacts only gravitationally and so remained fixed at the origin of the overdensity. At around the time of recombination, the photons and baryons decoupled leaving the baryons to form a shell at a fixed radius from the origin of the overdensity. This radius is called the sound horizon.

The original overdensity at the centre of the shell and the baryonic overdensity created at sound horizon contributed to the evolution of the large scale structure observed in the present day Universe. As the Universe expands, so does the sound horizon. This implies that there should be a greater number of galaxies separated by the distance of the sound horizon at a given redshift. One can therefore statistically infer the scale of the sound horizon by looking at the separations of a large number of galaxies. One can also measure the sound horizon at recombination using the temperature anisotropies observed in the CMB. Measurements of the sound horizon at different redshifts provide another method of probing the expansion history of the Universe.

The BAO signal was first detected by the Sloan Digital Sky Survey (SDSS) in 2005 (Eisenstein et al. 2005). SDSS measured the two-point correlation function of $\sim$47000 luminous red galaxies (LRGs) and found a characteristic peak signal corresponding to a sound horizon at the present day epoch of $\sim 150\,\mathrm{Mpc}$. The measurement of the BAO signal is one of the key goals of current cosmological optical surveys, such as eBOSS (Dawson et al. 2015) and DES (The Dark Energy Survey Collaboration 2005), and future radio surveys, such as BINGO (Battye et al. 2013) and the SKA (Bull et al. 2015), are also planning to measure the signal.

1.3.4 Redshift-space distortions

Redshift-space distortions arise from the the peculiar velocities of galaxies within galaxy clusters. These peculiar velocities are caused by the gravitational attraction of the cluster and produce an additional redshift to that of the cosmic expansion (Kaiser 1987; Hamilton 1998; Percival & White 2009). This effect distorts the apparent redshift distribution of the galaxies and can be used to probe the history of structure formation and the nature of gravity on cosmological scales. The measurement of redshift space distortions is one of the primary objectives of future surveys such as the SKA (Raccanelli et al. 2015) and Euclid (Guzzo et al. 2008).

1.3.5 Galaxy clusters

Galaxy clusters are the largest gravitationally bound objects in the Universe. They are also the latest structures to form in the hierarchical scenario. Originating from high density fluctuations in the early Universe, the formation history of clusters is dependent on the underlying cosmological model, and hence by studying the properties of clusters, one can place constraints on cosmology (Allen et al. 2011). In particular, the number counts and spatial distribution of clusters can be used to place tight constraints on σ_8 and $\Omega_{\rm m}$, and by studying the distribution of clusters at multiple redshifts, one can also constrain the dark energy equation of state, ω (Wang & Steinhardt 1998; Haiman et al. 2001; Weller et al. 2002; Battye & Weller 2003; Cunha et al. 2009; Sartoris et al. 2012).

Galaxy cluster surveys have already been used to probe cosmology at various wavelengths, such as the X-ray band (e.g. using the ROSAT All-Sky Survey and the Chandra X-ray Observatory (Rapetti et al. 2013)), the optical band (e.g. using the SDSS (Rozo et al. 2010)) and using detections of clusters through their Sunyaev-Zeldovich signal in the radio band (e.g. using Planck (Planck Collaboration et al. 2015b)).

Future surveys, such as those made with Euclid (Sartoris et al. 2015), will detect a large number of clusters over a wide redshift range and thus provide data that is ideal

for performing cosmology using cluster observations.

Chapter 2

Weak gravitational lensing

Einstein's general theory of relativity describes gravitation as a consequence of the curvature of spacetime due to the presence of matter and energy. A number of predictions came from this theory, such as the existence of black holes and the existence of gravitational waves. Gravitational lensing is the prediction that light rays from distant background objects are deflected by a massive foreground object, such as a galaxy or a clump of dark matter. Such a phenomenon had already been predicted by means of a Newtonian argument. Under the assumption that light consists of particles, a Newtonian treatment of the path of a light ray passing a massive object predicts a deflection angle that is half of the magnitude of the angle predicted by general relativity. This discrepancy between the Newtonian and Einsteinian theories provided a means of testing general relativity. In 1919 during a total solar eclipse, the deflection of the light rays from a star close to the Sun's limb was shown (Dyson et al. (1920)) to follow the predictions made through general relativity and helped to confirm Einstein's theory.

Strong gravitational lensing is concerned with the large deflection of light from a background galaxy by a massive foreground object close to the line of sight, which leads to multiple images of the source galaxy; a phenomenon first observed by Walsh et al. (1979). Weak lensing is concerned with observations where the deflections of the light rays are much smaller, resulting in small distortions in the observed shapes of background galaxies. Cosmological weak lensing (or cosmic shear) aims to detect the

coherent shape distortions in the images of background galaxies due to the intervening large scale structure of the Universe. This is achieved by performing a statistical analysis of the observed shapes of the background galaxies in order to extract noisy estimates of the weak lensing distortion (or "shear") field. The effect is difficult to detect due to the intrinsic randomness of galaxy shapes, and it was only conclusively detected at the turn of the Millennium (Bacon et al. 2000; Kaiser et al. 2000; Wittman et al. 2000; Van Waerbeke et al. 2000). Since then, much progress has been made in the precision of the measurements of galaxy shapes, and weak lensing is now established as a powerful cosmological tool.

In this chapter, we outline the theoretical framework of weak gravitational lensing (an in-depth discussion can be found in Bartelmann & Schneider (2001)) and discuss how the effects of cosmic shear can be measured and used to constrain cosmological models.

2.1 Lensing deflection angle

We begin by discussing the deflection angle of light passing by a spherically symmetric lens as predicted by general relativity and viewed by a distant observer. Starting with the Einstein field equations (equation (1.1)), it can be shown that (see D'Inverno (1992) for an example of the derivation) the deflection angle, $\hat{\alpha}$, of a light ray due to a spherically symmetric lens of mass M is given by

$$\hat{\alpha} = \frac{4GM}{c^2\xi}. \tag{2.1}$$

Equation (2.1) is valid for a spherically symmetric mass with an impact parameter, ξ, (see Figure 2.1) that is much greater than the Schwarzschild radius, $r_{\rm s}$. The Schwarzschild radius is defined such that, if an object of a given mass is compressed into a sphere of radius $r_{\rm s}$, the escape velocity at the surface of the object is greater than the speed of light. Given the condition $\xi \ll r_{\rm s}$, the deflection angle will be small.

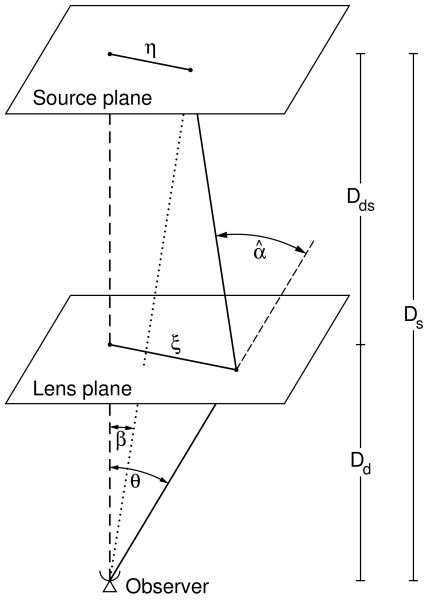

Figure 2.1: Diagram of a typical lens system (Bartelmann & Schneider (2001)).

If the gravitational field is weak, it is possible to linearize the field equations. This linearization allows us to express the total deflection angle due to an ensemble of point masses as the sum of the deflection angles due to each individual point.

Let us now consider a mass distribution with volume density $\rho(\boldsymbol{r})$ and mass element $\mathrm{d}m = \rho(\boldsymbol{r})\,\mathrm{d}V$. The path of a light ray can be described by a set of cylindrical coordinates $(\xi_1(\lambda), \xi_2(\lambda), r_3(\lambda))$, such that at large distances from the mass, the incoming light ray propagates along r_3. If it is assumed that the light ray moves along a straight line close to the mass, then the coordinates are independent of the affine parameter λ, and the total deflection angle is found by vectorially summing the individual point mass deflections, such that the total deflection angle is the two-dimensional vector

$$\begin{aligned}\hat{\boldsymbol{\alpha}} &= \frac{4G}{c^2}\sum \mathrm{d}m\,(\xi_1', \xi_2', r_3')\,\frac{\boldsymbol{\xi}-\boldsymbol{\xi'}}{|\boldsymbol{\xi}-\boldsymbol{\xi'}|^2} \\ &= \frac{4G}{c^2}\int \mathrm{d}^2\xi' \int \mathrm{d}r_3'\rho\,(\xi_1', \xi_2' r_3')\,\frac{\boldsymbol{\xi}-\boldsymbol{\xi'}}{|\boldsymbol{\xi}-\boldsymbol{\xi'}|^2}. \end{aligned} \tag{2.2}$$

We can now define the surface mass density to be

$$\Sigma\left(\boldsymbol{\xi}\right) \equiv \int \mathrm{d}r_3 \rho\left(\xi_1, \xi_2, r_3\right), \tag{2.3}$$

so that the mass density is projected onto a 2D plane which lies perpendicular to the oncoming light ray. Thus, the total deflection angle due to the mass distribution is

$$\hat{\boldsymbol{\alpha}}\left(\boldsymbol{\xi}\right) = \frac{4G}{c^2} \int \mathrm{d}^2\xi' \Sigma\left(\boldsymbol{\xi'}\right) \frac{\boldsymbol{\xi} - \boldsymbol{\xi'}}{\left|\boldsymbol{\xi} - \boldsymbol{\xi'}\right|^2}. \tag{2.4}$$

It can be shown, using the diagram in Figure 2.1 and assuming all angles to be small, that

$$\boldsymbol{\beta} = \boldsymbol{\theta} - \frac{D_{\mathrm{ds}}}{D_{\mathrm{s}}} \hat{\boldsymbol{\alpha}}\left(D_{\mathrm{d}}\boldsymbol{\theta}\right) \equiv \boldsymbol{\theta} - \boldsymbol{\alpha}\left(\boldsymbol{\theta}\right), \tag{2.5}$$

where D_{d} is the angular diameter distance from the observer to the lens, D_{s} is the angular diameter distance from the observer to the source, and D_{ds} is the angular diameter distance from the lens to the source. We have defined the angular coordinates $\boldsymbol{\beta} = \boldsymbol{\eta}/D_{\mathrm{s}}$ and $\boldsymbol{\theta} = \boldsymbol{\xi}/D_{\mathrm{d}}$, and the scaled deflection angle $\boldsymbol{\alpha}\left(\boldsymbol{\theta}\right) = \frac{D_{\mathrm{ds}}}{D_{\mathrm{s}}}\hat{\boldsymbol{\alpha}}$ has been introduced. Equation (2.5) implies that given a source with true position $\boldsymbol{\beta}$, an image will be viewed by an observer at angular position $\boldsymbol{\theta}$. If equation (2.5) has more than one solution, then multiple images of the background object are observed. We now define the dimensionless surface mass density (or convergence), $\kappa\left(\boldsymbol{\theta}\right)$, as

$$\kappa\left(\boldsymbol{\theta}\right) = \frac{\Sigma\left(D_{\mathrm{d}}\boldsymbol{\theta}\right)}{\Sigma_{\mathrm{cr}}}, \tag{2.6}$$

where Σ_{cr} is the critical mass density, and

$$\Sigma_{\mathrm{cr}} = \frac{c^2}{4\pi G} \frac{D_{\mathrm{s}}}{D_{\mathrm{d}} D_{\mathrm{ds}}}. \tag{2.7}$$

If a mass distribution has a value of $\kappa \geq 1$ (or equivalently $\Sigma \geq \Sigma_{\mathrm{cr}}$) at some position in the distribution, then multiple images will be produced for sources with a particular position $\boldsymbol{\beta}$. Lenses that produce multiple images are termed "strong" lenses. Hence, a

mass distribution that contains $\kappa \geq 1$ is a strong lens. A mass distribution where $\kappa < 1$ everywhere in the distribution is termed a "weak" lens.

Writing the scaled deflection angle in terms of κ, we obtain

$$\boldsymbol{\alpha}(\boldsymbol{\theta}) = \frac{1}{\pi}\int_{\Re^2} \mathrm{d}^2\theta' \kappa(\boldsymbol{\theta'}) \frac{\boldsymbol{\theta} - \boldsymbol{\theta'}}{|\boldsymbol{\theta} - \boldsymbol{\theta'}|^2}, \tag{2.8}$$

which can be written as the gradient of some potential, ψ, such that $\boldsymbol{\alpha} = \nabla\psi$ and

$$\psi(\boldsymbol{\theta}) = \frac{1}{\pi}\int_{\Re^2} \mathrm{d}^2\theta' \kappa(\boldsymbol{\theta'}) \ln|\boldsymbol{\theta} - \boldsymbol{\theta'}|. \tag{2.9}$$

This potential is called the deflection potential and satisfies the Poisson equation

$$\nabla^2\psi(\boldsymbol{\theta}) = 2\kappa(\boldsymbol{\theta}). \tag{2.10}$$

2.2 Linearized lensing formalism

Assuming the source is much smaller than the scale on which the properties of the lens change, we can linearly map the unlensed coordinate system to the lensed coordinate system via the Jacobian matrix

$$A_{ij} = \frac{\partial\beta_i}{\partial\theta_j} = \left(\delta_{ij} - \frac{\partial^2\psi(\boldsymbol{\theta})}{\partial\theta_i\partial\theta_j}\right). \tag{2.11}$$

It is now convenient to define the complex shear $\boldsymbol{\gamma} \equiv \gamma_1 + i\gamma_2$, where

$$\gamma_1 = \frac{1}{2}\left(\frac{\partial^2\psi(\boldsymbol{\theta})}{\partial\theta_1^2} - \frac{\partial^2\psi(\boldsymbol{\theta})}{\partial\theta_2^2}\right), \qquad \gamma_2 = \frac{\partial^2\psi(\boldsymbol{\theta})}{\partial\theta_1\partial\theta_2}. \tag{2.12}$$

With this definition, the Jacobian matrix is

$$\mathbf{A}(\boldsymbol{\theta}) = \begin{pmatrix} 1-\kappa-\gamma_1 & -\gamma_2 \\ -\gamma_2 & 1-\kappa+\gamma_1 \end{pmatrix}. \tag{2.13}$$

Liouville's theorem implies that, as no photons are absorbed or emitted during deflection, surface brightness must be conserved. Hence, the observed intensity profile of an object, $I^{\rm obs}$, can be expressed in terms of the intrinsic intensity profile, $I^{\rm int}$, as

$$I^{\rm obs}\left(\boldsymbol{\theta}\right) = I^{\rm int}\left[\boldsymbol{\beta}\left(\boldsymbol{\theta}\right)\right], \tag{2.14}$$

which, when $\boldsymbol{\beta}$ is linearized and expanded around the point $\boldsymbol{\theta}_0$, becomes

$$I^{\rm obs}\left(\boldsymbol{\theta}\right) = I^{\rm int}\left[\boldsymbol{\beta}_0 + \mathbf{A}\left(\boldsymbol{\theta}\right)\cdot\left(\boldsymbol{\theta}-\boldsymbol{\theta}_0\right)\right]. \tag{2.15}$$

The effects of the matrix $\mathbf{A}$ on an intensity profile with elliptical isophotes is to change the ellipticity of the isophotes whilst conserving the surface brightness within any given isophote. Hence, if one knows the intrinsic ellipticity of a galaxy, one could, in principle, infer the shear by measuring the galaxy's observed ellipticity. This is not possible in a real survey as the intrinsic shapes of the galaxies are unknown. Instead, the standard method of performing weak lensing is to assume that the galaxies are randomly orientated, such that the average ellipticity of a galaxy is zero. This allows an estimate of the shear to be recovered from a single galaxy image, but at the cost of an irreducible contribution from shape noise.

Comparing equations (2.14) and (2.15) and defining the magnification, μ, as the ratio of the image flux to the source flux, we find

$$\mu = \frac{1}{\det(\mathbf{A})} = \frac{1}{\left(1-\kappa\right)^2 - |\boldsymbol{\gamma}|^2}. \tag{2.16}$$

This means that, as well as the shape distortion described by the shear, there is also a magnification resulting from focusing by both the local matter density, κ, and the shear, $\boldsymbol{\gamma}$.

2.3 Cosmic shear

The results in the previous section assume a single thin lens situated along the line of sight. However, an incoming light ray will be deflected by any density perturbation along the line of sight. Using the geodesic lensing equation and assuming the gravitational potential, Φ, is slowly varying, the deflection angle can be derived as a weighted integral of the gradient of the potential perpendicular to the line of sight (see e.g. Kilbinger (2015) for a detailed discussion)

$$\boldsymbol{\alpha}\left(\boldsymbol{\theta},\chi\right)=\frac{2}{c^{2}}\int_{0}^{\chi}\mathrm{d}\chi'\frac{f_{K}\left(\chi-\chi'\right)}{f_{K}\left(\chi\right)}\boldsymbol{\nabla}_{\perp}\Phi\left[f_{K}\left(\chi'\right)\boldsymbol{\theta},\chi'\right], \tag{2.17}$$

where $f_K\left(\chi-\chi'\right)$ is the comoving angular diameter distance from the deflecting potential to the source, and $f_K\left(\chi\right)$ is the comoving angular diameter distance from the observer to the source.

Using a method analogous to that employed for the thin lens approximation, the effective convergence for a fixed redshift is now defined as

$$\kappa_{\mathrm{eff}}\left(\boldsymbol{\theta},\chi\right)=\frac{1}{2}\boldsymbol{\nabla}\cdot\boldsymbol{\alpha}\left(\boldsymbol{\theta},\chi\right). \tag{2.18}$$

For sources that have a distribution of comoving distances, the effective convergence must be averaged over the source distribution, $n\left(\chi\right)$,

$$\bar{\kappa}\left(\boldsymbol{\theta}\right)=\int_{0}^{\chi_{\mathrm{lim}}}\mathrm{d}\chi n\left(\chi\right)\kappa_{\mathrm{eff}}\left(\boldsymbol{\theta},\chi\right)=\frac{3H_{0}^{2}\Omega_{\mathrm{m}}}{2c^{2}}\int_{0}^{\chi_{\mathrm{lim}}}\mathrm{d}\chi\bar{W}\left(\chi\right)f_{K}\left(\chi\right)\frac{\delta\left(f_{K}\left(\chi\right)\boldsymbol{\theta},\chi\right)}{a\left(\chi\right)}, \tag{2.19}$$

where the lensing efficiency, $\bar{W}$, is

$$\bar{W}\left(\chi\right)=\int_{\chi}^{\chi_{\mathrm{lim}}}\mathrm{d}\chi' n\left(\chi'\right)\frac{f_{K}\left(\chi'-\chi\right)}{f_{K}\left(\chi'\right)}, \tag{2.20}$$

and χ_{lim} is the limiting comoving distance of the galaxy sample. The effective convergence therefore depends on the geometry of the universe through the distance ratios

and the distribution of galaxies as a function of redshift, with $n(\chi)\,\mathrm{d}\chi = n(z)\,\mathrm{d}z$.

2.4 The lensing power spectrum

Assuming that the convergence field is statistically homogeneous and isotropic on large scales (which is implied by the cosmological principle), we define the convergence power spectrum in Fourier space in terms of the two-point correlation function

$$\langle \tilde{\kappa}(\boldsymbol{l})\,\tilde{\kappa}^{*}(\boldsymbol{l}')\rangle = (2\pi)^{2}\,\delta_{\mathrm{D}}(\boldsymbol{l}-\boldsymbol{l}')\,P_{\kappa}(l)\,, \tag{2.21}$$

where δ_{D} is the Dirac delta function. The power spectrum depends only on the modulus of the 2D wave vector $\boldsymbol{l}$. This result assumes the flat-sky approximation, and for large scale lensing, curvature of the sky must also be accounted for (Loverde & Afshordi 2008).

Using equations (2.18) and (2.21), we can express the convergence power spectrum in terms of the density power spectrum:

$$P_{\kappa(i,j)}(l) = \frac{9H_{0}^{4}\Omega_{\mathrm{m}}^{2}}{4c^{4}}\int_{0}^{\chi_{\mathrm{lim}}}\mathrm{d}\chi\frac{\bar{W}_{i}(\chi)\,\bar{W}_{j}(\chi)}{a^{2}(\chi)}P_{\delta}\left(\frac{l}{f_{K}(\chi)},\chi\right), \tag{2.22}$$

where the subscripts i, j denote different redshift bins for the source galaxies. To derive this result, we employ the Limber projection (Limber 1953; Kaiser 1992; Hu 1999; Simon 2007; Giannantonio et al. 2012), which requires redshift bins to be much larger than the relevant fluctuations, thereby smearing out many features that would be present in the 3D density power spectrum, such as baryonic acoustic oscillations.

The convergence power spectrum in equation (2.22) is explicitly sensitive to cosmology through Ω_{m} in the pre-factor, the dependence of the lensing efficiency on the geometrical factor $f_{K}(\chi'-\chi)/f_{K}(\chi')$, the 3D matter power spectrum, P_{δ}, and its evolution with time. Hence, by measuring the matter power spectrum and assuming an underlying cosmology, one can place constraints on various cosmological parameters. This approach has already been used to constrain of a number of cosmological param-

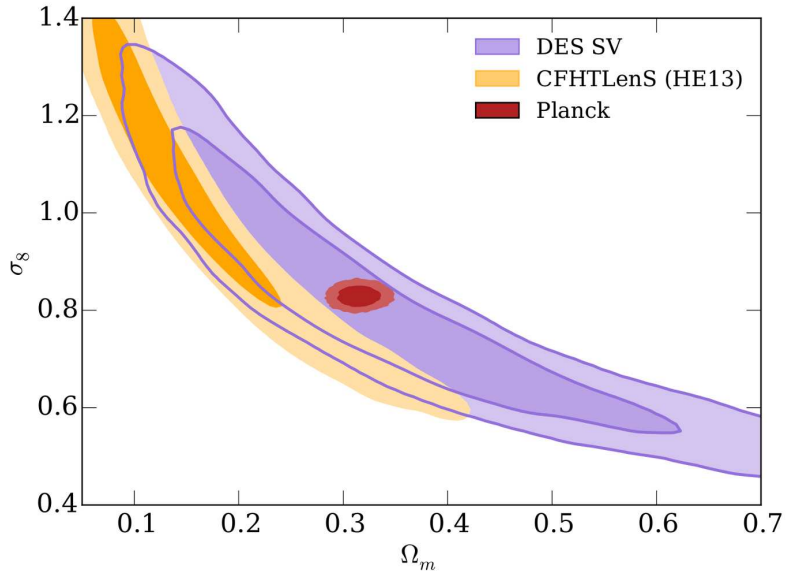

Figure 2.2: Constraints on the amplitude of fluctuations, σ_8, and the matter density parameter, $\Omega_{\rm m}$, from DES SV cosmic shear (The Dark Energy Survey Collaboration et al. 2015) (purple contours) and assuming a flat ΛCDM model. As a comparison, the constraints from Planck (Planck Collaboration et al. 2015a) (red contours), and the Canada France Hawaii Lensing Survey (CFHTLenS) (orange contours) using the correlation functions and covariances presented in Heymans et al. (2013), are also shown.

eters, such as $\Omega_{\rm m}$, the amplitude of the matter power spectrum, σ_8, (e.g. Brown et al. 2003; Hoekstra et al. 2006; Fu et al. 2008) and the dark energy equation of state (e.g. Schrabback et al. 2010; Kilbinger et al. 2013), while future surveys will provide unprecedented sensitivity to dark energy parameters (e.g. Albrecht et al. 2006; Peacock et al. 2006). Figure 2.2 shows recent constraints placed on $\Omega_{\rm m}$ and σ_8 using the Dark Energy Survey verification data (DES SV) (The Dark Energy Survey Collaboration et al. 2015).

In practice, weak lensing is typically concerned with measuring the coherent shape distortions of galaxies induced by the shear. Observed lensed background galaxies appear to align tangentially with the large scale structure of the Universe. It is this coherence that is exploited when estimating the lensing power spectrum. In analogy with the effective convergence given in equation (2.18), one can define the effective shear.

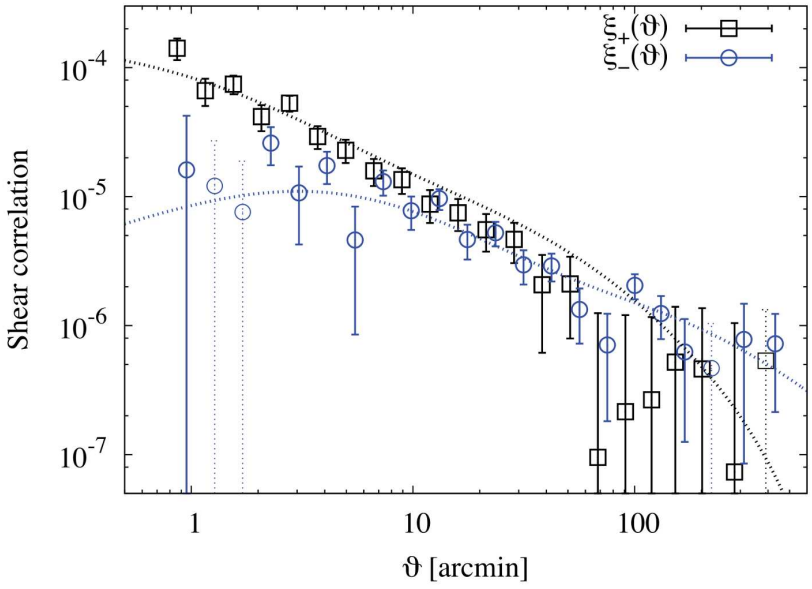

Figure 2.3: The components of the shear two-point correlation function, ξ_+ and ξ_-, measured by CFHTLenS (Kilbinger et al. 2013). The theoretical predictions using the WMAP7 best-fit cosmology (Komatsu et al. 2011) are shown as the dotted lines.

The definition of the shear in terms of the lensing potential (equation (2.12)) provides a direct link between the convergence and the shear. Through this relationship, it can be shown that the shear power spectrum is identical to the convergence power spectrum given in equation (2.22). Hence, by measuring the shear power spectrum, one can place constraints on cosmological models. This is the primary goal of weak lensing.

The most basic non-trivial observable of cosmic shear is the real-space shear two-point correlation function, which can be measured simply by correlating the observed galaxy shapes. The shear can be decomposed into a tangential component, $\gamma_{\rm t}$, and a cross-component, $\gamma_\times$, with respect to a given angular position $\boldsymbol{\theta}$:

$$\begin{aligned}\gamma_{\rm t} &= -\,\Re\left(|\boldsymbol{\gamma}|\exp\left(-2i\phi\right)\right),\\ \gamma_\times &= -\,\Im\left(|\boldsymbol{\gamma}|\exp\left(-2i\phi\right)\right),\end{aligned} \tag{2.23}$$

where ϕ is the polar angle of the vector $\boldsymbol{\theta}$. We can then define the shear two-point

correlation function in terms of the lensing power spectrum (Kaiser 1992) as

$$\xi_{\pm}\left(\boldsymbol{\theta}\right) = \left\langle \gamma_{\mathrm{t}}\left(\boldsymbol{\theta}'\right)\gamma_{\mathrm{t}}\left(\boldsymbol{\theta}-\boldsymbol{\theta}'\right)\right\rangle \pm \left\langle \gamma_{\times}\left(\boldsymbol{\theta}'\right)\gamma_{\times}\left(\boldsymbol{\theta}-\boldsymbol{\theta}'\right)\right\rangle = \int \frac{ldl}{2\pi} P_{\kappa} J_{0/4}\left(l\theta\right), \quad (2.24)$$

where $J_{0/4}$ are the zeroth-order and fourth-order Bessel functions, which correspond to the ξ_{+} and ξ_{-} correlation functions respectively. Figure 2.3 shows the correlation functions measured by CFHTLenS (Kilbinger et al. 2013).

2.5 Principles of galaxy shape estimation

In order to estimate the shear, one must first measure the shape of a galaxy. The effect of shear changes the ellipticity of an elliptical object. However, galaxy morphologies are irregular and not generally elliptical in nature. Therefore, one must seek a way of defining galaxy shapes in a model independent way.

To achieve this, Blandford et al. (1991) defined the quadrupole moments of the surface brightness as

$$Q_{ij} = \frac{\int \mathrm{d}^2\theta q_I\left[I\left(\boldsymbol{\theta}\right)\right]\left(\theta_i - \bar{\theta}_i\right)\left(\theta_j - \bar{\theta}_j\right)}{\int \mathrm{d}^2\theta q_I\left[I\left(\boldsymbol{\theta}\right)\right]}, \quad (2.25)$$

where $I\left(\boldsymbol{\theta}\right)$ is the surface brightness of the image at position $\boldsymbol{\theta}$ and $\bar{\boldsymbol{\theta}}$ is the centre of the galaxy image, defined as

$$\bar{\boldsymbol{\theta}} \equiv \frac{\int \mathrm{d}^2\theta q_I\left[I\left(\boldsymbol{\theta}\right)\right]\boldsymbol{\theta}}{\int \mathrm{d}^2\theta q_I\left[I\left(\boldsymbol{\theta}\right)\right]}, \quad (2.26)$$

with $q_I(I)$ chosen as a suitable weighting function which causes the integrals of equations (2.25) and (2.26) to converge whilst preserving the shape of the galaxy. It is now possible to define the size of the image as the trace of $\mathbf{Q}$ and the shape of the image as the traceless part of $\mathbf{Q}$ which contains the ellipticity information. From this, we can

obtain different definitions of ellipticity parameters, two of which are given as

$$\boldsymbol{\chi} \equiv \frac{Q_{11} - Q_{22} + 2iQ_{12}}{Q_{11} + Q_{22}}, \tag{2.27}$$

$$\boldsymbol{\epsilon} \equiv \frac{Q_{11} - Q_{22} + 2iQ_{12}}{Q_{11} + Q_{22} + 2\left(Q_{11}Q_{22} - Q_{12}^2\right)^{1/2}}. \tag{2.28}$$

For a circular image, $Q_{11} = Q_{22}$ and $Q_{12} = Q_{21} = 0$. Hence, as required, both of the above definitions are zero for a circle. Equations (2.27) and (2.28) can also be expressed in polar form (and similarly for the shear) as

$$\begin{aligned} \boldsymbol{\epsilon} &= |\boldsymbol{\epsilon}| \exp\left(2i\alpha\right), \\ \boldsymbol{\chi} &= |\boldsymbol{\chi}| \exp\left(2i\alpha\right), \end{aligned} \tag{2.29}$$

where α is the position angle with respect to a set of principle axes. The factor of two before α in equation (2.29) ensures that the ellipticity is invariant under a rotation of 180°. If the object under observation has elliptical isophotes, then α is the position angle of the major axis and (Miralda-Escude 1991)

$$\begin{aligned} |\boldsymbol{\epsilon}| &= \frac{(1-r)}{(1+r)}, \\ |\boldsymbol{\chi}| &= \frac{(1-r^2)}{(1+r^2)}, \end{aligned} \tag{2.30}$$

where r is the ratio of the minor and major axes.

The quadrupole moments of the intrinsic galaxy surface brightness, $Q_{ij}^{\rm int}$, are related to the quadrupole moments of the image, $Q_{ij}^{\rm obs}$, via the transformation (Kochanek 1990)

$$\mathbf{Q}^{\rm int} = \mathbf{A}^T \mathbf{Q}^{\rm obs} \mathbf{A}, \tag{2.31}$$

where the Jacobian matrix $\mathbf{A}$ is evaluated at the image position $\bar{\boldsymbol{\theta}}$. Upon defining the reduced shear, $\boldsymbol{g}$, as

$$\boldsymbol{g}(\boldsymbol{\theta}) \equiv \frac{\boldsymbol{\gamma}(\boldsymbol{\theta})}{1 - \kappa(\boldsymbol{\theta})}, \tag{2.32}$$

it can be shown (Seitz & Schneider 1997) that the intrinsic ellipticity, $\boldsymbol{\epsilon}^{\rm int}$, can be written in terms of the observed ellipticity, $\boldsymbol{\epsilon}^{\rm obs}$,

$$\boldsymbol{\epsilon}^{\rm int} = \begin{cases} \frac{\boldsymbol{\epsilon}^{\rm obs} - \boldsymbol{g}}{1 - \boldsymbol{g}^{*}\boldsymbol{\epsilon}^{\rm obs}} & \text{for} |\boldsymbol{g}| \leq 1, \\ \frac{1 - \boldsymbol{g}\boldsymbol{\epsilon}^{\rm obs^{*}}}{\boldsymbol{\epsilon}^{\rm obs^{*}} - \boldsymbol{g}^{*}} & \text{for} |\boldsymbol{g}| > 1, \end{cases} \tag{2.33}$$

where the asterisk denotes complex conjugation. A similar treatment of the ellipticity definition $\boldsymbol{\chi}$, given in equation (2.27), yields

$$\boldsymbol{\chi}^{\rm int} = \frac{\boldsymbol{\chi}^{\rm obs} - 2\boldsymbol{g} + \boldsymbol{g}^{2}\boldsymbol{\chi}^{\rm obs^{*}}}{1 + |\boldsymbol{g}|^{2} - \Re\left(\boldsymbol{g}\boldsymbol{\chi}^{\rm obs^{*}}\right)}. \tag{2.34}$$

If we assume a value of $\kappa << 1$, which is the case when we are working well within the weak lensing regime, then we have $|\boldsymbol{\gamma}| << 1$ and $|\boldsymbol{g}| << 1$. Hence, from equations (2.32), (2.33) and (2.34), and provided $\left|\boldsymbol{\epsilon}^{\rm int}\right| \lesssim 1/2$, it is clear that

$$\begin{aligned} \boldsymbol{\epsilon}^{\rm obs} &\approx \boldsymbol{\epsilon}^{\rm int} + \boldsymbol{\gamma}, \\ \boldsymbol{\chi}^{\rm obs} &\approx \boldsymbol{\chi}^{\rm int} + 2\boldsymbol{\gamma}. \end{aligned} \tag{2.35}$$

If the average intrinsic ellipticity of a galaxy is zero, it can be shown from equation (2.33) that

$$\left\langle \boldsymbol{\epsilon}^{\rm obs} \right\rangle = \boldsymbol{g}. \tag{2.36}$$

If we now assume that a group of galaxies are observed at a given redshift and that the average source ellipticity is zero, an unbiased estimator of the average reduced shear is given by

$$\hat{\boldsymbol{g}} = \frac{\sum_{i=1}^{N} u_i \boldsymbol{\epsilon}_i}{\sum_{i=1}^{N} u_i}, \tag{2.37}$$

where u_i is a suitably chosen weight function. Assuming a negligible error on the ellipticity measurements and a uniform weighting, this estimator has a r.m.s error of $\sigma_g \approx \sigma_\epsilon N^{-1/2}$, where σ_ϵ is the 1D dispersion of the intrinsic ellipticities of the source galaxies.

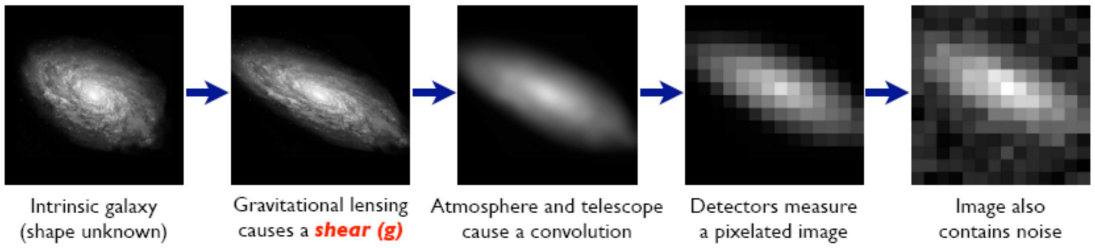

Figure 2.4: An example of how shear, atmospheric and instrumental PSF, pixelization and noise modify the image of an observed source galaxy.

For the ellipticity definition $\boldsymbol{\chi}$, assuming that the mean intrinsic ellipticity is zero, we have

$$\left\langle \boldsymbol{\chi}^{\mathrm{int}} \right\rangle = \left\langle \frac{\boldsymbol{\chi}^{\mathrm{obs}} - 2\boldsymbol{g} + \boldsymbol{g}^2 \boldsymbol{\chi}^{\mathrm{obs}^*}}{1 + |\boldsymbol{g}|^2 - \Re\left(\boldsymbol{g}\boldsymbol{\chi}^{\mathrm{obs}^*}\right)} \right\rangle = 0, \tag{2.38}$$

which has no analytic solution. Instead, one must either solve for the solution numerically or by performing a Taylor expansion around $\boldsymbol{g} = 0$. A first-order Taylor expansion yields the approximate solution

$$\hat{\boldsymbol{g}} \approx \frac{\left\langle \boldsymbol{\chi}^{\mathrm{obs}} \right\rangle}{2} \left(\frac{1}{1 - \sigma_\chi^2} \right), \tag{2.39}$$

where the term in brackets is the shear responsivity.

2.6 Measuring the shapes of galaxies

In order to perform weak lensing, one requires accurate measurements of the galaxy shapes. For any realistic weak lensing survey, measurements of galaxy shapes need to be recovered from noisy, pixelized images. These images are convolved with an instrumental and/or atmospheric point spread function (PSF). An example of how these effects distort a galaxy image can be seen in Figure 2.4. If one is to recover accurate measurements of galaxy shapes, these effects must be accounted for. There are generally two classes of shape measurement techniques (Viola et al. 2014); these are the moments-based and the model-based methods.

2.6.1 Moments-based methods

Moments-based methods measure the ellipticity of a galaxy by calculating the quadrupole moments of the light distribution of the pixelized galaxy image. Examples of this approach include the Kaiser-Squires-Broadhurst (KSB) method (Kaiser et al. 1995) and the DEIMOS method (Melchior et al. 2011). The moments-based approach provides a model independent estimate of the galaxy shape. It was first developed for the KSB method, which estimates the shear using the definition of ellipticity given in equation (2.27).

The KSB method is built on the assumption that the distortion of the galaxy image due to convolution with an anisotropic PSF can be described by a small but highly anisotropic component convolved with a large circularly symmetric disk. With this assumption, it is possible to define an approximate corrected galaxy ellipticity, $\boldsymbol{\chi}^{\rm cor}$, in terms of the observed ellipticity, $\boldsymbol{\chi}^{\rm obs}$, as

$$\chi^{\rm cor}_{\alpha} = \chi^{\rm obs}_{\alpha} - P^{\rm sm}_{\alpha\beta} p_{\beta}, \tag{2.40}$$

where $P^{\rm sm}_{\alpha\beta}$ is a tensor describing how easily the galaxy responds to the PSF. The vector p_{β} describes the PSF ellipticity and is given as

$$p_{\beta} = \left(P^{\rm sm^*}\right)^{-1}_{\beta\mu} \chi^{\rm obs^*}_{\mu}. \tag{2.41}$$

The isotropic smearing due to the atmosphere and a circular weighting function are accounted for by introducing the pre-seeing shear polarizability tensor, $P^{\gamma}_{\alpha\beta}$, (Luppino & Kaiser 1997) which describes how easily the galaxy responds to the shear. This allows the shear to be estimated such that

$$\hat{\gamma}_{\alpha} = \left(P^{\gamma}\right)^{-1}_{\alpha\beta} \left[\chi^{\rm obs}_{\beta} - P^{\rm sm}_{\beta\mu} p_{\mu}\right]. \tag{2.42}$$

The KSB method has been widely employed with success in previous weak lensing

studies (e.g. Romano et al. (2010)). It also has the benefit of being model independent. However, to fully exploit future weak lensing surveys, one requires very accurate estimates of the shear. The assumption of the PSF model in the KSB method is often insufficient to recover shear estimates with this accuracy (Kuijken 1999). The KSB method is also found to be more accurate for low elliptical PSFs, low elliptical galaxies and small shear values (Viola et al. 2011).

2.6.2 Model-based methods

Model-based methods fit a parametrized galaxy model to a pixelized galaxy image by finding the extremum of a loss function. Examples of this approach include `lensfit` (Miller et al. 2007; Kitching et al. 2008), `IM3SHAPE` (Zuntz et al. 2013) and `NGMIX` (Sheldon 2014).

As an example, `IM3SHAPE` uses a maximum-likelihood technique to fit a galaxy model consisting of an elliptical bulge component and an elliptical disc component to the galaxy image. It is assumed that each component can be described by a Sérsic profile. The likelihood fit incorporates the applied PSF, which must be provided to `IM3SHAPE` as either a known function or a high signal-to-noise star field image.

Model-based methods require prior assumptions about the galaxy shapes and morphologies. The shapes of the galaxies are usually assumed to be elliptical. In reality, galaxies are not elliptical, and this assumption can result in model biases propagating into the shear estimates (Voigt & Bridle 2010).

The model-based approach has recently been used to analyse galaxy images for a number of weak lensing surveys. These include the application of an improved version of `lensfit` to the CFHTLenS data (Miller et al. 2013), and the application of `IM3SHAPE` and `NGMIX` to the Dark Energy Survey verification data (Becker et al. 2015; Jarvis et al. 2015).

2.6.3 Lensing using galaxy orientations

Isotropic PSFs reduce the apparent ellipticity of a galaxy shape. Incorrectly calibrating for this effect can lead to multiplicative biases in shear estimates recovered using galaxy ellipticities. Based on an idea originally proposed by Kochanek (1990), Schneider & Seitz (1995) were able to show that, in the limit of $\boldsymbol{\gamma} \ll 1$, galaxy position angle measurements alone can yield surprisingly accurate shear estimates. This method has the advantage that the orientation of a galaxy is unaffected by convolution with an isotropic PSF[1]. Defining the complex distortion as

$$\boldsymbol{\delta} \equiv \frac{2\boldsymbol{g}}{1+|\boldsymbol{g}|^2}, \tag{2.43}$$

and defining the probability distribution of the modulus of the intrinsic ellipticities as $f_{\rm int}\left(\left|\boldsymbol{\chi}^{\rm int}\right|\right)$, Schneider & Seitz (1995) were able to show that, in the full nonlinear regime, the probability distribution for the angle ψ, $f_a\left(\psi\right)$, is found to be

$$\begin{aligned} f_a\left(\psi\right) =& 2\int_0^1 \mathrm{d}\left|\boldsymbol{\chi}^{\rm obs}\right| \left|\boldsymbol{\chi}^{\rm obs}\right| f_{\rm int}\left(\sqrt{1-\frac{\left(1-|\boldsymbol{\delta}|^2\right)\left(1-|\boldsymbol{\chi}^{\rm obs}|^2\right)}{\left(1-|\boldsymbol{\delta}|\left|\boldsymbol{\chi}^{\rm obs}\right|\cos\left(2\psi\right)\right)^2}}\right) \\ & \times \frac{\left(1-|\boldsymbol{\delta}|^2\right)^{3/2}}{\left[1-|\boldsymbol{\delta}|\left|\boldsymbol{\chi}^{\rm obs}\right|\cos\left(2\psi\right)\right]^3}. \end{aligned} \tag{2.44}$$

The angle ψ has the range $-\pi/2 < \psi < \pi/2$ and is defined as the angle between the major axis of the image ellipse and the local direction of $\boldsymbol{\delta}$, such that, if $\boldsymbol{\chi}^{\rm obs} = \left|\boldsymbol{\chi}^{\rm obs}\right|\exp\left(i2\alpha\right)$ and $\boldsymbol{\delta} = |\boldsymbol{\delta}|\exp\left(i2\phi\right)$, then $\psi = \alpha - \phi$. The different angles are illustrated in Figure 2.5. In their analysis, Schneider and Seitz assume that $f_{\rm int}$ is a truncated Gaussian distribution with a dispersion of σ_χ. Given the probability distribution of equation (2.44), the mean $\cos\left(2\psi\right)$ is

$$\left\langle\cos\left(2\psi\right)\right\rangle = \int_{-\pi/2}^{\pi/2} \mathrm{d}\psi f_a\left(\psi\right)\cos\left(2\psi\right), \tag{2.45}$$

[1]The orientation of a galaxy is only unaffected by convolution with an isotropic PSF if the galaxy has no rotation in its isophotes.

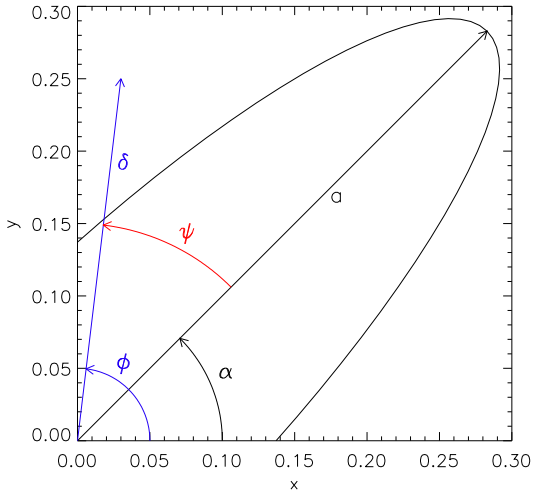

Figure 2.5: An illustration of the different angles used by Schneider & Seitz (1995). The elliptical contour represents the observed galaxy in the image plane. The vector $\boldsymbol{a}$ is the semi-major axis of the observed galaxy. This defines the observed position angle of the galaxy, α. The local distortion, $\boldsymbol{\delta}$, is the blue vector, which has the position angle ϕ. The angle ψ is the difference between these two angles.

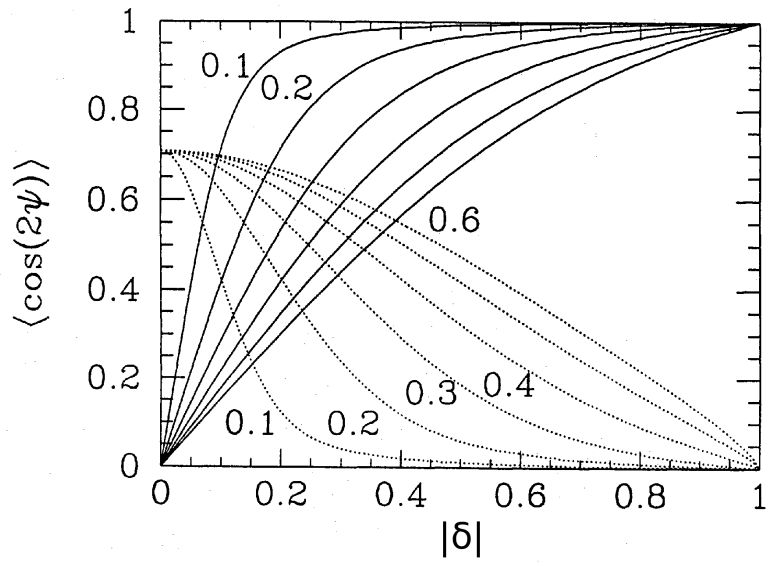

Figure 2.6: The mean cosine, $\langle \cos(2\psi) \rangle$, (solid lines) and the dispersion, $\sigma(\cos(2\psi))$, (dotted lines) as a function of $|\boldsymbol{\delta}|$. The curves are labeled by the value of $\sqrt{2}\sigma_\chi$ (Schneider & Seitz (1995)).

which has the dispersion

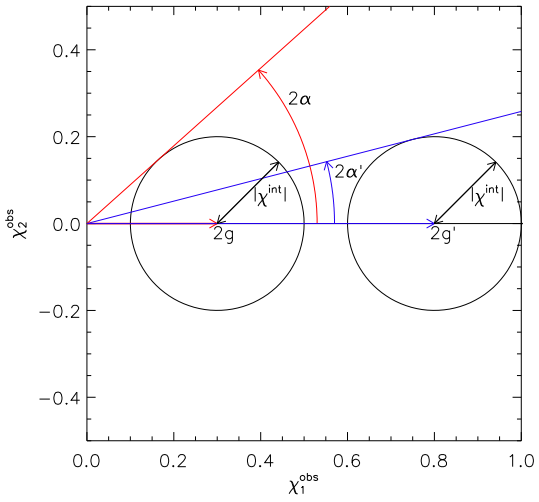

Figure 2.7: A simplified illustration of the dependence of the mean cosine on the shear where, for simplicity, we assume that $\boldsymbol{\chi} = \boldsymbol{\chi}^{\rm int} + 2\boldsymbol{g}$. For a small shear in the direction of χ_1, g, and for a fixed value of $\left|\boldsymbol{\chi}^{\rm int}\right|$, the maximum value that the observed position angle can obtain given a uniformly distributed set of intrinsic position angles is shown as α. For a large shear, g', the maximum position angle is α'. It is clear that $\alpha' < \alpha$, and that the difference in these position angles depends on the values of the shears. The mean cosine of the observed position angles given a constant value of $\left|\boldsymbol{\epsilon}^{\rm int}\right|$ will be greater for the case of the larger shear than for the case of the smaller shear as the position angles are confined to a tighter region about zero. For the case of a zero shear, the observed position angles are distributed uniformly, and the mean cosine is zero. For this simplified model, as the shear approaches infinity, the range of observed position angles becomes a tighter about zero and the mean cosine asymptotes to one. For the case of the lensing transformations given in equations (2.33) and (2.34), it can be shown that $\langle\cos\left(2\alpha\right)\rangle = 1$, when $|\boldsymbol{g}| = 1$.

$$\sigma\left(\cos\left(2\psi\right)\right) = \sqrt{\langle\cos^2\left(2\psi\right)\rangle - \langle\cos\left(2\psi\right)\rangle^2}. \tag{2.46}$$

Looking at Figure 2.6, it clear that $\langle\cos\left(2\psi\right)\rangle$ increases as $|\boldsymbol{\delta}|$ increases. The dependence of the mean cosine on the shear is illustrated in Figure 2.7. Therefore, one can recover an estimate of the distortion by calculating the value of $\langle\cos\left(2\psi\right)\rangle$ from the observed data and then numerically inverting the function, $\langle\cos\left(2\psi\right)\rangle\left(|\boldsymbol{\delta}|\right)$.

In Chapter 3, we extend the idea of using only galaxy orientations to recover estimates of the shear by constructing a position angle-only shear estimator under the assumption that we have a knowledge of the intrinsic ellipticity distribution. We apply

this method to the CFHTLenS data and show that our results are consistent with those recovered using full ellipticity information. We generalize the approach to incorporate the effects of an anisotropic PSF in Chapter 4, where we test the method on the GREAT3 simulations and demonstrate that our approach yields shear estimates with a performance comparable with existing well established shape measurement techniques.

2.7 Intrinsic alignments

When performing weak lensing, we are usually interested in the shear two-point correlation function. However, we cannot measure this directly. Instead, we measure the correlations of galaxy ellipticities. If we assume that we are working well in the weak lensing regime, the observed ellipticity of a galaxy can be written as

$$\boldsymbol{\epsilon}^{\rm obs} = \boldsymbol{\epsilon}^{\rm int} + \boldsymbol{\gamma}. \tag{2.47}$$

Assuming that $\boldsymbol{\epsilon}^{\rm int}$ is drawn from a random distribution, and hence there is zero intrinsic shape correlation between galaxy pairs, the two-point correlation function of the ellipticities is

$$\begin{aligned}\left\langle \boldsymbol{\epsilon}_i^{\rm obs}\boldsymbol{\epsilon}_j^{\rm obs}\right\rangle &= \left\langle \boldsymbol{\epsilon}_i^{\rm int}\boldsymbol{\epsilon}_j^{\rm int}\right\rangle + \left\langle \boldsymbol{\epsilon}_i^{\rm ran}\boldsymbol{\gamma}_j\right\rangle + \left\langle \boldsymbol{\gamma}_i\boldsymbol{\epsilon}_j^{\rm ran}\right\rangle + \left\langle \boldsymbol{\gamma}_i\boldsymbol{\gamma}_j\right\rangle \\ &\approx \left\langle \boldsymbol{\gamma}_i\boldsymbol{\gamma}_j\right\rangle . \end{aligned} \tag{2.48}$$

where the subscripts i and j correspond to two galaxies separated by angle θ. This result relies on the assumption that the source galaxies are randomly orientated, that is, there is zero intrinsic alignment (IA) of the source galaxies. However, tidal effects during galaxy formation can cause galaxies to align radially with the large scale structure of the Universe. Non-zero IA signals were predicted as early as 2000 (Heavens et al. 2000; Croft & Metzler 2000; Crittenden et al. 2001; Catelan et al. 2001), with a

subsequent detection being made in low-redshift surveys soon after this (Brown et al. 2002).

If we model the effect of IA, $\boldsymbol{\gamma}^{\mathrm{IA}}$, on a galaxy's observed ellipticity as (see e.g. Troxel & Ishak (2015))

$$\boldsymbol{\epsilon}^{\mathrm{obs}} = \boldsymbol{\epsilon}^{\mathrm{ran}} + \boldsymbol{\gamma}^{\mathrm{IA}} + \boldsymbol{\gamma}, \tag{2.49}$$

where the vector $\boldsymbol{\epsilon}^{\mathrm{ran}}$ is the random component of the galaxy's intrinsic ellipticity, the correlation function of the ellipticities is

$$\left\langle \boldsymbol{\epsilon}_i^{\mathrm{obs}} \boldsymbol{\epsilon}_j^{\mathrm{obs}} \right\rangle = \left\langle \boldsymbol{\gamma}_i^{\mathrm{IA}} \boldsymbol{\gamma}_j^{\mathrm{IA}} \right\rangle + \left\langle \boldsymbol{\gamma}_i^{\mathrm{IA}} \boldsymbol{\gamma}_j \right\rangle + \left\langle \boldsymbol{\gamma}_i \boldsymbol{\gamma}_j^{\mathrm{IA}} \right\rangle + \left\langle \boldsymbol{\gamma}_i \boldsymbol{\gamma}_j \right\rangle . \tag{2.50}$$

The first term on the right hand side is the IA two-point correlation function or II term. The next two terms, the GI terms, are more problematic and correspond to correlations between the IA and shear signals (Hirata & Seljak 2004). The shear tends to align galaxies tangentially with the large scale structure and the IA tends to align them radially. This manifests as an anti-correlation between the shear and IA signals. Therefore, the GI terms contribute a negative signal to the observed correlation functions. The sum of these two effects biases measurements of the shear power spectra in the standard approach. Although it has not had a significant impact on the present generation of surveys (e.g. Heymans et al. (2012)), it is likely to be important in forthcoming surveys such as those performed by, for example, DES (The Dark Energy Survey Collaboration 2005), Euclid (Cimatti & Scaramella 2012) and the LSST (LSST Dark Energy Science Collaboration 2012).

A number of methods have already been used to mitigate the impact of intrinsic alignments (see Kirk et al. (2015) for an in-depth discussion). These techniques generally require either downweighting potentially useful information or an accurate knowledge of the physics behind IA.

One method for removing the effects of IA is to assume a parameterized model for the contribution of the II and GI signals. However, this method is only reliable if one has an accurate knowledge of the functional forms of these systematics (Kitching

et al. 2009). This knowledge is difficult to achieve due to the current uncertainty in the physics governing galaxy formation and evolution. A linear alignment model which introduced a single free parameter was used to mitigate intrinsic alignments for the CFHTLenS analysis (Heymans et al. 2013). Including this free parameter increased the uncertainty on estimates of $\sigma_8 \left(\Omega_{\rm m}/0.27\right)^{\alpha}$ by 30%. The models fitted for the CFHTLenS analysis indicated a positive contribution for the GI terms. As discussed above, the GI terms are expected to contribute a negative signal, and if confirmed by future surveys, this contradiction could indicate that a single-parameter linear alignment model is too simplistic to be applied to future large-scale lensing surveys (Troxel & Ishak 2015). Bridle & King (2007) presented a more general technique which introduces a parameterized set of models which differ from a base model through some well-motivated parameter space. Using a base nonlinear alignment model, a parameterization with an arbitrary amplitude and redshift dependence, and allowing for scale dependence, Bridle & King (2007) demonstrated that increasing the freedom in the model reduces the figure of merit for constraints. However, one may increase the constraining power of this approach by including galaxy position information (Troxel & Ishak 2015).

Nulling is another approach for removing the GI systematic. This approach involves weighting the shear signal by redshift in such a way as to reduce the contribution from the GI signal. This is possible as the GI signal exhibits a different geometry and redshift dependence to the shear (Joachimi & Schneider 2008, 2009). By constructing a new measure of the shear signal with a reweighted redshift distribution, one may downweight the contribution from GI and reduce its effect on cosmological constraints. However, there is an inevitable decrease in statistical power due to the downweighting of part of the shear signal.

Morales (2006) proposed a method of estimating the shear using radio HI observations to construct galaxy velocity maps. Weak lensing changes the rotation axis of the galaxy such that it appears inconsistent with the observed galaxy shape. This method is insensitive to the impact of IA as one is concerned only with the difference between

the expected and observed rotation axis and not the ellipticity of the galaxy. In a similar approach, Huff et al. (2013) suggested using the Tully-Fisher relation (Tully & Fisher 1977) to determine the intrinsic inclination, and thus the intrinsic ellipticity of a galaxy, from velocity maps constructed using information from spectroscopic surveys. Both of these methods require well resolved galaxy velocity maps, but with the reduction in galaxy shape noise, they are promising techniques for estimating the shear in future weak lensing analyses. By avoiding the effects of IA or directly estimating the intrinsic ellipticities of the galaxies, we no longer require an accurate knowledge of the physics behind IA or the downweighting of a potentially useful shear signal.

In Chapter 5, we discuss novel methods which also avoid these requirements by using information from forthcoming radio observations. In particular, we build upon the idea first proposed by Brown & Battye (2011b) which suggests using radio polarization information from star forming galaxies as a tracer of their intrinsic orientation. We show that this information can be effectively incorporated into a variety of shear estimators and demonstrate that the bias due to IA can be successfully removed from shear power spectra reconstructions.

Chapter 3

Weak lensing using only galaxy position angles

We develop a method for performing a weak lensing analysis using only measurements of galaxy position angles. By analysing the statistical properties of the galaxy orientations given a known intrinsic ellipticity distribution, we show that it is possible to obtain estimates of the shear by minimizing a χ^2 statistic. The method is demonstrated using simulations where the components of the intrinsic ellipticity are taken to be Gaussian distributed. Uncertainties in the position angle measurements introduce a bias into the shear estimates which can be reduced to negligible levels by introducing a correction term into the formalism. We generalize our approach by developing an algorithm to obtain direct shear estimators given any azimuthally symmetric intrinsic ellipticity distribution. We introduce a method of measuring the position angles of the galaxies from noisy pixelized images and propose a method to correct for biases which arise due to pixelization and correlations between measurement errors and galaxy ellipticities. We also develop a method to constrain the sample of galaxies used to obtain an estimate of the intrinsic ellipticity distribution such that fractional biases in the resulting shear estimates are below a given threshold value. We demonstrate the angle-only method by applying it to simulations where the ellipticities are taken to

follow a log-normal distribution. We compare the performance of the position angle only method with the standard method based on full ellipticity measurements by reconstructing lensing convergence maps from both numerical simulations and from the CFHTLenS data. We find that the difference between the convergence maps reconstructed using the two methods is consistent with noise.

3.1 Introduction

The standard method of performing a weak lensing analysis requires measurements of the ellipticities of a set of background galaxies. These measurements require the application of complex correction and/or fitting algorithms (e.g. Kaiser et al. 1995; Bridle et al. 2002; Miller et al. 2007; Kitching et al. 2008), which can introduce systematic biases into the measurements if the point spread function is not accurately accounted for, or if the prior galaxy model is incorrect. In order to achieve unbiased ellipticity estimates, these algorithms generally require the application of additive and multiplicative calibration corrections derived from simulations (see e.g. Heymans et al. 2012). If the multiplicative bias is identical for both components of the ellipticity, then this bias will be absent from the unit vectors that describe the galaxy orientation. It is therefore conceivable that measurements of the orientations of galaxies will not be subject to the multiplicative biases inherent in the full ellipticity analysis and may consequently be more robust to residual biases resulting from an incorrect calibration.

In this chapter, we describe a method for performing weak lensing using only the measurements of the position angles of a set of background galaxies. Based on an original suggestion by Kochanek (1990), this approach was first explored in Schneider & Seitz (1995), where it was assumed that the modulus of the intrinsic ellipticities follows a Gaussian distribution. Under this assumption, it was shown that the mean unit vectors describing the galaxy position angles can be written as a function of the complex distortion (see Subsection 2.6.3). By inverting this relationship, Schneider & Seitz (1995) were able to obtain an estimate of both the modulus and the orientation of

the lensing distortion field.

Working in the regime of weak lensing, this chapter develops the ideas presented in Schneider & Seitz (1995). Under the assumption of an azimuthally symmetric (in the $\{\epsilon_1, \epsilon_2\}$ plane) intrinsic ellipticity distribution and a prior knowledge of the ellipticity dispersion, we develop a χ^2 statistic in Section 3.2 which can be minimized numerically in order to obtain estimates of the shear. It is found that inherent biases arise from measurement errors on the position angles. However, a method for reducing these biases to negligible levels is then proposed. In Section 3.3, we develop a method of measuring the position angles of galaxies from noisy pixelized images. We use the position angle measurements to recover shear estimates and compare the performance of this method with the KSB method, where full ellipticity information is used. In Section 3.4, we investigate the impact of an imperfect knowledge of the intrinsic ellipticity distribution. We place constraints on the size of the sample of galaxies and the errors on the ellipticity measurements used to estimate the distribution necessary to ensure that biases in the shear estimates resulting from an imperfect distribution are below a given threshold value. We compare the performance of the position angle-only approach with the standard (full ellipticity) approach by performing mass reconstructions using simulated data (Section 3.5) and using the data from the Canada France Hawaii Lensing Survey (CFHTLenS, Section 3.6). We conclude with a discussion in Section 3.7.

3.2 Constructing angle-only shear estimators

The standard method for performing a weak lensing measurement involves averaging over the observed ellipticities of a set of galaxies. We begin by pixelizing the sky such that we concentrate on an area small enough that the shear can be considered constant. Working within the regime of weak lensing, we can then express the observed (complex) ellipticity of a galaxy, $\boldsymbol{\epsilon}^{\rm obs} = \epsilon_1^{\rm obs} + i\,\epsilon_2^{\rm obs}$, in terms of the intrinsic ellipticity

of the galaxy, $\boldsymbol{\epsilon}^{\rm int}$, and the constant reduced shear signal in a given pixel, $\boldsymbol{g}$, such that

$$\boldsymbol{\epsilon}^{\rm obs} = \frac{\boldsymbol{\epsilon}^{\rm int} + \boldsymbol{g}}{1 + \boldsymbol{g}^{*}\boldsymbol{\epsilon}^{\rm int}}, \tag{3.1}$$

If we now assume that the expectation value of the intrinsic ellipticities, $\left\langle \boldsymbol{\epsilon}^{\rm int} \right\rangle$, is zero, we can write the standard shear estimator as

$$\hat{\boldsymbol{g}} = \frac{\sum_{i=1}^{N} w_i \boldsymbol{\epsilon}_i^{\rm obs}}{\sum_{i=1}^{N} w_i}, \tag{3.2}$$

where w_i is a weight, which could, for example, be dependent on the intrinsic distribution in the ellipticities and ellipticity measurement errors. If we make the further assumption that the measurement error on $\boldsymbol{\epsilon}^{\rm obs}$ is much smaller than the intrinsic dispersion in galaxy ellipticities, σ_ϵ, then uniform weighting ($w_i = 1$) is an optimal choice. In this case, the error on the standard estimator is a result of the intrinsic shape dispersion only, i.e.,

$$\sigma_{\hat{\boldsymbol{g}}} = \frac{\sigma_\epsilon}{\sqrt{N}}. \tag{3.3}$$

Denoting the observed position angle as α, we can express the observed ellipticity in polar form, such that

$$\begin{aligned} \epsilon_1^{\rm obs} &= \left|\boldsymbol{\epsilon}^{\rm obs}\right| \cos\left(2\alpha\right), \\ \epsilon_2^{\rm obs} &= \left|\boldsymbol{\epsilon}^{\rm obs}\right| \sin\left(2\alpha\right), \end{aligned} \tag{3.4}$$

where the modulus of the observed ellipticity is defined as $\left|\boldsymbol{\epsilon}^{\rm obs}\right| = \sqrt{\boldsymbol{\epsilon}^{\rm obs}\boldsymbol{\epsilon}^{\rm obs*}}$. Let us assume that the distribution of the intrinsic ellipticities of the galaxies can be described by an azimuthally symmetric probability density function, $f\left(\left|\boldsymbol{\epsilon}^{\rm int}\right|\right)$. As the shear in a pixel is constant, this implies that the observed ellipticity can be modelled as

$$\boldsymbol{\epsilon}^{\rm obs} = \boldsymbol{g} + \boldsymbol{\epsilon}^{\rm ran}, \tag{3.5}$$

where $\boldsymbol{\epsilon}^{\rm ran}$ is a random vector which is dependent on the intrinsic distribution and with a mean of zero. In this chapter, we are interested in using measurements of the galaxy position angles (α) alone to estimate the shear. We must therefore consider the statistics of the sine and cosine functions. Defining the components of the shear as

$$\begin{aligned} g_1 &= |\boldsymbol{g}| \cos\left(2\alpha_0\right), \\ g_2 &= |\boldsymbol{g}| \sin\left(2\alpha_0\right), \end{aligned} \tag{3.6}$$

it can be shown that for any distribution of $\boldsymbol{\epsilon}^{\rm obs}$ which exhibits reflection symmetry about the vector $\boldsymbol{g}$[1], the mean of the cosines and sines of the position angles, $\langle\cos\left(2\alpha\right)\rangle$ and $\langle\sin\left(2\alpha\right)\rangle$, can be written as

$$\begin{aligned} \langle\cos\left(2\alpha\right)\rangle =& F_1\left(|\boldsymbol{g}|\right)\cos\left(2\alpha_0\right), \\ \langle\sin\left(2\alpha\right)\rangle =& F_1\left(|\boldsymbol{g}|\right)\sin\left(2\alpha_0\right). \end{aligned} \tag{3.7}$$

Defining $\left|\boldsymbol{\epsilon}^{\rm int}_{\rm max}\right|$ as the maximum value of the modulus of the intrinsic ellipticity, the function $F_1\left(|\boldsymbol{g}|\right)$ can be written in terms of the intrinsic ellipticity distribution, such that

$$\begin{aligned} F_1\left(|\boldsymbol{g}|\right) = \frac{1}{\pi}\int_0^{\left|\boldsymbol{\epsilon}^{\rm int}_{\rm max}\right|}\int_{-\frac{\pi}{2}}^{\frac{\pi}{2}} {\rm d}\alpha^{\rm int}{\rm d}\left|\boldsymbol{\epsilon}^{\rm int}\right| f\left(\left|\boldsymbol{\epsilon}^{\rm int}\right|\right) \\ \times h_1\left(|\boldsymbol{g}|, \left|\boldsymbol{\epsilon}^{\rm int}\right|, \alpha^{\rm int}\right), \end{aligned} \tag{3.8}$$

where $\alpha^{\rm int}$ is the intrinsic position angle, and the function $h_1\left(|\boldsymbol{g}|, \left|\boldsymbol{\epsilon}^{\rm int}\right|, \alpha^{\rm int}\right)$ is found to be

$$h_1\left(|\boldsymbol{g}|, \left|\boldsymbol{\epsilon}^{\rm int}\right|, \alpha^{\rm int}\right) = \frac{\epsilon_1'}{\sqrt{\epsilon_1'^2 + \epsilon_2'^2}}, \tag{3.9}$$

[1] $\boldsymbol{\epsilon}^{\rm obs}$ is symmetrically distributed about $\boldsymbol{g}$ for any azimuthally symmetric intrinsic ellipticity distribution.

with

$$\epsilon_1' = |\boldsymbol{g}| \left(1 + \left|\boldsymbol{\epsilon}^{\rm int}\right|^2\right) + \left(1 + |\boldsymbol{g}|^2\right) \left|\boldsymbol{\epsilon}^{\rm int}\right| \cos\left(2\alpha^{\rm int}\right),$$
$$\epsilon_2' = \left(1 - |\boldsymbol{g}|^2\right) \left|\boldsymbol{\epsilon}^{\rm int}\right| \sin\left(2\alpha^{\rm int}\right). \tag{3.10}$$

A detailed derivation of the $F_1\left(|\boldsymbol{g}|\right)$ function is given in Appendix A.

From equation (3.7), it is clear that we can estimate the orientation of the shear as

$$\alpha_0 = \frac{1}{2} \tan^{-1}\left(\frac{\langle \sin\left(2\alpha\right)\rangle}{\langle \cos\left(2\alpha\right)\rangle}\right), \tag{3.11}$$

which is equal to the mean observed position angle, $\langle\alpha\rangle$.

Letting $2\alpha = \theta$ and $2\alpha_0 = \theta_0$, a more general form of equation (3.7) can be written as

$$\langle \cos\left(n\theta\right)\rangle = F_n\left(|\boldsymbol{g}|\right) \cos\left(n\theta_0\right),$$
$$\langle \sin\left(n\theta\right)\rangle = F_n\left(|\boldsymbol{g}|\right) \sin\left(n\theta_0\right), \tag{3.12}$$

where n is any positive integer.

By considering a general function $h_n\left(|\boldsymbol{g}|, \left|\boldsymbol{\epsilon}^{\rm int}\right|, \alpha^{\rm int}\right)$, we can write the general $F_n\left(|\boldsymbol{g}|\right)$ function for any azimuthally symmetric intrinsic probability distribution as

$$F_n\left(|\boldsymbol{g}|\right) = \frac{1}{\pi} \int_0^{\left|\boldsymbol{\epsilon}^{\rm int}_{\rm max}\right|} \int_{-\frac{\pi}{2}}^{\frac{\pi}{2}} {\rm d}\alpha^{\rm int} {\rm d}\left|\boldsymbol{\epsilon}^{\rm int}\right| f\left(\left|\boldsymbol{\epsilon}^{\rm int}\right|\right)$$
$$\times\, h_n\left(|\boldsymbol{g}|, \left|\boldsymbol{\epsilon}^{\rm int}\right|, \alpha^{\rm int}\right). \tag{3.13}$$

The $F_2\left(|\boldsymbol{g}|\right)$ function will be useful in later discussions regarding the variance of $\cos\left(2\alpha\right)$ and $\sin\left(2\alpha\right)$. The corresponding $h_2 \equiv h_2\left(|\boldsymbol{g}|, \left|\boldsymbol{\epsilon}^{\rm int}\right|, \alpha^{\rm int}\right)$ function is

$$h_2 = \frac{\epsilon_1'^2 - \epsilon_2'^2}{\epsilon_1'^2 + \epsilon_2'^2} \tag{3.14}$$

From equation (3.7), it is clear that the mean sine and cosine functions trace the sine and cosine of the shear orientation subject to a scaling factor which depends on $|\boldsymbol{g}|$.

3.2.1 Shear estimation using χ^2 minimization

It is possible to obtain constraints on the shear parameters from measurements of the galaxy position angles, $\alpha^{(i)}$, alone using the least-squares method (Press et al. 1992). For any azimuthally symmetric intrinsic ellipticity distribution, equation (3.7) suggests the definition of a general χ^2 as

$$\chi^2 = \sum_{i,j=1}^{N} \left(\boldsymbol{n}^{(i)} - F_1\left(|\boldsymbol{g}|\right) \frac{\boldsymbol{g}}{|\boldsymbol{g}|} \right)^{\mathrm{T}} \mathbf{C}_{ij} \left(\boldsymbol{n}^{(j)} - F_1\left(|\boldsymbol{g}|\right) \frac{\boldsymbol{g}}{|\boldsymbol{g}|} \right), \tag{3.15}$$

where we have defined the observed unit vector for the i^{th} galaxy as

$$\boldsymbol{n}^{(i)} = \begin{pmatrix} \cos(2\alpha^{(i)}) \\ \sin(2\alpha^{(i)}) \end{pmatrix}, \tag{3.16}$$

and $\mathbf{C}$ is the covariance matrix.

For the case when there are no measurement errors on α, it can be shown, using equation (3.12), that the variance on the unit vector components is

$$\sigma^2_{n_{1,2}} = \frac{1}{2}\left(1 - F_1^2\right) \pm \frac{1}{2}\left(F_2 - F_1^2\right)\cos\left(4\alpha_0\right), \tag{3.17}$$

where we define $F_k \equiv F_k\left(|\boldsymbol{g}|\right)$, and the plus and minus signs correspond to the first and second components of $\boldsymbol{n}$ respectively. In the limit of zero shear, the value of the variance is 0.5 for both components as there is no preferred observed position angle.

The form of the covariance is found to be

$$\mathrm{cov}\left(\cos\left(2\alpha\right), \sin\left(2\alpha\right)\right) = \frac{1}{2}\left(F_2 - F_1^2\right)\sin\left(4\alpha_0\right), \tag{3.18}$$

which is zero in the limit of zero shear.

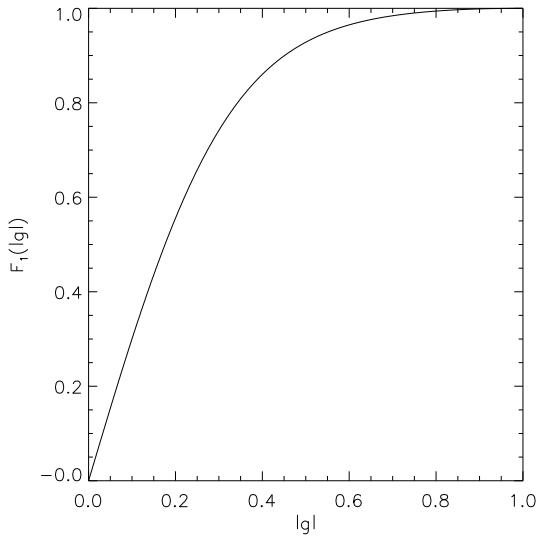

Figure 3.1: The $F_1\left(|\boldsymbol{g}|\right)$ function for case of the Rayleigh distribution given in equation (3.19).

If the components of the intrinsic ellipticity are Gaussian distributed, then $\left|\boldsymbol{\epsilon}^{\rm int}\right|$ is Rayleigh distributed (for a discussion on the motivation for this form of distribution see, for example, Viola et al. 2014):

$$f\left(\left|\boldsymbol{\epsilon}^{\rm int}\right|\right) = \frac{\left|\boldsymbol{\epsilon}^{\rm int}\right|}{\sigma_\epsilon^2\left(1-\exp\left(-\frac{|\boldsymbol{\epsilon}^{\rm int}_{\rm max}|^2}{2\sigma_\epsilon^2}\right)\right)}\exp\left(-\frac{\left|\boldsymbol{\epsilon}^{\rm int}\right|^2}{2\sigma_\epsilon^2}\right). \tag{3.19}$$

Using this form for the distribution of $\left|\boldsymbol{\epsilon}^{\rm int}\right|$, with $\sigma_\epsilon = 0.3/\sqrt{2}$ and $\left|\boldsymbol{\epsilon}^{\rm int}_{\rm max}\right| = 1.0$, we constructed $F_1\left(|\boldsymbol{g}|\right)$, shown in Figure 3.1, and $F_2\left(|\boldsymbol{g}|\right)$. Using these two functions we found that for shear values in the range $|\boldsymbol{g}| \leq 0.1$, equation (3.17) gives a variance in the range $0.44 \lesssim \sigma^2_{\boldsymbol{n}} \leq 0.5$, while equation (3.18) predicts a covariance in the range $-0.014 \lesssim \mathrm{cov}\left(\cos\left(2\alpha\right), \sin\left(2\alpha\right)\right) \lesssim 0.014$. For the subsequent numerical calculations we use $\sigma^2 = \sigma^2_{\boldsymbol{n}} = 0.5$ and $\mathrm{cov}\left(\cos\left(2\alpha\right), \sin\left(2\alpha\right)\right) = 0$ in every χ^2 that we construct. If we make the further assumption that the measurements of the position angles of different galaxies are independent, we can simplify the χ^2, such that it now

takes the form

$$\chi^2 = \sum_{i=1}^{N} \frac{\left| \boldsymbol{n}^{(i)} - F_1\left(|\boldsymbol{g}|\right) \frac{\boldsymbol{g}}{|\boldsymbol{g}|} \right|^2}{\sigma^2}. \tag{3.20}$$

The minimization of this χ^2 gives us an estimate of the shear, $\hat{\boldsymbol{g}}$, which satisfies the equations

$$\begin{aligned} \frac{1}{N}\sum_{i=1}^{N} \cos(2\alpha^{(i)}) &= F_1\left(|\hat{\boldsymbol{g}}|\right) \frac{\hat{g}_1}{|\hat{\boldsymbol{g}}|}, \\ \frac{1}{N}\sum_{i=1}^{N} \sin(2\alpha^{(i)}) &= F_1\left(|\hat{\boldsymbol{g}}|\right) \frac{\hat{g}_2}{|\hat{\boldsymbol{g}}|}. \end{aligned} \tag{3.21}$$

Taking the ratio of these two equations yields an estimate of the orientation of the shear:

$$\frac{\hat{g}_2}{\hat{g}_1} = \frac{\sum_{i=1}^{N} \sin(2\alpha^{(i)})}{\sum_{i=1}^{N} \cos(2\alpha^{(i)})}. \tag{3.22}$$

If, instead, we square and sum them together, we obtain an estimate of the $F_1\left(|\boldsymbol{g}|\right)$ function which, in turn, depends on the modulus of the shear:

$$F_1\left(|\hat{\boldsymbol{g}}|\right) = \sqrt{\left[\frac{1}{N}\sum_{i=1}^{N} \cos\left(2\alpha^{(i)}\right)\right]^2 + \left[\frac{1}{N}\sum_{i=1}^{N} \sin\left(2\alpha^{(i)}\right)\right]^2}. \tag{3.23}$$

Equation (3.23) can be solved numerically to yield an estimate of the shear modulus using, for example, the Secant method (Press et al. 1992), or by tabulating $F_1\left(|\boldsymbol{g}|\right)$ and inverting the function to recover $|\hat{\boldsymbol{g}}|$. By combining equations (3.22) and (3.23) we can therefore obtain estimates for both components of the shear. The error on the shear estimates can then be estimated as

$$\sigma_{\hat{\boldsymbol{g}}} = \frac{|\hat{\boldsymbol{g}}|}{F_1\left(|\hat{\boldsymbol{g}}|\right)} \frac{\hat{\sigma}_{\boldsymbol{n}}}{\sqrt{N}}, \tag{3.24}$$

where $\hat{\sigma}_{\boldsymbol{n}}$ is found by substituting the estimated shear values into equation (3.17).

Using a simulation composed of 500 galaxies with input shear values of $g_1 = -0.05$ and $g_2 = 0.05$, and assuming a Rayleigh distribution for $\left|\boldsymbol{\epsilon}^{\rm int}\right|$ with $\sigma_\epsilon =$

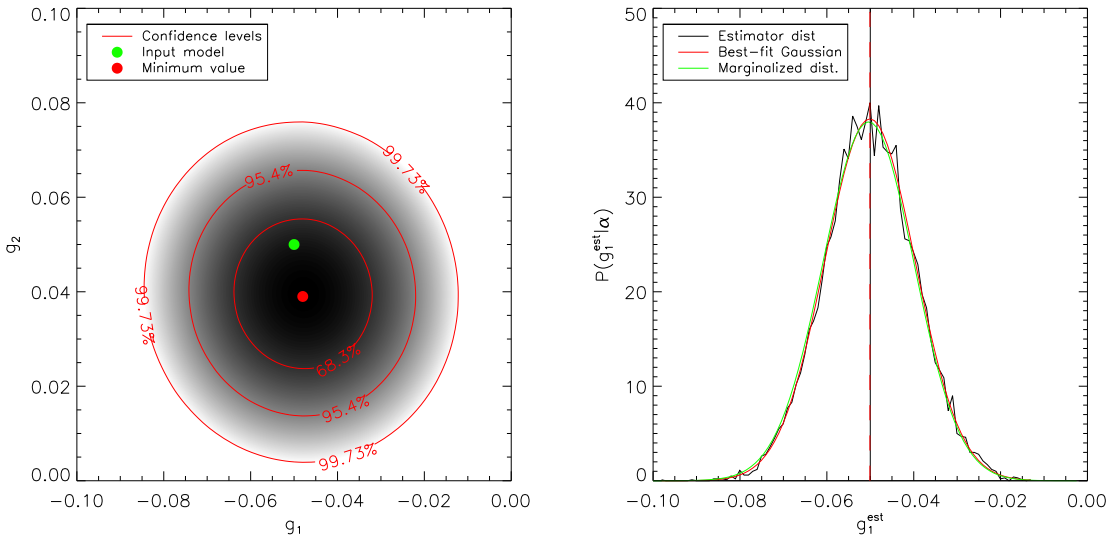

Figure 3.2: *Left panel:* The grey-scale shows the χ^2 of equation (3.20) recovered from a set of simulated galaxy position angles with input shear values of $g_1 = -0.05$ and $g_2 = 0.05$ and where we assume a Rayleigh distribution for $\left|\epsilon^{\rm int}\right|$. The best-fit shear is given by the minimum value of the χ^2, and the contours show the 68.3%, 95.4% and 99.73% confidence levels plotted under the assumption that the shear estimates are Gaussian distributed. *Right panel:* The distribution of the best-fit $\hat{g}_1$ values obtained from 10^4 realizations. The red curve is a Gaussian distribution constructed using the variance and the mean of the best-fit values. The green curve shows a marginalized plot of the distribution of the left panel, and hence is the distribution of g_1 for one realization. The agreement between the curves demonstrates that the shear estimates are approximately Gaussian distributed and validates the use of the χ^2 contours plotted in the left panel.

$0.3/\sqrt{2}$, we tested the performance of this method. A zero measurement error on α was assumed for this initial test. To estimate the shear, we performed a grid-based search over the shear parameters, calculating the χ^2 corresponding to each parameter value. The best-fit values were those which minimized the χ^2 statistic, and these were found to be consistent with equation (3.21). The results of the test are shown in the left panel of Fig. 3.2. The best-fit values were found to be $\hat{g}_1 = -0.048$ and $\hat{g}_2 = 0.039$, with $\chi^2 = 964$; using 500 galaxies we expect a value of $\chi^2 \approx 1000$, and therefore this value of χ^2 is consistent with our model providing a good fit to the data. The right hand panel of Fig. 3.2 shows the distribution of the best-fit g_1 values obtained over 10^4 realizations; with each realization consisting of 500 galaxies and where we have used

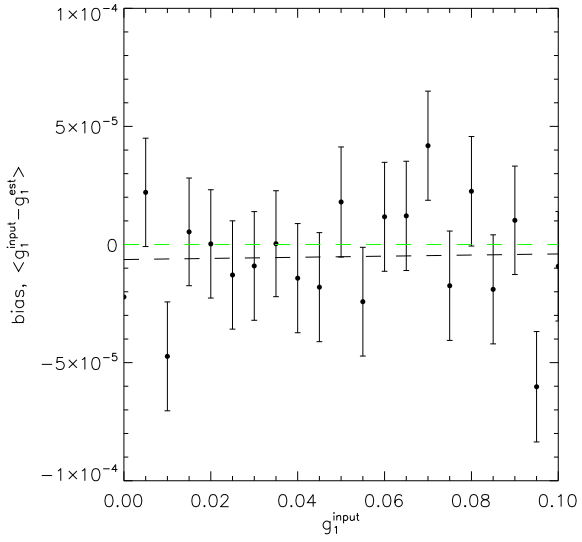

Figure 3.3: Residual bias in the shear estimates obtained using equations (3.22) and (3.23) as a function of the input shear value, g_1. For each simulation, the input value of g_2 was randomly selected from a uniform distribution in the range $-0.1 \leq g_2 \leq 0.1$. The green-dashed line shows the line of zero bias and the black-dashed line is the line of best fit for the data. The line of best fit is consistent with an overall bias of zero.

a bin size of $\Delta\hat{g}_1 = 0.001$.

We also ran simulations for a range of input shear values in order to check for biases. For each input shear value, we performed 10^4 simulations with each simulation composed of 10^4 galaxies. The result is shown in Fig. 3.3. Note that in order to obtain the shear estimates for this test, rather than using the grid-based approach, we used equation (3.22) to estimate the shear orientation and we solved equation (3.23) by tabulating $F_1\left(|\boldsymbol{g}|\right)$ and then inverting the function to find the modulus of the shear.[2]

3.2.2 Removal of noise bias

Estimators based on equation (3.20) are found to be biased in the presence of measurement errors on α. We can write the measured position angles as $\hat{\alpha} = \alpha + \delta\alpha$, where $\delta\alpha$ is a random measurement error on the position angle. It is possible to correct for

[2]A small bias is expected in this approach due to the numerical integration of the $F_1\left(|\boldsymbol{g}|\right)$ function which is performed during the estimation process. However, this bias was found to be negligible in all of the tests that we have performed.

the resulting noise bias by examining the averages of equation (3.21). Allowing for the measurement error on α, we have

$$\begin{aligned}\langle\cos(2\hat{\alpha})\rangle &= \langle\cos(2\alpha + 2\delta\alpha)\rangle\,,\\ \langle\sin(2\hat{\alpha})\rangle &= \langle\sin(2\alpha + 2\delta\alpha)\rangle\,.\end{aligned} \tag{3.25}$$

If we take the limit as $N \to \infty$ and assume that $\delta\alpha$ is independent of α, then we can expand the trigonometric functions, such that

$$\begin{aligned}\langle\cos(2\hat{\alpha})\rangle &= \langle\cos(2\alpha)\rangle\langle\cos(2\delta\alpha)\rangle - \langle\sin(2\alpha)\rangle\langle\sin(2\delta\alpha)\rangle\,,\\ \langle\sin(2\hat{\alpha})\rangle &= \langle\sin(2\alpha)\rangle\langle\cos(2\delta\alpha)\rangle + \langle\cos(2\alpha)\rangle\langle\sin(2\delta\alpha)\rangle\,.\end{aligned} \tag{3.26}$$

If we further assume that the error distribution is symmetric about zero, then

$$\begin{aligned}\langle\cos(2\hat{\alpha})\rangle &= \langle\cos(2\alpha)\rangle\langle\cos(2\delta\alpha)\rangle\,,\\ \langle\sin(2\hat{\alpha})\rangle &= \langle\sin(2\alpha)\rangle\langle\cos(2\delta\alpha)\rangle\,.\end{aligned} \tag{3.27}$$

Upon defining

$$\beta_n \equiv \langle\cos(n\delta\alpha)\rangle\,, \tag{3.28}$$

we can invert equation (3.27) and correct for the bias, so that the corrected mean unit vector is now given by

$$\langle\boldsymbol{n}\rangle^{\mathrm{corrected}} = \frac{\langle\boldsymbol{n}\rangle}{\beta_2}. \tag{3.29}$$

For the specific case where $\delta\alpha$ is a Gaussian distributed measurement error with zero mean and variance σ_α^2, it can be shown that

$$\beta_n = \exp\left(-\frac{n^2}{2}\sigma_\alpha^2\right). \tag{3.30}$$

We can incorporate this correction into the formulation of the χ^2 by defining

$$\chi^2 = \sum_{i=1}^{N} \frac{\left| \boldsymbol{n}^{(i)} - F_1\left(|\boldsymbol{g}|\right) \frac{\boldsymbol{g}}{|\boldsymbol{g}|} \beta_2 \right|^2}{\sigma^2}. \tag{3.31}$$

Equation (3.31) is minimized when

$$\begin{aligned} \frac{1}{N} \sum_{i=1}^{N} \cos\left(2\hat{\alpha}^{(i)}\right) &= F_1\left(|\hat{\boldsymbol{g}}|\right) \frac{\hat{g}_1}{|\hat{\boldsymbol{g}}|} \beta_2, \\ \frac{1}{N} \sum_{i=1}^{N} \sin\left(2\hat{\alpha}^{(i)}\right) &= F_1\left(|\hat{\boldsymbol{g}}|\right) \frac{\hat{g}_2}{|\hat{\boldsymbol{g}}|} \beta_2. \end{aligned} \tag{3.32}$$

Following the same procedure as for the case of $\sigma_\alpha = 0$ in the previous section, we can now estimate the orientation of the shear as

$$\frac{\hat{g}_2}{\hat{g}_1} = \frac{\sum_{i=1}^{N} \sin(2\hat{\alpha}^{(i)})}{\sum_{i=1}^{N} \cos(2\hat{\alpha}^{(i)})}, \tag{3.33}$$

while the estimate of the $F_1\left(|\boldsymbol{g}|\right)$ function, which depends on the modulus of the shear, becomes

$$F_1\left(|\hat{\boldsymbol{g}}|\right) = \frac{1}{\beta_2} \sqrt{\left[\frac{1}{N} \sum_{i=1}^{N} \cos\left(2\hat{\alpha}^{(i)}\right)\right]^2 + \left[\frac{1}{N} \sum_{i=1}^{N} \sin\left(2\hat{\alpha}^{(i)}\right)\right]^2}. \tag{3.34}$$

From equations (3.33) and (3.34), we see that the estimator for the shear orientation remains unchanged in the presence of a measurement error on the position angle. However, the expression for $F_1\left(|\boldsymbol{g}|\right)$ is modified; failing to include this noise correction term will result in an estimate of $|\boldsymbol{g}|$ that is too small.

We can also examine the impact on the variance on the trigonometric functions when a measurement error on α is included. This variance is found to be

$$\sigma^2_{n_{1,2}} = \frac{1}{2}\left(1 - F_1^2\beta_2^2\right) \pm \frac{1}{2}\left(F_2\beta_4 - F_1^2\beta_2^2\right)\cos\left(4\alpha_0\right), \tag{3.35}$$

Estimator	$\sigma_{\hat{g}_1}$	$\sigma_{\hat{g}_1}^{\rm theory}$	$\langle \hat{g}_1 \rangle$
original est.	0.0103	0.0102	-0.0436 ± 0.0001
corrected est	0.0119	0.0117	-0.0502 ± 0.0001

Table 3.1: The mean and standard deviation of the shear estimates recovered from 10^4 simulations. Values are quoted for both the original χ^2 (equation (3.20)) and the corrected χ^2 (equation (3.31)). The input shear value used was $g_1 = -0.05$.

where the plus and minus signs correspond to the first and second components of $\boldsymbol{n}$. By substituting the estimated shear values into equation (3.35), we can estimate the error on the corrected shear estimator as

$$\sigma_{\hat{\boldsymbol{g}}} = \frac{|\hat{\boldsymbol{g}}|}{F_1\left(|\hat{\boldsymbol{g}}|\right)\beta_2}\frac{\hat{\sigma}_{\boldsymbol{n}}}{\sqrt{N}}. \tag{3.36}$$

Fig. 3.4 demonstrates the reduction in bias when this correction is applied to simulations that include measurement errors on the galaxy position angles. Table 3.1 shows the mean estimated value of g_1, $\langle \hat{g}_1 \rangle$, and the standard deviation in the estimated values, $\sigma_{\hat{g}_1}$, obtained from the 10^4 realizations that were used to produce Fig. 3.4. The right column shows how using the corrected form of the χ^2 greatly reduces the bias introduced by the 15° error on the position angle measurements. However, from the left column, we see that there is a modest increase ($\sim$16%) in the dispersion of the estimates. The middle column shows the theoretical dispersion in the estimators obtained using the input values with equations (3.24) and (3.36).

We also ran the simulation for a range of input shear values and for a range of Gaussian measurement error values. Fig. 3.5 shows the residual bias in the derived shear estimates as a function of these two quantities. These results show that the bias in the uncorrected estimator (equation 3.20) increases approximately linearly with the input shear and exponentially with the measurement error. The success of the correction obtained in equation (3.29) is clearly demonstrated in this figure.

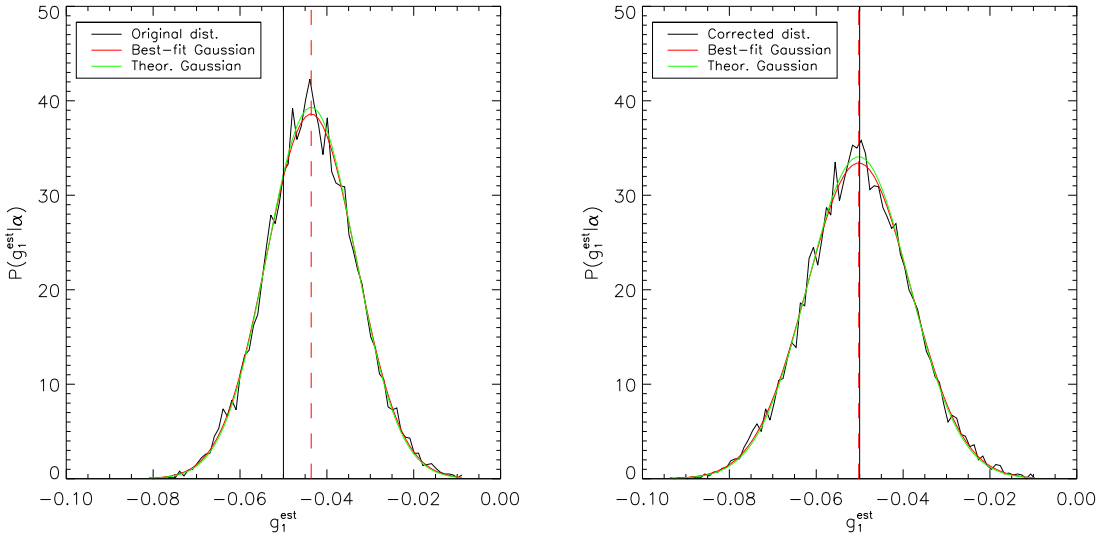

Figure 3.4: The distribution of the best-fit estimates obtained using the original χ^2 of equation (3.20) (*left panel*) and the corrected form of the χ^2 of equation (3.31) (*right panel*) in the presence of a Gaussian-distributed measurement error on the galaxy position angles with $\sigma_\alpha = 15^\circ$. The simulations consisted of 10^4 realizations with 500 galaxies in each realization and assumed a Rayleigh distribution for $\left|\boldsymbol{\epsilon}^{\rm int}\right|$. The vertical black line shows the input shear value and the red-dashed line shows the mean recovered best-fit value. The red curves are Gaussian distributions with the mean and variance of the estimators. The green curves are Gaussian distributions using the input shear value to obtain theoretical predictions for the variance from equations (3.24) and (3.36) for the left and right panels respectively. This figure demonstrates that the bias introduced by measurement errors on the position angles is reduced to negligible levels when the corrected form of the χ^2 given in equation (3.31) is used. It also indicates that equations (3.24) and (3.36) provide good descriptions of the errors in both cases.

3.3 Measuring position angles

In this section, we introduce a method of estimating the position angles directly from the data. We use this method to recover a constant shear signal from sets of simulated galaxy images and compare these results with those obtained using the KSB method. For the simulations in this section, we follow the approach outlined in Viola et al. (2011) and consider sets of simulated galaxies assuming a Sérsic brightness profile:

$$I(r) = I_0 \exp\left[-b_{n_s}\left(\left(\frac{r}{R_e}\right)^{\frac{1}{n_s}} - 1\right)\right], \tag{3.37}$$

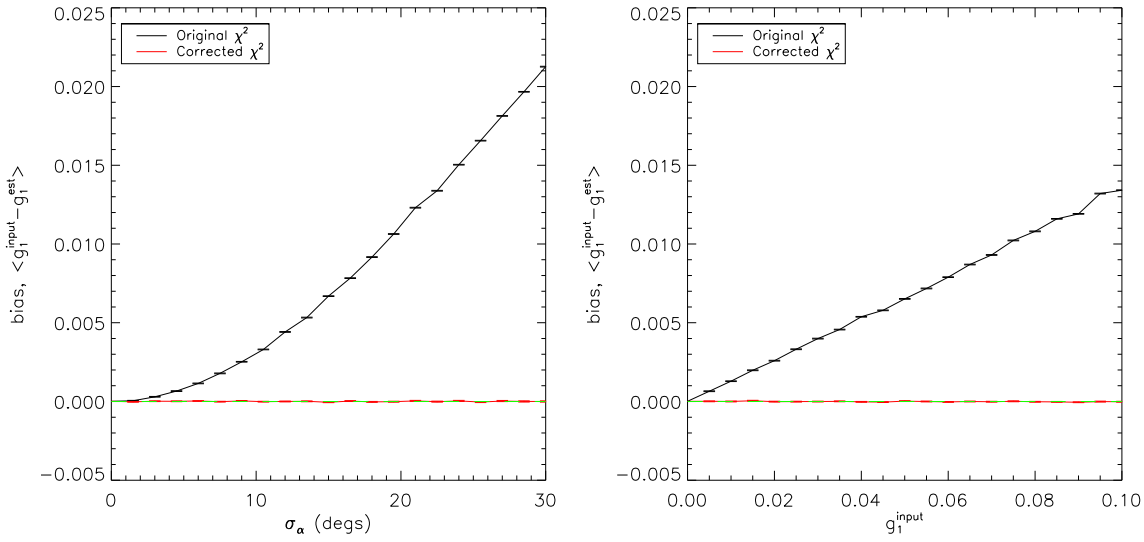

Figure 3.5: The residual bias in the best-fit shear estimates in the presence of a Gaussian measurement error on α and obtained by minimizing the two forms of the χ^2 (equations (3.20) and (3.31)). For each point plotted, we used 10^4 realizations, with each realization composed of 10^4 galaxies in order to suppress numerical error. The left panel shows the bias as a function of σ_α with $g_1 = 0.05$ and with g_2 uniformly distributed in the range $-0.1 \leq g_2 \leq 0.1$. The right panel shows the bias as a function of g_1 with $\sigma_\alpha = 15°$, and where g_2 is again uniformly distributed in the range $-0.1 \leq g_2 \leq 0.1$. These figures show that the noise bias due to measurement errors on the position angles is reduced to negligible levels when the bias correction is used.

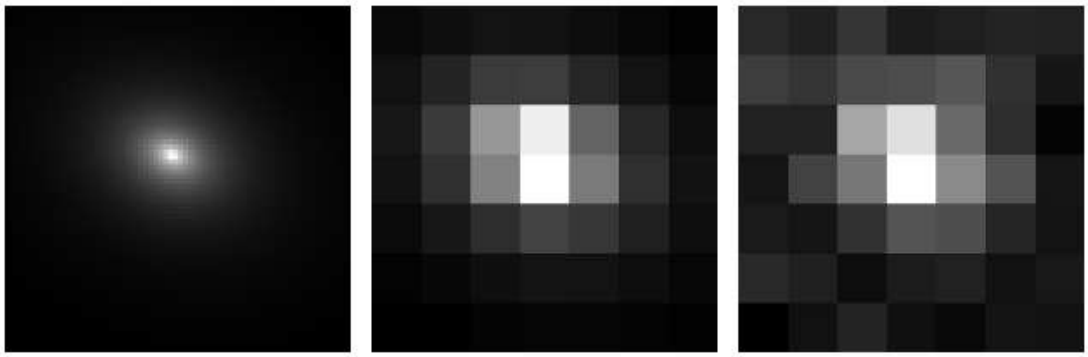

Figure 3.6: An example of the simulated galaxy images used in this section. Here we have displayed the central region of the images, with the scale identical for each image. *Left panel*: First we simulated the galaxy using a high resolution grid consisting of 510×510 pixels. *Centre panel*: The pixelized noise free galaxy image is then produced by averaging over the pixel values in the high resolution grid to produce a grid of 51×51 pixels. *Right panel*: Gaussian noise is then added to the galaxy image with $\mathrm{SNR} = 30$, in accordance with equation (3.38).

where n_s is the Sérsic index and where we assume that $n_s = 1.5$, which is the average value for bright galaxies in the Cosmic Evolution Survey (COSMOS) field (Sargent et al. 2007). R_e is the half light radius and b_{n_s} is a constant which depends on n_s. A value of $n_s = 1.5$ gives $b_{n_s} = 2.674$. I_0 is the surface brightness of the galaxy at the half light radius. The size of each image is 51×51 pixels with each galaxy model 10-fold oversampled, and we set $R_e = 2$ pixels.

When background noise is introduced into the images, we assume a Gaussian noise and fix the variance of the noise distribution so that the resulting signal to noise ratio is 30. The signal to noise ratio (SNR) is defined as (Bridle et al. 2010)

$$\mathrm{SNR} = \frac{\sqrt{\sum_{i=1}^{N} I_i^2}}{\sigma_{\mathrm{b}}}, \tag{3.38}$$

where I_i is the intensity in the i^{th} pixel of the low resolution image prior to the addition of noise and σ_{b} is the dispersion in the background noise. An example of the process used to create the galaxy images in shown in Figure 3.6.

We simulate sets of galaxies using a Rayleigh intrinsic ellipticity distribution and then apply a constant shear to these galaxies. These sheared galaxies are then pixelized, and Gaussian noise is added following the above procedure. We ignore the effects of PSF convolution and when using a Gaussian weighting function to suppress noise at large scales, we set the width of the weighting function to $2R_e$. The effects of PSF convolution are explored in Chapter 4. We recover estimates of the shear using a common variant of the KSB method and using the angle-only method and compare the results. In order to use the angle-only method, we introduce a method of measuring the position angles of the galaxies using the light distribution of the galaxy images.

As discussed in Section 2.5, we can define the ellipticity of the galaxy image in terms of the second order moments given in equation (2.25). The form of ellipticity which corresponds to the shear transformation given is equation (3.1) is given in equation (2.27). The form of ellipticity used for the KSB method is given in equation (2.28)

and corresponds to a shear transformation such that

$$\boldsymbol{\chi}^{\rm obs} = \frac{\boldsymbol{\chi}^{\rm int} + 2g + g^2\boldsymbol{\chi}^{\rm int^*}}{1 + |g|^2 + 2\Re\left(g\boldsymbol{\chi}^{\rm int^*}\right)}. \tag{3.39}$$

When estimating the shear using the KSB method, we follow the method outlined in Viola et al. (2011) and first discussed by Kaiser et al. (1995), where the estimator is found to be

$$\hat{g}_\alpha = \left\langle \left(P^{\rm sh}_{\alpha\beta}\right)^{-1} \chi^{\rm obs}_\beta \right\rangle, \tag{3.40}$$

such that the tensor, $P^{\rm sh}_{\alpha\beta}$, is approximated by half its trace

To find the centroid of the galaxy image in the presence of noise, we first apply the weighting function centred on the brightest pixel. We then recalculate the centroid using equation (2.26) and re-apply the weighting function centred on this new estimate of the centroid. We iterate this step until the difference between successive estimates is less than 10^{-4} of a pixel.

3.3.1 Using the angle-only method

The $F_1\left(|\boldsymbol{g}|\right)$ function corresponding to the definition of ellipticity given in equation (3.1) is given in equation (3.8). It is also possible to derive the $F_1\left(|\boldsymbol{g}|\right)$ function which corresponds to the χ-ellipticity definition given in equation (3.39), $F_1^\chi\left(|\boldsymbol{g}|\right)$. The form of this function is

$$\begin{aligned} F_1^\chi\left(|\boldsymbol{g}|\right) =& \frac{1}{\pi}\int_0^{\left|\boldsymbol{\chi}^{\rm int}_{\rm max}\right|} {\rm d}\alpha^{\rm int}{\rm d}\left|\chi^{\rm int}\right| f\left(\left|\boldsymbol{\chi}^{\rm int}\right|\right) \\ & \times h_1^\chi\left(|\boldsymbol{g}|, \left|\boldsymbol{\chi}^{\rm int}\right|, \alpha^{\rm int}\right), \end{aligned} \tag{3.41}$$

where $\alpha^{\rm int}$ is the intrinsic position angle and the function $h_1^\chi\left(|\boldsymbol{g}|, \left|\boldsymbol{\chi}^{\rm int}\right|, \alpha^{\rm int}\right)$ is

$$h_1^\chi\left(|\boldsymbol{g}|, \left|\boldsymbol{\chi}^{\rm int}\right|, \alpha^{\rm int}\right) = \frac{\chi_1'}{\sqrt{\chi_1'^2 + \chi_2'^2}}, \tag{3.42}$$

with

$$\begin{aligned}\chi_1' =& 2\left|\boldsymbol{g}\right| + \left(1+\left|\boldsymbol{g}\right|^2\right)\left|\chi^{\rm int}\right|\cos\left(2\alpha^{\rm int}\right),\\ \chi_2' =& \left(1-\left|\boldsymbol{g}\right|^2\right)\left|\chi^{\rm int}\right|\sin\left(2\alpha^{\rm int}\right).\end{aligned} \tag{3.43}$$

We use this form of the $F_1\left(|\boldsymbol{g}|\right)$ function in the following analysis in order to make a direct comparison of the shear estimates recovered when using an angle-only method - where we measure the position angles directly from the image data - with those obtained using the KSB method. For this analysis, we also assume a perfect knowledge of the intrinsic ellipticity distribution, $f\left(\left|\boldsymbol{\chi}^{\rm int}\right|\right)$; the effects of an imperfect knowledge of $f\left(\left|\boldsymbol{\chi}^{\rm int}\right|\right)$ are discussed in Section 3.4.

An estimate of the shear is obtained such that

$$\begin{aligned}F_1^{\chi}\left(|\hat{\boldsymbol{g}}|\right) =& \sqrt{\left[\frac{1}{N}\sum_{i=1}^{N}\cos\left(2\alpha^{(i)}\right)\right]^2 + \left[\frac{1}{N}\sum_{i=1}^{N}\sin\left(2\alpha^{(i)}\right)\right]^2},\\ \hat{\alpha}_0 =& \frac{1}{2}\tan^{-1}\left(\frac{\sum_{i=1}^{N}\sin\left(2\alpha^{(i)}\right)}{\sum_{i=1}^{N}\cos\left(2\alpha^{(i)}\right)}\right).\end{aligned} \tag{3.44}$$

3.3.2 A method for measuring the position angles

We now consider a method of obtaining an estimate of the position angle by considering the intensity profile of the galaxy as a function of the assumed position angle, under the assumption that the galaxy exhibits reflection symmetry about its major axis.

Given a noisy pixelized galaxy image, we begin by obtaining an estimate of the centroid. To find the centroid of the galaxy image, we follow a similar procedure to that discussed above. First we multiply by the weighting function centred on the brightest pixel. However, for the angle-only method, we then convolve the image with a Gaussian kernel to reduce pixelization effects (the advantage of this step is discussed shortly) and then recalculate the centroid using equation (2.26). We re-apply the weighting function to the original image centred on the new estimate of the

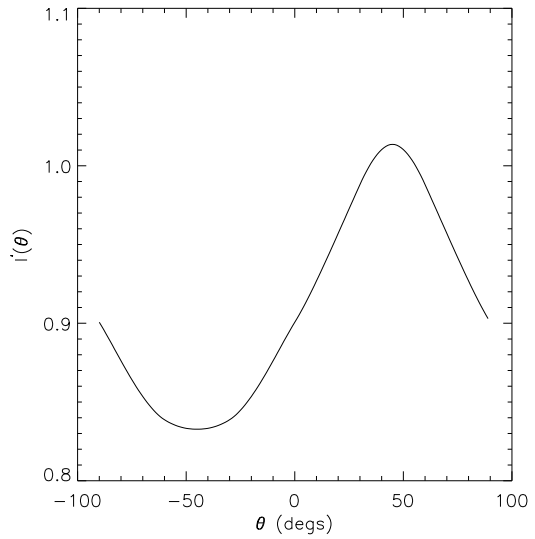

Figure 3.7: The integrated light distribution as a function of the assumed galaxy orientation for the ideal case of zero noise and with the centroid of the galaxy situated at the centre of a pixel. The input position angle is $45°$.

centroid and convolve this image with the Gaussian kernel. We iterate this step until the difference between successive estimates is less than 10^{-4} of a pixel.

We then integrate the convolved, weighted surface brightness, $I_w(r, \alpha)$, over the radial direction, such that

$$I'(\theta) = \int \mathrm{d}r I_w(r, \theta), \tag{3.45}$$

where $r = 0$ corresponds to the centroid of the galaxy image and where θ is the assumed galaxy orientation. This gives us the integrated light distribution as a function of θ.

Defining a set of axes which align with the edges of the pixels, we propose a method of performing this integration by rotating the image about the centroid and integrating along the x-axis of the image through the centroid, such that

$$I'(\theta) = \int_{x_{min}}^{x_{max}} \mathrm{d}x I_\theta(x, \hat{y}), \tag{3.46}$$

where I_θ is the convolved, weighted surface brightness distribution rotated by $-\theta$ about

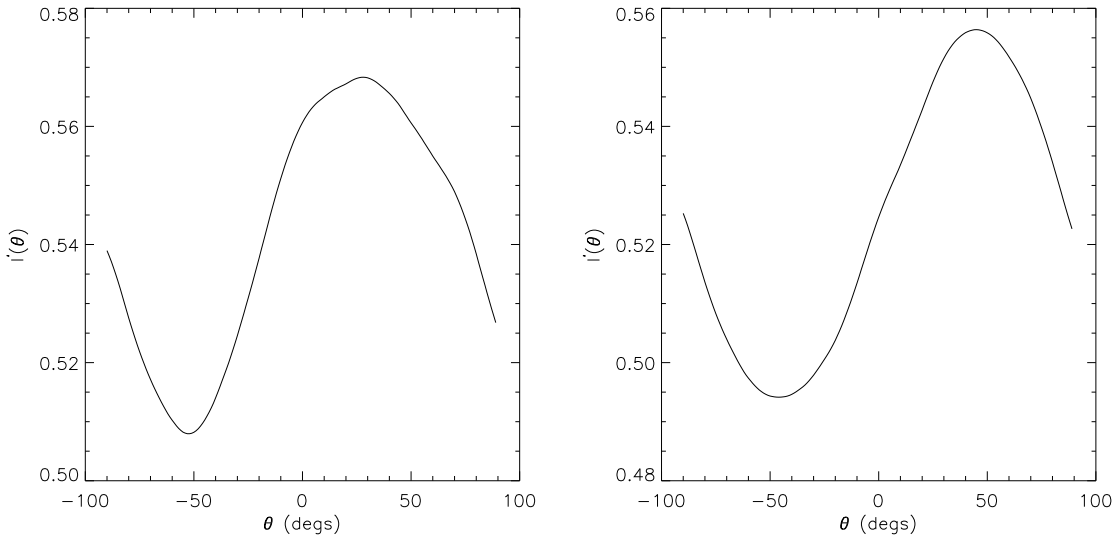

Figure 3.8: *left panel*: The integrated light distribution as a function of the assumed galaxy orientation for the case of a randomly positioned galaxy. This distribution leads to an incorrect estimate of the true position angle. *Right panel*: The integrated light distribution once the image has been convolved with a Gaussian kernel of width 1 pixel; this reduces the effects of pixelization

the centroid, and $\hat{y}$ is the y component of the estimated centroid, $(\hat{x}, \hat{y})$. This allows us to carry out the integration by simply summing the intensity over the row of pixels with $y = \hat{y}$.

If we omit the convolution with a Gaussian kernel, an example of this distribution is shown in Figure 3.7 where we obtain the integrated light distribution for a galaxy with ellipticity $|\boldsymbol{\chi}| = 0.27$, position angle $\alpha = 45^{\circ}$ and situated at the centre of the central pixel with zero noise. Using this distribution, we can recover an estimate of the position angle of the galaxy such that

$$\hat{\alpha} = \frac{1}{2} \tan^{-1} \left(\frac{\int \mathrm{d}\theta I'(\theta) \sin(2\theta)}{\int \mathrm{d}\theta I'(\theta) \cos(2\theta)} \right). \tag{3.47}$$

Applying this equation to the above distribution leads to the exact estimate of $\hat{\alpha} = 45^{\circ}$. However, if we now consider the case where the centroid of the galaxy

is not positioned at the centre of a pixel, the integrated light distribution is not so well behaved. The left-hand panel in Figure 3.8 shows one particular distribution using a randomly centred galaxy. This distribution leads to an estimated position angle of 31.0° for an input angle of 45°. This error in the estimate is due to the pixelization of the image. One can soften the effect of pixelization by convolving the image with a Gaussian kernel as described above. After we have done this with a kernel of width one pixel, we recover the distribution shown in the right-hand panel of Figure 3.8. Using this distribution, we obtain the estimate of $\hat{\alpha} = 45.1^\circ$. For the remainder of this section, we use a Gaussian kernel of width one pixel in every position angle measurement performed.

3.3.3 Debiasing angle-only shear estimates using simulations

For the analysis in Section 3.2, we assumed that measurement errors on the position angles were independent of the true position angles. However, for a fixed signal to noise ratio, we find that there are two sources of non-zero covariance between the measurement errors and the position angles; these are pixelization and a correlation between the measurement errors and galaxy ellipticities in the presence of a non-zero shear. To understand why these covariances present a problem, we begin by writing the mean estimated cosines and sines of the measured position angles, $\hat{\alpha}$, in terms of the true position angles, α, and an error on the measurement, $\delta\alpha$, such that

$$\begin{aligned} \langle \cos(2\hat{\alpha}) \rangle &= \langle \cos(2\alpha + 2\delta\alpha) \rangle \\ \langle \sin(2\hat{\alpha}) \rangle &= \langle \sin(2\alpha + 2\delta\alpha) \rangle \,. \end{aligned} \tag{3.48}$$

If we now abandon the assumption that the measurement errors are independent of the position angles of the galaxies and make no assumption about the distribution of the errors, we can write equation (3.48) in terms of the covariance between the true

position angles and the measurement errors, such that

$$\begin{aligned} C' &= \langle \cos(2\alpha) \rangle \, \beta_c - \langle \sin(2\alpha) \rangle \, \beta_s \\ S' &= \langle \sin(2\alpha) \rangle \, \beta_c + \langle \cos(2\alpha) \rangle \, \beta_s, \end{aligned} \tag{3.49}$$

where we define

$$\begin{aligned} C' = &\langle \cos(2\hat{\alpha}) \rangle - \mathrm{cov}\left(\cos(2\alpha), \cos(2\delta\alpha)\right) + \\ &\mathrm{cov}\left(\sin(2\alpha), \sin(2\delta\alpha)\right), \\ S' = &\langle \sin(2\hat{\alpha}) \rangle - \mathrm{cov}\left(\sin(2\alpha), \cos(2\delta\alpha)\right) - \\ &\mathrm{cov}\left(\cos(2\alpha), \sin(2\delta\alpha)\right), \\ \beta_c = &\langle \cos(2\delta\alpha) \rangle, \\ \beta_s = &\langle \sin(2\delta\alpha) \rangle. \end{aligned} \tag{3.50}$$

We can now use equation (3.49) to write the means of the cosines and sines of the true position angles as

$$\begin{aligned} \langle \cos(2\alpha) \rangle = &\frac{1}{\beta_c^2 + \beta_s^2} \left(C'\beta_c + S'\beta_s\right), \\ \langle \sin(2\alpha) \rangle = &\frac{1}{\beta_c^2 + \beta_s^2} \left(S'\beta_c - C'\beta_s\right). \end{aligned} \tag{3.51}$$

It is these averages which must be used to estimate the shear when using equation (3.44)[3]. Incorrectly accounting for the covariance terms in equation (3.51) will introduce a bias into the shear estimates.

To understand how pixelization of the galaxy images introduces non-zero covariance terms into equation (3.51), let us assume that the centre of a galaxy coincides with the centre of a pixel. In the absence of noise, the central pixel of this image will be the brightest. If we define the pixel axes as a set of axes with the origin at the centre

[3]This result is general and is expected to hold for any method used to measure galaxy position angles.

of the brightest pixel and with the axes aligned with the edges of the pixel, then the contribution of light from the central pixel will be greatest in the directions of $\pm 45^{\circ}$ and least in the directions of 0° and 90°. This effect will bias the angle measurements towards angles of $\pm 45^{\circ}$ and away from angles of 0° and 90°. Convolving the galaxy image with a Gaussian kernel reduces this effect. However, for a randomly positioned galaxy centroid, with a signal to noise ratio of 30, using a Gaussian kernel with a width of 1 pixel results in correlations on the order of 1%, which produces significant biases in the shear estimates. The covariance terms in equation (3.50) due to this effect can be obtained using a set of simulated galaxy images under the assumption of zero shear. From these simulations, we can also recover a first estimate of β_c and β_s. If we align the shear axes with the pixel axes, then the g_1 component of the shear will be aligned with the pixel axes and the g_2 component will align with the directions of $\pm 45^{\circ}$, this will lead to a biasing in the direction of g_2 and away from the direction of g_1. In order to avoid this effect, we choose to orientate our shear axes, when performing the angle-only analysis, such that the direction of the g_1 component is orientated at -22.5° to the pixel axes.

The second source of bias arises from correlations between measurement errors and galaxy ellipticities in the presence of a non-zero shear. For a fixed signal to noise ratio, it is found that the measurement error on the position angle is dependent on the modulus of the ellipticity - galaxies with high ellipticities have smaller measurement errors on the position angles than galaxies with low ellipticities. In the absence of a shear, there will be no correlation between orientation and ellipticity, and hence there will be no bias contribution due to this effect. However, in the presence of a non-zero shear, there will be a preference for galaxies with a higher ellipticity to align with the direction of the shear. This implies that, on average, the measurement errors on galaxy position angles where the galaxies are aligned with the shear are smaller than those where the galaxies are anti-aligned with the shear. This effect is also large enough to produce significant biases in the shear estimates. In the following subsection, we introduce an iterative method using simulations to significantly reduce this effect.

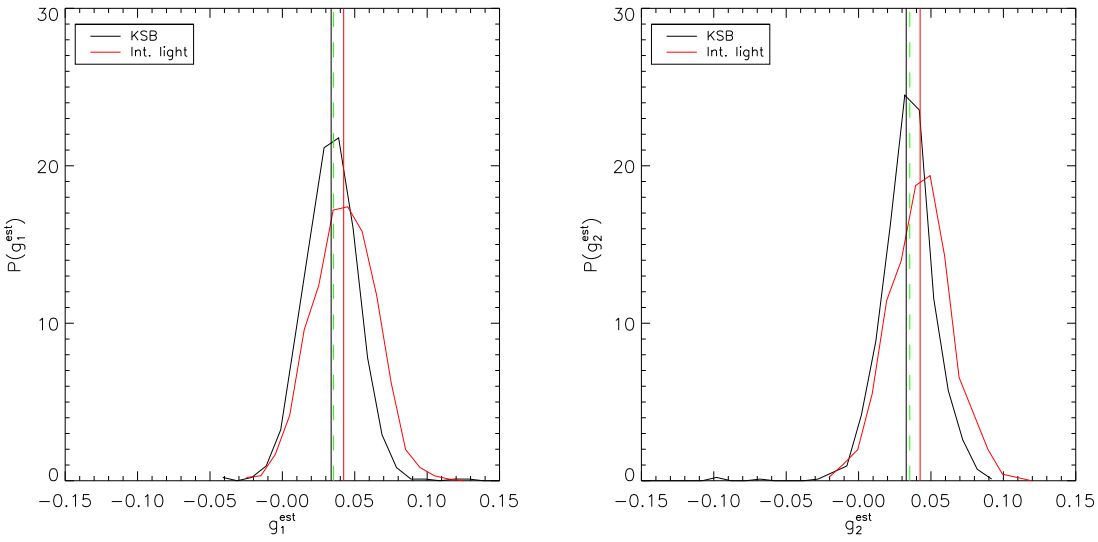

Figure 3.9: The distribution of the estimates for the two components of the shear including correction for pixelization. The black curves show the distributions in shear estimates using the KSB method, with the vertical black line indicating the mean estimate. The red curves show the distributions in shear estimates using the angle-only method, where we measure the position angles of the galaxies using the integrated light distribution and use sets of zero-shear realizations in order to reduce the bias due to pixelization; the vertical red line indicates the mean estimate. The green-dashed line indicates the input shear signal. The residual bias in the angle-only estimates is due to correlations between the measurement errors and the position angles which result from a non-zero shear signal.

3.3.4 A comparison of angle-only shear estimates with the KSB method

Using sets of simulated galaxy images with a signal to noise ratio of 30, assuming a Rayleigh intrinsic ellipticity distribution with a dispersion $\sigma_\chi = 0.3/\sqrt{2}$, using an input shear signal of $g_1 = g_2 = 0.05/\sqrt{2}$ and with 100 galaxies per realization, we recovered shear estimates from 960 realizations. We compared the estimates recovered using the angle-only estimator, where the angles were measured using the method described above, with those recovered using the KSB method. For the angle-only method we also used 960 zero-shear realizations in order to obtain a first estimate of the covariance terms in equation (3.51); this corrects for the effect of pixelization on the shear estimates. The results of these simulations are shown in Figure 3.9. The

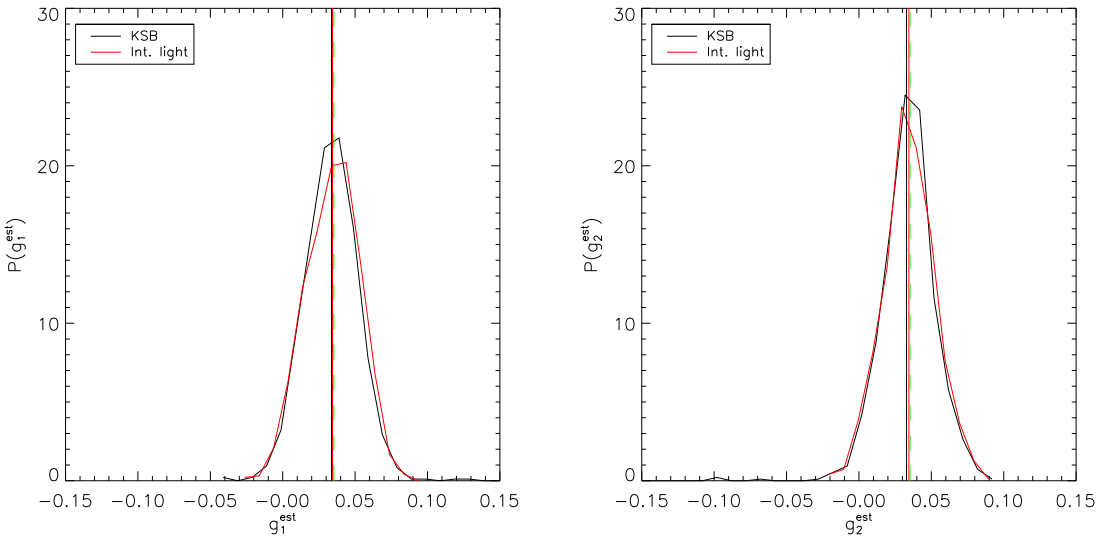

Figure 3.10: The distribution in shear estimates for the two components of the shear including corrections for pixelization and an iterative scheme for removing the bias due to shape dependent noise. The black curves show the distributions in shear estimates using the KSB method. The red curves show the distributions in shear estimates using the angle-only method, where we have used the estimated shear values shown in Figure 3.9 as the input shear signal in a set of simulations which we then use to re-evaluate the covariance terms in equation (3.50). The bias in the angle-only shear estimates has been greatly reduced.

two panels show the distribution of estimates for the two components of the shear. The black curves show the distributions of recovered shear estimates using the KSB method. The red curves show the distributions of recovered shear estimates using the angle-only method. Here we see that the width of the distribution is slightly larger for the angle-only method. Also, the bias in the shear estimates using the angle-only method is clearly visible. As explained above, this bias is due to the correlation between measurement errors and galaxy ellipticities, which is introduced in the presence of a non-zero shear. However, one can obtain a better estimate of these covariance terms by using the estimated shear values as the input shear for a new set of simulated galaxy images.

Using each of the shear estimates shown in Figure 3.9 as the input shear for a further 960 realizations, we re-evaluated the covariance and β terms in equation (3.50). We then used these values of the covariances to obtain new estimates of the shear. The

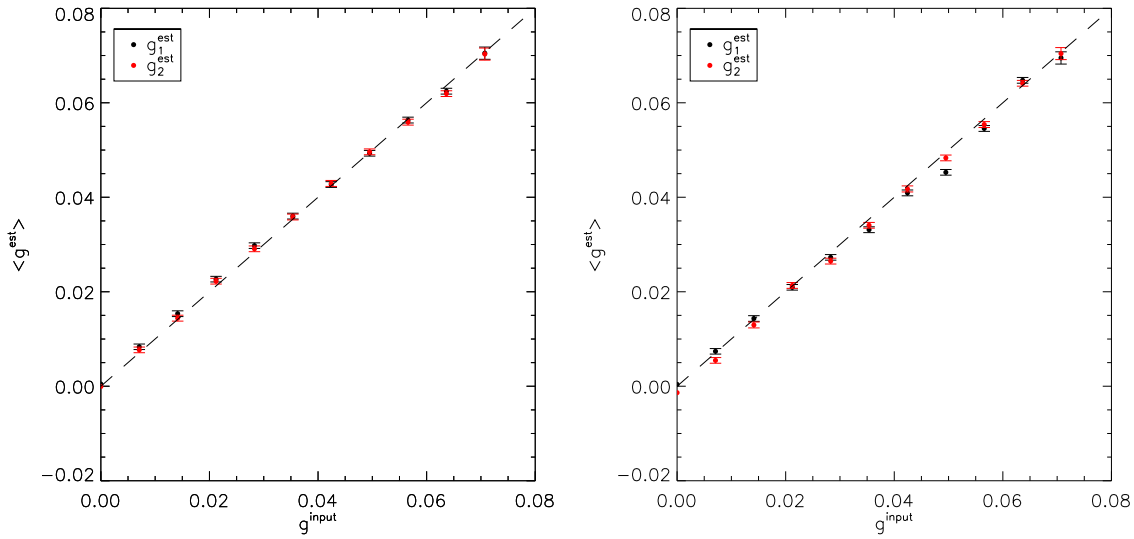

Figure 3.11: The recovered shear estimates as a function of the input shear values. The *left panel* shows the recovered shear values obtained using the angle-only method and upon using one iteration in order to calculate the covariance terms in equation (3.50). The *right panel* shows the recovered shear values using the KSB method.

distribution in these estimates is shown in Figure 3.10 as the red curve. From these plots, we see that the bias in the shear estimates has been greatly reduced. We also see that the width of the distribution of the shear estimates using the angle-only method has been reduced and is now similar to the width of the distribution of shear estimates using the KSB method.

Next, we carried out this analysis for a range of input $|\boldsymbol{g}|$ values, keeping the input shear position angle fixed at $\alpha_0 = 22.5°$. The results of this test are shown in Figure 3.11. The left panel shows the results of the angle-only method upon carrying out the iterative procedure described above using just one iteration. The right panel shows the results of the KSB method. Each point plotted consists of 960 realizations, with each realization consisting of 100 galaxies. From these plots, we see that the performance of the angle-only method is comparable with the KSB method, and that the distribution of the recovered shear values is consistent with noise for the number of galaxies and realizations used.

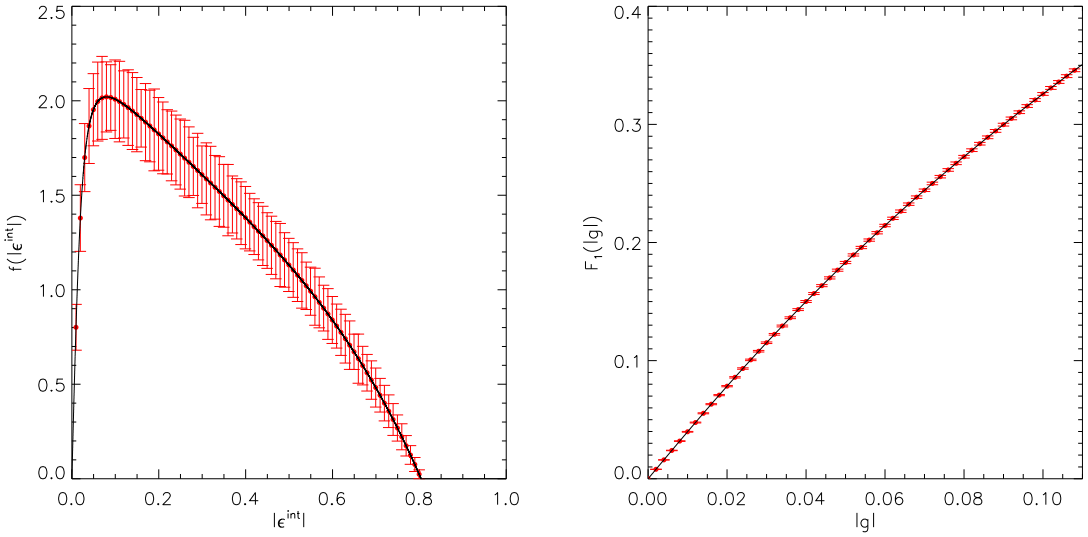

Figure 3.12: *left panel*: The $f\left(\left|\boldsymbol{\epsilon}^{\rm int}\right|\right)$ for the case of 5×10^4 galaxies. The red points indicate the mean of $f\left(\left|\boldsymbol{\epsilon}^{\rm int}\right|_i\right)$ recovered from 100 realizations. The error bars indicate the standard deviation of the values of $f\left(\left|\boldsymbol{\epsilon}^{\rm int}\right|_i\right)$ over 100 realizations (note that only 1 in 10 points have been plotted for clarity). The black curve shows the true $f\left(\left|\boldsymbol{\epsilon}^{\rm int}\right|\right)$. *Right panel*: The estimated $F_1\left(|\boldsymbol{g}|\right)$ function obtained from the estimated $f\left(\left|\boldsymbol{\epsilon}^{\rm int}\right|\right)$. The red points show the mean estimated $F_1\left(|\boldsymbol{g}|_i\right)$ over 100 realizations. The error bars indicate the standard deviation over 100 realizations (note that only 1 in 20 points have been plotted for clarity). The black curve shows the true $F_1\left(|\boldsymbol{g}|\right)$ function, calculated using the true $f\left(\left|\boldsymbol{\epsilon}^{\rm int}\right|\right)$.

3.4 Impact of errors on $f\left(\left|\boldsymbol{\epsilon}^{\rm int}\right|\right)$ estimates

All of the work prior to this section has assumed an exact knowledge of $f\left(\left|\boldsymbol{\epsilon}^{\rm int}\right|\right)$. In practice, an estimate of $f\left(\left|\boldsymbol{\epsilon}^{\rm int}\right|\right)$ is necessary in order to allow an estimation of the shear using the angle-only method. Errors on the form of $f\left(\left|\boldsymbol{\epsilon}^{\rm int}\right|\right)$ will therefore propagate as a bias into estimates of $|\boldsymbol{g}|$. In this section, we examine the effects of the size of the sample of galaxies and of measurement errors on the ellipticities of galaxies in the sample on estimates of the shear. For the following analysis, we assumed the underlying form of $f\left(\left|\boldsymbol{\epsilon}^{\rm int}\right|\right)$ to be that given in equation (3.67).

We began by assuming a negligible measurement error on the galaxy ellipticities. We are thus implicitly assuming that a high signal to noise sample of galaxies are available from which $f\left(\left|\boldsymbol{\epsilon}^{\rm int}\right|\right)$ can be estimated with negligible measurement errors.

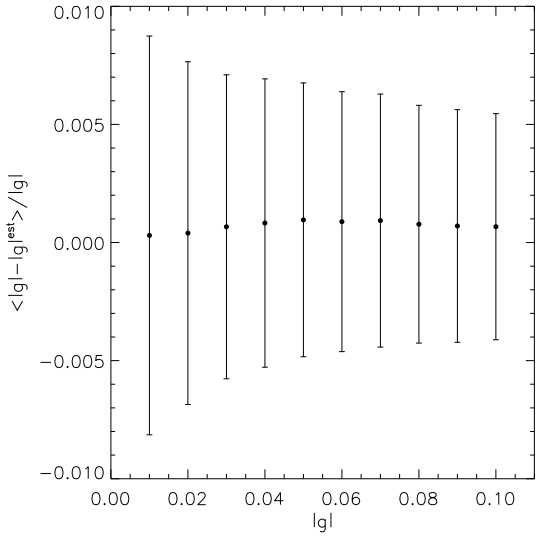

Figure 3.13: The fractional bias in the recovered $|\boldsymbol{g}|$ estimates for the case of 5×10^4 galaxies. The error bars indicate the fractional standard deviation of the estimates over 100 realizations.

In order to explore how the size of the galaxy sample used to estimate $f\left(\left|\boldsymbol{\epsilon}^{\rm int}\right|\right)$ affects the shear estimates, we reconstructed $f\left(\left|\boldsymbol{\epsilon}^{\rm int}\right|\right)$ using sample sizes consisting of a various number of galaxies, N, by producing histograms of $\left|\boldsymbol{\epsilon}^{\rm int}\right|$ which were randomly drawn from the underlying distribution. For each sample size, we repeated this process for 100 realizations.

For each estimate of $f\left(\left|\boldsymbol{\epsilon}^{\rm int}\right|\right)$, we calculated the corresponding $F_1\left(|\boldsymbol{g}|\right)$ function, $\hat{F}_1\left(|\boldsymbol{g}|\right)$. The results of this analysis are shown for the case of 5×10^4 galaxies in Figure 3.12. From this plot, we see that the errors on the estimates of $F_1\left(|\boldsymbol{g}|\right)$ are small compared to the errors on the $f\left(\left|\boldsymbol{\epsilon}^{\rm int}\right|\right)$. This is because the calculation of the $F_1\left(|\boldsymbol{g}|\right)$ function involves an integral over the estimated values of $f\left(\left|\boldsymbol{\epsilon}^{\rm int}\right|_i\right)$ which smooths the $f\left(\left|\boldsymbol{\epsilon}^{\rm int}\right|\right)$.

We propagated the errors on $\hat{F}_1\left(|\boldsymbol{g}|\right)$ into errors on the estimates of $|\boldsymbol{g}|$. This procedure was carried out for a variety of input shear signals, with the results displayed in Figure 3.13.

In order to quantify the errors introduced due to an imprecise knowledge of $f\left(\left|\boldsymbol{\epsilon}^{\rm int}\right|\right)$, we can, for example, constrain the number of galaxies in the sample used to estimate

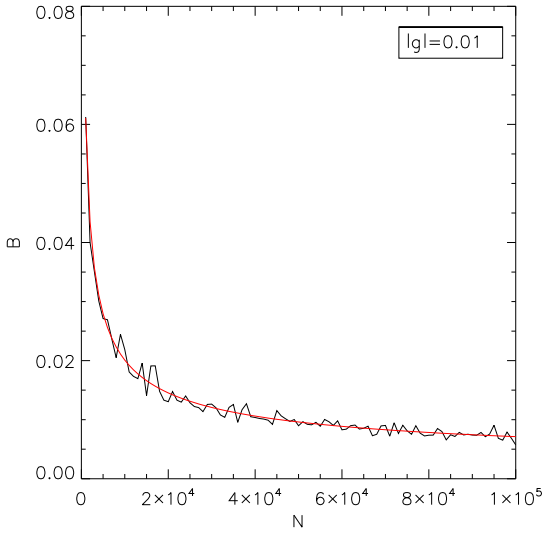

Figure 3.14: The absolute value of the fractional bias plus the fractional error (equation (3.52)) as a function of the number of galaxies in the sample used to estimate $f\left(\left|\boldsymbol{\epsilon}^{\rm int}\right|\right)$. The black curve shows the values obtained from the simulations. Over-plotted in red is a curve of the form $M/\sqrt{N}+C$.

$f\left(\left|\boldsymbol{\epsilon}^{\rm int}\right|\right)$ such that biases in the estimates of $|\boldsymbol{g}|$ are below some threshold value at a particular confidence level. As an example, let us define

$$B \equiv \frac{|\langle|\boldsymbol{g}|-|\hat{\boldsymbol{g}}|\rangle|+\sigma_{|\hat{\boldsymbol{g}}|}}{|\boldsymbol{g}|}, \tag{3.52}$$

which is the fractional absolute value of the bias plus the fractional standard deviation of the recovered estimates of $|\boldsymbol{g}|$. We can find the number of galaxies required to estimate $f\left(\left|\boldsymbol{\epsilon}^{\rm int}\right|\right)$ such that B is below some value for a specific set of $|\boldsymbol{g}|$ values. From Figure 3.13, we see that the range of the fractional error bars on the recovered estimates of $|\boldsymbol{g}|$ decreases as the input $|\boldsymbol{g}|$ increases. Therefore, for the analysis which follows, we focused our attention on the case when $|\boldsymbol{g}|=0.01$.

In Figure 3.14, we have plotted B as a function of the number of galaxies in the sample (black curve). We see, as expected, that the value of B decreases as the number of galaxies increases. For a fixed bin size, this is a result of the fractional error decreasing as the number of galaxies increases. The red curve in Figure 3.14 is a curve

of the form $M/\sqrt{N}+C$, where M and C are parameters fitted to the data. The form of this curve requires no assumption about the form of $f\left(\left|\boldsymbol{\epsilon}^{\rm int}\right|\right)$. The factor of $1/\sqrt{N}$ describes how the error on $\langle|\hat{\boldsymbol{g}}|\rangle$ decreases as the number of galaxies in the sample increases. For this data, we find $M \approx 1.90$ and $C \approx 1.13 \times 10^{-3}$. The additional constant, C, quantifies the residual bias due to the finite bin width used when reconstructing $f\left(\left|\boldsymbol{\epsilon}^{\rm int}\right|\right)$.

From the fitted curve, we can calculate the number of galaxies that one would require in order to ensure that B is less than some value. We have verified that the recovered estimates of $|\boldsymbol{g}|$ are approximately Gaussian distributed about the mean estimate. We can therefore state that the bias in the estimates of $|\boldsymbol{g}|$ arising as a result of a finite number of galaxies in the sample will be less than or equal to 1.0% for all values of $|\boldsymbol{g}| \geq 0.01$, at a confidence level of 68%, if $B = 0.01$. We can then invert the fitted curve in Figure 3.14 to find that for this constraint we need $N \gtrsim 5 \times 10^4$. Looking again at Figure 3.13, which displays the fractional bias for the case when $N = 5\times10^4$, we see that the error bars are indeed contained within the range $[-0.01, 0.01]$.

For any true ellipticity measurements, there will of course be measurement errors. These errors modify the form of the estimated $f\left(\left|\boldsymbol{\epsilon}^{\rm int}\right|\right)$ by distributing the measured $\left|\boldsymbol{\epsilon}^{\rm int}\right|$ more evenly between the bins. This is true even if the measurements of $\left|\boldsymbol{\epsilon}^{\rm int}\right|$ are unbiased.

Assuming 2×10^5 galaxies in the sample used to estimate $f\left(\left|\boldsymbol{\epsilon}^{\rm int}\right|\right)$, we repeated the analysis above. This time we added a Gaussian measurement error to the components of the ellipticity before estimating $\left|\boldsymbol{\epsilon}^{\rm int}\right|$. To achieve this, we first randomly draw 2×10^5 samples of $\left|\boldsymbol{\epsilon}^{\rm int}\right|_i$ from the underlying ellipticity distribution. We then simulated the measured components of the ellipticity, such that

$$\begin{aligned}\hat{\epsilon}_1^{\rm int} &= \left|\boldsymbol{\epsilon}^{\rm int}\right| \cos\left(2\alpha^{\rm int}\right) + \delta_{\epsilon_1},\\ \hat{\epsilon}_2^{\rm int} &= \left|\boldsymbol{\epsilon}^{\rm int}\right| \sin\left(2\alpha^{\rm int}\right) + \delta_{\epsilon_2},\end{aligned} \tag{3.53}$$

where $\alpha^{\rm int}$ is uniform distributed in the range $-\pi/2 < \alpha^{\rm int} \leq \pi/2$ and where δ_{ϵ_1}

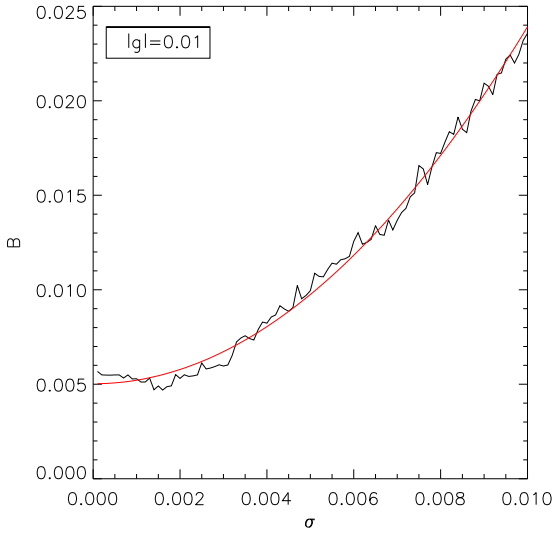

Figure 3.15: The absolute value of the fractional bias plus the fractional error for the case of 2×10^5 galaxies as a function of the ellipticity measurement error. The black curve shows the values obtained from the simulations. Over-plotted in red is a curve of the form $M\sigma^2 + C$.

and δ_{ϵ_2} are Gaussian distributed measurement errors with zero mean and variance σ^2. We used these noisy ellipticity values to calculate the measured $\left|\boldsymbol{\epsilon}^{\rm int}\right|$ of the galaxies, such that $\left|\hat{\boldsymbol{\epsilon}}^{\rm int}\right| = \sqrt{\hat{\epsilon}_1^{\rm int^2} + \hat{\epsilon}_2^{\rm int^2}}$. The $\left|\hat{\boldsymbol{\epsilon}}^{\rm int}\right|_i$ were then binned to give the estimated $f\left(\left|\boldsymbol{\epsilon}^{\rm int}\right|\right)$.

The number of galaxies in the sample was chosen so that the error bars shown in figure 3.13 were reduced by approximately a factor of two. This reduction in the size of the error bars resulting from a finite sample size allows a value of $B \leq 0.01$ to be achieved when measurement errors on the ellipticities are included.

Figure 3.15 shows B as a function of σ for the case of 2×10^5 galaxies and for $|\boldsymbol{g}| = 0.01$. Over plotted in red is a curve of the form $M\sigma^2 + C$ and fitted with $M \approx 189$ and $C \approx 5.03 \times 10^{-3}$. We can now constrain the allowed value of σ such that B is less than some value. From the curve fitted in Figure 3.15, we find that for 2×10^5 galaxies, $B \leq 0.01$ for $|\boldsymbol{g}| \geq 0.01$ if $\sigma \lesssim 0.005$. Therefore, we conclude that galaxies with a high signal to noise must be used if we are to avoid significant biases in the shear estimates arising from an imperfect estimate of $f\left(\left|\boldsymbol{\epsilon}^{\rm int}\right|\right)$.

3.5 Tests on simulations

To compare the performance of the position angle-only method with the standard method based on full ellipticity measurements, we have compared the convergence fields reconstructed from numerical simulations using both approaches. These tests were performed following the procedure outlined in Brown & Battye (2011a). Briefly, we used a single field from the simulated lensing convergence and shear maps of White (2005), which consist of ≈ 1000 deg^2 of simulated sky based on a ΛCDM cosmology with the parameters: $\Omega_m = 0.28$, $\Omega_b h^2 = 0.024$, $h = 0.7$, $\sigma_8 = 0.9$ and $n_s = 1$. The input convergence distribution used for the simulation is shown in the upper-left panel of Fig. 3.16. The upper-right panel shows the input convergence distribution smoothed on a scale of 1.5 arcmin.

We simulated a population of source galaxies assuming that the intrinsic ellipticities, $\left|\boldsymbol{\epsilon}^{\rm int}\right|$, follow the log-normal distribution

$$f\left(\left|\boldsymbol{\epsilon}^{\rm int}\right|\right) = \frac{K}{\left|\boldsymbol{\epsilon}^{\rm int}\right|} \exp\left(-\frac{\left(\ln\left(\left|\boldsymbol{\epsilon}^{\rm int}\right|\right) - \mu\right)^2}{2\sigma^2}\right), \tag{3.54}$$

where the mean and variance are given by

$$\begin{aligned} \text{mean} &= \exp\left(\mu + \frac{\sigma^2}{2}\right), \\ \sigma_\epsilon^2 \equiv \text{variance} &= \left(\exp\left(\sigma^2\right) - 1\right) \exp\left(2\mu + \sigma^2\right), \end{aligned} \tag{3.55}$$

and where the normalization constant, K, was determined numerically.

In anticipation of our tests on the CFHTLenS data (see Section 3.6), we set the mean value of $\left|\boldsymbol{\epsilon}^{\rm int}\right|$ to be 0.3370; which we estimated from the CFHTLenS data by finding the average of the modulus of the observed ellipticity value, $\left\langle\left|\boldsymbol{\epsilon}^{\rm obs}\right|\right\rangle$. The variance is taken to be $\sigma_\epsilon^2 = 0.2539^2$, which is the square of the dispersion fitted to the disc dominated galaxies in the CFHTLenS data. We also applied a maximum cut-off to the ellipticity of $\left|\boldsymbol{\epsilon}^{\rm int}_{\rm max}\right| = 0.804$ (Miller et al. 2013). It should be noted

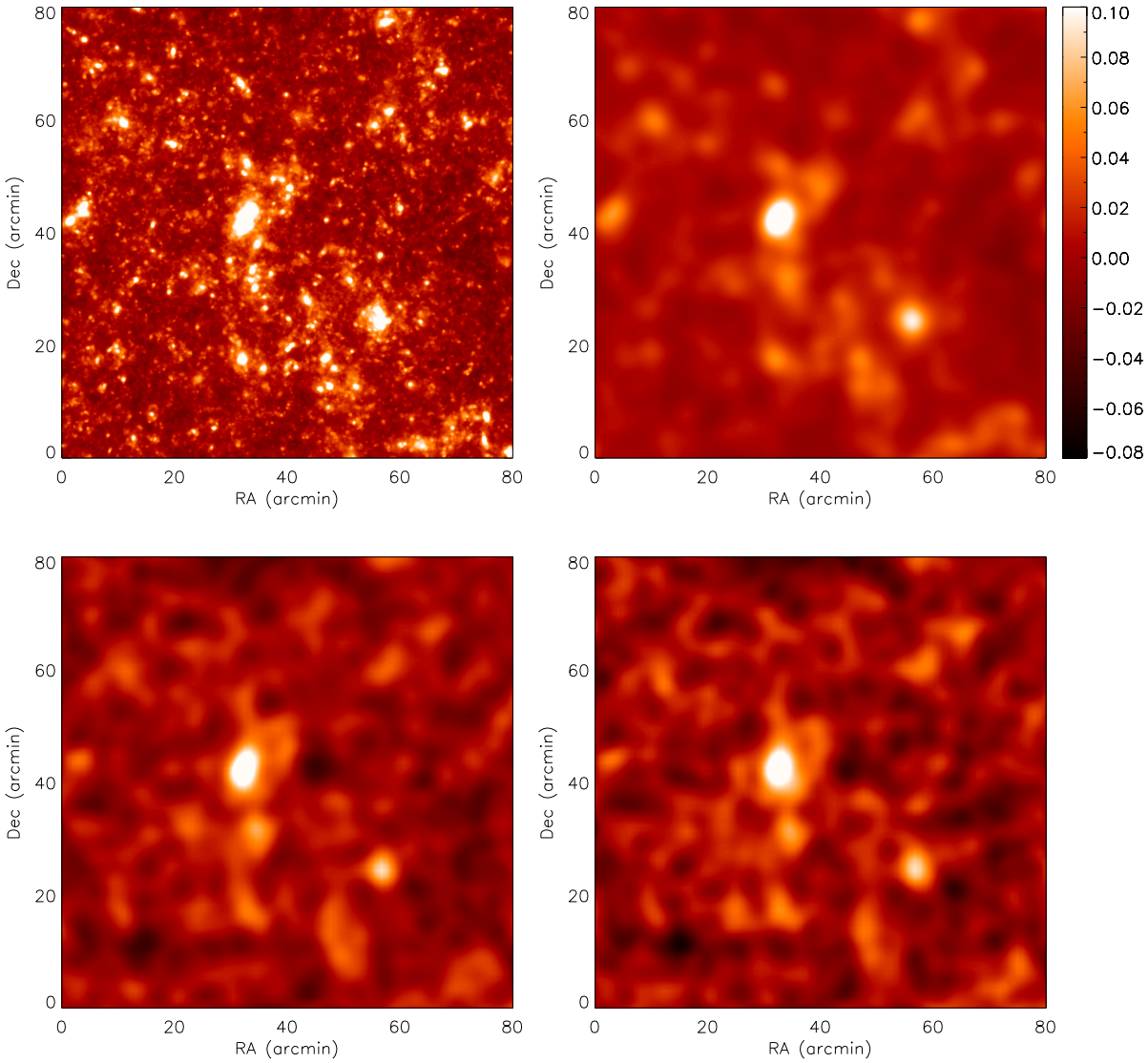

Figure 3.16: Reconstruction of the distribution of dark matter in a $1.75\,\mathrm{deg}^2$ region of the simulations. The upper-left panel shows the input convergence field, with the upper-right panel showing the input convergence field smoothed on a scale of 1.5 arcmin. The lower left panel shows the simulated reconstruction using the standard method with full ellipticity information and with zero measurement errors. The lower right panel shows the reconstruction using the 3rd order estimator of the position angle-only approach in the presence of measurement errors on the galaxy position angles with $\sigma_\alpha = 15°$.

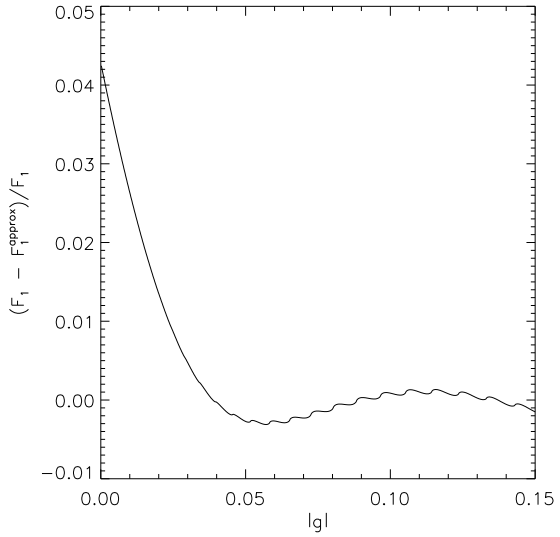

Figure 3.17: The fractional difference between the full $F_1\left(|\boldsymbol{g}|\right)$ function and the 3rd order approximation used to estimate the shear for the simulations. We see that the fractional difference is less than 5% for the range of $|\boldsymbol{g}|$ considered.

at this point that the ellipticities of the CFHTLenS data are not well described by a log-normal distribution. However, this distribution is easily simulated and is useful in demonstrating our method.

The number density of the background galaxies was taken to be $\bar{n} = 17$ arcmin^{-2} in accordance with the number density of resolved galaxy images observed by the CFHTLenS (Heymans et al. 2012).

When performing the reconstruction using the position angle-only method, we assume that $f\left(\left|\boldsymbol{\epsilon}^{\rm int}\right|\right)$ has been estimated from a large sample of high signal to noise galaxy images (see Section 3.4), such that residual biasing due to an imperfect knowledge of the distribution is negligible. To recover the shear estimates, we used the corrected form of the 3rd order estimator given in equation (C.12); where the best fit parameters are found to be $u = 2.423$, $v = 4.557$ and $w = -17.465$. Figure 3.17 shows the fractional difference between the full $F_1\left(|\boldsymbol{g}|\right)$ function and the approximate form used in this analysis. The latter is accurate to within 5% for all values of $|\boldsymbol{g}|$ in the range considered.

For this set of simulations, we assume that the measurement errors on the position angles are independent of the true position angles and are Gaussian distributed with zero mean and standard deviation $\sigma_\alpha = 15^\circ$. We are thus ignoring any effects which may contribute to the covariance terms in equation (3.51) and which would arise as a result of the method used to measure the position angles. Since it is difficult to identify a level of ellipticity measurement error that directly corresponds to our choice of σ_α, for the purpose of our simulations, we have assumed a zero measurement error on the ellipticity measurements. This would obviously not be the case in real data and so the reader should bear in mind that the precision of the ellipticity-based reconstruction relative to that of the position angle-only reconstruction will be somewhat over-estimated.

If we assume that the shear is small enough so that, for a given ellipticity distribution, we can use a first order approximation of the $F_1(|\boldsymbol{g}|)$ function, then one can easily obtain a first order approximation to the error on the angle-only estimator. In such a case, the first order corrected estimator is found to be

$$\hat{\boldsymbol{g}} = \frac{1}{u\beta_2 N}\sum_{i=1}^{N}\boldsymbol{n}^{(i)}, \tag{3.56}$$

where u is the first order coefficient of the expansion given in equation (C.3), and where β_2 is the noise bias correction term corresponding to a Gaussian measurement error on the position angles of 15°. The first order error is therefore given by

$$\sigma_{\hat{\boldsymbol{g}}} = \frac{1}{u\beta_2\sqrt{N}}\sigma_{\boldsymbol{n}}. \tag{3.57}$$

If we also assume that the shear is small enough that we can approximate $\sigma^2_{\boldsymbol{n}} \approx 0.5$ (which is the maximum value that $\sigma^2_{\boldsymbol{n}}$ can take and, from equation (3.24), is correct to first order in $|\boldsymbol{g}|$), then equation (3.57) simplifies to

$$\sigma_{\hat{\boldsymbol{g}}} \approx \frac{1}{u\beta_2\sqrt{2N}}. \tag{3.58}$$

From equation (3.58), we estimate the error on the shear estimates from these simula-

tions to be $\sigma_{\hat{\boldsymbol{g}}} \approx 0.33/\sqrt{N}$. The error on the shear estimates when using the standard method is $\sigma_{\rm st} = \sigma_\epsilon/\sqrt{N}$, as we have assumed zero measurement error on the ellipticities. Therefore, we can estimate the ratio of the errors using the two methods to be

$$\frac{\sigma_{\hat{\boldsymbol{g}}}}{\sigma_{\rm st}} \approx 1.3. \tag{3.59}$$

To perform the reconstruction, for each map pixel of side 1 arcmin, the shear is estimated by assigning a weight to each of the galaxies in the field so that the shear estimate for each map pixel contains a contribution from all of the galaxies in the field. For this analysis, we adopted the Gaussian weighting function:

$$W_k^{(i,j)} = \exp\left(-\frac{\left(\boldsymbol{\theta}_{i,j} - \boldsymbol{\theta}_k\right)^2}{2\theta_0^2}\right), \tag{3.60}$$

where θ_0 is the smoothing scale, which, in this case, is taken to be 1.5 arcmin.

The shear in each pixel in then estimated using both the standard estimator and the position angle-only estimator in order to produce two shear maps. When using the position angle-only approach, the weighting is applied to the observed unit vectors so that the average unit vector, which describes the average orientation, is given by

$$\langle \boldsymbol{n} \rangle_{i,j} = \frac{\sum_{k=1}^{N} W_k^{(i,j)} \boldsymbol{n}_k}{\sum_{k=1} W_k^{(i,j)}}. \tag{3.61}$$

In the standard approach, the weighting is applied to the galaxy ellipticities.

The convergence field is estimated separately for the two approaches using the discrete Kaiser-Squires inversion (Kaiser & Squires 1993), which is given as a convolution of the shear with the kernel

$$\mathcal{D}\left(\boldsymbol{\theta}\right) = -\frac{1}{\left(\theta_1 - i\theta_2\right)^2}, \tag{3.62}$$

such that the convergence is estimated as

$$\hat{\kappa}\left(\boldsymbol{\theta}\right) = \frac{1}{\pi}\sum_{i,j} = \mathrm{Re}\left[\mathcal{D}^{*}\left(\boldsymbol{\theta} - \boldsymbol{\theta}_{i,j}\right)\hat{\boldsymbol{g}}\left(\boldsymbol{\theta}_{i,j}\right)\left(1 - \hat{\kappa}\left(\boldsymbol{\theta}_{i,j}\right)\right)\right], \tag{3.63}$$

which is solved iteratively.

The reconstructed convergence maps are shown in the lower panels of Fig. 3.16. We see that the position angle-only approach successfully recovers the major mass concentrations with a performance that is qualitatively similar to that of the standard estimator.

In order to quantify the level of agreement between the two reconstructions, we have compared the residual map obtained from the difference between the two reconstructions to the residuals one would expect to see solely due to noise. To perform the comparison, we simulated 100 maps containing only galaxy shape noise (and measurement noise with $\sigma_{\alpha} = 15^{\circ}$ in the case of the position angle analysis). We then repeated the mass reconstructions for each realization for both the position angle-only approach and for the standard approach. A set of 100 simulated residual maps was then constructed by taking the difference between the noise-only maps recovered by the two approaches.

Fig. 3.18 shows a histogram of the r.m.s. residuals, σ_{res}, as measured from the suite of noise-only difference maps. When calculating the residuals, we ignored all pixels that lay within 5 arcmin of the edge of the reconstructed maps in order to avoid edge effects. The vertical red line shows the value of σ_{res} obtained from the difference of the two lower panels shown in Fig. 3.16. Since this is consistent with having been drawn randomly from the histogram distribution, we conclude that the two convergence reconstructions are consistent with each other. The simulated noise maps also provide us with an estimate of the error on both the standard estimator and the position angle-only estimator for the case of zero shear. The ratio of these errors was found to be $\sigma_{\hat{\boldsymbol{g}}}/\sigma_{\mathrm{st}} \approx 1.3$, which agrees with equation (3.59).

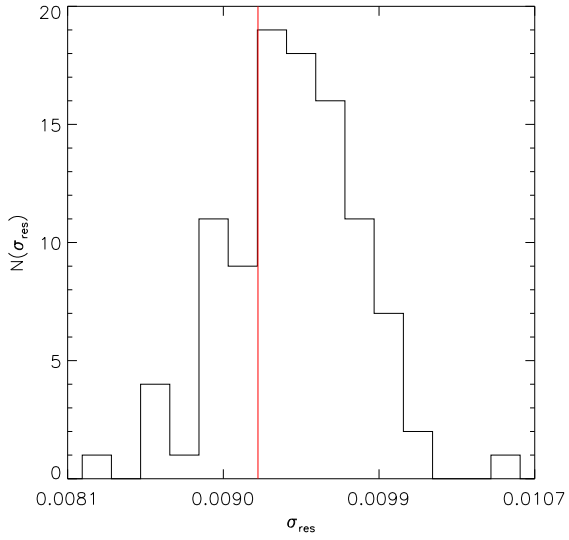

Figure 3.18: The distribution of the r.m.s. residuals, $\sigma_{\rm res}$, obtained from 100 simulated and differenced maps containing only noise contributions. The vertical red line shows the r.m.s. residual obtained from the difference of the reconstructed mass maps shown in Fig. 3.16. This plot shows that the difference between the two reconstructed mass maps is consistent with noise.

3.6 Demonstration on the CFHTLenS data

The CFHTLenS (Heymans et al. 2012) has observed four distinct fields, W1 ($\sim$63.8deg^2), W2 ($\sim$22.6 deg^2), W3 ($\sim$44.2deg^2) and W4 ($\sim$23.3 deg^2), providing full ellipticity measurements for each detected galaxy in addition to weights associated with each measurement. As a means of comparing our position angle-only approach with the standard approach using real data, we have reconstructed the mass maps of all four fields using both techniques.

The weighting provided for each ellipticity measurement has a contribution from the intrinsic shape dispersion and a measurement error, such that the weighting of the $i^{\rm th}$ galaxy is given as (Miller et al. 2013)

$$w_i = \left[\frac{\sigma_i^2 \left| \boldsymbol{\epsilon}_{\rm max}^{\rm int} \right|^2}{\left| \boldsymbol{\epsilon}_{\rm max}^{\rm int} \right|^2 - 2\sigma_i^2} + \sigma_\epsilon^2 \right]^{-1} , \tag{3.64}$$

where σ_i is the measurement error associated with the ellipticity of the $i^{\rm th}$ galaxy. The 1D dispersion in the intrinsic galaxy shapes is taken to be $\sigma_\epsilon = 0.2539$ (Miller et al. 2013). There are also two calibration values for each galaxy: $(1 + m_i)$ and $c_{2,i}$, which are respectively multiplicative and additive corrections. The $c_{2,i}$ correction is deducted from the $\epsilon_2^{\rm obs}$ component of the ellipticity and the $(1 + m_i)$ correction is applied to the average ellipticity in a given pixel, such that the standard shear estimator for each pixel is found to be (Van Waerbeke et al. 2013)

$$\hat{\boldsymbol{g}} = \frac{\sum_{i=1}^{N} w_i \left(\boldsymbol{\epsilon}_i^{\rm obs} - \boldsymbol{c}_i\right)}{\sum_{i=1}^{N} w_i \left(1 + m_i\right)}, \tag{3.65}$$

where $\boldsymbol{c}_i = (0, c_{2,i})$. Following the same procedure as in Section 5.4, we applied the Gaussian weight given in equation (3.60) to each galaxy so that the estimated shear in each pixel contains a contribution from all of the galaxies in a particular field. When considering the CFHTLenS data, this weighting process allows for a shear to be obtained for the regions that are masked. A cut-off was applied such that if the contribution to a given pixel has a maximum weighting of less than 0.5, then this pixel is ignored during the reconstruction.

In order to perform the position angle-only analysis, we have chosen to reconstruct the orientation of each galaxy by using equation (3.4) to obtain the relation

$$\alpha = \frac{1}{2} \tan^{-1} \left(\frac{\epsilon_2^{\rm obs} - c_2}{\epsilon_1^{\rm obs}} \right). \tag{3.66}$$

The multiplicative calibration factor is identical for both components of the ellipticity and so cancels out during the calculation of the position angles. However, the additive correction must be applied. We note that position angles reconstructed from the ellipticity measurements in this way would presumably retain many of the systematics that might already be present in the ellipticity measurements. In Chapter 4, we assess the potential advantages of a position angle approach to weak lensing in a more comprehensive manner by measuring the galaxy position angles directly from the imaging

data using, for example, the method discussed in Section 3.3. However, our current goal is to demonstrate the feasibility of our proposed technique for which reconstructing the position angles from the already carefully measured and calibrated ellipticity estimates suffices.

To implement the position angle-only approach, we also require an estimate of the intrinsic ellipticity distribution. To obtain this, we assumed that all of the galaxies in the CFHTLenS data are disc dominated – Miller et al. (2013) state that this accounts for approximately 90% of the galaxy population in the survey. In this case, and assuming that the shear signal is small, the functional form of the intrinsic ellipticity distribution can be approximated using the prior distribution (Miller et al. 2013)

$$f\left(\left|\boldsymbol{\epsilon}^{\mathrm{int}}\right|\right) = \frac{K\left(1-\exp\left(\frac{\left|\boldsymbol{\epsilon}^{\mathrm{int}}\right|-\left|\boldsymbol{\epsilon}^{\mathrm{int}}_{\mathrm{max}}\right|}{\sigma_{\epsilon}}\right)\right)}{\left(1+\left|\boldsymbol{\epsilon}^{\mathrm{int}}\right|\right)\left(\left|\boldsymbol{\epsilon}^{\mathrm{int}}\right|^{2}+\epsilon_{0}^{2}\right)^{\frac{1}{2}}}, \tag{3.67}$$

where K is a constant which was determined numerically to normalize the probability. The maximum ellipticity cut-off used was $\left|\boldsymbol{\epsilon}^{\mathrm{int}}_{\mathrm{max}}\right| = 0.804$, which arises primarily from the finite thickness of the galaxy discs. The dispersion was $\sigma_{\epsilon} = 0.2539$ and the "circularity" parameter was $\epsilon_0 = 0.0256$. We tabulated the $F_1\left(|\boldsymbol{g}|\right)$ function corresponding to equation (3.67) and inverted the function, using equation (3.34), to obtain an estimate of $|\boldsymbol{g}|$.

Finally, to complete the position angle-only estimator, we require a correction term in order to remove the noise bias associated with the measurement errors on the galaxy position angles. As described above, the position angle estimates were derived from the ellipticity measurements. For our current implementation, the position angle errors will therefore arise due to the propagation of the ellipticity errors through equation (3.66).

Assuming that the measurement errors are independent of the galaxy orientation, we obtained the noise bias correction term using the procedure outlined in Appendix B. We began by assuming that the measurement errors on the ellipticities are Gaus-

sian distributed (Miller et al. 2013). In this case, the probability distribution for the estimated ellipticity, $\hat{\boldsymbol{\epsilon}}$, of the $i^{\rm th}$ galaxy is

$$f^{(i)}\left(\hat{\boldsymbol{\epsilon}}\right) = K \exp\left(-\frac{\left|\hat{\boldsymbol{\epsilon}} - \boldsymbol{\epsilon}_i^{\rm true}\right|^2}{2\sigma_i^2}\right), \tag{3.68}$$

where $\boldsymbol{\epsilon}_i^{\rm true}$ is the true ellipticity of the galaxy and the measurement error, σ_i, can be calculated using equation (3.64). To arrive at the probability distribution for the estimated position angle ($\hat{\alpha}$), we must now marginalize over $|\hat{\boldsymbol{\epsilon}}|$:

$$f^{(i)}\left(\hat{\alpha}\right) = \int_0^1 f^{(i)}\left(\hat{\boldsymbol{\epsilon}}\right) |\hat{\boldsymbol{\epsilon}}| \, d|\hat{\boldsymbol{\epsilon}}|. \tag{3.69}$$

An exact implementation of equation (3.69) requires knowledge of the true value of the ellipticity of each galaxy, $\boldsymbol{\epsilon}_i^{\rm true}$, which is obviously not known. In order to calculate the noise bias correction term, we have therefore used equation (3.69) with the approximation that $\boldsymbol{\epsilon}_i^{\rm true} \approx \boldsymbol{\epsilon}_i^{\rm obs}$, where $\boldsymbol{\epsilon}_i^{\rm obs}$ is the observed ellipticity. While this will obviously not hold for each individual galaxy, we expect that after averaging over all of the galaxies in the survey, the derived mean correction term will be approximately correct.

The marginalized distribution returned by equation (3.69) will be symmetrically distributed about the observed position angle value. When this distribution is shifted so that the mean value is at zero, we recover the distribution of the measurement error on the position angle, $\delta\alpha$. For each galaxy, we then found the value of $\left\langle \cos\left(2\delta\alpha\right)\right\rangle_i$. Doing this for all galaxies in a particular field of the CFHTLenS data, the final correction term is simply the mean of all of the values of $\left\langle \cos\left(2\delta\alpha\right)\right\rangle_i$. The bias correction was found independently for each field. All four corrections were found to be $\beta_2 \approx 0.8$ which corresponds to an equivalent Gaussian measurement error of $\sigma_\alpha \approx 19^\circ$. It is conceivable that this error could be reduced if, in future surveys, measurements of the position angles are obtained directly from the imaging data as discussed in Section 3.3.

Using the angle-only method and following the approach adopted in Section 3.5,

we constructed mass maps for each of the four fields in the CFHTLenS. The pixel size used to reconstruct the maps was 4 arcmin, with a smoothing scale of 8.9 arcmin, which is the same as used in Van Waerbeke et al. (2013). The resulting maps are shown in Figs. 3.19–3.22, where we also present maps reconstructed using the standard (full ellipticity) approach for visual comparison. One can immediately see the qualitative agreement in the maps reconstructed using the two methods – the position angle-only approach recovers mass concentrations at the same locations as the standard estimator and on a similar scale. However, there appears to be a difference between the peak values of the mass concentrations when using the two methods. The standard approach uses a weighting scheme which downweights the contribution from noisy shape measurements when estimating the shear. However, the angle-only analysis does not implement such a weighting scheme, and hence the angle-only shear estimates contain noisier information. This noise propagates into the mass reconstructions and reduces the apparent peak values. For our purpose, this approach successfully demonstrates the potential of performing weak lensing using only galaxy position angles, and reliably recovering weighted averages of the trigonometric functions is left for future work.

Following the approach described in Section 3.5 we have attempted to quantify the level of agreement between the two sets of mass reconstructions by making use of simulations including only the effects of shape and measurement noise. For the case of the CFHTLenS data we created noise realizations by assigning a random orientation to every galaxy in the dataset. We performed two mass reconstructions for each realization – one using the standard method and one using the position angle-only method to estimate the shear. We produced a histogram of the r.m.s. residuals as measured from the difference between the reconstructed maps. The results are shown in Fig. 3.23 (black curves). When calculating the residuals we ignored all pixels in the mass maps that lie within $\sim$30 arcmin of a masked region in order to reduce edge effects. The vertical red lines show the r.m.s. residuals obtained from difference maps constructed from the mass reconstructions shown in Figs. 3.19–3.22. For each of the

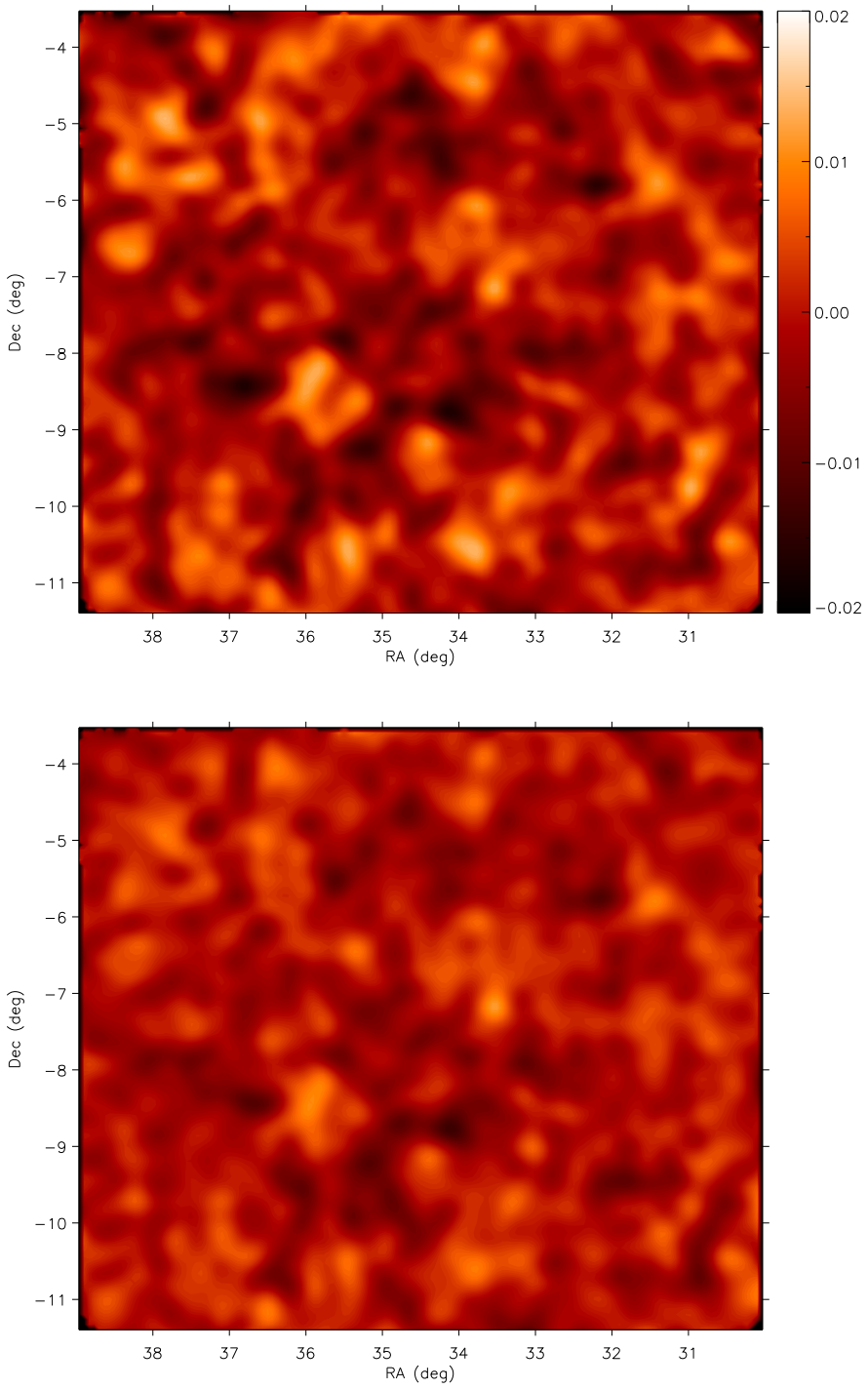

Figure 3.19: Mass reconstructions for the W1 field of the CFHTLenS. The top panel shows the reconstruction obtained using the standard method and the bottom panel is performed using the position angle-only approach. The smoothing scale for these reconstructions is 8.9 arcmin. The colour bars indicate the scale of the convergence fields.

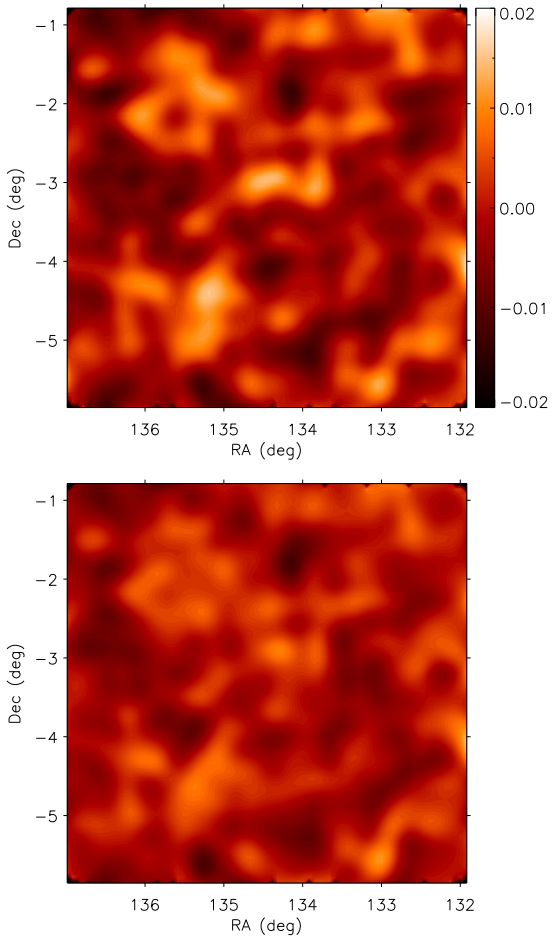

Figure 3.20: Mass reconstructions for the W2 field of the CFHTLenS. The top panel shows the reconstruction obtained using the standard method and the bottom panel is performed using the position angle-only approach. The smoothing scale for these reconstructions is 8.9 arcmin. The colour bars indicate the scale of the convergence fields.

four fields, the residual maps obtained by differencing the mass reconstructions are shown to be consistent with the corresponding difference maps from the simulations containing only noise. These results suggest that systematic differences between the two shear estimation techniques are sub-dominant to the noise in the reconstructions.

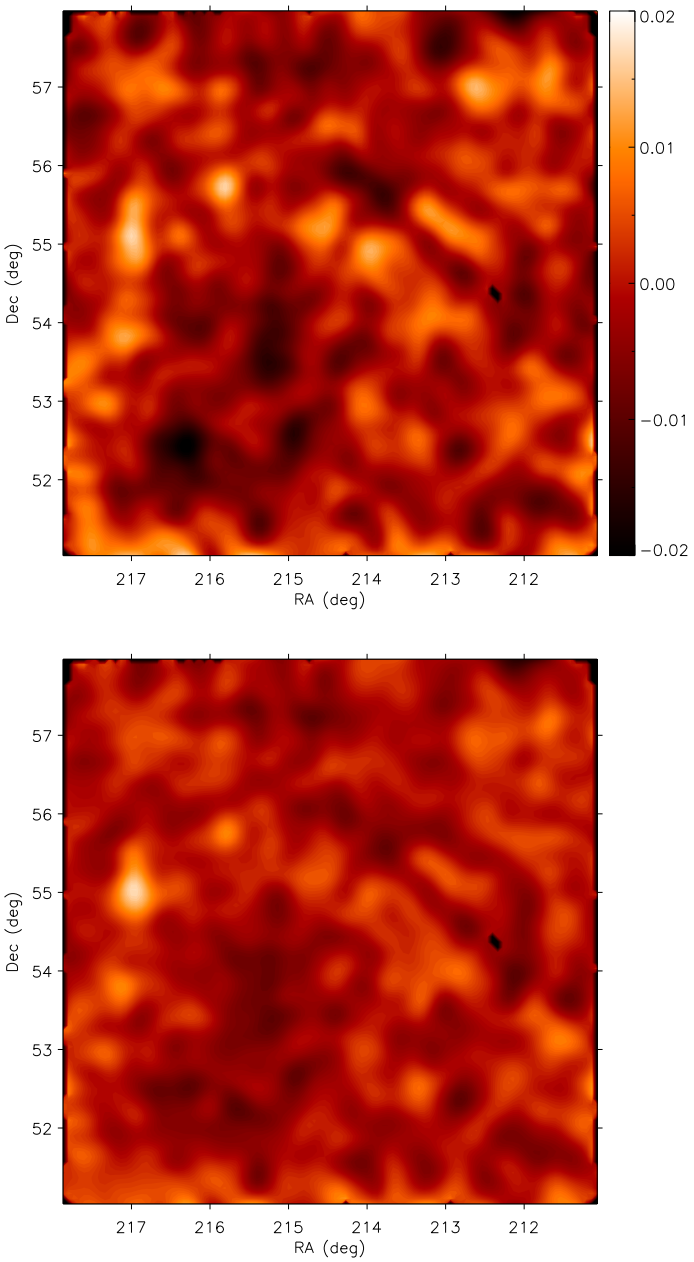

Figure 3.21: Mass reconstructions for the W3 field of the CFHTLenS. The top panel shows the reconstruction obtained using the standard method and the bottom panel is performed using the position angle-only approach. The smoothing scale for these reconstructions is 8.9 arcmin. The colour bars indicate the scale of the convergence fields.

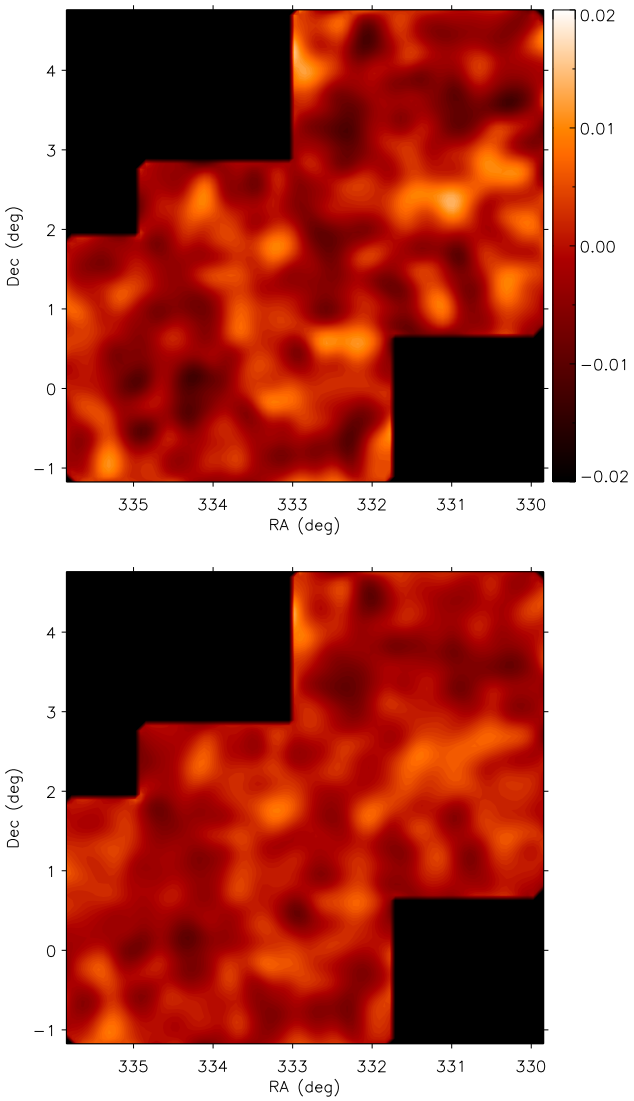

Figure 3.22: Mass reconstructions for the W4 field of the CFHTLenS. The top panel shows the reconstruction obtained using the standard method and the bottom panel is performed using the position angle-only approach. The smoothing scale for these reconstructions is 8.9 arcmin. The colour bars indicate the scale of the convergence fields.

3.7 Conclusions

Building on the work of Schneider & Seitz (1995), we have demonstrated a method of performing a weak lensing analysis using only the position angle measurements for a set of galaxies. By using the probability distribution for the intrinsic ellipticities of the galaxies, one can express the mean of the trigonometric functions in terms of

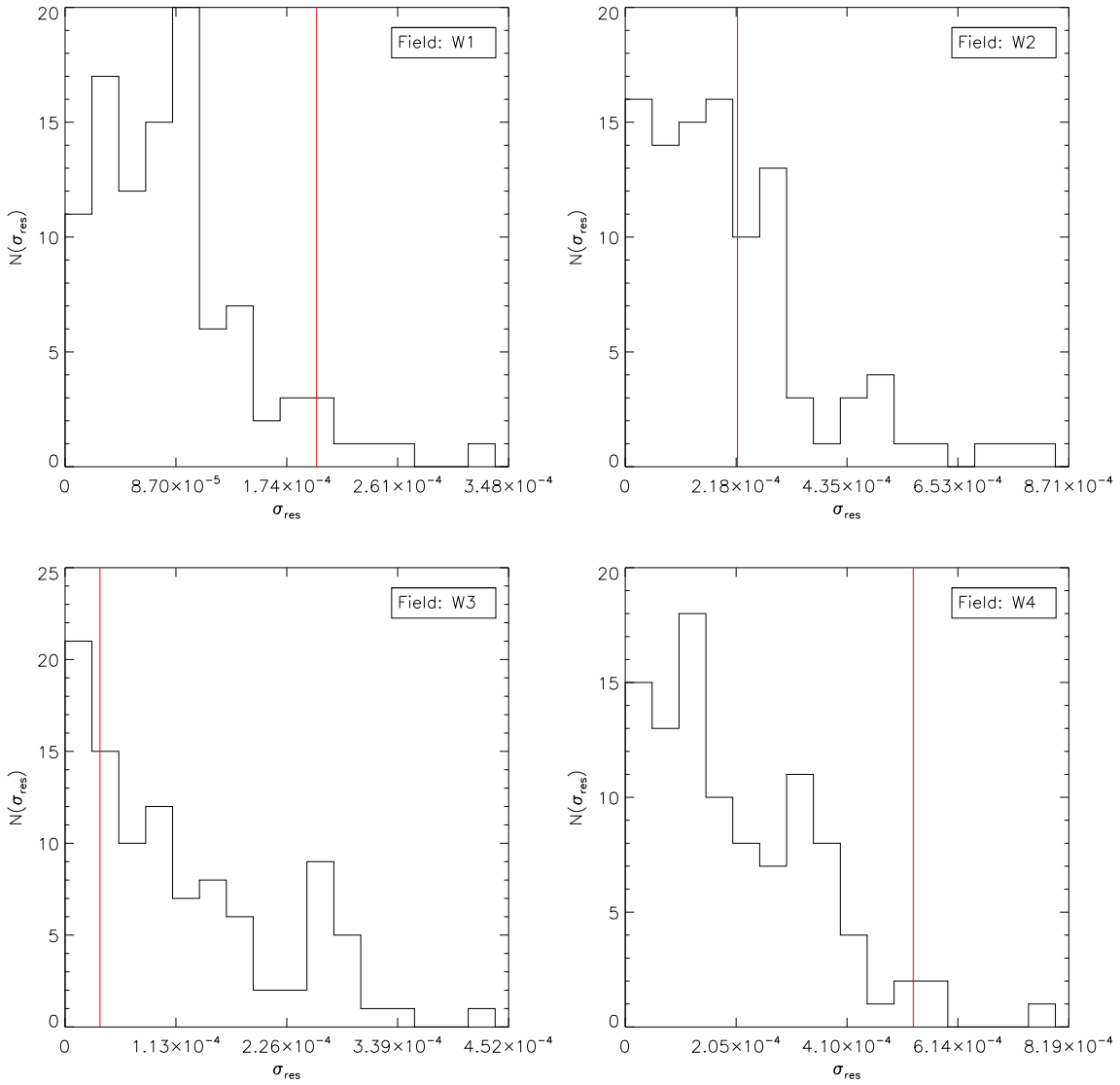

Figure 3.23: The distribution of the r.m.s residuals, $\sigma_{\rm res}$, obtained from 100 pairs of reconstructed maps containing only noise for each of the four fields of the CFHTLenS. The vertical red lines show the values of $\sigma_{\rm res}$ obtained from the difference between the reconstructed maps shown in Figs. 3.19–3.22. These results indicate that the difference between the two sets of reconstructed mass maps is consistent with noise.

the underlying shear unit vector and a function that depends on the modulus of the shear. Obtaining an estimate of the shear components is then possible by means of inverting this relationship. It has been shown that the bias introduced by position angle measurement errors can be reduced to negligible levels by the introduction of a correction term, which can be calculated numerically for a general error distribution.

The method has been successfully demonstrated using both simulations and using the data from the CFHTLenS. Upon comparing the residuals of the mass maps constructed using both the standard method and the position angle-only method, we have demonstrated that the difference between the two approaches is consistent with noise. This demonstration was performed using simulations where the intrinsic ellipticity distribution was assumed to be a log-normal distribution and using the data from the CFHTLenS, where we used the best-fit intrinsic ellipticity distribution for the disc dominated galaxies (Miller et al. 2013).

For the demonstration of our method on the CFHTLenS data, we derived the position angle estimates from the ellipticity measurements provided with the CFHTLenS data release. In order to fully exploit the potential advantages of position angle based weak lensing analyses, we have introduced a method of measuring the position angles of the galaxies directly from the imaging data. This method is developed in the next chapter, where the angle-only approach is applied to the GREAT3 simulations. It will be further developed in future work with the goal of reducing systematics and complementing parallel weak lensing analyses based on the full ellipticity information.

In the absence of direct position angle measurements, we find that when we calculate the position angles from the ellipticities provided by CFHTLenS, the multiplicative bias cancels out. Our position angle-only shear estimates will therefore only be sensitive to additive biases. However, for the position angle-only method to be successful, it is vital that the correct form of the intrinsic ellipticity distribution is used for any particular survey. If an incorrect form is used, then the form of the $F_1\left(|\boldsymbol{g}|\right)$ function will be incorrect and this will itself lead to mis-calibrated shear estimates. It has been shown that a realistic sample size of high resolution galaxy images can be used to ob-

tain an estimate of the intrinsic ellipticity distribution such that residual biases in the shear estimates resulting from an incorrect distribution are negligible.

Chapter 4

Demonstrating position angle-only shear estimators on the GREAT3 simulations

We develop and apply the position angle-only shear estimator of Chapter 3 to realistic galaxy images. This is done by demonstrating the method on the simulations of the GREAT3 challenge (Mandelbaum et al. 2014b), which include contributions from anisotropic PSFs. We measure the position angles of the galaxies using three distinct methods - the integrated light method, quadrupole moments of surface brightness, and using model-based ellipticity measurements provided by `IM3SHAPE`. A weighting scheme is adopted to address biases in the position angle measurements which arise in the presence of an anisotropic PSF. Biases on the shear estimates, due to measurement errors on the position angles and correlations between the measurement errors and the true position angles, are corrected for using simulated galaxy images and an iterative procedure. The properties of the simulations are estimated using the deep field images provided as part of the challenge. A method is developed to match the distributions of galaxy fluxes and half-light radii from the deep fields to the corresponding distributions in the field of interest. We recover angle-

only shear estimates with a performance close to current well-established model and moments-based methods for all three angle measurement techniques. The Q-values for all three methods are found to be $Q \sim 400$. The code is freely available online at `http://www.jb.man.ac.uk/~mbrown/angle_only_shear/`.

4.1 Introduction

As discussed in Section 2.6, measurements of the galaxy shapes need to be recovered from noisy, pixelized images. These images are convolved with an instrumental and/or atmospheric point spread function (PSF), and both moments and model-based methods must correct for the PSF contribution. Moments-based methods generally also implement a weighting function to reduce the effects of noise at large scales, and this function must subsequently be corrected for. For the case of an isotropic PSF, an incorrect calibration of the required correction will lead to multiplicative biases in the shear estimates. However, an isotropic PSF does not alter the orientations of the galaxies. We note that, for the generic case, regardless of the precise form of the PSF, there will be a small bias in position angle measurements due to pixelization. The same is true if one multiplies the galaxy image by a circular weighting function centred on the centroid of the galaxy. In Chapter 3 (hereafter C3), we proposed a method of performing weak lensing using only measurements of the galaxy orientations with the aim of exploiting this property. We demonstrated the method using simple simulations where we ignored the effects of a PSF and considered a simple Sérsic galaxy model for the intrinsic galaxy shapes. We found that the position angle-only method has the potential to yield shear estimates with a performance comparable with the KSB method.

An anisotropic PSF will bias position angle measurements, and therefore estimates of the shear if not corrected for. This bias is addressed in this chapter where we build upon the ideas introduced in C3 and apply the angle-only method to the simulations of the control-ground-constant (`cgc`) branch of the GREAT3 simulations (Mandelbaum et al. 2014b). These simulations were designed to test the performance of a shear

estimator on realistic galaxy images and include the effects of noise, pixelization, an anisotropic PSF, and realistic distributions of galaxy flux, size and shape.

In Section 4.2, we describe the three methods used to measure the position angles of the galaxies. The application of the angle-only method to the GREAT3 simulations is presented in Section 4.3.

From equation (3.49), we see that errors on the position angles of the galaxies and correlations between the true lensed position angles and the measurement errors bias our estimates of the mean trigonometric functions. This in turn biases the shear estimates. C3 addressed this issue, in the absence of a PSF, by estimating the β and covariance terms using simulations and applying an iterative procedure. However, we find that this approach is inadequate for fields which have a large anisotropic PSF. In Section 4.3, we introduce an alternative iterative procedure. We use an initial estimate of the shear recovered using weighted averages of the trigonometric functions to simulate the expected bias in the shear estimates and subsequently correct our estimates.

The results are presented in Section 4.4, where we compare the angle-only method, using the three angle measurement techniques, with the results of a naive application of `IM3SHAPE` and also with the highest entries to the GREAT3 challenge from `IM3SHAPE` and the KSB method. We conclude with a discussion in Section 4.5.

4.2 Measuring the position angles

When analysing the `cgc` branch of the GREAT3 simulations, we use three distinct methods to measure the position angles from the simulated galaxy images. The first is the integrated light method discussed in C3. The second uses the second order moments of brightness of the galaxy image. The third uses ellipticities measured by `IM3SHAPE` to determine the position angles. Here we briefly discuss the three approaches.

4.2.1 The integrated light method

The integrated light method for measuring galaxy position angles is discussed in detail in Section 3.3. Here we briefly explain the application of the method to the images of the `cgc` simulations.

We begin by estimating the mean half-light radius of the galaxies in the field of interest using the relationship between the mean half-light radius and the mean flux of the galaxies discussed in Section 4.3 and given in equation (4.6). For each galaxy in the `cgc` branch, we initially assume the centroid of the galaxy to be the centre of the image. We apply a circular Gaussian weighting function to the image centred on this initial estimate of the centroid. The half-light radius of the weighting function is equal to twice the mean half-light radius of the galaxies in the field. The image is then convolved with a circular Gaussian kernel with a width of two pixels to reduce the effects of pixelization. The centroid is then recalculated using the first-order moments of the convolved weighted surface brightness distribution, $I_w(\boldsymbol{\theta})$, using equation (2.26). This step is iterated until the difference between subsequent estimates of the components of the centroid are less than 10^{-3} of a pixel.

We then estimate the 1D integrated light distribution, $I'(\theta)$, of the galaxy as a function of assumed position angle, θ, using equation (3.46). Finally, the estimated position angle of the galaxy is given by equation (3.47).

4.2.2 A moments-based method

The moments-based method uses second order moments of the convolved weighted brightness distribution, $I_w(\boldsymbol{\theta})$, to estimate the position angle (Kaiser et al. 1995). We follow the approach outlined in the previous subsection to estimate the width of the weighting function used for each field and the centroid of the individual galaxy images. The position angles of the galaxies are then calculated using the second-order moments

of $I_w(\boldsymbol{\theta})$, as defined in equation (2.25), such that

$$\hat{\alpha} = \frac{1}{2}\tan^{-1}\left(\frac{2Q_{12}}{Q_{11}-Q_{22}}\right). \tag{4.1}$$

4.2.3 Using `IM3SHAPE`

Using `IM3SHAPE`, we measure the observed ellipticities of the galaxies in each field and use the ellipticity measurements to determine the galaxy position angles. When fitting a model of the galaxy shape to the galaxy image, `IM3SHAPE` takes into account the contribution of the PSF by convolving the model galaxy with a star field image. The GREAT3 challenge provides star field images at the same resolution as the galaxy images for each field of the `cgc` branch. When using `IM3SHAPE` to measure the position angles of the galaxies, we use these star field images directly to calibrate for the PSF. However, when we require full ellipticity information (i.e. when estimating $f\left(\left|\boldsymbol{\epsilon}^{\rm int}\right|\right)$ in Section 4.3 and when using `IM3SHAPE` to estimate the shear, as a comparison with the angle-only method, in Section 4.4), we use star field images which are upsampled by a factor of seven. The upsampled star field images were created by interpolating from the low resolution image using the quintic interpolation scheme (`InterpolatedImage`) provided by `GalSim` (Rowe et al. 2014). We use original star field images for the position angle measurements to reduce computation time when calibrating the angle-only shear estimates using simulations. Since `IM3SHAPE` corrects for the PSF when measuring the ellipticities, the angle-only method using `IM3SHAPE` differs from the integrated light and moments-based methods which do not include any PSF correction at this stage. Upon recovering measurements of $\boldsymbol{\epsilon}^{\rm obs}$, we estimate the position angles of the galaxies as

$$\hat{\alpha} = \frac{1}{2}\tan^{-1}\left(\frac{\epsilon_2^{\rm obs}}{\epsilon_1^{\rm obs}}\right). \tag{4.2}$$

4.3 Application to the GREAT3 simulations

The `cgc` branch of the GREAT3 challenge simulates ground-based observations of 200 $10 \times 10\,\mathrm{deg}^2$ fields. Each simulated observation contains 10^4 resolved galaxy images. A constant shear is applied to all of the galaxies within a particular field. The images of the galaxies within each field are convolved with a constant anisotropic PSF, and a constant level of background Gaussian noise is assumed. The applied PSF and background noise levels are varied between the different observations, and the applied shear is different for each field observed. Noiseless star field images are included for each field providing an image of the PSF. The `cgc` branch also includes five deep field observations for use as a training dataset. These observations consist of galaxy images that are one magnitude deeper than the challenge observations, but the dataset retains only images of the galaxies which would be present in the rest of the challenge. The properties of the simulations are discussed in detail in Mandelbaum et al. (2014b).

In this section, we describe the application of the angle-only method to the `cgc` branch of the GREAT3 simulations. We measure the position angles of the galaxies from the simulated images using the three methods discussed in the previous section. We begin by outlining the steps of the procedure followed in the angle-only analysis.

1. Calculate the $F_1\left(|\boldsymbol{g}|\right)$ function using equation (3.8). This requires an estimate of $f\left(\left|\boldsymbol{\epsilon}^{\mathrm{int}}\right|\right)$ which we obtain from the GREAT3 deep field calibration sets using `IM3SHAPE`.

2. Measure the fluxes of the galaxies in the deep field images by summing over the pixel values and recover measurements of the half-light radii and the bulge to total flux ratio of the galaxies from `IM3SHAPE`, to be used in calibration simulations.

3. Determine the relationship between the mean fluxes and the mean half-light radii of the five deep fields.

4. Measure the mean flux of the galaxies in the field of interest and use this measurement to modify the fluxes and half-light radii of the deep field measurements output from step 2 above.

5. Use the modified fluxes and half-light radii with the intrinsic ellipticity estimates, bulge to total flux ratio measurements, and a suite of random uniform distributed intrinsic position angles to simulate zero shear galaxy images using `GalSim`. The noise in the simulated images is estimated from the GREAT3 image being analysed.

6. Measure the position angles of the galaxies in the zero shear simulations using one of the three methods discussed in the previous section. These measurements are used to construct a weighting function the purpose of which is to correct for PSF anisotropy and pixelization effects.

7. Measure the position angles of the galaxies in the field of interest and estimate the shear using weighted averages of the trigonometric functions.

8. Use the shear estimates to produce an updated set of simulations which include information about the shear.

9. Estimate the shear in the updated simulations using the same weighting function as in step 6. Use these estimates to determine the bias in the estimates recovered in step 7 and correct for the bias.

10. Repeat steps 7-9 using the corrected shear estimates as the input shear for the simulations until the estimated bias is below a desired threshold value.

We now discuss our application of this procedure to the `cgc` branch in detail.

We began by estimating the form of the $F_1\left(|\boldsymbol{g}|\right)$ function (step 1) using `IM3SHAPE` to measure the observed ellipticities of the galaxies for each of the deep fields of the `cgc` branch. When measuring a galaxy's ellipticity using `IM3SHAPE`, we used star

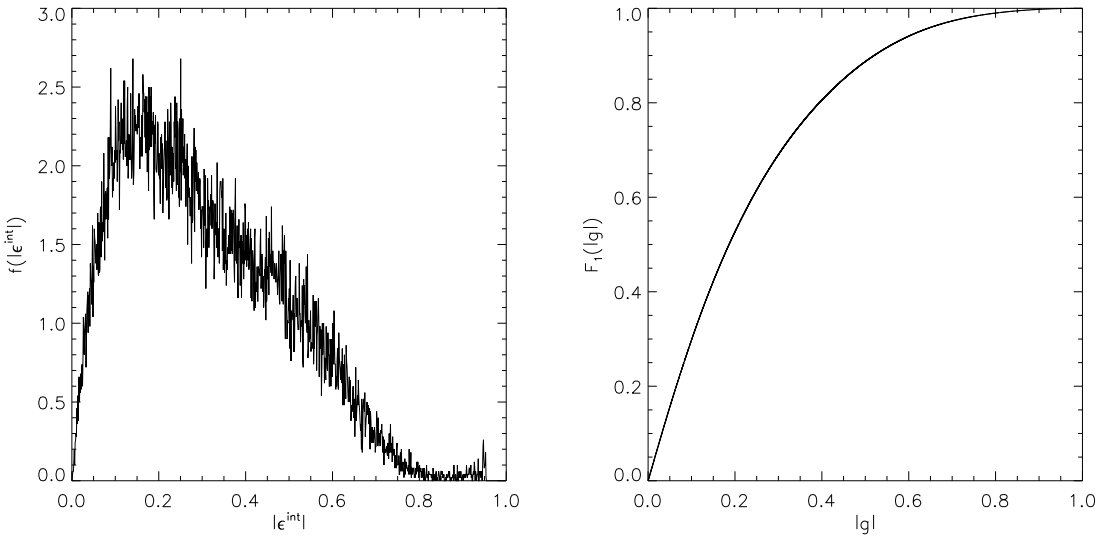

Figure 4.1: Left-hand panel: The reconstructed $f\left(\left|\boldsymbol{\epsilon}^{\rm int}\right|\right)$ using `IM3SHAPE` to recover the estimates of the intrinsic ellipticities of the galaxies in the deep field images of the `cgc` branch and with a binwidth of $\Delta\left|\boldsymbol{\epsilon}^{\rm int}\right| = 5\times10^{-3}$. Right-hand panel: The $F_1\left(|\boldsymbol{g}|\right)$ function calculated using equation (3.8) and the reconstructed $f\left(\left|\boldsymbol{\epsilon}^{\rm int}\right|\right)$ shown in the left-hand panel.

images which were upsampled by a factor of seven to correct for the PSF contribution (as opposed to the original star images used when we were concerned only with a galaxy's position angle). For each of the deep fields, we averaged over the observed ellipticity measurements to estimate the shear for that field. Using the estimated shears and the measured ellipticities, we recovered estimates of the intrinsic ellipticities of the galaxies by inverting equation (3.1) and reconstructed $f\left(\left|\boldsymbol{\epsilon}^{\rm int}\right|\right)$, shown in Figure 4.1. From this estimate of the distribution, we calculated the $F_1\left(|\boldsymbol{g}|\right)$ function numerically using equation (3.8); this is shown in the right panel of Figure 4.1. As discussed in Section 3.4, the integral carried out when calculating the $F_1\left(|\boldsymbol{g}|\right)$ function smooths the $f\left(\left|\boldsymbol{\epsilon}^{\rm int}\right|\right)$ distribution. However, if we use a large binsize for the distribution we lose information. We therefore chose a binsize of 5×10^{-3} in accordance with the binsize used in Section 3.4.

The effects of the PSF on a galaxy's observed ellipticity and orientation depend on the underlying ellipticity of the galaxy. When using the angle-only estimator, we do not recover information about the ellipticities, and therefore a complete understand-

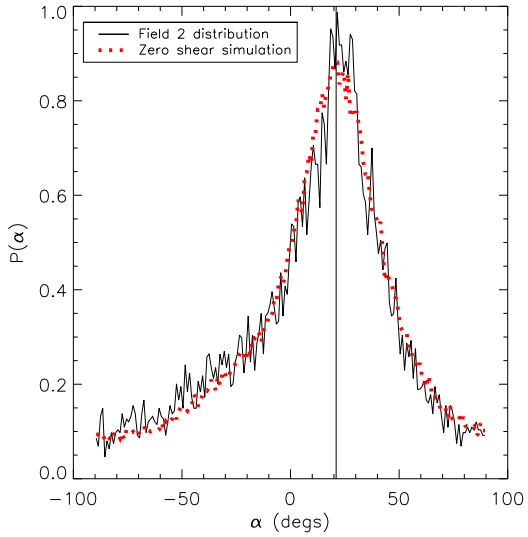

Figure 4.2: The distribution of position angles measured from field 2 using the integrated light method (black curve). The vertical black line shows the position angle of the PSF. Here we see that the measured position angles are biased in the direction of the PSF. The red dotted curve shows the distribution of measured position angles recovered from the zero shear simulations. We see that the distribution from the simulations provides a good description of the distribution from the image data, with the difference between the two being attributed to the shear signal for the zeroth-order shear estimate.

ing of the effects of the PSF on an individual galaxy's orientation cannot be realized. Instead, we chose to examine the impact of the PSF on the ensemble of galaxies. In the absence of a PSF (and pixelization), we expect the distribution of position angle measurements to be approximately uniform, with any deviation from uniformity being attributed to the underlying shear signal. In Figure 4.2, we show the distribution of measured position angles from field 2 of the GREAT3 `cgc` simulation set measured using the integrated light method. We see the unsurprising result that the position angles are biased in the direction of the PSF. This results in non-zero correlations between the galaxy position angles and the errors on the measurements which biases the shear estimates via equation (3.49).

To correct for this effect, we adopt a weighting scheme in which we downweight the contribution to the mean trigonometric functions (see equations (3.22) and (3.23)) from galaxies which align with the PSF. To understand how the galaxies should be

weighted, let us assume a large sample of galaxies with a zero shear signal. In the absence of a PSF, we expect a uniform distribution of measured position angles and therefore the mean trigonometric functions to be zero. The observed unit vector of the galaxy is

$$\boldsymbol{n}\left(\hat{\alpha}\right) = \begin{pmatrix} \cos\left(2\hat{\alpha}\right) \\ \sin\left(2\hat{\alpha}\right) \end{pmatrix}. \tag{4.3}$$

In the presence of a PSF, the angle distribution becomes non-uniform, and the mean unit vector, $\langle\hat{\boldsymbol{n}}\rangle$, will be

$$\langle\hat{\boldsymbol{n}}\rangle = \int_{-\frac{\pi}{2}}^{\frac{\pi}{2}} \mathrm{d}\hat{\alpha}\, \boldsymbol{n}\left(\hat{\alpha}\right) f_{\mathrm{PSF}}\left(\hat{\alpha}\right), \tag{4.4}$$

where $f_{\mathrm{PSF}}\left(\hat{\alpha}\right)$ is the distribution of measured position angles given a non-zero PSF. If we introduce a weighting function, $w\left(\hat{\alpha}\right)$, such that

$$\langle\hat{\boldsymbol{n}}\rangle = \int_{-\frac{\pi}{2}}^{\frac{\pi}{2}} \mathrm{d}\hat{\alpha}\, w\left(\hat{\alpha}\right) \boldsymbol{n}\left(\hat{\alpha}\right) f_{\mathrm{PSF}}\left(\hat{\alpha}\right), \tag{4.5}$$

it is clear that one can correct for the effects of the PSF, such that we recover mean trigonometric functions equal to zero, if we set $w\left(\hat{\alpha}\right) = 1/f_{\mathrm{PSF}}\left(\hat{\alpha}\right)$. To proceed, we therefore require an estimate of the distribution of measured position angles when a PSF is included.

To achieve this, we used `GalSim` to simulate 10^5 galaxy images with specific properties provided by `IM3SHAPE` and assuming a zero input shear signal. For each galaxy in the five deep fields, we measured $\boldsymbol{\epsilon}^{\mathrm{obs}}$, the bulge to total flux ratio (B/S), and the half-light radius (R_{e}). For each field, we also estimated the shear by averaging over $\boldsymbol{\epsilon}^{\mathrm{obs}}$ allowing us to estimate the $\boldsymbol{\epsilon}^{\mathrm{int}}$ of each galaxy by inverting equation (3.1). For each of these galaxies, we simulate a corresponding galaxy using the measured properties as a template. The intensity profile of each simulated galaxy was assumed to be a Sérsic profile consisting of a bulge with Sérsic index $n_{\mathrm{s}} = 4$ and a disc with $n_{\mathrm{s}} = 1$, and with the half-light radii of each of these components being identical. The

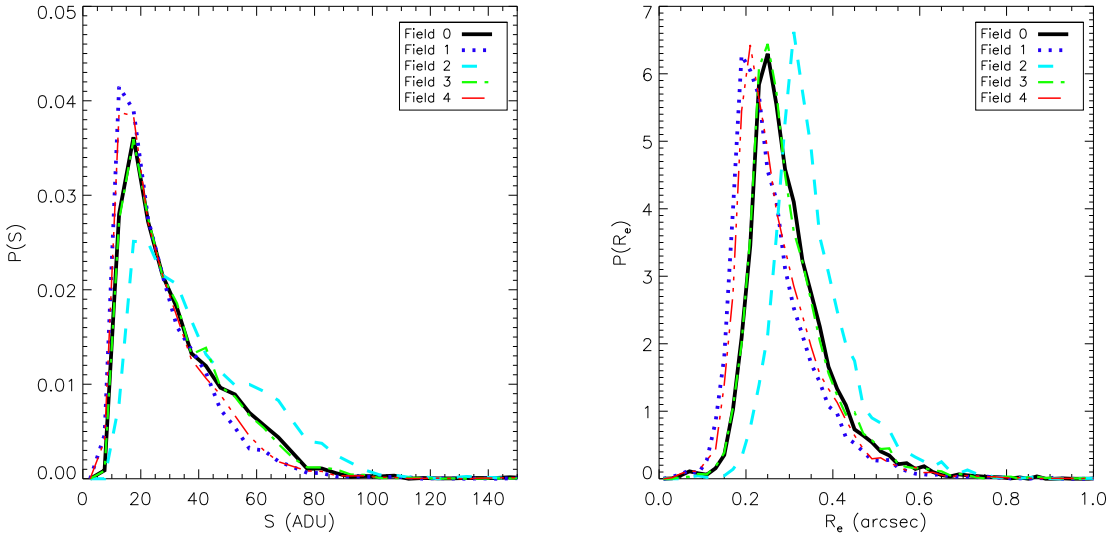

Figure 4.3: The left-hand panel shows the distributions of galaxy fluxes for the five deep fields of the `cgc` branch. The right-hand panel shows the distributions of half-light radii for the galaxies in these fields. The half-light radii have been measured using `IM3SHAPE`.

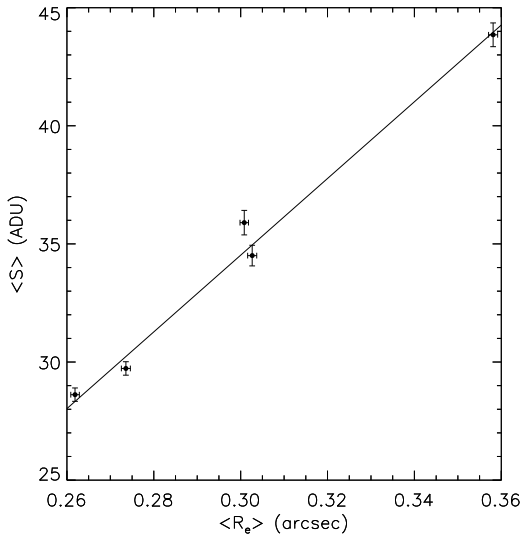

Figure 4.4: The mean flux of the galaxies plotted as a function of the mean half-light radius for each of the five deep fields. Here we see a linear relationship between the two quantities. The line is the best fit to the data.

simulated galaxy is created with an intrinsic ellipticity of $\left|\epsilon^{\rm int}\right|$ and with a position angle drawn randomly from a uniform distribution with the range $[-90°, 90°)$.

For each field in the `cgc` branch, the galaxy images are convolved with a different PSF, and only resolved galaxy images are included in the sample. Including only resolved galaxy images implies that the distributions of the half-light radii, and therefore the fluxes of the galaxies, are different for each field. In order to construct accurate calibration simulations, we require the distributions of these properties in the simulations to match the distributions in the field being analysed. We used the properties estimated by `IM3SHAPE` when analysing the deep field images to investigate how this can be achieved. First, we measured the flux of each galaxy by summing over the pixel values in each galaxy image, and we recovered the half-light radii estimates provided by `IM3SHAPE` (step 2). Figure 4.3 shows the distributions of galaxy fluxes and half-light radii for each of the five deep fields. We see the difference between the distributions for each field. In Figure 4.4, we plot the mean galaxy flux for each field as a function of the mean half-light radius. This indicates a linear relationship between the two quantities. We fitted a linear function of the form $\langle S \rangle = m \langle R_{\rm e} \rangle + c$ to this data (step 3) with the fitted parameters given by $m = 162.4\,\mathrm{ADU\,arcsec^{-1}}$ and $c = -14.19\,\mathrm{ADU}$. This relationship allows for a direct estimate of $\langle R_{\rm e} \rangle$ simply by summing over the pixel values in a particular field, such that

$$\langle R_{\rm e} \rangle = \frac{\langle S \rangle - c}{m}. \tag{4.6}$$

One should not assign significance to the relationship shown in Figure 4.4. The method for recovering estimates of $\langle R_{\rm e} \rangle$ works as long as one can characterize a relation between $\langle R_{\rm e} \rangle$ and $\langle S \rangle$. In real data, it is expected that the correlation between these two quantities would be undetectable due to the randomness in the sizes and morphologies of the source galaxies. However, we have exploited this characteristic of the GREAT3 simulations to provide us with accurate calibration simulations when constructing the weighting function. If this correlation cannot be detected in real data, alternative methods for constructing accurate calibration simulations based the source population must be used.

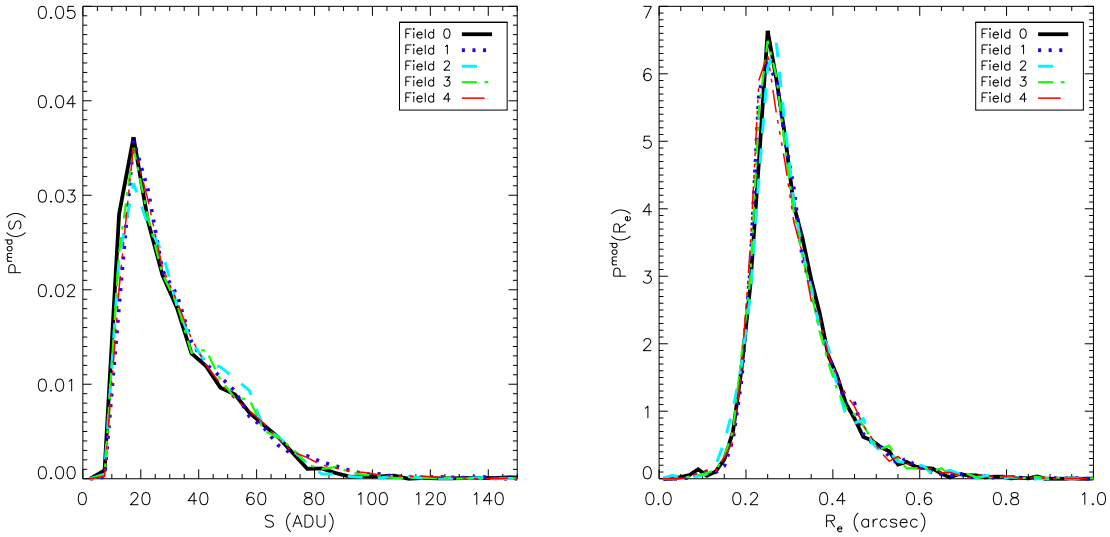

Figure 4.5: The distributions of flux and half-light radii shown in Figure 4.3 modified using the relationships given by equations (4.7-4.10) so that they match the distributions of field 0. These plots indicate that the flux and half-light radii distributions in a particular field can be accurately reproduced using these relationships.

If $P_S^n(S)$ is the distribution of the fluxes in field n and $\langle S \rangle_n$ is the mean flux of a galaxy for that field, we find that we can write an approximate relationship for the flux distributions of two fields a and b as

$$P_S^a(S) = P_S^b(KS), \tag{4.7}$$

where

$$K = \frac{\langle S \rangle_a}{\langle S \rangle_b}. \tag{4.8}$$

We find we can also write a similar relationship for the distributions of half-light radii of the two fields, $P_{R_e}^a(R_e)$ and $P_{R_e}^b(R_e)$,

$$P_{R_e}^a(R_e) = P_{R_e}^b(R_e + K'), \tag{4.9}$$

where

$$K' = \langle R_e \rangle_a - \langle R_e \rangle_b . \tag{4.10}$$

If one measures the means of the fluxes of the galaxies in fields a and b, one can recover estimates of the means of the half-light radii in these fields using the linear relationship shown in Figure 4.4 and equation (4.6). It is then possible to modify the distributions of the fluxes and half-light radii in field b so that they approximately match those in field a. An example of this procedure is shown in Figure 4.5, where we have modified the distributions of the deep fields 1-4 (shown in Figure 4.3) to match deep field 0. We see that the distributions of the fluxes and half-light radii of a particular field can be accurately reproduced if the mean of the galaxy fluxes can be accurately measured and, as this requires simply summing over the image pixels within a particular field, we expect this to be achievable.

When applying this method to the challenge data, we measured the mean flux of the galaxies in the field of interest. We then modified the fluxes and half-light radii of all the galaxies in the five deep fields. We combined the modified fluxes and half-light radii with the estimated values of $\left|\boldsymbol{\epsilon}^{\rm int}\right|$ and B/S, and a suite of uniform random intrinsic position angles to provide us with the inputs required for 5×10^4 simulated galaxies (step 4). The GREAT3 simulations use galaxy pairs whereby for each galaxy with an intrinsic orientation of $\alpha^{\rm int}$, there is an identical galaxy with an intrinsic orientation of $\alpha^{\rm int} + 90^\circ$. This is done to reduce intrinsic shape noise in the shear estimates, and hence the number of galaxies needed to average over. For each of our 5×10^4 simulated galaxies, we therefore created an identical galaxy image but rotated by 90° with respect to the first, mimicking the procedure implemented by GREAT3. This provided us with 10^5 simulated galaxy images. These images were convolved with the upsampled star field images to simulate the effects of the PSF. The pixel scale of the simulations was chosen to match the pixel scale used by GREAT3. The noise in the images was assumed to be Gaussian with the variance estimated from the values of the outermost pixels of each $48 \times 48\,\text{pixel}^2$ stamp in the field and with all 10^4 stamps used in the estimate (step 5).

Once the simulated galaxy images were created, we measured the position angles of the galaxies using each of the three methods discussed above (step 6). The results

of this for field 2 when using the integrated light method are presented as the red curve in Figure 4.2. This distribution was binned with a bin size of 1° to give the distribution of position angles, $P\left(\alpha_i\right)$. As described above, the required weighting function is the reciprocal of this distribution

$$w\left(\alpha_i\right) = \frac{1}{P\left(\alpha_i\right)}. \tag{4.11}$$

We used this weighting function to correct the averages of the observed trigonometric functions for the PSF and pixelization, such that

$$\langle \hat{\boldsymbol{n}} \rangle = \frac{\sum_{i=1}^{N} w\left(\hat{\alpha}_i\right) \hat{\boldsymbol{n}}_i}{\sum_{i=1}^{N} w\left(\hat{\alpha}_i\right)}. \tag{4.12}$$

Ideally, the weighting applied to each galaxy in the image would depend on the position angle of the galaxy without the effect of lensing (but with the effects of PSF, pixelization and noise still present). However, this is obviously not possible for real data. Assuming that the rotation induced by lensing is small, the weighting of the trigonometric functions will not be significantly affected by lensing and, provided the simulations are accurate, any resulting bias to the shear estimates should be corrected for by the iterative procedure discussed below.

Using the weighted averages given by equation (4.12), we recover a zeroth-order estimate of the input shear signal, $\hat{\boldsymbol{g}}^{(0)}$, in each field via equations (3.22) and (3.23) (step 7). Let m'_j and c'_j respectively denote the multiplicative and additive biases on the j^{th} component of the zeroth-order shear estimates (Heymans et al. 2006; Huterer et al. 2006; Massey et al. 2007) in a reference frame aligned with the simulated images. The estimates can then be written as

$$\hat{g}_j^{(0)} = g_j + m'_j g_j + c'_j + \delta g_j^{(0)}, \tag{4.13}$$

where $\delta g_j^{(0)}$ is an error on the estimate with zero mean. If we assume that the weighting function successfully mitigates the effects of an additive bias, the zeroth-order estimate is expected to underestimate the modulus of the true shear signal as there is no correc-

tion for the measurement error bias arising from β_c in equation (3.50). It is possible to correct for this bias using the zero shear simulations to model the measurement error for each field as discussed in C3. However, for cases where there are large contributions from anisotropic PSFs, we find that the errors on the position angle measurements can be large leading to small values of β_c. Hence, attempting to correct for these biases can lead to substantial outliers in the shear estimates. Also, errors on the estimates of β_c propagate nonlinearly into estimates of the shear. We therefore choose to simulate a further suite of 10^5 galaxy images using the procedure described above, and we shear the galaxies using the estimates $\hat{\boldsymbol{g}}^{(0)}$ (step 8) for each field. We measure the shear from these updated simulations and use these estimates to determine and correct for the bias in the initial estimates recovered for each field (step 9), such that

$$\hat{\boldsymbol{g}}^{(1)} = \hat{\boldsymbol{g}}^{(0)} - \left(\hat{\boldsymbol{g}}^{(1)}_{\rm sim} - \hat{\boldsymbol{g}}^{(0)}\right), \tag{4.14}$$

where the shear estimate recovered from the first-order simulations is

$$\hat{g}^{(1)}_{j,\rm sim} = \hat{g}^{(0)}_j + m'_j \hat{g}^{(0)}_j + c'_j + \delta g^{(1)}_j. \tag{4.15}$$

This method therefore corrects for the bias introduced to the estimates of the shear and does not correct for the bias on the individual galaxy position angle estimates. We can iterate this step until estimates of the shear between subsequent iterations are consistent (step 10).

For a large number of simulated galaxy images, noise in the estimated bias will be sub-dominant to noise in the zeroth-order shear estimate. However, using this iterative method, noise in the simulated shear estimates, $\hat{\boldsymbol{g}}^{(1)}_{\rm sim}$, due to a finite number of simulated galaxy images propagates linearly into the final shear estimates. Therefore, if we assume that the details of the simulations are accurate, there is no additional noise bias expected from this procedure. For the $n^{\rm th}$ iteration, we can write

$$\hat{\boldsymbol{g}}^{(n)} = \hat{\boldsymbol{g}}^{(0)} - \left(\hat{\boldsymbol{g}}^{(n)}_{\rm sim} - \hat{\boldsymbol{g}}^{(n-1)}\right). \tag{4.16}$$

Assuming that the simulations provide an accurate description of the true field, we show in Appendix D that the residual bias for the $n^{\rm th}$ iteration is

$$\left\langle \hat{g}_j^{(n)} - g_j \right\rangle = \left(-m'_j\right)^n \left(m'_j g_j + c'_j)\right), \tag{4.17}$$

which converges to zero for $\left|m'_j\right| < 1$. As explained above, the zeroth-order shear estimates are expected to underestimate the modulus of the true shear. Hence, we expect m'_j to be confined to the range $-1 < m'_j < 0$, and therefore the shear estimates to converge for all fields.

4.4 Results

Here we compare the results of the angle-only approach using each of the three methods to measure the position angles of the galaxies discussed in Section 4.2. We include the results obtained from a naive application of `IM3SHAPE` where full ellipticity information is used (measured using the upsampled star images to correct for the PSF) with no additional calibration scheme.

The Q-value is the metric used to quantify the performance of the estimators in the GREAT3 challenge (Mandelbaum et al. 2014b). It is defined as a function of the multiplicative and additive biases (m and c respectively) where the biases satisfy the approximation (Heymans et al. 2006; Huterer et al. 2006; Massey et al. 2007)

$$\hat{g}_k = (1 + m_k)\, g_k + c_k + \delta g_k. \tag{4.18}$$

The subscript k denotes the components of the shear in a reference frame aligned with the PSF in the field being analysed. The biases are estimated using a linear regression over the 200 fields given the known input shears. The Q value is then calculated as

$$Q = \frac{2000\eta}{\sqrt{\sigma^2_{\rm min} + \sum_{k=+,\times}\left(\frac{m_k}{m_{\rm target}}\right)^2 + \sum_{k=+,\times}\left(\frac{c_k}{c_{\rm target}}\right)^2}}, \tag{4.19}$$

where the subscript $+$ corresponds to the components of the biases in the direction aligned with the PSF for each field and the subscript $\times$ denotes the direction perpendicular to the PSF. The target values of the biases, m_{target} and c_{target}, are based on the requirements of the ESA Euclid space mission (Massey et al. 2013) and are given as $m_{\text{target}} = 2 \times 10^{-3}$ and $c_{\text{target}} = 2 \times 10^{-4}$. The constant η normalizes the metric such that a value of $Q \approx 1000$ is expected for estimates of the shear which achieve the target values of m and c. The term σ^2_{min} corresponds to the typical dispersion of the biases due to pixel noise and is determined using trial submissions to the GREAT3 challenge. For the challenge, the values adopted for the `cgc` branch were $\eta = 1.232$ and $\sigma^2_{\text{min}} = 4$. We estimated the Q-values for our methods using the publicly available GREAT3 metric evaluation script[1]. This script also provides the estimates of m_k and c_k used to calculate the Q-value and their corresponding error bars.

In the discussion that follows, we include the highest Q-value entry to the `cgc` branch of the GREAT3 challenge[2] from `IM3SHAPE` - for a comparison of the performance of the angle-only method with the challenge submission of a model-based method. This entry implements a multiplicative calibration factor to correct for noise biases expected to arise in Maximum-Likelihood shape estimation. Additive biases are expected in the presence of anisotropic PSFs. However, no calibration for this bias is included. We also include the highest entry submitted to the challenge using the KSB method - for a comparison with a moments-based method. The details of the submissions using `IM3SHAPE` and the KSB method are presented in Mandelbaum et al. (2014a). For the angle-only analyses, the results presented made use of a single iteration of the procedure discussed in Section 4.3.

Figure 4.6 shows the difference between the recovered angle-only shear estimates and the input shear when using the integrated light and moments-based methods to measure the position angles. These plots display the estimates for the components of the shear in a reference frame aligned with the simulated images. It should be empha-

[1] `https://github.com/barnabytprowe/great3-public/wiki/Metric-evaluation-scripts-and-truth-data`

[2] `http://great3.jb.man.ac.uk/leaderboard/board/post\_challenge/24`

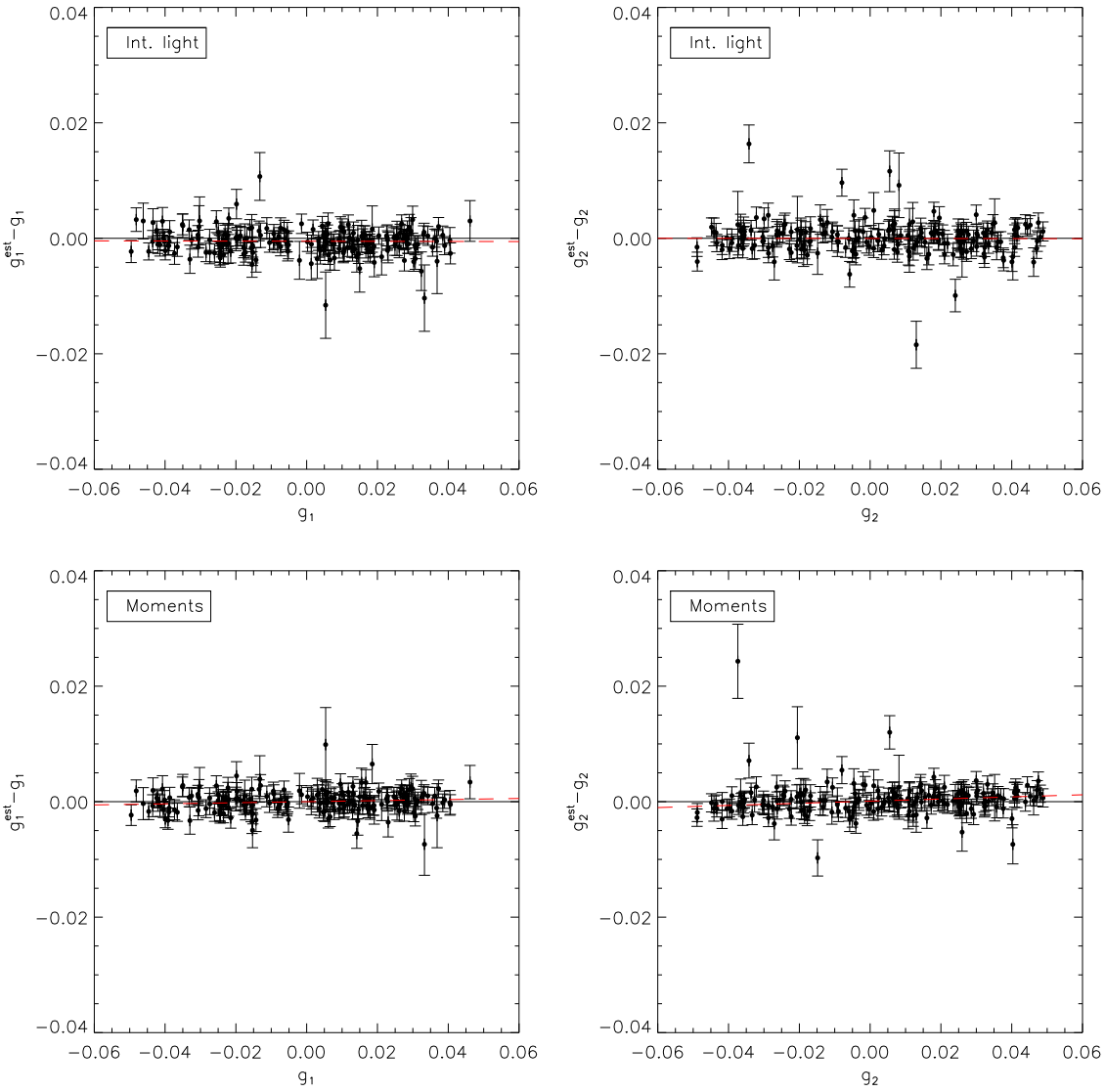

Figure 4.6: The top panels show the difference between the recovered and input shear values for each of the 200 fields of the `cgc` branch plotted against the input shear values and using the integrated light method to measure the position angles of the galaxies. The bottom panels show the same when using the moments-based method to measure the position angles. In all cases, the black line is the line of zero difference and the red-dashed line is the line of best fit for the data.

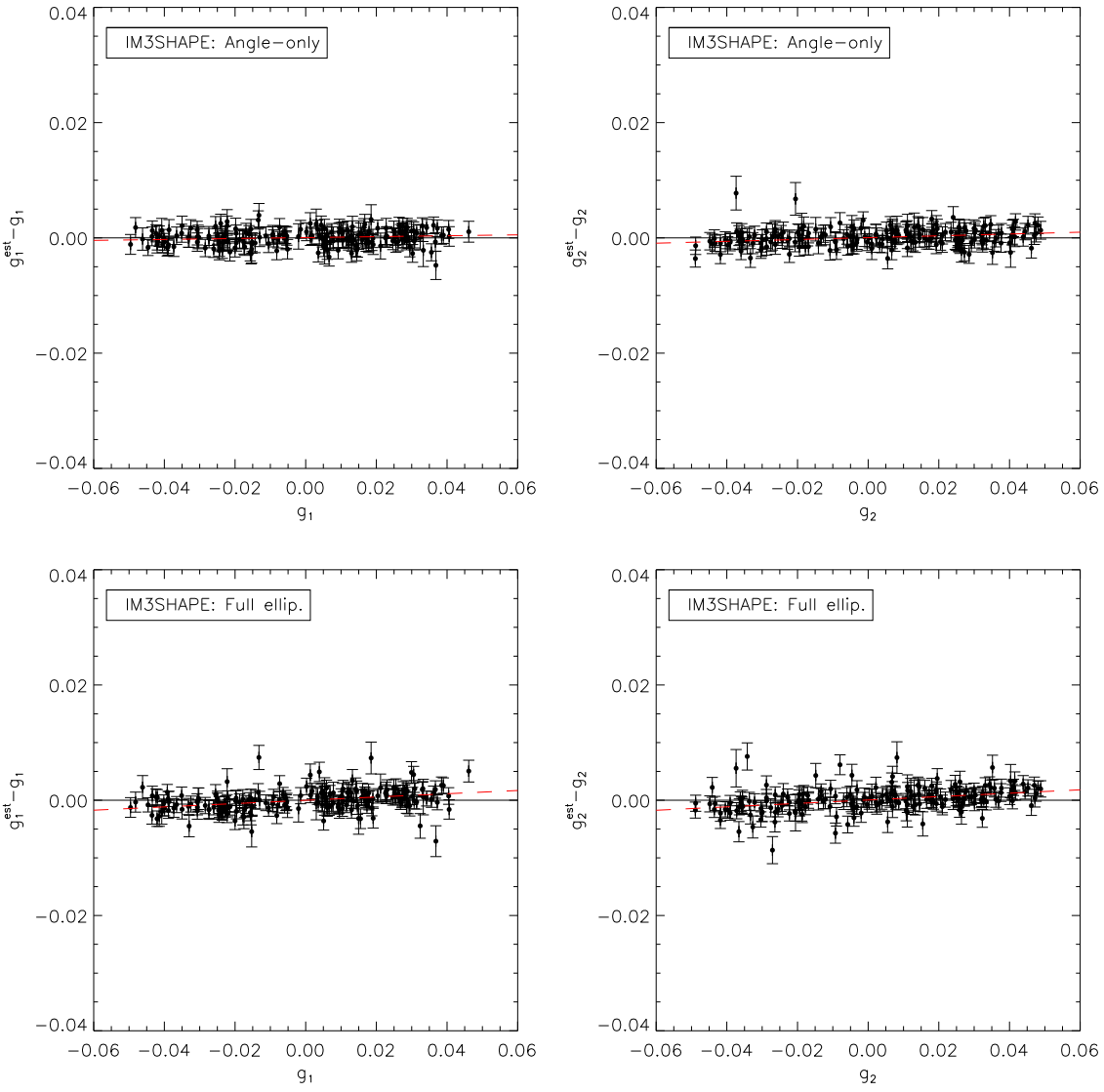

Figure 4.7: The top panels show the difference between the recovered and input shear values for each of the 200 fields of the `cgc` branch plotted against the input shear values and using `IM3SHAPE` to measure the position angles of the galaxies. The bottom panels show the same when using the full ellipticity information from `IM3SHAPE` but with no additional calibration scheme. In all cases, the black line is the line of zero difference and the red-dashed line is the line of best fit for the data.

sized that this is not the reference frame used to measure the Q-value, which employs a coordinate system that is aligned with the PSF for that field as described above. The error bars have been estimated using a linear approximation of the $F_1\left(|\boldsymbol{g}|\right)$ function as discussed in Appendix E. Figure 4.7 shows the results of `IM3SHAPE` using both the angle-only method and full ellipticity information - where no further calibration scheme is implemented. We see that the errors are reduced for the angle-only method when using the ellipticities from `IM3SHAPE` to measure the position angles as compared with the integrated light and moments-based methods. This reduction is due to the correction for the PSF when measuring the ellipticities which increases the uniformity of the weighting function and reduces the errors on the angle measurements. Hence, the value of $\sum_{i=1}^{N} w_i^2$ is lower, and the multiplicative bias for the zeroth-order estimate is smaller (or equivalently, the $\beta_{\rm wc}$ term as defined in Appendix E is larger) reducing the errors on the shear estimates in accordance with equations (E.4) and (E.6). For all methods using the angle-only estimator, a residual bias is expected when using a finite number of iterations (for these tests we use a single iteration), as shown in equation (4.17). However, the limiting factor in this method is expected to be the accuracy with which we can simulate the galaxies in the branch.

The scatter on the shear estimates recovered using full ellipticity information is smaller than when using the integrated light and moments-based methods. This is partly due to form of the $F_1\left(|\boldsymbol{g}|\right)$ function, as discussed in C3. However, there is also an increase in the errors due to the iterative procedure employed to remove the biases in the angle-only method; this is quantified in equation (E.6). The dispersion in the estimates is reduced when using only the position angle measurements from `IM3SHAPE` as compared with the full ellipticity information. This is likely due to there being no additional calibration scheme used in the full ellipticity analysis.

The results of our analyses of the `cgc` branch are presented in Table 4.1. The error bars on each Q-value were determined by assuming that the estimates of m_k and c_k are the true values. We used simulations to confirm that the errors on the m_k and c_k estimates are approximately Gaussian. We then simulated a suite of 5×10^5 uncorrelated

Method	Q	m_+ $(\times 10^{-3})$	$m_\times$ $(\times 10^{-3})$	c_+ $(\times 10^{-4})$	$c_\times$ $(\times 10^{-4})$
Int. light	324^{+115}_{-110}	-11.26 ± 8.25	-7.34 ± 6.22	-4.03 ± 2.08	4.34 ± 1.58
Moments	403^{+104}_{-101}	2.44 ± 7.96	9.38 ± 4.83	5.32 ± 2.01	3.32 ± 1.23
IM3SHAPE: Angle-only	371^{+96}_{-98}	6.80 ± 3.88	10.35 ± 4.05	1.89 ± 0.98	1.78 ± 1.03
IM3SHAPE: Full ellip.	117^{+13}_{-13}	29.47 ± 5.18	27.35 ± 4.31	-11.33 ± 1.31	0.36 ± 1.10
IM3SHAPE: Highest entry	416^{+49}_{-50}	0.00 ± 5.00	-2.09 ± 4.14	-11.0 ± 1.26	0.44 ± 1.05
KSB: Highest entry	122^{+18}_{-19}	22.7 ± 7.3	32.5 ± 5.9	6.19 ± 1.85	-1.07 ± 1.51

Table 4.1: The results of the analyses we have performed on the GREAT3 cgc branch. The first column shows the Q-values achieved for each method. The next two columns are the multiplicative biases estimated for each method. The final two columns show the estimated additive biases.

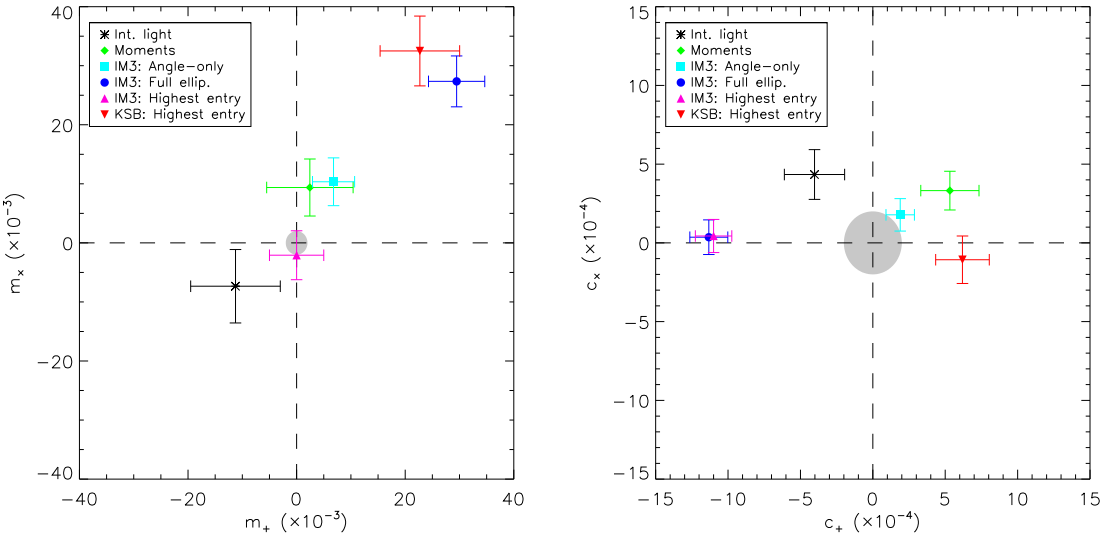

Figure 4.8: The multiplicative and additive biases for each test on the cgc branch. The grey region indicates the target bias values for future precision cosmic shear experiments, which are based on the target values evaluated for the Euclid space mission (Massey et al. 2013).

Gaussian random variables distributed about each of the estimated bias parameters with the dispersions provided by the metric evaluation script. These simulated bias parameters were used to calculate the 5×10^5 corresponding Q-values using the least squares method, and then a histogram of these values was constructed. The error bars were calculated as the 68.3% confidence regions of the simulated Q-values distributed about the mean recovered value.

From Table 4.1 we see that the Q-values for the three angle-only analyses are competitive with the highest entry submitted using IM3SHAPE to within one standard deviation. The Q-values achieved in all of the analyses performed with the angle-only approach are greater than the highest entry submitted using the KSB method. Figure 4.8 displays the values of m_k and c_k calculated using the GREAT3 metric evaluation script. The plus subscript corresponds to the direction parallel with the PSF and the cross subscript to the direction perpendicular to the PSF. We see that the multiplicative biases of the integrated light and moments-based angle-only methods lie within two standard deviations of the target values identified for future "Stage IV" weak lensing experiments aimed at precision dark energy constraints. There appears to be a greater residual additive bias when using these methods to measure the position angles than when using the angles recovered by IM3SHAPE. This is likely to be due to there being no correction for the PSF during the angle measurement stage, and hence there is a larger additive bias for the zeroth-order shear estimate. Assuming that this is the case, the bias should decrease as the number of iterations is increased, as indicated by equation (4.17), until the threshold enforced by the accuracy of the simulations is reached. The angle-only method using IM3SHAPE exhibits a reduction in the multiplicative bias as compared with that of the naive full ellipticity approach, and we also see a reduction in the component of the additive bias which aligns with the PSF.

4.5 Discussion

We have demonstrated an algorithm for applying the angle-only weak lensing estimator of C3 to realistic galaxy images. We find that the performance of this technique is competitive with state-of-the-art shape measurement techniques. To measure the position angles of the galaxies, we considered three separate approaches: the integrated light method, a moments-based method, and using ellipticities measured by IM3SHAPE. All three methods yield Q-values consistent with those of the highest IM3SHAPE submission and greater than the highest KSB submission.

The angle-only estimator requires a measurement of the $F_1(|\boldsymbol{g}|)$ function. We have shown that this function can be successfully recovered from deep field images using `IM3SHAPE`. Constraints on the accuracy of the recovered $F_1(|\boldsymbol{g}|)$ function required to provide reliable shear estimates are discussed in Section 3.4. When measuring the ellipticities of the galaxies in the deep field images using `IM3SHAPE`, we necessarily fit for the half-light radii and the bulge to total flux ratios of the galaxies. We have introduced a method of using this information to construct accurate calibration simulations. To do this, we modify the distributions of the fluxes and half-light radii measured from the deep fields to match the distributions in the field being analysed by simply summing over the pixel values in that field. This approach could be useful for any analysis which requires calibration simulations. It is, as yet, unclear as to how general the calibration methods developed in this chapter are with regards to how the galaxies of a particular survey are selected. A detailed investigation of this issue is left for future work. However, provided that one can construct accurate zero shear calibration simulations, the multiplicative and additive biases present in the zeroth-order shear estimates can be corrected for using the iterative approach.

The presence of an anisotropic PSF and pixelization bias position angle estimates. We have employed a weighting scheme to reduce this effect. The weighting function is estimated using calibration simulations which assume a zero input shear signal. Using the iterative method employed for this chapter, we have argued that residual biases in the shear estimates can be reduced below a threshold which is determined by the accuracy of the calibration simulations. For a perfect suite of calibration simulations, the multiplicative bias in the zeroth-order shear estimate is essentially due to noise in the image, pixelization and the PSF. The magnitude of the multiplicative bias in the zeroth-order shear estimate determines the rate of convergence for the estimator. Therefore, correcting for the PSF prior to the zeroth-order estimate should increase the rate of convergence. However, the effect of the PSF on a galaxy's orientation is model dependent and is therefore difficult to correct for when using an angle measurement method which is independent of the ellipticity.

The purpose of this chapter is to demonstrate the feasibility of performing an angle-only shear analysis on realistic galaxy images. To demonstrate this, we have focused on the simulated images of the `cgc` branch of the GREAT3 challenge. In future work, we will look at how the angle-only method can be applied to fields with a variable shear and a variable PSF. We also aim to reduce the dependence of the method on simulations and develop a deeper understanding of the level at which the angle-only method can complement ellipticity based methods and ultimately reduce systematics in weak lensing surveys.

Chapter 5

Separating weak lensing and intrinsic alignments using radio observations

We discuss methods for performing weak lensing using radio observations to recover information about the intrinsic structural properties of the source galaxies. Radio surveys provide unique information that can benefit weak lensing studies, such as HI emission, which may be used to construct galaxy velocity maps, and polarized synchrotron radiation; both of which provide information about the unlensed galaxy and can be used to reduce galaxy shape noise and the contribution of intrinsic alignments. Using a proxy for the intrinsic position angle of an observed galaxy, we develop techniques for cleanly separating weak gravitational lensing signals from intrinsic alignment contamination in forthcoming radio surveys. Random errors on the intrinsic orientation estimates introduce biases into the shear and intrinsic alignment estimates. However, we show that these biases can be corrected for if the error distribution is accurately known. We demonstrate our methods using simulations, where we reconstruct the shear and intrinsic alignment auto and cross-power spectra in three overlapping redshift bins. We find that the intrinsic position angle information can be used to successfully reconstruct both the lensing and intrinsic alignment power spectra with negligible residual bias.

5.1 Introduction

The standard method for performing a cosmic shear measurement requires averaging over the observed ellipticities of a sufficient number of background galaxies and assuming that the average ellipticity is the consequence of cosmic shear. This method is built on the assumption that there is a zero intrinsic alignment (IA) of the source galaxies. However, as galaxies evolve, tidal effects can radially align the galaxies with the large scale structure. As explained in Section 2.7, the presence of IA has the effect of producing a false shear signal and hence a bias in the standard method.

Most weak lensing surveys so far have been performed in the optical waveband, but the SKA promises the possibility of performing surveys in the radio waveband (Brown et al. 2015). Such a survey offers some unique advantages. Firstly, based on an idea originally proposed by Blain (2002), Morales (2006) introduced a method for performing weak lensing using resolved galaxy velocity maps. Radio HI emission is the most promising part of the electromagnetic spectrum to construct the velocity maps, due to the brightness of the emission lines and the well understood luminosity characteristics. Gravitational lensing leads to a velocity map which is inconsistent with the observed galaxy image, and Morales (2006) showed that this effect can be used to recover estimates of the underlying shear signal. In principle, this method removes the contribution of both galaxy shape noise and the effects of intrinsic alignments from weak lensing surveys. It does, however, require velocity maps from well resolved galaxy images which reduces the number density of available galaxies in the survey. However, using a toy model, Morales (2006) showed that this method may be competitive in future radio surveys, such as with the SKA.

Secondly, Brown & Battye (2011b) (hereafter BB11) suggested a new technique in radio weak lensing which would use the polarization information contained in the radio emission of a source galaxy as a tracer for the intrinsic position angle (IPA) of the galaxy. It had previously been shown (Dyer & Shaver 1992) that the net polarization position angle (PPA) is unaffected by a gravitational lens. A gravitational lens

maps individual photons from the source plane to the image plane; however, the polarizations of the photons are not changed. This implies that the integrated Stokes Q and U, and hence the PPA, are also unaffected by lensing. For future deep radio surveys, the population of observed galaxies is expected to be dominated by star forming galaxies. The dominant source of radio emission from such a galaxy is expected to be synchrotron radiation emitted as electrons are accelerated by the large scale magnetic fields within that galaxy. This emission gives rise to a PPA which, on average, is anti-aligned with the plane of the galaxy (Stil et al. 2009), providing information about the galaxy's intrinsic orientation. It was shown that such information can be used to construct a shear estimator which greatly reduces the biases resulting from intrinsic alignments compared to the standard method and also reduces the errors on the shear estimates. It was shown (Brown & Battye 2011a) that this new method can be used to create foreground mass reconstructions with accuracies comparable with the standard method, subject to specific assumptions on the size of the errors on the estimates of the intrinsic orientations of the galaxies and the fraction of galaxies with reliable polarization information. In principle, the method can be applied to estimates of the IPA from any source, and a similar analysis could also be applied to the technique described by Morales (2006).

The method displays great promise. However, there is a small residual bias in the estimator when there is both a non-zero error in the IPA estimates and a non zero IA signal. In this chapter, we develop improved estimators which remove this bias. In Section 5.2, we present an overview of the method proposed by BB11. We discuss the noise properties of the method and the residual bias which is introduced in the presence of both an IA signal and an error on the intrinsic position angle estimates. We address this bias by introducing a correction term, which depends on the form of the error distribution.

In Section 5.3, we extend the angle-only estimator, introduced in Chapter 3, to include IPA information, and we also introduce a hybrid method that combines an angle-only estimate of the intrinsic alignment with full ellipticity information. In Sec-

tion 5.4, we test the methods using simulations by reconstructing the shear and IA auto and cross-power spectra in three overlapping redshift bins. We conclude in Section 5.5.

Throughout the chapter we assume that we have reliable IPA information for every galaxy for which we have reliable ellipticity or observed position angle measurements. For a real radio survey, this would not be the case. However, the purpose of this chapter is to demonstrate the potential of the methods presented provided that we have a sufficient number of galaxies to recover a reliable shear estimate. A detailed discussion of the fraction of galaxies expected to have reliable polarization information can be found in BB11.

5.2 Methods and techniques

Working well within the weak lensing regime, we can express the observed ellipticity of a galaxy, $\boldsymbol{\epsilon}^{\rm obs}$, as the sum of the intrinsic ellipticity, $\boldsymbol{\epsilon}^{\rm int}$, the shear, $\boldsymbol{\gamma}$, and a measurement error, $\delta\boldsymbol{\epsilon}$, such that

$$\boldsymbol{\epsilon}^{\rm obs} = \boldsymbol{\epsilon}^{\rm int} + \boldsymbol{\gamma} + \delta\boldsymbol{\epsilon}. \tag{5.1}$$

Considering a small region of the sky, or a cell, such that the shear can be considered constant within that cell, and assuming that the mean intrinsic ellipticity of the galaxies in that particular cell is zero, we can recover an unbiased estimate of the shear by averaging over the observed galaxy ellipticities:

$$\hat{\boldsymbol{\gamma}} = \frac{1}{N}\sum_{i=1}^{N} \boldsymbol{\epsilon}_i^{\rm obs}. \tag{5.2}$$

If the unlensed galaxies within a particular region of sky are randomly orientated, then the average intrinsic ellipticity is zero. However, there is theoretical motivation (Catelan et al. 2001; Crittenden et al. 2001; Jing 2002; Mackey et al. 2002; Hirata

& Seljak 2004) and observational evidence (Brown et al. 2002; Heymans et al. 2004; Mandelbaum et al. 2006, 2011; Hirata et al. 2007; Brainerd et al. 2009) indicating that during galaxy formation, correlations between the intrinsic position angles of galaxies, $\alpha^{\rm int}$, may arise if those galaxies share an evolutionary history. This is the source of the IA signal. If we now assume that the mean intrinsic ellipticity (or, equivalently, that the IA signal) is non-zero, then the standard estimator of equation (5.2) is biased, such that

$$\langle \hat{\boldsymbol{\gamma}} - \boldsymbol{\gamma} \rangle = \left\langle \boldsymbol{\epsilon}^{\rm int} \right\rangle . \tag{5.3}$$

If we assume that the intrinsic ellipticity of a single galaxy can be expressed as the sum of the intrinsic alignment signal, $\boldsymbol{\gamma}^{\rm IA}$, and a randomly orientated ellipticity, $\boldsymbol{\epsilon}^{\rm ran}$, then

$$\boldsymbol{\epsilon}^{\rm int} = \boldsymbol{\gamma}^{\rm IA} + \boldsymbol{\epsilon}^{\rm ran}, \tag{5.4}$$

and the bias in the standard estimator becomes

$$\langle \hat{\boldsymbol{\gamma}} - \boldsymbol{\gamma} \rangle = \boldsymbol{\gamma}^{\rm IA}. \tag{5.5}$$

Hence, an estimate of the shear recovered using the standard method yields a result which is biased by the IA signal.

5.2.1 The Brown & Battye (BB) estimator

In order to mitigate the effects of the bias introduced by IA, BB11 proposed using polarization information from radio surveys to recover an estimate of the IPA, $\hat{\alpha}^{\rm int}$. It was found that, for the ideal case where there is a zero error on the IPA measurement and where the PPA is an exact tracer of $\alpha^{\rm int}$, the shear can be recovered exactly using only two source galaxies.

Expressing the intrinsic ellipticity in polar coordinates, the components of the ob-

served ellipticity can be written as

$$\begin{aligned}\epsilon_1^{\rm obs} &= \left|\boldsymbol{\epsilon}^{\rm int}\right| \cos\left(2\alpha^{\rm int}\right) + \gamma_1 + \delta\epsilon_1, \\ \epsilon_2^{\rm obs} &= \left|\boldsymbol{\epsilon}^{\rm int}\right| \sin\left(2\alpha^{\rm int}\right) + \gamma_2 + \delta\epsilon_2. \end{aligned} \tag{5.6}$$

If we define the pseudo-vector

$$\hat{\boldsymbol{n}}_i = \begin{pmatrix} \sin\left(2\hat{\alpha}_i^{\rm int}\right) \\ -\cos\left(2\hat{\alpha}_i^{\rm int}\right) \end{pmatrix}, \tag{5.7}$$

where $\hat{\alpha}^{\rm int}$ is an estimate of the intrinsic position angle provided by a measurement of the IPA, a new estimator for the shear can be derived, such that

$$\hat{\boldsymbol{\gamma}} = \mathbf{A}^{-1}\boldsymbol{b}, \tag{5.8}$$

where $\mathbf{A}$ is a 2×2 matrix and $\boldsymbol{b}$ is a two-component vector

$$\mathbf{A} = \sum_{i=1}^{N} w_i \hat{\boldsymbol{n}}_i \hat{\boldsymbol{n}}_i^T, \tag{5.9}$$

$$\boldsymbol{b} = \sum_{i=1}^{N} w_i \left(\boldsymbol{\epsilon}_i^{\rm obs} \cdot \hat{\boldsymbol{n}}_i\right) \hat{\boldsymbol{n}}_i, \tag{5.10}$$

and w_i is a normalized arbitrary weight assigned to each galaxy. The form of this estimator is independent of the intrinsic ellipticity distribution.

In the presence of a non-zero IA signal and a non-zero error on the estimate of $\alpha^{\rm int}$, it is found that the estimator given in equation (5.8) is biased, although this bias is suppressed significantly with respect to that of the standard estimator. If we assume that the components of the intrinsic ellipticity are isotropically distributed about the IA vector, $\boldsymbol{\gamma}^{\rm IA}$, and use a uniform weighting, such that $w_i = 1$, it is possible to gain some insight into the nature of this bias. If we make the further assumptions that $N \gg 1$ and the IA signal is much smaller than the spread in intrinsic ellipticities, σ_ϵ, that is if

$|\boldsymbol{\gamma}|^{\rm IA} \ll \sigma_\epsilon$, we can approximate $\mathbf{A}$ to leading order in $\boldsymbol{\gamma}^{\rm IA}$ as

$$\mathbf{A} \approx \frac{N}{2}\mathbf{I}, \tag{5.11}$$

and hence the estimator can then be approximated as

$$\hat{\boldsymbol{\gamma}} \approx \frac{2}{N}\boldsymbol{b}. \tag{5.12}$$

The noise properties inherent in using measurements of the PPA as a tracer of $\alpha^{\rm int}$ are discussed in BB11. For this discussion, we assume that the measurement error, $\delta\alpha^{\rm int}$, is independent of the true IPA and distributed symmetrically about zero. If we then make the substitution $\hat{\alpha}^{\rm int} = \alpha^{\rm int} + \delta\alpha^{\rm int}$, we can write the expectation value of the trigonometric functions of the IPA as

$$\begin{aligned}\left\langle \cos\left(2\hat{\alpha}^{\rm int}\right)\right\rangle &= \left\langle \cos\left(2\alpha^{\rm int}\right)\right\rangle \beta_2^{\rm int},\\ \left\langle \sin\left(2\hat{\alpha}^{\rm int}\right)\right\rangle &= \left\langle \sin\left(2\alpha^{\rm int}\right)\right\rangle \beta_2^{\rm int},\end{aligned} \tag{5.13}$$

where, in analogy to equation (3.28),

$$\beta_n^{\rm int} \equiv \left\langle \cos\left(n\delta\alpha^{\rm int}\right)\right\rangle, \tag{5.14}$$

which is the mean cosine of the distribution of $\delta\alpha^{\rm int}$, and where n is an integer. For a Gaussian measurement error, this can be simplified to

$$\beta_n^{\rm int} = \exp\left(-\frac{n^2}{2}\sigma^2_{\alpha^{\rm int}}\right), \tag{5.15}$$

where $\sigma_{\alpha^{\rm int}}$ is the standard deviation of the measurement error and is expressed in radians. Taking the limit $N \to \infty$ and using the result of equation (5.13), it can be shown that equation (5.12) may be expanded to first order in the shear and IA, such

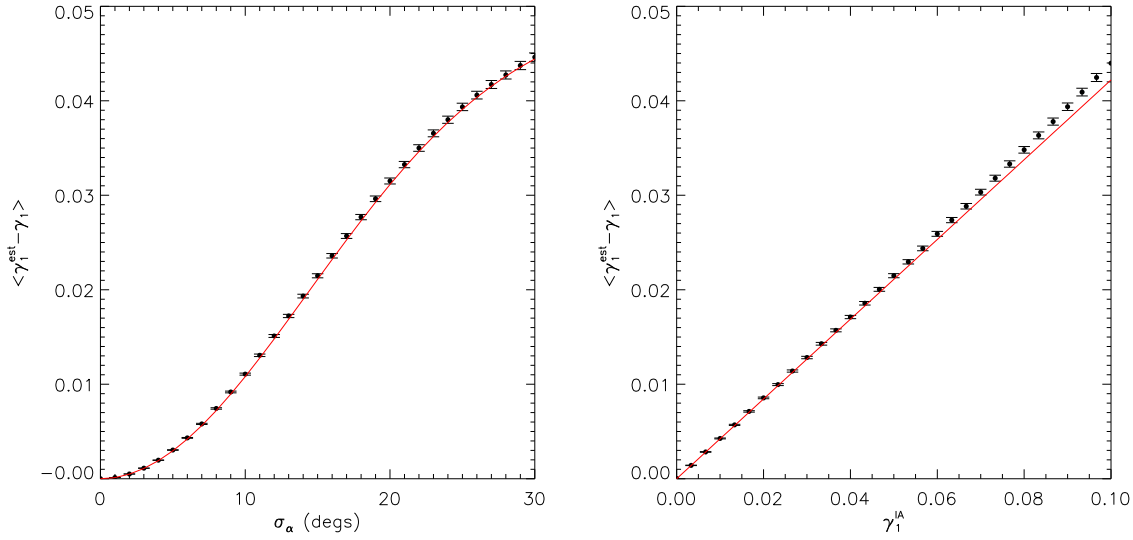

Figure 5.1: The residual bias in the BB estimator from 10^4 realizations, with 10^4 galaxies in each realization. For each realization γ_1, γ_2 and $\gamma_2^{\rm IA}$ are selected randomly with a range $[-0.1, 0.1]$. The *left panel* shows the bias in the BB estimator as a function of $\sigma_{\alpha^{\rm int}}$ with $\gamma_1^{\rm IA} = 0.05$. The *right panel* shows the bias as a function of $\gamma_1^{\rm IA}$ with $\sigma_{\rm int} = 15°$. In both cases, the red curve is the linear approximation of the bias, given in equation (5.16).

that the bias in the estimator is

$$\langle \hat{\boldsymbol{\gamma}} - \boldsymbol{\gamma} \rangle \approx \left(1 - \beta_2^{\rm int}\right) \boldsymbol{\gamma}^{\rm IA}. \tag{5.16}$$

The bias in the BB estimator is therefore independent of $f\left(|\boldsymbol{\epsilon}^{\rm ran}|\right)$ to first order in $\boldsymbol{\gamma}^{\rm IA}$. For $\sigma_{\alpha^{\rm int}} \ll 1$, one finds that $\langle \hat{\boldsymbol{\gamma}} - \boldsymbol{\gamma} \rangle \approx 2\sigma^2_{\alpha^{\rm int}} \boldsymbol{\gamma}^{\rm IA}$, and therefore we see that the bias is suppressed by a factor of $2\sigma^2_{\alpha^{\rm int}}$ relative to the standard estimator. The bias in the BB estimator is illustrated in Figure 5.1, where we assume a Gaussian measurement error on the estimate of $\alpha^{\rm int}$ and a Rayleigh distribution for the intrinsic ellipticity distribution (which we define as the distribution of $|\boldsymbol{\epsilon}^{\rm ran}|$), such that

$$f\left(|\boldsymbol{\epsilon}^{\rm ran}|\right) = \frac{|\boldsymbol{\epsilon}^{\rm ran}|}{\sigma_\epsilon^2 \left(1 - \exp\left(-\frac{|\boldsymbol{\epsilon}^{\rm ran}_{\rm max}|^2}{2\sigma_\epsilon^2}\right)\right)} \exp\left(-\frac{|\boldsymbol{\epsilon}^{\rm ran}|^2}{2\sigma_\epsilon^2}\right), \tag{5.17}$$

where $|\boldsymbol{\epsilon}^{\rm ran}_{\rm max}|$ is the maximum allowed value of the modulus of $\boldsymbol{\epsilon}^{\rm ran}$; for all of the

simulations in this chapter we have assumed a Rayleigh distribution for $|\boldsymbol{\epsilon}^{\rm ran}|$ with values of $|\boldsymbol{\epsilon}^{\rm ran}_{\rm max}| = 1$ and $\sigma_\epsilon = 0.3/\sqrt{2}$. From Figure 5.1, we see that the estimator successfully reduces the bias introduced by the IA. There is, however, a residual bias introduced when both the measurement error on $\alpha^{\rm int}$ and the IA signal are non-zero.

In the limit $\left|\boldsymbol{\gamma}^{\rm IA}\right| \ll \sigma_\epsilon$ the standard error for the shear estimator can be written as

$$\sigma_{\hat{\gamma}} \approx \left[\frac{2\sigma_\epsilon^2\left(1-\beta_4^{\rm int}\right)+2\sigma^2}{N}\right]^{\frac{1}{2}}, \tag{5.18}$$

where σ is the measurement error on the components of $\boldsymbol{\epsilon}^{\rm obs}$. Assuming this error to be zero and assuming $\sigma_{\alpha^{\rm int}} \ll 1$, the error can be approximated as

$$\sigma_{\hat{\gamma}} \approx \frac{4\sigma_{\alpha^{\rm int}}\sigma_\epsilon}{\sqrt{N}}, \tag{5.19}$$

and hence we see that $\sigma_{\hat{\gamma}}$ is suppressed by a factor of $4\sigma_{\alpha^{\rm int}}$ relative to the standard estimator, in agreement with the findings of BB11.

Given an estimate of the shear and assuming that the effects of the intrinsic ellipticity can be modelled using equation (5.4), an estimate of the IA signal can be recovered trivially, such that

$$\hat{\boldsymbol{\gamma}}^{\rm IA} = \left(\frac{1}{N}\sum_{i=1}^{N}\boldsymbol{\epsilon}_i^{\rm obs}\right) - \hat{\boldsymbol{\gamma}}. \tag{5.20}$$

The bias in the estimate of the IA signal arises from the bias in the shear estimator and hence to first order, has the same magnitude as the bias given in equation (5.16), but with the opposite sign.

To first order in the shear and intrinsic alignment, the error on the IA estimator is due to the random shape noise,

$$\sigma_{\hat{\boldsymbol{\gamma}}^{\rm IA}} = \frac{\sigma_\epsilon}{\sqrt{N}}. \tag{5.21}$$

From equation (5.21) we see that the error on the IA estimator is independent of the error on $\alpha^{\rm int}$ and therefore there is no suppression of this error by $\sigma_{\alpha^{\rm int}}$.

Battye & Browne (2009) investigated the difference between the structural position

angles of galaxies measured in the optical with those measured for the same galaxies in the radio. They found an agreement between the two position angles compatible with a dispersion of approximately $15°$. For radio and optical surveys which overlap, this agreement between the optical and radio position angles implies that, if one measures the shape of a galaxy in the optical, one may combine this measurement with an estimate of $\alpha^{\rm int}$ recovered from the radio; albeit at the cost of an addition contribution to the error on $\alpha^{\rm int}$ from the astrophysical dispersion between the optical and radio structural position angles.

5.2.2 The corrected BB (CBB) estimator

It is possible to construct an unbiased shear estimator in the limit $N \rightarrow \infty$ by following the approach outlined in BB11. This corrected form of the BB estimator (hereafter the CBB estimator) can be written as

$$\hat{\boldsymbol{\gamma}} = \mathbf{D}^{-1}\boldsymbol{h}, \tag{5.22}$$

where $\mathbf{D}$ is a 2×2 matrix

$$\mathbf{D} = \sum_{i=1}^{N} \mathbf{M}_i, \tag{5.23}$$

and where $\boldsymbol{h}$ is a 2-component vector

$$\boldsymbol{h} = \sum_{i=1}^{N} \mathbf{M}_i \boldsymbol{\epsilon}_i^{\rm obs}. \tag{5.24}$$

In Appendix F, it is shown that the matrix $\mathbf{M}_i$ is given by

$$\mathbf{M}_i = \begin{pmatrix} \beta_4^{\rm int} - \cos\left(4\hat{\alpha}_i^{\rm int}\right) & -\sin\left(4\hat{\alpha}_i^{\rm int}\right) \\ -\sin\left(4\hat{\alpha}_i^{\rm int}\right) & \beta_4^{\rm int} + \cos\left(4\hat{\alpha}_i^{\rm int}\right) \end{pmatrix}, \tag{5.25}$$

where the term $\beta_4^{\rm int}$ is defined in equation (5.14) and corrects for the bias on the trigonometric functions introduced by a measurement error on $\alpha^{\rm int}$. As with the BB estimator,

Estimator ($\times 10^{-2}$)	$\sigma_{\hat{\gamma}_1}$	$\sigma_{\hat{\gamma}_2}$	$\langle\hat{\gamma}_1\rangle$	$\langle\hat{\gamma}_2\rangle$	$\sigma_{\hat{\gamma}_1^{\rm IA}}$	$\sigma_{\hat{\gamma}_2^{\rm IA}}$	$\langle\hat{\gamma}_1^{\rm IA}\rangle$	$\langle\hat{\gamma}_2^{\rm IA}\rangle$
Original BB	1.40	1.40	-2.79 ± 0.01	3.58 ± 0.01	2.13	2.12	0.71 ± 0.02	-1.55 ± 0.02
Corrected BB	1.71	1.70	-3.00 ± 0.02	4.02 ± 0.02	2.75	2.73	0.92 ± 0.03	-1.99 ± 0.03

Table 5.1: The mean and standard deviation of the shear and IA estimates recovered from 10^4 simulations. Values are quoted for both the original BB estimator (equations (5.8) and (5.20)) and the CBB estimator (equations (5.20)) and (5.22). The input shear and IA values are $\gamma_1 = -0.03$, $\gamma_2 = 0.04$, $\gamma_1^{\rm IA} = 0.01$ and $\gamma_2^{\rm IA} = -0.02$.

the form of the CBB estimator is independent of $f\left(|\boldsymbol{\epsilon}^{\rm ran}|\right)$. Hence, the CBB estimator will be unbiased for any distribution of $\boldsymbol{\epsilon}^{\rm ran}$. Once one has an estimate of $\boldsymbol{\gamma}$, an estimate of the IA can be recovered using equation (5.20).

We have tested the performance of the CBB estimator using simulations composed of 100 galaxies and assuming an input shear signal of $\gamma_1 = -0.03$ and $\gamma_2 = 0.04$, and an input IA signal of $\gamma_1^{\rm IA} = 0.01$ and $\gamma_2^{\rm IA} = -0.02$. It should be noted that this intrinsic alignment signal is larger than one would expect in a real survey. By measuring shape correlations in the blue galaxies of the SDSS and the WiggleZ Dark Energy Survey, Mandelbaum et al. (2011) measured the amplitude of the projected intrinsic alignment auto-correlation function and found it to be consistent with zero in all cases. A similar analysis was carried out by Joachimi et al. (2011) for the MegaZ-LRG sample, with the results again consistent with zero. More recently, Sifón et al. (2015) measured the intrinsic alignment signal of satellite galaxies in two large non-overlapping X-ray selected cluster surveys carried out with the Canada-France-Hawaii Telescope (CFHT) and the Multi-Epoch Nearby Cluster Survey (MENeaCS). They constrained the radial alignment signal of satellite galaxies within r_{200} to be $\left\langle \epsilon^{\rm obs^+} \right\rangle = -0.0037 \pm 0.0027$. Singh et al. (2015) measured the intrinsic alignment signal of SDSS-III BOSS low-redshift ($0.16 < z < 0.36$) galaxies on scales of $0.1 - 200\, h^{-1}\,{\rm Mpc}$. They measured the radial alignment of satellite galaxies within a projected radius of $1\, h^{-1}\,{\rm Mpc}$ to be $\left\langle \epsilon^{\rm obs^+} \right\rangle = 0.005 \pm 0.001$.

We recovered shear and IA estimates from 10^4 realizations using the original form of the BB estimator (equations (5.8) and (5.20)) and the CBB estimator (equations (5.20) and (5.22)). Note that the exact numbers of galaxies and realizations used in

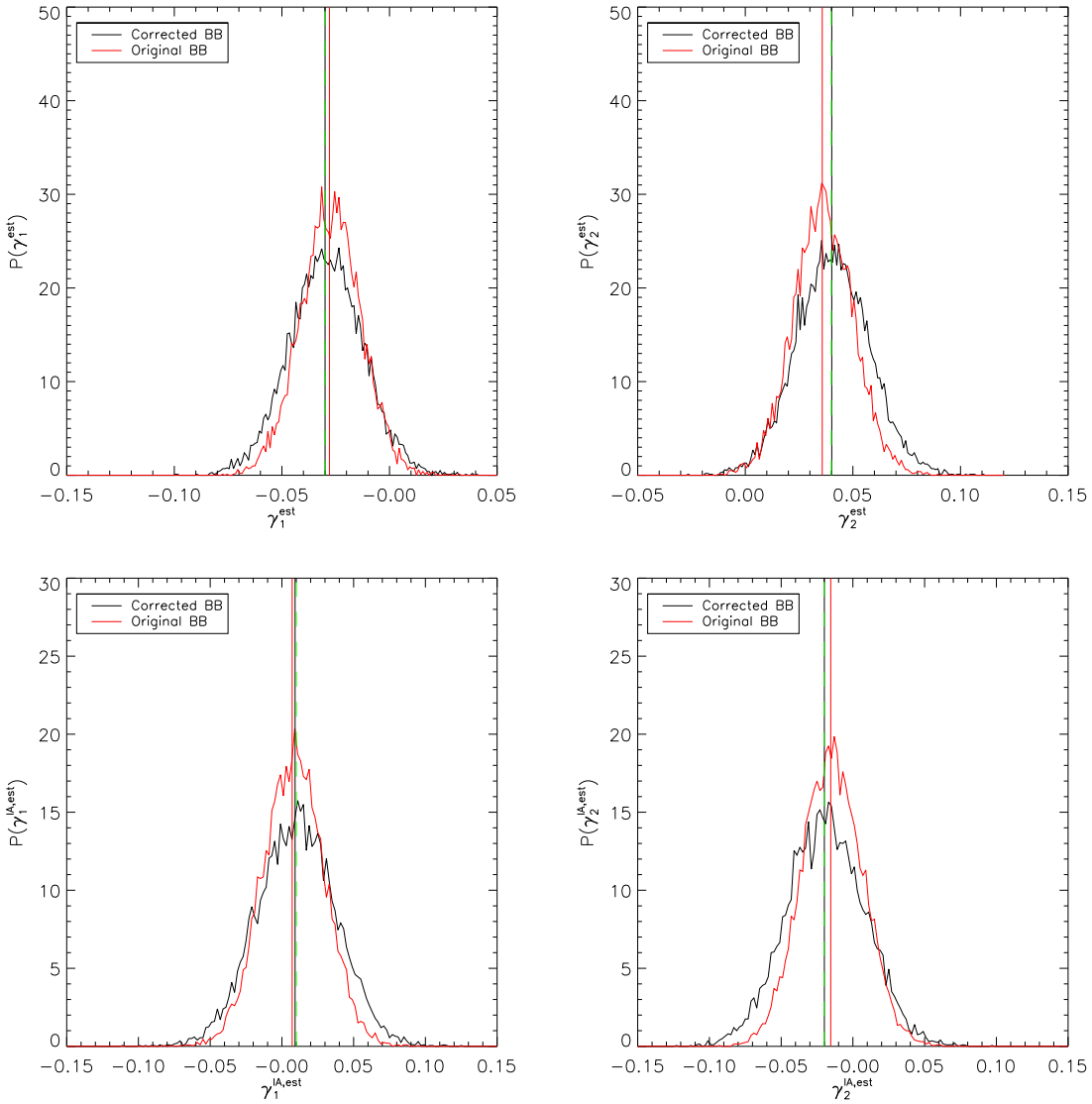

Figure 5.2: The recovered shear and IA estimates from 10^4 realizations, with each realization consisting of 100 galaxies and assuming a measurement error on the IPA of $\sigma_{\alpha^{\rm int}} = 10°$. The black curves show the distributions of recovered shear and IA estimates when using the CBB estimator (equations (5.20) and (5.22)), and the vertical black lines show the mean recovered shear estimates when using this estimator. The red curves show the distributions of recovered shear estimates when using the original BB estimator (equations (5.8) and (5.20)), and the vertical red line shows the mean recovered shear estimates when using this estimator. The green-dashed lines, which lie on top of the black lines, show the input shear signal. The success of the correction to the original BB estimator is clearly visible in these plots. There is, however, a modest increase ($\sim$20%) in the dispersion of the shear estimates and a $\sim$30% increase in the dispersion of the IA estimates when using the corrected form of the estimator with this set of input values; this is quantified in Table 5.1.

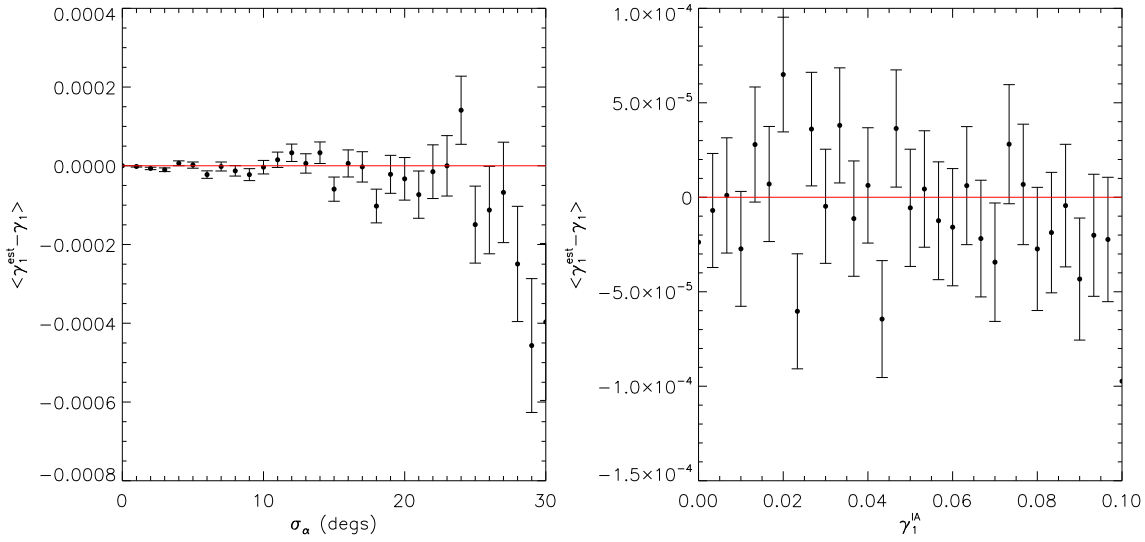

Figure 5.3: Same as for Figure 5.1 but for the CBB shear estimator. We see a residual bias which is a result of the finite number of source galaxies. However, this residual bias is much smaller than the residual bias in the original BB estimator, shown in Figure 5.1.

the simulations are not crucial and were chosen to reduce the numerical uncertainties on the derived biases and errors on the estimates whilst maintaining a reasonable computation time. We assumed a zero error on measurements of $\boldsymbol{\epsilon}^{\rm obs}$ and a Gaussian measurement error with r.m.s. 10° on $\alpha^{\rm int}$. The results of this test are shown in Figure 5.2. Table 5.1 presents the mean recovered shear and IA estimates and the standard deviation of the estimates.

Figure 5.3 shows the residual bias in the CBB estimator. The bias correction term, $\beta_4^{\rm int}$, corrects for the bias introduced to the mean trigonometric functions in the BB estimator when there is an error on the estimates of $\alpha^{\rm int}$. However, for a finite number of source galaxies, there will also be noise in the estimates of the mean trigonometric functions (which enters into the CBB estimator via the inverse of matrix $\mathbf{D}$). This noise propagates nonlinearly into estimates of the shear resulting in a residual bias which is not corrected for. In the tests we have conducted, we find that this residual bias is always much smaller than the dispersion in the shear estimates and contributes to a negligible residual bias in the power spectra reconstructions discussed in Section 5.4.

In order to estimate the dispersion in the shear and IA estimates, we can write an approximate form of the CBB estimator. To leading order in $\boldsymbol{\gamma}$ and $\boldsymbol{\gamma}^{\rm IA}$, the CBB estimator can be written as

$$\begin{aligned}
\hat{\gamma}_1 =& \frac{1}{N\beta_4^{\rm int}} \sum_{i=1}^{N} \Bigg[\beta_4^{\rm int} \epsilon_1^{{\rm obs},(i)} - \epsilon_1^{{\rm obs},(i)} \cos\left(4\hat{\alpha}_i^{\rm int}\right) \\
& - \epsilon_2^{{\rm obs},(i)} \sin\left(4\hat{\alpha}_i^{\rm int}\right) \Bigg], \\
\hat{\gamma}_2 =& \frac{1}{N\beta_4^{\rm int}} \sum_{i=1}^{N} \Bigg[\beta_4^{\rm int} \epsilon_2^{{\rm obs},(i)} - \epsilon_1^{{\rm obs},(i)} \sin\left(4\hat{\alpha}_i^{\rm int}\right) \\
& + \epsilon_2^{{\rm obs},(i)} \cos\left(4\hat{\alpha}_i^{\rm int}\right) \Bigg], \\
\hat{\gamma}_1^{\rm IA} =& \frac{1}{N\beta_4^{\rm int}} \sum_{i=1}^{N} \left[\epsilon_1^{{\rm obs},(i)} \cos\left(4\hat{\alpha}_i^{\rm int}\right) + \epsilon_2^{{\rm obs},(i)} \sin\left(4\hat{\alpha}_i^{\rm int}\right) \right], \\
\hat{\gamma}_2^{\rm IA} =& \frac{1}{N\beta_4^{\rm int}} \sum_{i=1}^{N} \left[\epsilon_1^{{\rm obs},(i)} \sin\left(4\hat{\alpha}_i^{\rm int}\right) - \epsilon_2^{{\rm obs},(i)} \cos\left(4\hat{\alpha}_i^{\rm int}\right) \right]. \qquad (5.26)
\end{aligned}$$

The error on the CBB estimator can then be approximated as

$$\begin{aligned}
\sigma_{\hat{\gamma}_1} =& \sigma_{\hat{\gamma}_2} = \left[\frac{\sigma_\epsilon^2 \left(1 - \beta_4^{\rm int^2}\right) + \sigma^2 \left(1 + \beta_4^{\rm int^2}\right)}{N\beta_4^{\rm int^2}} \right]^{\frac{1}{2}}, \\
\sigma_{\hat{\gamma}_1^{\rm IA}} =& \sigma_{\hat{\gamma}_2^{\rm IA}} = \left[\frac{\sigma_\epsilon^2 + \sigma^2}{N\beta_4^{\rm int^2}} \right]^{\frac{1}{2}}. \qquad (5.27)
\end{aligned}$$

There is a contribution to the errors on the CBB estimator from intrinsic shape noise through the term σ_ϵ. As with the BB estimator (equation (5.18)), the contribution of shape noise to the shear estimates is suppressed by a factor which depends upon $\beta_4^{\rm int}$.

Using equation (5.27) with the input values used to produce Figure 5.2, we recovered approximate values for the dispersion in the estimators of $\sigma_{\hat{\gamma}_1} = \sigma_{\hat{\gamma}_2} = 1.68 \times 10^{-2}$ and $\sigma_{\hat{\gamma}_1^{\rm IA}} = \sigma_{\hat{\gamma}_2^{\rm IA}} = 2.71 \times 10^{-2}$, which are in good agreement with the measured values quoted in Table 5.1. For completeness, we also used equations (5.18) and (5.21) to recover approximate values for the dispersion in the original BB estimator. These

values were $\sigma_{\hat{\gamma}_1} = \sigma_{\hat{\gamma}_2} = 1.40 \times 10^{-2}$ and $\sigma_{\hat{\gamma}_1^{\rm IA}} = \sigma_{\hat{\gamma}_2^{\rm IA}} = 2.12 \times 10^{-2}$, which are also in agreement with the values in quoted Table 5.1.

5.2.3 Required galaxy numbers for the CBB estimator

The CBB estimator becomes unstable when there is a low number of background galaxies available in a particular cell. To gain some insight into the source of this issue, we can examine the behaviour of the determinant of matrix $\mathbf{D}$ when a low number of galaxies is considered. The determinant of matrix $\mathbf{D}$ is

$$\begin{aligned}\det\left(\mathbf{D}\right) =& {\beta_4^{\rm int}}^2 - \left[\frac{1}{N}\sum_{i=1}^{N}\cos\left(4{\hat{\alpha}_i}^{\rm int}\right)\right]^2 \\ &- \left[\frac{1}{N}\sum_{i=1}^{N}\sin\left(4{\hat{\alpha}_i}^{\rm int}\right)\right]^2 . \end{aligned} \tag{5.28}$$

As the measurement error on $\alpha^{\rm int}$ is increased, the bias correction, $\beta_4^{\rm int}$, decreases. For a finite number of background galaxies, chance alignments of the random components of the intrinsic galaxy orientations can force this determinant to approach zero, with the effect being more likely when the number of galaxies in a cell is low. This in turn can produce substantial outliers in the estimated shear values as the modulus of a particular shear estimate is scaled with the reciprocal of the determinant. It is possible to place constraints on the number of background galaxies required for a reliable shear estimate by assuming that there are enough galaxies in the sample such that the central limit theorem can be applied to the distributions of the means of the trigonometric functions in equation (5.28). We can use this assumption to examine the probability that the sum of the square of the mean trigonometric functions in equation (5.28) will lie within a given range of ${\beta_4^{\rm int}}^2$. The determinant is independent of the shear and is only dependent on the IA signal at $4^{\rm th}$ order, so we can safely assume the IA signal to be zero. With these assumptions in place, we choose to constrain the number of galaxies such that we can exclude values of the reciprocal $> 2/{\beta_4^{\rm int}}^2$ at a confidence

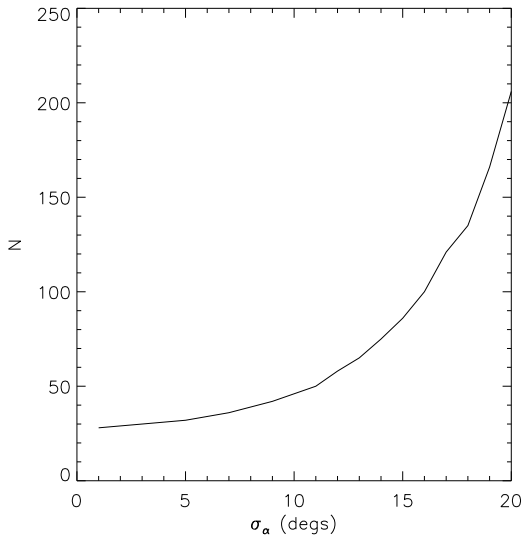

Figure 5.4: The number of galaxies in the sample as a function of the error on $\alpha^{\rm int}$ such that the reciprocal of the determinant $< 2/\beta_4^{\rm int^2}$ with a confidence level of 5σ.

level of 99.99994%, which is equivalent to a confidence level of 5σ for the Gaussian distribution. The choice of 5σ is selected to mitigate the issue of outliers when considering the simulations in Section 5.4, where we reconstruct the shear and IA auto and cross-power spectra using $\sim 10^6$ cells per redshift bin and therefore expect typically one cell per reconstruction to have a reciprocal value $> 2/\beta_4^{\rm int^2}$. The constraint on the values of the reciprocal $> 2/\beta_4^{\rm int^2}$ is somewhat arbitrary but serves to provide an upper limit on the dispersion of the shear estimates.

This choice of constraint parameters results in Figure 5.4, where we plot the number of galaxies required in the sample as a function of $\sigma_{\alpha^{\rm int}}$. As an example, let us assume a measurement error on $\alpha^{\rm int}$ of 10°. Then, from Figure 5.4, we find that we need $\sim$46 galaxies in each cell so that values of the reciprocal of the determinant $> 2/\beta_4^{\rm int^2}$ are ruled out at a confidence level of 5σ. For Figure 5.2, we considered 100 galaxies per realization, and hence outliers were not an issue for these tests. The number density of background galaxies will be fixed for any specific set of observations. However, for a fixed number density of galaxies, the size of the cells may be chosen so that the number of source galaxies within each cell is greater or equal to the number

of galaxies required to recover a reliable shear estimate. For a low number density of background galaxies, this will of course result in a large cell size and hence the loss of small scale information.

5.3 Alternative approaches

5.3.1 Full angle-only estimator (FAO)

In this section, we extend the angle-only shear estimator, introduced in Chapter 3, to include measurements of the IPA. Assuming a prior knowledge of the intrinsic ellipticity distribution, we showed that it is possible to recover an estimate of the shear using only measurements of galaxy position angles. Using measurements of the IPA, as opposed to the observed position angles, this method can be used to recover a direct estimate of the IA signal.

We begin by writing the IA in polar form, such that

$$\begin{aligned} \gamma_1^{\rm IA} &= \left|\boldsymbol{\gamma}^{\rm IA}\right| \cos\left(2\alpha^{\rm IA}\right), \\ \gamma_2^{\rm IA} &= \left|\boldsymbol{\gamma}^{\rm IA}\right| \sin\left(2\alpha^{\rm IA}\right). \end{aligned} \tag{5.29}$$

Following the approach outlined in Chapter 3, we can estimate $\alpha^{\rm IA}$ as

$$\hat{\alpha}^{\rm IA} = \frac{1}{2}\tan^{-1}\left(\frac{\sum_{i=1}^{N}\sin\left(2\hat{\alpha}_i^{\rm int}\right)}{\sum_{i=1}^{N}\cos\left(2\hat{\alpha}_i^{\rm int}\right)}\right). \tag{5.30}$$

We can also recover an estimate of $\left|\boldsymbol{\gamma}^{\rm IA}\right|$, which satisfies the equation

$$F_1\left(\left|\hat{\boldsymbol{\gamma}}^{\rm IA}\right|\right) = \frac{1}{N\beta_2^{\rm int}}\sqrt{\left(\sum_{i=1}^{N}\cos\left(2\hat{\alpha}_i^{\rm int}\right)\right)^2 + \left(\sum_{i=1}^{N}\sin\left(2\hat{\alpha}_i^{\rm int}\right)\right)^2}, \tag{5.31}$$

where the correction term $\beta_2^{\rm int}$ follows the definition given in equation (5.14). The form of the $F_1\left(\left|\boldsymbol{\gamma}^{\rm IA}\right|\right)$ function is given in Appendix G.

If we express the observed ellipticity in polar coordinates,

$$\begin{aligned}\epsilon_1^{\rm obs} &= \left|\boldsymbol{\epsilon}^{\rm obs}\right| \cos\left(2\alpha^{\rm obs}\right), \\ \epsilon_2^{\rm obs} &= \left|\boldsymbol{\epsilon}^{\rm obs}\right| \sin\left(2\alpha^{\rm obs}\right),\end{aligned} \tag{5.32}$$

we can follow the approach of Chapter 3 to recover estimates of the vector $\boldsymbol{\gamma} + \boldsymbol{\gamma}^{\rm IA}$ from the observed galaxy orientations.

Let us define the vector $\boldsymbol{\gamma}^{\rm tot}$ as

$$\begin{aligned}\gamma_1 + \gamma_1^{\rm IA} &= \left|\boldsymbol{\gamma}^{\rm tot}\right| \cos\left(2\alpha^{\rm tot}\right), \\ \gamma_2 + \gamma_2^{\rm IA} &= \left|\boldsymbol{\gamma}^{\rm tot}\right| \sin\left(2\alpha^{\rm tot}\right).\end{aligned} \tag{5.33}$$

Assuming that we are working well within the weak lensing regime, with $\boldsymbol{\epsilon}^{\rm obs}$ described using equation (5.1), we can recover an estimate of $\alpha^{\rm tot}$ as

$$\hat{\alpha}^{\rm tot} = \frac{1}{2}\tan^{-1}\left(\frac{\sum_{i=1}^{N}\sin\left(2\hat{\alpha}_i^{\rm obs}\right)}{\sum_{i=1}^{N}\cos\left(2\hat{\alpha}_i^{\rm obs}\right)}\right), \tag{5.34}$$

and an estimate of $|\boldsymbol{\gamma}^{\rm tot}|$ which satisfies the equation

$$F_1\left(\left|\hat{\boldsymbol{\gamma}}^{\rm tot}\right|\right) = \frac{1}{N\beta_2^{\rm obs}}\sqrt{\left(\sum_{i=1}^{N}\cos\left(2\hat{\alpha}_i^{\rm obs}\right)\right)^2 + \left(\sum_{i=1}^{N}\sin\left(2\hat{\alpha}_i^{\rm obs}\right)\right)^2}, \tag{5.35}$$

and which provides us with an estimate of the vector $\boldsymbol{\gamma}^{\rm tot}$ using measurements of the observed position angles, $\hat{\alpha}_i^{\rm obs}$, only. A detailed discussion on the form of equation (5.35) is given in Appendix G. The correction term $\beta_2^{\rm obs}$ follows the definition given in equation (G.10).

Once we have recovered estimates of $\boldsymbol{\gamma}^{\rm IA}$ and $\boldsymbol{\gamma}^{\rm tot}$, an estimate of the shear can be recovered trivially, such that

$$\hat{\boldsymbol{\gamma}} = \hat{\boldsymbol{\gamma}}^{\rm tot} - \hat{\boldsymbol{\gamma}}^{\rm IA}. \tag{5.36}$$

Estimator ($\times 10^{-2}$)	$\sigma_{\hat{\gamma}_1}$	$\sigma_{\hat{\gamma}_2}$	$\langle\hat{\gamma}_1\rangle$	$\langle\hat{\gamma}_2\rangle$	$\sigma_{\hat{\gamma}_1^{\rm IA}}$	$\sigma_{\hat{\gamma}_2^{\rm IA}}$	$\langle\hat{\gamma}_1^{\rm IA}\rangle$	$\langle\hat{\gamma}_2^{\rm IA}\rangle$
Full angle-only	1.02	1.07	-3.02 ± 0.01	4.02 ± 0.01	2.56	2.57	0.99 ± 0.03	-1.99 ± 0.03
Hybrid	1.42	1.42	-3.00 ± 0.01	4.01 ± 0.01	2.56	2.57	0.99 ± 0.03	-1.99 ± 0.03

Table 5.2: The mean and standard deviation of the shear and IA estimates recovered from 10^4 simulations. Values are quoted for both the full angle-only estimator (equations (5.30) and (5.31), and equations (5.34) - (5.36)) and the hybrid estimator (equations (5.30) and (5.31), and equation (5.41)). The input shear and IA values are $\gamma_1 = -0.03$, $\gamma_2 = 0.04$, $\gamma_1^{\rm IA} = 0.01$ and $\gamma_2^{\rm IA} = -0.02$.

To summarize, the full angle-only estimator (hereafter the FAO estimator) first requires an estimate of the intrinsic ellipticity distribution, $f\left(|\boldsymbol{\epsilon}^{\rm ran}|\right)$. We can use this information with measurements of the IPA only to recover an estimate of $\boldsymbol{\gamma}^{\rm IA}$ via equations (5.30) and (5.31). An estimate of the vector $\boldsymbol{\gamma} + \boldsymbol{\gamma}^{\rm IA}$ can also be obtained using the same method via equations (5.34) and (5.35). Finally, we use equation (5.36) to recover an estimate of $\boldsymbol{\gamma}$.

Assuming the same input values as used in Figure 5.2, we recovered shear and IA estimates from 10^4 realizations using the FAO estimator. The error on $\alpha^{\rm int}$ was assumed to be 10° and the error on $\alpha^{\rm obs}$ was assumed to be zero to allow for a direct comparison of the performance of this estimator with the CBB estimator, where we assumed zero errors on the ellipticity measurements ($\boldsymbol{\epsilon}^{\rm obs}$). The results of this test are shown in Figure 5.5. Note that the reduction in the dispersion of the shear and IA estimates is a result of the fact that we have assumed a perfect knowledge of the intrinsic ellipticity distribution. Errors on the prior knowledge of the intrinsic ellipticity distribution introduce multiplicative biases to the estimates of the shear and IA. This issue is addressed in Section 3.4, where constraints are placed on the size of the errors on the measurements of the ellipticities and the size of the sample used to estimate the intrinsic ellipticity distribution such that this multiplicative bias is below a desired threshold value. Table 5.2 shows the mean recovered shear and IA estimates and the standard deviation of the estimates.

A linear form of the estimator can be obtained by following the approach outlined

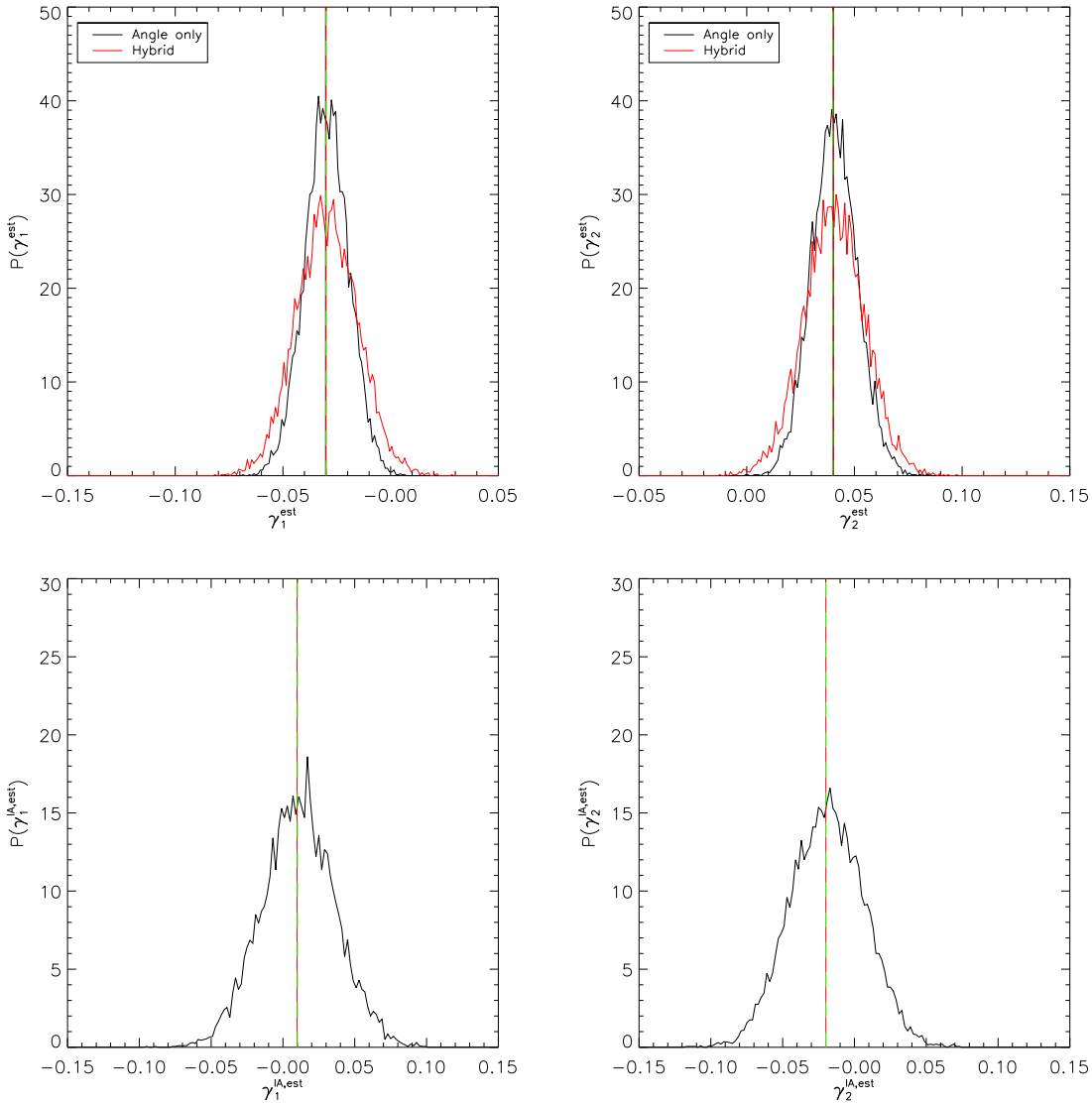

Figure 5.5: The recovered shear and IA estimates from 10^4 realizations, with each realization consisting of 100 galaxies and assuming a measurement error on $\alpha^{\rm int}$ of $\sigma_{\alpha^{\rm int}} = 10°$. The black curves show the distributions of recovered shear and IA estimates when using the FAO estimator. The vertical black lines show the mean recovered estimates using this method. The red curves show the distributed shear estimates when using the hybrid method, with the IA estimates identical for both methods. The vertical red lines show the mean recovered estimates using this method. The dashed green lines show the input signal. Here we see that both methods have successfully recovered shear and IA estimates with negligible bias. The dispersion in the FAO shear estimates is $\sim$40% lower than those recovered using the CBB estimator, and the dispersion in the IA estimates is $\sim$6% lower for this set of input values. The dispersion in the hybrid shear estimates is $\sim$15% lower than those recovered using the CBB estimator. The results are quantified in Table 5.2.

in Chapter 3. Assuming that the $F_1\left(|\boldsymbol{\gamma}|\right)$ function can be approximated as

$$F_1\left(|\boldsymbol{\gamma}|\right) \approx u\,|\boldsymbol{\gamma}|\,, \tag{5.37}$$

for a general intrinsic ellipticity distribution we can find the coefficient u numerically. However, assuming a Rayleigh distribution for $|\boldsymbol{\epsilon}^{\rm ran}|$ and assuming that σ_ϵ is small enough for us to safely allow the limit in the integral, $\left|\boldsymbol{\epsilon}^{\rm int}_{\rm max}\right|$, to tend to infinity, it is possible to obtain u analytically. This is found to be

$$u = \left(\frac{\pi}{8\sigma_\epsilon^2}\right)^{\frac{1}{2}}. \tag{5.38}$$

The linear approximation of the FAO estimator can then be written as

$$\begin{aligned}
\hat{\gamma}_1 =& \frac{1}{uN}\sum_{i=1}^{N}\left[\frac{\cos\left(2\hat{\alpha}_i^{\rm obs}\right)}{\beta_2^{\rm obs}} - \frac{\cos\left(2\hat{\alpha}_i^{\rm int}\right)}{\beta_2^{\rm int}}\right],\\
\hat{\gamma}_2 =& \frac{1}{uN}\sum_{i=1}^{N}\left[\frac{\sin\left(2\hat{\alpha}_i^{\rm obs}\right)}{\beta_2^{\rm obs}} - \frac{\sin\left(2\hat{\alpha}_i^{\rm int}\right)}{\beta_2^{\rm int}}\right],\\
\hat{\gamma}_1^{\rm IA} =& \frac{1}{uN}\sum_{i=1}^{N}\frac{\cos\left(2\hat{\alpha}_i^{\rm int}\right)}{\beta_2^{\rm int}},\\
\hat{\gamma}_2^{\rm IA} =& \frac{1}{uN}\sum_{i=1}^{N}\frac{\sin\left(2\hat{\alpha}_i^{\rm int}\right)}{\beta_2^{\rm int}}.
\end{aligned} \tag{5.39}$$

From here, it is possible to recover an approximation for the dispersion in the estimator, given by

$$\begin{aligned}
\sigma_{\hat{\gamma}_1} =& \frac{1}{u\sqrt{N}}\left[\frac{1}{2\beta_2^{\rm obs^2}} + \frac{1}{2\beta_2^{\rm int^2}} - 2\left\langle\cos\left(2\alpha^{\rm obs}\right)\cos\left(2\alpha^{\rm int}\right)\right\rangle\right]^{\frac{1}{2}},\\
\sigma_{\hat{\gamma}_2} =& \frac{1}{u\sqrt{N}}\left[\frac{1}{2\beta_2^{\rm obs^2}} + \frac{1}{2\beta_2^{\rm int^2}} - 2\left\langle\sin\left(2\alpha^{\rm obs}\right)\sin\left(2\alpha^{\rm int}\right)\right\rangle\right]^{\frac{1}{2}},\\
\sigma_{\hat{\gamma}_1^{\rm IA}} =& \sigma_{\hat{\gamma}_2^{\rm IA}} = \frac{1}{u\sqrt{N}}\left[\frac{1}{2\beta_2^{\rm int^2}}\right]^{\frac{1}{2}}.
\end{aligned} \tag{5.40}$$

The dispersion in the shear estimates depends on the correlations between the cosines and sines of the true observed and intrinsic position angles. These in turn depend upon the intrinsic ellipticity distribution, the IA and the shear. In the absence of a shear signal, these correlation terms will, to first order in the IA signal, equal $1/2$. If we also neglect measurement errors, such that $\beta_2^{\rm obs} = \beta_2^{\rm int} = 1$, then the dispersion in the shear estimates becomes zero. However, the presence of a non-zero shear signal reduces the correlation between the trigonometric functions and an error is introduced to the estimates. Hence, in the absence of measurement errors on the position angle measurements, the leading order term in the dispersion is dependent on the true shear. Measurement errors on the position angles also increase the dispersion in the estimates, as expected. Using the input values assumed in Figure 5.5 with equation (5.40), we recovered approximations for the errors on the shear and IA estimates by calculating the correlation terms numerically. The errors were found to be $\sigma_{\gamma_1} = 1.06 \times 10^{-2}$, $\sigma_{\gamma_2} = 1.13 \times 10^{-2}$ and $\sigma_{\gamma_1^{\rm IA}} = \sigma_{\gamma_2^{\rm IA}} = 2.54 \times 10^{-2}$, which are in good agreement with the values quoted in Table 5.2.

Assuming that the shear signal is zero, we can also recover estimates of the dispersion in the shear estimates, which are $\sigma_{\gamma_1} = 0.87 \times 10^{-2}$ and $\sigma_{\gamma_2} = 0.85 \times 10^{-2}$. These values are approximately 20% lower than the values quoted above where shear was included. Hence, we can conclude that the dispersion in the shear estimates depends strongly on the input shear signal even if measurement errors on the position angles are included. This is an issue when trying to remove noise bias in power spectra estimates and is discussed in more detail in Section 5.4. The dispersion in the IA estimates are independent of the true IA signal to first order.

Figure 5.6 shows the residual bias in the FAO estimator. As with the CBB estimator, it is expected that there will be some residual bias from the nonlinear propagation of noise on the mean trigonometric functions into estimates of the shear. However, in all of the tests conducted, this residual bias is found to be negligible.

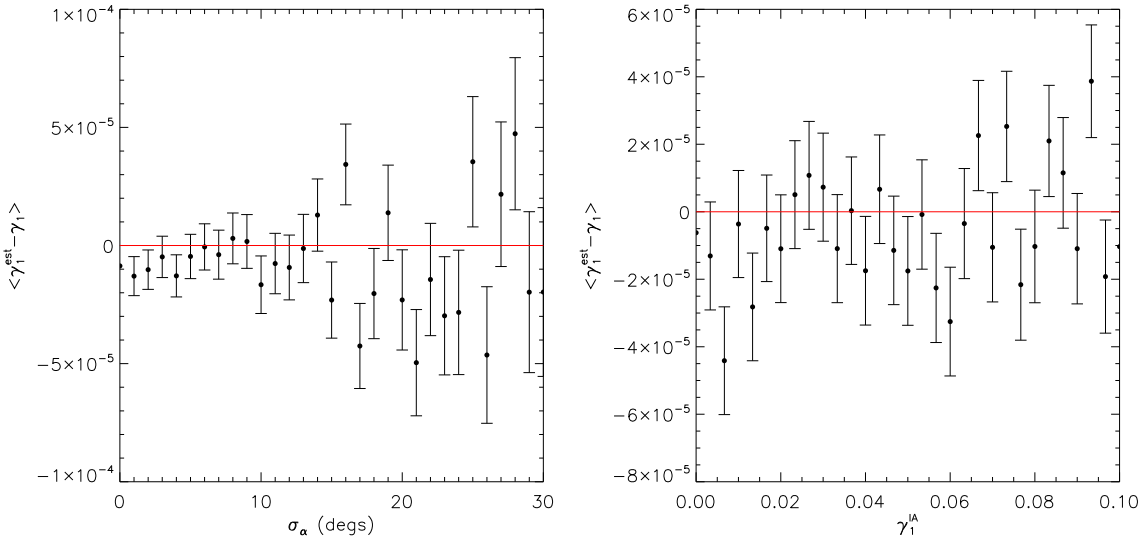

Figure 5.6: Same as for Figure 5.1 but for the FAO shear estimator. From this plot, we see that any residual bias in the estimator can be considered negligible.

5.3.2 Hybrid method

In this subsection, we introduce a hybrid method combining the standard method, which averages over galaxy ellipticity measurements, with the angle-only IA estimator.

Using a knowledge of the intrinsic ellipticity distribution, $f\left(|\boldsymbol{\epsilon}^{\rm ran}|\right)$, with measurements of the IPA only, we first recover an estimate of the IA signal via equations (5.30) and (5.31). We can then combine this estimate of the IA signal with an estimate of the vector $\boldsymbol{\gamma}+\boldsymbol{\gamma}^{\rm IA}$ provided by the mean of the observed ellipticities to recover an estimate of the shear:

$$\hat{\boldsymbol{\gamma}} = \left(\frac{1}{N}\sum_{i=1}^{N}\boldsymbol{\epsilon}_i^{\rm obs}\right) - \hat{\boldsymbol{\gamma}}^{\rm IA}. \tag{5.41}$$

Using the same set of realizations as used to test the FAO method in Figure 5.5 (black curves), we recovered shear estimates from 10^4 realizations using the hybrid shear estimator (equation (5.41)). The error on $\alpha^{\rm int}$ (which can be estimated using a measurement of the PPA) was assumed to be 10° and the error on $\boldsymbol{\epsilon}^{\rm obs}$ was assumed to be zero. The results of this test are shown in Figure 5.5 as the red curves. It should be noted that, since the same realizations have been used to test the hybrid and FAO

methods, the IA estimates are identical. As for the FAO estimator discussed in Subsection 5.3.1, the reduction in the dispersion of the shear estimates as compared with the CBB estimator is a result of assuming a prior knowledge of the intrinsic ellipticity distribution when estimating the IA. Table 5.2 shows the mean recovered shear and IA estimates and the standard deviation of the estimates.

Upon assuming a linear approximation of the $F_1\left(\left|\boldsymbol{\gamma}^{\rm IA}\right|\right)$ function using equation (5.37), we can write a linear approximation of the hybrid shear estimator as

$$\begin{aligned}\hat{\gamma}_1 =&\frac{1}{N}\sum_{i=1}^{N}\left[\epsilon_{1,i}^{\rm obs}-\frac{\cos\left(2\hat{\alpha}_i^{\rm int}\right)}{u\beta_2^{\rm int}}\right],\\ \hat{\gamma}_2 =&\frac{1}{N}\sum_{i=1}^{N}\left[\epsilon_{2,i}^{\rm obs}-\frac{\sin\left(2\hat{\alpha}_i^{\rm int}\right)}{u\beta_2^{\rm int}}\right].\end{aligned} \tag{5.42}$$

From here, we can recover an approximation of the dispersion in the shear estimates:

$$\begin{aligned}\sigma_{\hat{\gamma}_1} =&\frac{1}{\sqrt{N}}\left[\sigma_\epsilon^2+\frac{1}{2u^2\beta_2^{\rm int^2}}-\frac{2}{u}\left\langle\epsilon_1^{\rm obs}\cos\left(2\alpha^{\rm int}\right)\right\rangle\right]^{\frac{1}{2}},\\ \sigma_{\hat{\gamma}_2} =&\frac{1}{\sqrt{N}}\left[\sigma_\epsilon^2+\frac{1}{2u^2\beta_2^{\rm int^2}}-\frac{2}{u}\left\langle\epsilon_2^{\rm obs}\sin\left(2\alpha^{\rm int}\right)\right\rangle\right]^{\frac{1}{2}},\end{aligned} \tag{5.43}$$

which depends upon the correlations between the true total ellipticities and the true intrinsic trigonometric functions. It can be shown that these correlation terms can be written as

$$\begin{aligned}\left\langle\epsilon_1^{\rm obs}\cos\left(2\alpha^{\rm int}\right)\right\rangle =&\left\langle\epsilon_2^{\rm obs}\sin\left(2\alpha^{\rm int}\right)\right\rangle\\ \approx&u'+\mathcal{O}\left(|\boldsymbol{\gamma}|\left|\boldsymbol{\gamma}^{\rm IA}\right|\right)+\mathcal{O}\left(\left|\boldsymbol{\gamma}^{\rm IA}\right|^2\right),\end{aligned} \tag{5.44}$$

where u' is a zeroth order term, which is independent of the input shear and IA signals but is dependent on the form of the intrinsic ellipticity distribution, $f\left(|\boldsymbol{\epsilon}^{\rm ran}|\right)$. Hence, to first order in the shear and IA, the correlation terms are constant, and therefore we

can approximate the dispersion in the shear estimates to be

$$\sigma_{\hat{\gamma}_1} \approx \sigma_{\hat{\gamma}_2} \approx \frac{1}{\sqrt{N}} \left[\sigma_\epsilon^2 + \frac{1}{2u^2 \beta_2^{\mathrm{int}^2}} - \frac{2u'}{u} \right]^{\frac{1}{2}}. \tag{5.45}$$

For a Rayleigh distribution it is possible to recover the coefficient u' analytically if we adopt the same assumptions used to derive equation (5.38). This is found to be

$$u' = \left(\frac{\pi \sigma_\epsilon^2}{8} \right)^{\frac{1}{2}}. \tag{5.46}$$

Therefore, we can conclude that in the absence of shear and IA signals and assuming zero measurement errors on the estimates of α^{int}, there is a dispersion in the shear estimates which arises from random shape noise. With these assumptions, we found in the previous subsection that the dispersion in the FAO shear estimator was zero. For the case of the FAO estimator, a knowledge of the intrinsic ellipticity distribution is assumed for the random component of both the observed and intrinsic ellipticities. This allows us to recover estimates of the vectors $\left(\boldsymbol{\gamma} + \boldsymbol{\gamma}^{\mathrm{IA}}\right)$ and $\boldsymbol{\gamma}$ using only measurements of $\hat{\alpha}^{\mathrm{obs}}$ and $\hat{\alpha}^{\mathrm{int}}$. Using only measurements of the position angles eliminates the contribution of random shape noise in the FAO shear estimates. However, the hybrid estimator requires measurements of $\boldsymbol{\epsilon}^{\mathrm{obs}}$ which contributes random shape noise to the estimates of the shear. This noise is, to first order, independent of both the shear and IA signals.

Using equation (5.45) with the input values used in Figure 5.5, we recovered approximations for the dispersion in the shear estimates using the hybrid method. These were found to be $\sigma_{\hat{\gamma}_1} = \sigma_{\hat{\gamma}_2} = 1.40 \times 10^{-2}$, which are in good agreement with the values quoted in Table 5.2.

Figure 5.7 shows the residual bias in the hybrid estimator. Here we see a residual bias which is a result of the nonlinear propagation of noise on the mean trigonometric functions into estimates of the IA signal and hence into the shear estimates. However, we find that this bias is much smaller than the dispersion in the estimates in all of

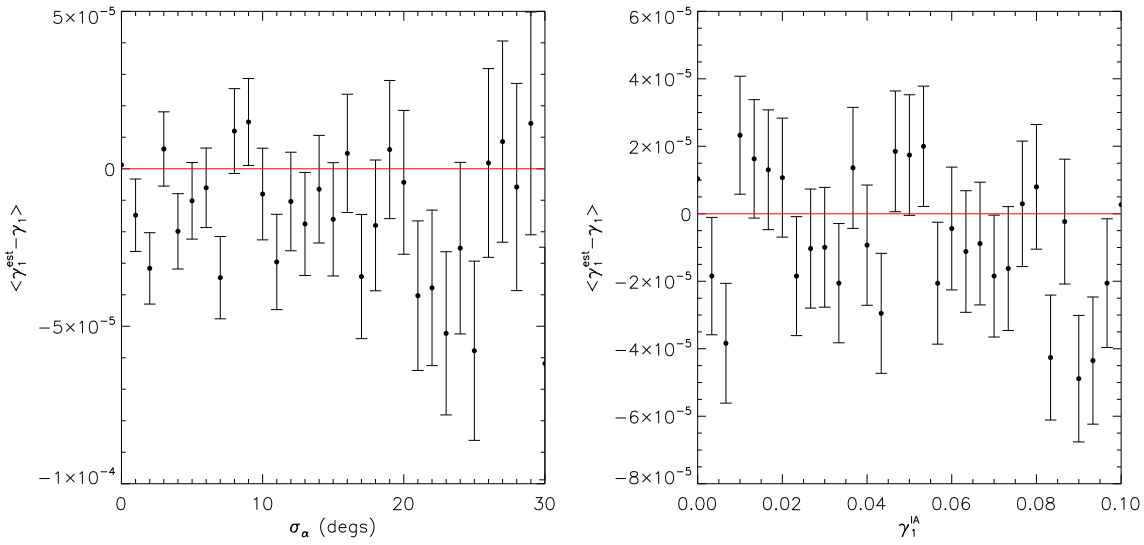

Figure 5.7: Same as for Figure 5.1 but for the hybrid shear estimator. Here we see a small residual bias due to the finite number of source galaxies. However, this bias is much smaller than the bias in the original BB estimator (Figure 5.1).

the tests we have conducted and is negligible when we consider the power spectra reconstructions in Section 5.4.

5.4 Tests on simulations

In this section, we test the three estimators described in the previous sections by reconstructing the lensing and IA auto and cross-power spectra following the approach described in BB11. All of the simulated fields are assumed to be pure Gaussian fields and, as our aim is to demonstrate the power of the estimators to separate the shear and IA signals given an unbiased estimate of the intrinsic position angle, we ignore the effects of observational systematics.

In all simulations, we assume a ΛCDM background cosmology with the matter density parameter $\Omega_{\rm m} = 0.262$, the amplitude of density fluctuations $\sigma_8 = 0.798$, the Hubble constant $H_0 = 71.4\,{\rm km\,s^{-1}\,Mpc^{-1}}$, the baryon density parameter $\Omega_{\rm b} = 0.0443$ and the scalar spectral index $n_{\rm s} = 0.962$.

We simulate the weak lensing and IA fields in three different redshift bins and include all of the possible cross-correlations between the fields in the different bins. The selected bins are $0.00 < z_1 < 1.40$, $1.40 < z_2 < 2.60$ and $z_3 > 2.60$, with the bin limits selected such that each bin contains approximately the same number density of sources. It should be noted that the binning of the galaxies by redshift is no different than for other tomographic studies. Further details on how the binning of sources impacts estimates of the power-spectra are given in BB11. We simulate the IA signal using the modified non-linear alignment model introduced by Bridle & King (2007), and we use a normalization for the IA power spectrum which is five times the observed SuperCOSMOS level in order to make it easier to see the effects we are dealing with. We assume a correlation coefficient of $\rho_c = -0.2$. A detailed discussion of the simulated fields is given in BB11. Here we focus on the performance of the estimators.

We construct our observed galaxy ellipticities ($\boldsymbol{\epsilon}^{\rm obs}$) using the simulated IA and shear fields with equations (5.1) and (5.4), where we assume that the measurement errors on the ellipticities are zero and that the $\boldsymbol{\epsilon}^{\rm ran}$ are drawn from an isotropic Gaussian distribution, with a 1D dispersion of $\sigma_\epsilon = 0.3/\sqrt{2}$. The IPAs are calculated from the $\boldsymbol{\epsilon}^{\rm int}$ as

$$\alpha^{\rm int} = \frac{1}{2}\tan^{-1}\left(\frac{\epsilon_2^{\rm int}}{\epsilon_1^{\rm int}}\right). \tag{5.47}$$

Similarly, for the case of the FAO estimator, the observed position angles are calculated using $\boldsymbol{\epsilon}^{\rm obs}$.

In order to demonstrate the methods discussed, we assume that all of the galaxies have sufficient information to measure the IPA. We assume a measurement error on the $\alpha^{\rm int}$ (IPA) estimates with r.m.s. 10° and a negligible error on the ellipticity and $\alpha^{\rm obs}$ measurements in order to make a fair comparison between the various methods.

To estimate the power spectra from the simulated observations, we pixelize the sky into 3.4×3.4 arcmin^2 cells and assume a background galaxy number density of 4 arcmin^{-2} for each redshift bin; this number density is chosen to avoid the issue dis-

cussed at the end of Subsection 5.2.3, though we note that this may be achievable in future deep surveys with the SKA. We then reconstruct shear and IA maps using each of the estimators discussed in the previous sections.

We estimate the recovered power spectra from the reconstructed shear and IA maps using the standard pseudo-C_l approach (Hivon et al. 2002; Brown et al. 2005; Brown & Battye 2011b).

In the presence of noise in the shear and IA estimates, we can write the general expectation value of the estimated pseudo-C_l power spectra, $\tilde{C}_l^{XY}$, as

$$\left\langle \tilde{C}_l^{XY} \right\rangle = C_l^{X_s Y_s} + C_l^{X_n Y_n} + C_l^{X_s Y_n} + C_l^{X_n Y_s}, \tag{5.48}$$

where the postscripts X and Y denote the fields being correlated and where the subscripts s and n respectively denote the signal and noise in that field. One can correct for biases due to noise and correlations between the signal and noise such that an unbiased estimate of the power spectra can be recovered using a suite of Monte-Carlo simulations:

$$\hat{C}_l^{XY} = \tilde{C}_l^{XY} - \left\langle C_l^{X_n Y_n} \right\rangle_{\rm mc} - \left\langle C_l^{X_s Y_n} \right\rangle_{\rm mc} - \left\langle C_l^{X_n Y_s} \right\rangle_{\rm mc}, \tag{5.49}$$

where the angle brackets indicate the mean over the suite of Monte-Carlo simulations. This is the form of the power spectra estimator used for the remainder of this chapter. In the presence of model dependent noise and correlations between the signal and noise, unbiased estimates of the power spectra are only achievable if the Monte-Carlo simulations include the input power spectra. In a real analysis, this will obviously not be possible. In order to address this issue, we adopt an iterative approach to estimating the spectra. To begin with, we construct a suite of 200 Monte-Carlo simulations under the assumption that the input shear and IA signals are zero. This provides us with an initial estimate of the power spectra using equation (5.49). As we shall see, this is sufficient when using the CBB and hybrid methods to recover the shear and IA

estimates. However, it is insufficient when using the FAO estimator. It does, however, provide us with initial estimates of the power spectra. These initial estimates can then be used to construct a suite of improved Monte-Carlo simulations which can be used to update our estimates of the power spectra.

Figure 5.8 shows the reconstructed shear and IA auto and cross-power spectra for each of the three overlapping redshift bins recovered using the CBB estimator (black points) and using a suite of 200 Monte-Carlo simulations under the assumption that the input shear and IA signal are zero. The blue points show the reconstructed power spectra using the original BB estimator to estimate the shear and IA. The red curves show the input power spectra. From this, we clearly see the success of the correction.

Figure 5.9 shows the reconstructed power spectra when using the FAO estimator (black points). The linear form of the FAO estimator, given in equation (5.39), has been used to reduce computation time. From this, we see that there is a residual bias in the shear power spectra which propagates into estimates of the shear-IA cross-power spectra. This bias is due to a dependence of the errors on the shear estimates on the input shear signal, as described at the end of Subsection 5.3.1. This bias is not successfully corrected for when using noise-only Monte-Carlo simulations. However, if we use these estimated power spectra as the input power spectra for a further set of Monte-Carlo simulations, we can construct noise and noise-signal power spectra which include an estimate of the shear and IA signal. These updated noise and noise-signal power spectra can then be used to recover an improved estimate of the input power spectra. This step can be iterated until subsequent estimates of the power spectra are deemed consistent. The blue points in Figure 5.9 are the result of this procedure using just one iteration. We see that the iterative step has indeed improved our estimates of the power spectra.

The green points in Figure 5.9 show the reconstructed power spectra using the hybrid estimator. The linear form of the hybrid estimator, given in equation (5.42), has been used to reduce computation time. This reconstruction did not require the use of the iterative procedure. It was shown in the discussion which follows from equa-

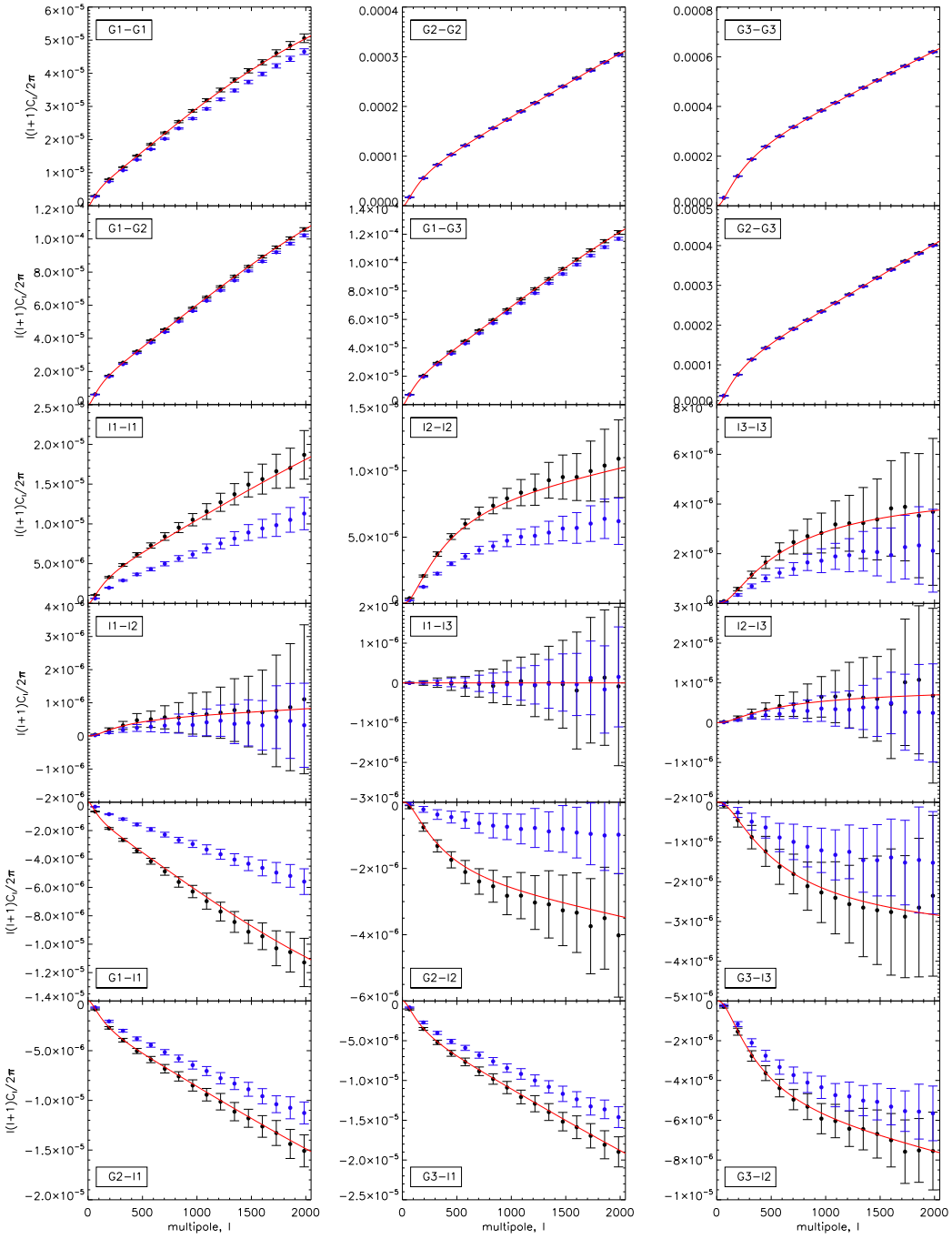

Figure 5.8: Reconstructions of the lensing and IA auto and cross-power spectra. In each panel, the red curve shows the model power spectra. The black points show the reconstructed power spectra using the CBB estimator to estimate the shear and IA signals. The blue points show the reconstructions using the original BB estimator, as a comparison. From these reconstructions, we clearly see that the residual bias has been reduced when using the CBB estimator.

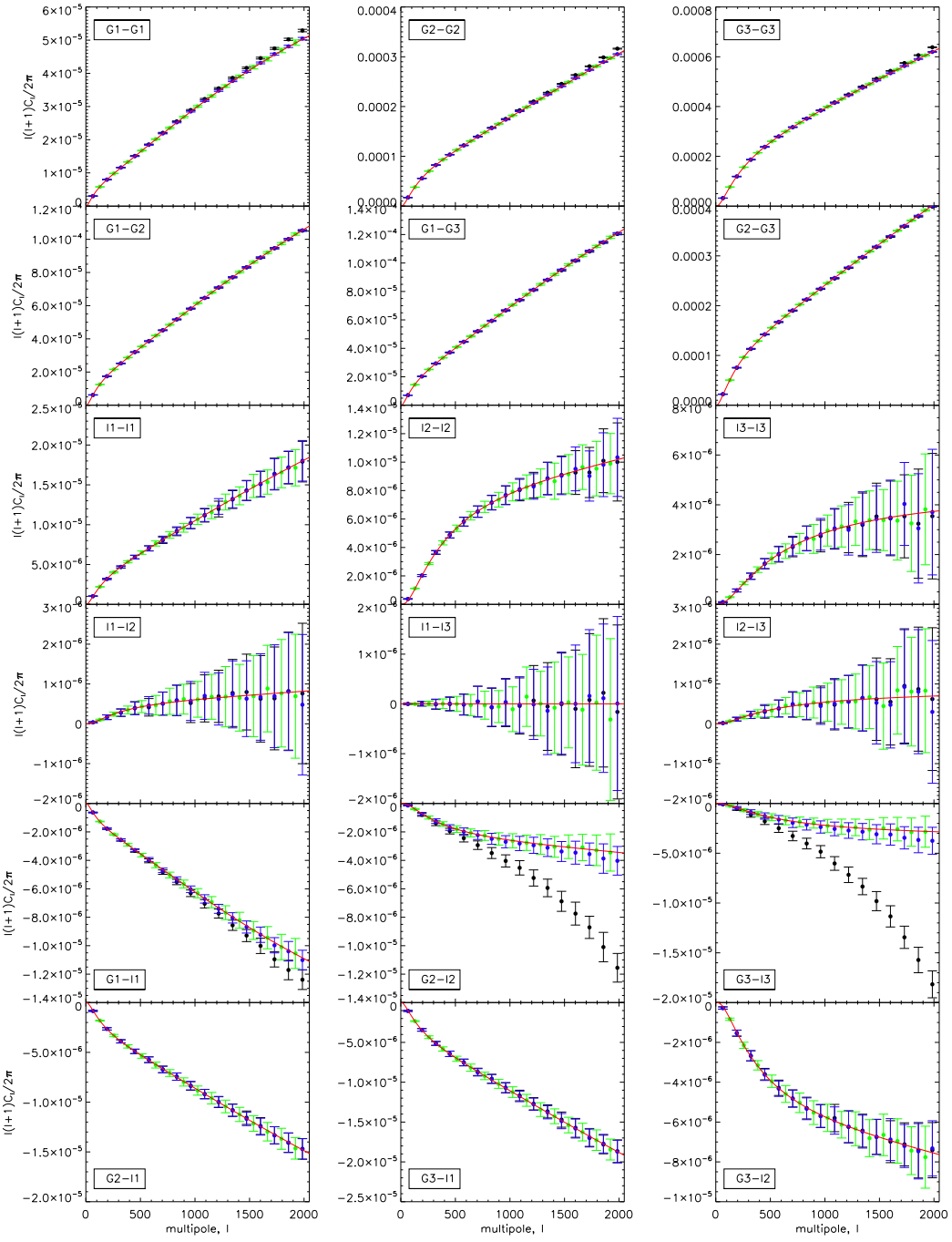

Figure 5.9: Reconstructions of the lensing and IA auto and cross-power spectra. In each panel, the red curve shows the model power spectra. The black points show the reconstructed power spectra using the FAO estimator to estimate the shear and IA signals and with the noise maps created under the assumption that the input shear and IA signals are zero. The blue points show the reconstructed power spectra recovered upon using the iterative procedure described in the main text. From this, we see the success of the iterative procedure. The green points show the reconstructed power spectra using the hybrid estimator to estimate the shear and IA signals, with no iterative procedure required.

Spectrum	Original BB	Corrected BB	FAO	Hybrid
G1-G1	$(-7.48 \pm 0.02) \times 10^{-2}$	$(7.45 \pm 0.29) \times 10^{-3}$	$(1.45 \pm 0.13) \times 10^{-3}$	$(0.17 \pm 0.21) \times 10^{-3}$
G2-G2	$(-3.99 \pm 0.10) \times 10^{-3}$	$(9.60 \pm 1.14) \times 10^{-4}$	$(3.90 \pm 0.96) \times 10^{-4}$	$(1.77 \pm 1.05) \times 10^{-4}$
G3-G3	$(-1.97 \pm 0.10) \times 10^{-3}$	$(4.02 \pm 1.01) \times 10^{-4}$	$(-6.27 \pm 0.93) \times 10^{-4}$	$(0.69 \pm 0.98) \times 10^{-4}$
G1-G2	$(-3.07 \pm 0.01) \times 10^{-2}$	$(2.44 \pm 0.16) \times 10^{-3}$	$(-0.38 \pm 0.11) \times 10^{-3}$	$(0.26 \pm 0.13) \times 10^{-3}$
G1-G3	$(-3.48 \pm 0.01) \times 10^{-2}$	$(2.68 \pm 0.17) \times 10^{-3}$	$(-0.83 \pm 0.12) \times 10^{-3}$	$(-0.05 \pm 0.15) \times 10^{-3}$
G2-G3	$(-4.73 \pm 0.10) \times 10^{-3}$	$(6.42 \pm 1.03) \times 10^{-4}$	$(-11.72 \pm 0.95) \times 10^{-4}$	$(0.79 \pm 0.99) \times 10^{-4}$
I1-I1	$(-3.85 \pm 0.01) \times 10^{-1}$	$(3.15 \pm 0.17) \times 10^{-2}$	$(0.17 \pm 0.14) \times 10^{-2}$	$(-0.27 \pm 0.14) \times 10^{-2}$
I2-I2	$(-3.85 \pm 0.02) \times 10^{-1}$	$(3.80 \pm 0.38) \times 10^{-2}$	$(-0.12 \pm 0.29) \times 10^{-2}$	$(-0.39 \pm 0.30) \times 10^{-2}$
I3-I3	$(-3.83 \pm 0.09) \times 10^{-1}$	$(-0.66 \pm 1.57) \times 10^{-2}$	$(2.79 \pm 1.33) \times 10^{-2}$	$(2.31 \pm 1.42) \times 10^{-2}$
I1-I2	$(-4.04 \pm 0.19) \times 10^{-1}$	$(1.15 \pm 0.32) \times 10^{-1}$	$(-0.56 \pm 0.27) \times 10^{-1}$	$(0.33 \pm 0.27) \times 10^{-1}$
I2-I3	$(-4.60 \pm 0.30) \times 10^{-1}$	$(1.85 \pm 0.49) \times 10^{-1}$	$(-0.09 \pm 0.42) \times 10^{-1}$	$(-0.23 \pm 0.42) \times 10^{-1}$

Table 5.3: The mean fractional bias in the power spectra reconstructions across all multipoles.

tion (5.45) that the dispersion in the shear estimates is independent of the input shear and IA signal to first order. Hence, the zero-signal noise power spectra successfully removes the noise bias from the power spectra without the need of the iterative procedure described above.

As explained in the discussion following equation (5.40), the error on the estimated shear has a strong dependence on the true shear signal when using the FAO estimator, and hence the term $\left\langle C_l^{X_n X_n} \right\rangle_{\rm mc}$ in equation (5.49) cannot be sufficiently estimated using simulations which assume zero input shear and IA signals. The iterative procedure uses subsequent estimates of the power spectra to improve the estimates of the contribution from noise bias. The errors on the estimated shear using the CBB (equation (5.27)) and hybrid (equation (5.43)) estimators are independent of the true shear and IA signals to leading order, and hence an estimate of the noise bias in the power spectra can be successfully recovered from simulations which assume zero input signals, and the iterative procedure is not required.

In Figure 5.10, we show the fractional errors on the reconstructed power spectra. From this, we see, as expected, that the errors are largest for the CBB estimator and smallest for the FAO estimator. However, we emphasize that we have assumed a perfect knowledge of $f\left(|\boldsymbol{\epsilon}^{\rm ran}|\right)$ when using the FAO and hybrid estimators. This would obviously not be the case in a real analysis where uncertainties on our knowledge of $f\left(|\boldsymbol{\epsilon}^{\rm ran}|\right)$ would lead to an increase in the errors of the FAO and hybrid approaches.

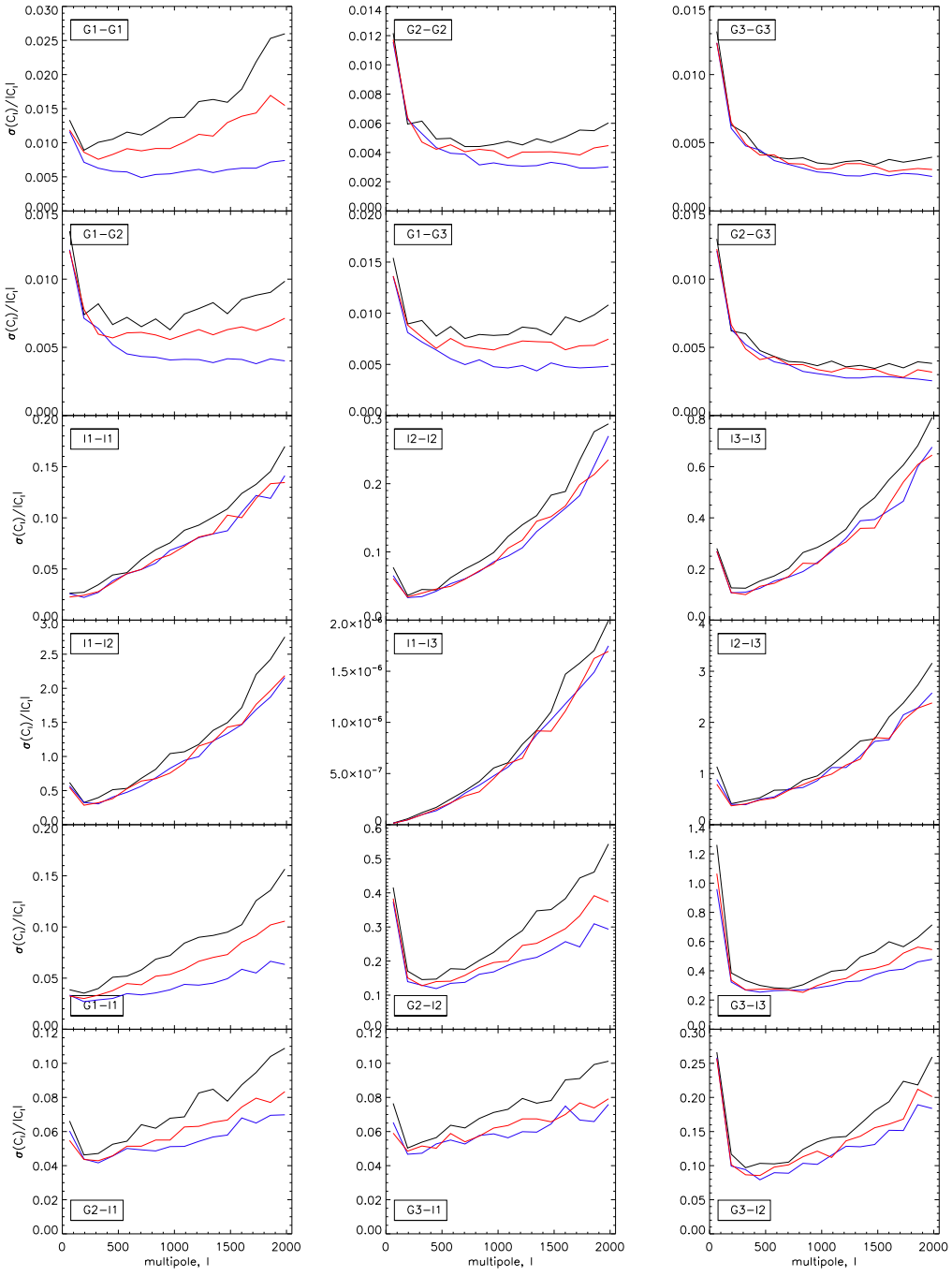

Figure 5.10: The fractional error in the power spectra reconstructions shown in Figures 5.8 and 5.9. The curves show the CBB estimator (black), the FAO estimator (blue) and the hybrid estimator (red). Note, the input I1-I3 cross-power spectrum is zero for all multipoles, and therefore we show the error as opposed to the fractional error for that panel.

Table 5.3 shows the mean fractional bias in the shear auto and cross-power spectra and the IA auto and cross-power spectra reconstructions. From this, we see that there is approximately an order of magnitude reduction in the fractional bias of the CBB estimator as compared with the original BB estimator. The reduction in bias is generally greater when using the FAO and hybrid methods. However, these methods require an accurate knowledge of $f\left(|\boldsymbol{\epsilon}^{\rm ran}|\right)$ and for the case of the FAO estimator an iterative method to remove noise bias.

5.5 Conclusions

When we include a correction term into the formalism of the estimator introduced by BB11, we have demonstrated that the residual bias in the estimator, which emerges in the presence of measurement errors on the intrinsic position angle estimates and a non-zero IA signal, can be reliably reduced to negligible levels as compared with the original BB estimator provided that a sufficient number of resolved background galaxies have reliable polarization information. When including the correction term, chance alignments of the measured IPA may result in substantial outliers in the distribution of the shear estimates if the number of background galaxies is small. However, we have introduced a method which may be used to place constraints on the number of background galaxies required to recover reliable shear estimates when using this estimator. This restriction may require large cells, such that the number of source galaxies within each cell is greater than or equal to the minimum number of galaxies required, and hence small scale information may not be attainable.

Building upon the angle-only estimator introduced in Chapter 3, we have constructed an angle-only IA estimator which uses IPA measurements and requires a knowledge of the intrinsic ellipticity distribution. From here, we can formulate two distinct shear estimators. The first is the FAO shear estimator, which requires measurements of the observed position angles. The second is the hybrid method, which combines the angle-only IA estimator with the standard shear estimator and requires

measurements of the observed ellipticities. We have demonstrated that both of these methods may be used to recover shear estimates which exhibit negligible residual biasing as compared with the original BB estimator. The FAO method, however, requires the implementation of an iterative procedure to mitigate the effects of a signal dependent noise bias in the shear and shear-IA power spectra. We further emphasize that the results presented in this chapter are based on the assumption that the distribution $f\left(|\boldsymbol{\epsilon}^{\rm ran}|\right)$ is known exactly. An incorrect knowledge of this distribution propagates as a multiplicative bias into the shear and IA estimates. However, it is expected that this distribution may be accurately measured using deep calibration observations in future surveys. Constraints on the accuracies required and the number of galaxies required to achieve these accuracies are discussed in Section 3.4.

Present radio surveys, such as SuperCLASS which is currently under observation using the JVLA and e-MERLIN[1] arrays, will hopefully provide information about the fraction of galaxies with reliable polarization information and the expected error on the intrinsic orientation estimates, $\sigma_{\alpha^{\rm int}}$, provided by measurements of the PPA. This information is essential if we are to gain an understanding of the cosmological scales which may be probed using these techniques. In addition to this, we hope to improve our understanding of the impact of Faraday rotation on measurements of the PPA. It is expected that this effect may be corrected for using information from multiple frequencies to extract the rotation measures of the source galaxies.

We aim to apply these techniques to future radio surveys, such as with the SKA, where the number density of galaxies will be higher than for current radio surveys enabling us to probe smaller cosmological scales. The high redshifts achieved by the SKA will also enable radio weak lensing to probe regions of the Universe which are inaccessible to other weak lensing surveys (Brown et al. 2015). This high redshift information will provide powerful constraints on the evolution of large-scale structure in the Universe. Another exciting prospect for future radio weak lensing is the cross-correlation of radio and optical weak lensing surveys, such as the correlation of shear

[1] http://www.e-merlin.ac.uk/legacy/projects/superclass.html

estimates from Euclid with those from the SKA. This method has the advantage that the systematics in the two telescopes are expected to be completely uncorrelated allowing the effects of systematics to be removed from shear analyses while avoiding the residual effects of an incorrect calibration.

Chapter 6

Conclusion

The theoretical framework of weak gravitational lensing is elegant and well established. By measuring the statistical coherence imprinted by the lensing signal into the distribution of observed galaxy shapes, one can estimate the distribution of matter and develop a deeper understanding of the nature of the Universe.

With the dawn of precision observational cosmology, this method has emerged as a powerful cosmological tool. Analyses of weak lensing surveys (e.g. CFHTLenS (Kilbinger et al. 2013) and DES (The Dark Energy Survey Collaboration et al. 2015)) have been used to place constraints on the normalization of the matter power spectrum, the matter density parameter and the dark energy equation of state. With the advances in precision expected in future surveys, such as Euclid and the SKA, weak lensing has the potential to greatly enhance our understanding of the late time evolution of the Universe. In order for the full potential of weak lensing to be exploited, it is essential that the observational and astrophysical systematics are well understood and calibrated for.

There are various sources of observational systematics which effect measurements of galaxy shapes, such as convolution with a PSF and the use of a weighting function to reduce noise at large scales. Incorrectly calibrating for these effects propagates biases into estimates of the shear. In Chapter 3, we developed a method that can potentially avoid the isotropic component of these effects by estimating the shear using

only galaxy orientations, thereby removing the need to calibrate the shapes of galaxies.

The plausibility of this approach was demonstrated using both simulations and the data from the CFHTLenS. We found that the angle-only method can potentially yield shear estimates with a performance comparable to the standard full ellipticity approach.

To recover position angle-only shear estimates, one requires an accurate knowledge of the intrinsic ellipticity distribution. We placed constraints on the accuracy required in Chapter 3. In Chapter 4, we used `IM3SHAPE` to measure the distribution from the deep calibration images of the GREAT3 simulations. The angle-only estimator was then successfully applied to the GREAT3 challenge data, and we demonstrated a performance comparable with current state-of-the-art shape measurement techniques.

Three separate methods were used to measure the position angles of the galaxies when analyzing the GREAT3 data. The integrated light method was introduced in Chapter 3. This approach involves integrating over the radial component of the intensity profile and uses this distribution to estimate the position angles. The moments based method calculates the position angles using the quadrupole moments defined by Blandford et al. (1991) and discussed in Chapter 2. The third method calculated the position angles using the ellipticities measured by `IM3SHAPE`. We found that all three methods yield results with a similar performance. It is expected that the systematics from the three approaches, which treat the light profile differently, will not be significantly correlated. If this is the case, it could be beneficial to combine two different approaches to mitigate systematics when using the angle-only method to estimate shear correlation functions in future surveys. Also, systematics in shear estimates arising from the modulus component when using full ellipticity information will not correlate with systematics in angle-only shear estimates. Hence, the angle-only method could be complimentary to current and future high precision shape based weak lensing analyses. In particular, the integrated light method provides independent measurements of the position angles. Therefore, it should be advantageous to combine angle-only shear estimates using the integrated light method with shape based shear estimates using

either moments or model based approaches.

When applying angle-only estimators to the GREAT3 challenge data, we focused on the ground based constant shear and constant PSF branch. Naturally, we hope to extend the angle-only estimator in future work to include variable shear and contributions from a variable PSF. Calibrating for a variable anisotropic PSF (variable isotropic PSFs are not a problem for the angle-only method) may be possible by modifying the weighting scheme adopted for the GREAT3 analysis to include the position of a galaxy on the sky, in addition to measured orientation. However, the weighting scheme employed for the GREAT3 challenge relies heavily on calibration simulations and, in future work, we would also like to reduce this dependence.

Reducing the systematics in estimates of the shear is vital if one is to utilize the precision of future surveys, such as those conducted with Euclid. Euclid is a space-based mission which aims to cover 15,000 square degrees and provide shape measurements of galaxies out to a redshift of $z \approx 2$. The goal is to probe the nature of dark energy and dark matter, and anticipate the future of the local Universe over the next 10 billion years. For such high precision surveys, the difference between the systematics in shape and angle-only shear estimates may be exploited to greatly increase the constraining power of weak lensing analyses.

The Large Synoptic Survey Telescope (LSST) (LSST Dark Energy Science Collaboration 2012) is a ground based telescope currently under construction in Chile. The main planned survey will cover 18,000 square degrees at a depth of $r \sim 27.5$, with the aim of determining the properties of dark energy and dark matter. The survey is expected to contain a large number of barely resolved galaxy images. Estimating the shapes of barely resolved galaxies is problematic. However, it is expected that estimates of the shear using position angles will be less susceptible to the effects of low resolution, provided that one corrects for PSF anisotropy and pixelization using, for example, the weighting scheme applied to the GREAT3 simulations in Chapter 4. One may also apply the angle-only estimator to data from present day surveys such as the Kilo-Degree Survey (KiDS) (de Jong et al. 2013; Kuijken et al. 2015) and the

Subaru Hyper Suprime-Cam survey (HSC) (Takada 2010), either as a stand alone estimator or as a complimentary approach to shape based methods, so as to mitigate the multiplicative effects of smearing.

The intrinsic alignment (IA) of the source galaxies is one example of an astrophysical systematic. IA mimics a shear signal and therefore biases the shear correlation functions. In Chapter 5, we developed three methods to include polarization information from radio observations in estimates of the shear. The integrated polarization position angle is unaffected by gravitational lensing and can be used to estimate a galaxy's intrinsic position angle. We showed that with this information, we can mitigate the contribution of IA when reconstructing estimates of the shear power spectra. We also showed that we can successfully recover estimates of the IA auto-power spectra and the IA-shear cross-power spectra.

The first of the three methods developed was a corrected version of the original estimator proposed by Brown & Battye (2011b). This estimator was modified to include a correction for the noise bias arising from measurement errors on the intrinsic position angles. The second was an extension of the angle-only estimator, introduced in Chapters 3 and 4, to include the intrinsic orientation information. The third method was a hybrid of the standard full ellipticity approach and the angle-only estimator; where the angle-only method was used to recover a direct estimate of the IA signal. All three methods were successful in removing the IA contaminant from the shear power spectra reconstructions, and the angle-only IA estimator was shown to provide reliable estimates of the IA signal using only the radio polarization information.

The work presented in Chapter 5 has the potential to mitigate the effects of intrinsic alignments in future high precision radio surveys, such as those conducted by the SKA. The SKA is a proposed radio interferometer with a collecting area equal to one square kilometer. The science goals of the SKA include tests of General Relativity, mapping the large scale structure of the Universe and placing constraints on dark energy and general cosmology. Weak lensing in the radio is still in its infancy. However, the extra information that comes from polarization implies that radio weak lensing has

the potential to increase the constraining power of surveys conducted by the SKA and other future radio telescopes. With the high number densities of galaxies expected in future radio surveys, it is hoped that the techniques discussed in Chapter 5 can be used to probe high redshift regions of the Universe currently inaccessible to weak lensing (Brown et al. 2015). Information from high redshifts can provide tighter constraints on the nature of dark energy. However, the unwanted GI terms in the shear correlation functions are expected to be larger when cross-correlating signals separated by large redshifts. The IA mitigation schemes presented in this thesis provide a way of removing this effect so that the the full potential of such a survey can be achieved. The cross-correlation of high precision optical and radio weak lensing surveys, such as those using Euclid with those using the SKA, also presents an exciting opportunity as the systematics from the two telescopes are expected to be uncorrelated.

The angle-only IA estimator introduced in Chapter 5 presents another exciting prospect. The IA signal has a dependency on the formation environment and shared histories of the galaxies. Measuring the IA signal directly, using radio polarization observations, for example, can therefore provide information on the physics of galaxy formation and evolution, and an insight into the evolution of the large scale structure of the Universe (Joachimi et al. 2013; Kirk et al. 2015).

Appendix A

Deriving the $F_1\left(|\boldsymbol{g}|\right)$ function

Here we derive the $F_1\left(\boldsymbol{g}\right)$ function, which is introduced in Chapter 3.

The observed position angle of a galaxy is α, and the shear position angle is α_0. Let us define ψ as the difference between these two angles, such that for the $i^{\rm th}$ galaxy

$$\psi^{(i)} = \alpha^{(i)} - \alpha_0. \tag{A.1}$$

The angle ψ depends on both the shear and intrinsic ellipticity of the galaxy. Assuming that the intrinsic orientations of the galaxies in the sample are drawn from a uniform distribution, the angle ψ is distributed symmetrically about zero. The expectation values of the sines and cosines of α can therefore be written as

$$\begin{aligned}\left\langle\cos\left(2\alpha\right)\right\rangle &= \left\langle\cos\left(2\psi + 2\alpha_0\right)\right\rangle, \\ &= \left\langle\cos\left(2\psi\right)\right\rangle\cos\left(2\alpha_0\right) - \left\langle\sin\left(2\psi\right)\right\rangle\sin\left(2\alpha_0\right), \\ &= \left\langle\cos\left(2\psi\right)\right\rangle\cos\left(2\alpha_0\right),\end{aligned} \tag{A.2}$$

$$\begin{aligned}\left\langle\sin\left(2\alpha\right)\right\rangle &= \left\langle\sin\left(2\psi + 2\alpha_0\right)\right\rangle, \\ &= \left\langle\cos\left(2\psi\right)\right\rangle\sin\left(2\alpha_0\right) + \left\langle\sin\left(2\psi\right)\right\rangle\cos\left(2\alpha_0\right), \\ &= \left\langle\cos\left(2\psi\right)\right\rangle\sin\left(2\alpha_0\right),\end{aligned} \tag{A.3}$$

where the term $\langle \sin(2\psi) \rangle$ is zero due to the distribution of ψ being symmetric about zero. Hence, we see that the means of the trigonometric functions trace the shear trigonometric functions subject to the scale factor $\langle \cos(2\psi) \rangle$. For an individual galaxy, ψ is a function of the orientation of the shear, the modulus of the shear and the vector $\boldsymbol{\epsilon}^{\rm int}$. However, as the intrinsic position angles of the galaxies are drawn randomly from a uniform distribution, $\langle \cos(2\psi) \rangle$ is a function of $|\boldsymbol{g}|$ only, with the form of the function depending on the intrinsic ellipticity distribution, $f\left(\left|\boldsymbol{\epsilon}^{\rm int}\right|\right)$. Let us define $F_1(|\boldsymbol{g}|) \equiv \langle \cos(2\psi) \rangle$.

The observed ellipticity of a galaxy is

$$\boldsymbol{\epsilon}^{\rm obs} = \frac{\boldsymbol{\epsilon}^{\rm int} + \boldsymbol{g}}{1 + \boldsymbol{g}^* \boldsymbol{\epsilon}^{\rm int}}. \tag{A.4}$$

As the $F_1(|\boldsymbol{g}|)$ function is independent of the shear position angle, let us focus on the case where $g_1 = |\boldsymbol{g}|$ and $g_2 = 0$. In this case,

$$\begin{aligned} \langle \cos(2\alpha) \rangle =& F_1(|\boldsymbol{g}|), \\ \langle \sin(2\alpha) \rangle =& 0, \end{aligned} \tag{A.5}$$

and equation(A.4) can be written in component form as

$$\begin{aligned} \epsilon_1^{\rm obs} =& \frac{|\boldsymbol{g}| \left(1 + \left|\boldsymbol{\epsilon}^{\rm int}\right|^2\right) + \left(1 + |\boldsymbol{g}|^2\right) \left|\boldsymbol{\epsilon}^{\rm int}\right| \cos\left(2\alpha^{\rm int}\right)}{1 + |\boldsymbol{g}|^2 \left|\boldsymbol{\epsilon}^{\rm int}\right|^2 + 2 |\boldsymbol{g}| \epsilon_1^{\rm int}}, \\ \epsilon_2^{\rm obs} =& \frac{\left(1 - |\boldsymbol{g}|^2\right) \left|\boldsymbol{\epsilon}^{\rm int}\right| \sin\left(2\alpha^{\rm int}\right)}{1 + |\boldsymbol{g}|^2 \left|\boldsymbol{\epsilon}^{\rm int}\right|^2 + 2 |\boldsymbol{g}| \epsilon_1^{\rm int}}, \end{aligned} \tag{A.6}$$

where the denominators are identical for both components. We define the numerators on the RHS of equation (A.6) as

$$\begin{aligned} \epsilon_1' =& |\boldsymbol{g}| \left(1 + \left|\boldsymbol{\epsilon}^{\rm int}\right|^2\right) + \left(1 + |\boldsymbol{g}|^2\right) \left|\boldsymbol{\epsilon}^{\rm int}\right| \cos\left(2\alpha^{\rm int}\right), \\ \epsilon_2' =& \left(1 - |\boldsymbol{g}|^2\right) \left|\boldsymbol{\epsilon}^{\rm int}\right| \sin\left(2\alpha^{\rm int}\right). \end{aligned} \tag{A.7}$$

The cosine of the observed position angle is then

$$\cos\left(2\alpha\right) = \frac{\epsilon_1'}{\sqrt{\epsilon_1'^2 + \epsilon_2'^2}}, \tag{A.8}$$

which is a function of $|\boldsymbol{g}|$, $\left|\boldsymbol{\epsilon}^{\rm int}\right|$ and $\alpha^{\rm int}$. We define

$$h_1\left(|\boldsymbol{g}|, \left|\boldsymbol{\epsilon}^{\rm int}\right|, \alpha^{\rm int}\right) \equiv \frac{\epsilon_1'}{\sqrt{\epsilon_1'^2 + \epsilon_2'^2}}. \tag{A.9}$$

From equation (A.5), the $F_1\left(|\boldsymbol{g}|\right)$ function can now be calculated as the mean of $h_1\left(|\boldsymbol{g}|, \left|\boldsymbol{\epsilon}^{\rm int}\right|, \alpha^{\rm int}\right)$ over the 2D distribution of the intrinsic ellipticities. Assuming that the distribution of $\alpha^{\rm int}$ is uniform, the $F_1\left(|\boldsymbol{g}|\right)$ function is therefore

$$\begin{aligned} F_1\left(|\boldsymbol{g}|\right) = \frac{1}{\pi} \int_0^{\left|\boldsymbol{\epsilon}^{\rm int}_{\rm max}\right|} \int_{-\frac{\pi}{2}}^{\frac{\pi}{2}} {\rm d}\alpha^{\rm int} {\rm d}\left|\boldsymbol{\epsilon}^{\rm int}\right| f\left(\left|\boldsymbol{\epsilon}^{\rm int}\right|\right) \\ \times h_1\left(|\boldsymbol{g}|, \left|\boldsymbol{\epsilon}^{\rm int}\right|, \alpha^{\rm int}\right). \end{aligned} \tag{A.10}$$

Appendix B

Including a variable σ_α

Assuming that the measurement errors are independent of the position angles and symmetrically distributed about zero, we derive the bias correction introduced in Chapter 3 for a general distribution of measurement errors.

We begin by writing the measured position angle as $\hat{\alpha} = \alpha + \delta\alpha$, where $\delta\alpha$ is a random measurement error. Assuming that this error is independent of α, we can write the mean unit vector components as

$$\begin{aligned} \langle \cos(2\hat{\alpha}) \rangle &= \langle \cos(2\alpha) \rangle \langle \cos(2\delta\alpha) \rangle - \langle \sin(2\alpha) \rangle \langle \sin(2\delta\alpha) \rangle , \\ \langle \sin(2\hat{\alpha}) \rangle &= \langle \sin(2\alpha) \rangle \langle \cos(2\delta\alpha) \rangle + \langle \cos(2\alpha) \rangle \langle \sin(2\delta\alpha) \rangle . \end{aligned} \tag{B.1}$$

Making the further assumption that $\delta\alpha$ is distributed symmetrically about zero, we obtain a relation between the mean measured unit vector components and the corrected unit vector components

$$\langle \boldsymbol{n} \rangle = \langle \boldsymbol{n} \rangle^{\text{corrected}} \langle \cos(2\delta\alpha) \rangle . \tag{B.2}$$

In practice the distribution of $\delta\alpha$ may be different for each galaxy, and therefore one would need to determine the multiplicative factor for the i^{th} galaxy, $\langle \cos(2\delta\alpha) \rangle_i$. If

we define the overall correction term, β_2, where

$$\langle \boldsymbol{n} \rangle^{\text{corrected}} = \frac{\langle \boldsymbol{n} \rangle}{\beta_2}, \tag{B.3}$$

we can determine β_2 by finding the mean of the individual multiplicative factors, $\langle \cos(2\delta\alpha) \rangle_i$, such that

$$\beta_2 = \frac{1}{N} \sum_{i=1}^{N} \langle \cos(2\delta) \rangle_i \,. \tag{B.4}$$

As an example, let us assume that the measurement errors are Gaussian distributed and that the variance on the error distribution for the i^{th} galaxy is $\sigma^2_{\alpha,i}$, then the mean unit vector becomes

$$\begin{aligned} \langle \boldsymbol{n} \rangle &= \langle \boldsymbol{n} \rangle^{\text{corrected}} \langle \cos(2\delta\alpha) \rangle \\ &= \langle \boldsymbol{n} \rangle^{\text{corrected}} \int \mathrm{d}\sigma_\alpha f(\sigma_\alpha) \exp\left(-2\sigma_\alpha^2\right), \end{aligned} \tag{B.5}$$

where $f(\sigma_\alpha)$ is the probability density function of σ_α. If we now make the further assumption that σ_α is Gaussian distributed about the mean error, $\bar{\sigma}_\alpha$, with a variance of $\sigma^2_{\sigma_\alpha}$, it can be shown that the corrected mean unit vector becomes

$$\langle \boldsymbol{n} \rangle^{\text{corrected}} = \langle \boldsymbol{n} \rangle \exp\left(\frac{2\bar{\sigma}_\alpha^2}{1+4\sigma^2_{\sigma_\alpha}}\right) \sqrt{1+4\sigma^2_{\sigma_\alpha}}, \tag{B.6}$$

such that the correction term is

$$\beta_2 = \frac{\exp\left(\frac{-2\bar{\sigma}_\alpha^2}{1+4\sigma^2_{\sigma_\alpha}}\right)}{\sqrt{1+4\sigma^2_{\sigma_\alpha}}}. \tag{B.7}$$

The correction due to a distribution in σ_α can therefore be attributed to an effective correction. This indicates that the distribution in errors can be viewed as a single Gaussian distribution which, for this case, has a variance of

$$\sigma_\alpha^2 = \frac{\bar{\sigma}^2}{1+4\sigma^2_{\sigma_\alpha}} + \frac{1}{4}\ln\left(1+4\sigma^2_{\sigma_\alpha}\right). \tag{B.8}$$

Appendix C

Deriving the 3rd order estimator

Here we construct a 3rd order angle-only shear estimator for the case of a general intrinsic ellipticity distribution. In order to obtain a direct estimator in the general case, one can numerically obtain the $F_1(|\boldsymbol{g}|)$ function that corresponds to a given intrinsic distribution, $f\left(\left|\boldsymbol{\epsilon}^{\rm int}\right|\right)$, by using equation (3.8). Assuming that the shear is much smaller than the dispersion in the intrinsic ellipticities, we can expand the $F_1(|\boldsymbol{g}|)$ function in powers of $|\boldsymbol{g}|$. For a zero shear signal there will be no preferred position angle so that $F_1(|\boldsymbol{g}|) \rightarrow 0$ as $|\boldsymbol{g}| \rightarrow 0$. We can therefore write an approximate form of the $F_1(|\boldsymbol{g}|)$ function as

$$F_1(|\boldsymbol{g}|) \approx u\,|\boldsymbol{g}| + v\,|\boldsymbol{g}|^2 + w\,|\boldsymbol{g}|^3\,, \tag{C.1}$$

for some u, v, w. We can fit the approximate form of the $F_1(|\boldsymbol{g}|)$ function to a numerically determined function.

From the measured position angles in a given pixel, we can estimate the value of $F_1(|\boldsymbol{g}|)$ such that

$$\hat{F}_1 = \sqrt{\left[\frac{1}{N}\sum_{i=1}^{N}\cos\left(2\alpha^{(i)}\right)\right]^2 + \left[\frac{1}{N}\sum_{i=1}^{N}\sin\left(2\alpha^{(i)}\right)\right]^2}\,. \tag{C.2}$$

By equating this expression with the right hand side of equation (C.1), we can obtain

an estimate of $|\boldsymbol{g}|$ which satisfies the condition

$$u\,|\hat{\boldsymbol{g}}| + v\,|\hat{\boldsymbol{g}}|^2 + w\,|\hat{\boldsymbol{g}}|^3 - \hat{F}_1 = 0. \tag{C.3}$$

Solutions of this equation are obtained from the general solution for the roots of a 3rd order polynomial, which is

$$\begin{aligned} |\hat{\boldsymbol{g}}| = &\left\{ q + \left[q^2 + \left(r - p^2 \right)^3 \right]^{\frac{1}{2}} \right\}^{\frac{1}{3}} + \\ &\left\{ q - \left[q^2 + \left(r - p^2 \right)^3 \right]^{\frac{1}{2}} \right\}^{\frac{1}{3}} + p, \end{aligned} \tag{C.4}$$

where

$$\begin{aligned} p =& -\frac{v}{3w}, \\ q =& \frac{\hat{F}_1}{2w} + \frac{uv}{6w^2} - \frac{v^3}{27w^3}, \\ r =& \frac{u}{3w}. \end{aligned} \tag{C.5}$$

Let us now consider the case where $q^2 + \left(r - p^2 \right)^3 < 0$. In this case, we can rewrite equation (C.4) as

$$\begin{aligned} |\hat{\boldsymbol{g}}| = &\left\{ q + i \left[\left(p^2 - r \right)^3 - q^2 \right]^{\frac{1}{2}} \right\}^{\frac{1}{3}} + \\ &\left\{ q - i \left[\left(p^2 - r \right)^3 - q^2 \right]^{\frac{1}{2}} \right\}^{\frac{1}{3}} + p. \end{aligned} \tag{C.6}$$

However, $|\boldsymbol{g}|$ must be a real solution of equation (C.3). Therefore, we can immediately assume the form of the solution to be

$$|\hat{\boldsymbol{g}}| = 2B_0^{\frac{1}{6}} \cos\left[\frac{1}{3} \tan^{-1}\left(\frac{\sqrt{B_1}}{A} \right) + \frac{2n\pi}{3} \right] - \frac{v}{3w}, \tag{C.7}$$

where $n = -1, 0, 1$ and

$$\begin{aligned} A =& q, \\ B_k =& \left(p^2 - r\right)^3 - kq^2. \end{aligned} \tag{C.8}$$

The specific choice of n is dependent on the form of the $F_1\left(|\boldsymbol{g}|\right)$ function, but it will always be the value of n which minimizes the absolute value of the cosine term in equation (C.7). In all of the simulations that we have conducted, we find that $n = -1$.

Let us now examine the case where $q^2 + \left(r - p^2\right)^3 \geq 0$. In such a case, $|\hat{\boldsymbol{g}}|$ can be obtained directly from equation (C.4), that is

$$|\hat{\boldsymbol{g}}| = \left(\sqrt{-B_1} + A\right)^{\frac{1}{3}} - \left(\sqrt{-B_1} - A\right)^{\frac{1}{3}} - \frac{v}{3w}, \tag{C.9}$$

which can have only one real solution.

An estimate for the orientation of the shear is obtained from equation (3.22), such that

$$2\alpha_0 = \tan^{-1}\left(\frac{\sum_{i=1}^{N} \sin\left(2\alpha^{(i)}\right)}{\sum_{i=1}^{N} \cos\left(2\alpha^{(i)}\right)}\right). \tag{C.10}$$

By taking the cosine and sine of equation (C.10) and dividing through by N, it can be shown that the estimated shear unit vector $\hat{\boldsymbol{n}}_0$ can be written as

$$\hat{\boldsymbol{n}}_0 = \frac{1}{\hat{F}_1}\begin{pmatrix} \frac{1}{N}\sum_{i=1}^{N} \cos\left(2\alpha^{(i)}\right) \\ \frac{1}{N}\sum_{i=1}^{N} \sin\left(2\alpha^{(i)}\right) \end{pmatrix}. \tag{C.11}$$

The full 3rd order estimator is then

$$\hat{\boldsymbol{g}} = |\hat{\boldsymbol{g}}|\, \hat{\boldsymbol{n}}_0. \tag{C.12}$$

If we assume a measurement error on the position angles which is independent of the true position angles and drawn from a distribution which is symmetric about zero, then we can correct for the measurement error bias using equation (3.29). It can be

shown that to correct the third order estimator we only need to modify the term q in equation (C.5) such that

$$q = \frac{\hat{F}_1}{2w\beta_2} + \frac{uv}{6w^2} - \frac{v^3}{27w^3}. \tag{C.13}$$

For a more general error distribution, we must use the form of the cosines and sines given in equation (3.51) which may be determined using an iterative method as outlined in Subsections 3.3.3 and 3.3.4.

Appendix D

Residual bias in the iterative method

For the iterative method used in Chapter 4, we derive the residual bias in the shear estimates as a function of the number of iterations used.

If we assume the zeroth-order shear estimate can be written as equation (4.13), the first-order iteration gives the shear estimate as

$$\begin{aligned}\hat{g}_j^{(1)} =& \hat{g}_j^{(0)} - \left(\hat{g}_{j,\mathrm{sim}}^{(1)} - \hat{g}_j^{(0)}\right), \\ =& \hat{g}_j^{(0)} - m'_j\hat{g}_j^{(0)} - c'_j + \delta g_j^{(1)}.\end{aligned} \tag{D.1}$$

We can substitute equation (4.13) into equation (D.1), giving

$$\hat{g}_j^{(1)} = g_j - m'_j\left(m'_j g_j + c'_j\right) + \left(1 - m'_j\right)\delta g_j^{(0)} + \delta g_j^{(1)}. \tag{D.2}$$

The second iteration yields

$$\begin{aligned}\hat{g}_j^{(2)} =& \hat{g}_j^{(0)} - m'_j\hat{g}_j^{(1)} - c'_j + \delta g_j^{(2)}, \\ =& g_j + m_j'^2\left(m'_j g_j + c'_j\right) + \left[1 - m'_j\left(1 - m'_j\right)\right]\delta g_j^{(0)} \\ & - m'_j\delta g_j^{(1)} + \delta g_j^{(2)}.\end{aligned} \tag{D.3}$$

From here, we see that the error terms propagate linearly through the iterations. Hence, as the mean of these terms is zero, there will be no residual bias contribution from these terms. If we ignore the noise terms, we see that the shear estimate from the $n^{\rm th}$ iteration can be written as

$$\hat{g}_j^{(n)} = g_j + \left(-m'_j\right)^n \left(m'_j g_j + c'_j\right), \tag{D.4}$$

and therefore the bias on the $n^{\rm th}$ iteration is

$$\left\langle \hat{g}_j^{(n)} - g_j \right\rangle = \left(-m'_j\right)^n \left(m'_j g_j + c'_j\right). \tag{D.5}$$

Appendix E

Error on the first iteration

We discuss the first-order approximation of the error on the angle-only shear estimates using one iteration of the weighting procedure discussed in Chapter 4. For each galaxy in the field, we assume that there is an identical galaxy with the intrinsic ellipticity rotated by 90°.

Let us begin by assuming a first-order approximation of the $F_1\left(|\boldsymbol{g}|\right)$ function (discussed in Chapter 3), such that

$$F_1\left(|\boldsymbol{g}|\right) \approx u\,|\boldsymbol{g}|\,, \tag{E.1}$$

where u is the first-order coefficient. We write the measured position angle of a galaxy as $\hat{\alpha} = \alpha + \delta\alpha$, where $\delta\alpha$ is an error on the measurement which we assume to be distributed symmetrically about zero. The zeroth-order estimate, $\hat{g}_1^{(0)}$ (with a similar analysis also holding for $\hat{g}_2^{(0)}$), can then be written as an average over the galaxy pairs

$$\begin{aligned}\hat{g}_1^{(0)} \approx & \frac{1}{u}\sum_{i=1}^{\frac{N}{2}}\Bigg[\bar{w}_i\left(\alpha_i + \delta\alpha_i^{(1)}\right)\cos\left(2\alpha_i + 2\delta\alpha_i^{(1)}\right) \\ & + \bar{w}_i\left(\alpha_i + \frac{\pi}{2} + \delta\alpha_i^{(2)}\right)\cos\left(2\alpha_i + \pi + 2\delta\alpha_i^{(2)}\right)\Bigg],\end{aligned} \tag{E.2}$$

where there are $N/2$ galaxy pairs, and where $\delta\alpha_i^{(1)}$ is the error on the position angle

of the first galaxy in the pair and $\delta\alpha_i^{(2)}$ is the error on the position angle of the corresponding 90° rotated galaxy. The weighting function $\bar{w}\left(\alpha_i\right)$ is normalized and given as

$$\bar{w}\left(\alpha_i\right) = \frac{w\left(\alpha_i\right)}{\sum_{i=1}^{N} w\left(\alpha_i\right)}, \tag{E.3}$$

where the summation is over all galaxies in the field.

From this form of the estimator, we can write an approximate form for the error on the zeroth-order estimate in the limit $\boldsymbol{g} \rightarrow 0$ as

$$\begin{aligned}\sigma^2_{\hat{g}_1^{(0)}} \approx & \frac{N}{2u^2}\Bigg\langle\Bigg[\bar{w}^{(1)}\cos\left(2\alpha + 2\delta\alpha^{(1)}\right) \\ & + \bar{w}^{(2)}\cos\left(2\alpha + \pi + 2\delta\alpha^{(2)}\right)\Bigg]^2\Bigg\rangle, \\ \approx & \frac{1}{2u^2}\left(\sum_{i=1}^{N}\left(\bar{w}\left(\alpha_i\right)\right)^2 - \frac{1}{N}\beta^2_{\mathrm{wc}}\right),\end{aligned} \tag{E.4}$$

where β_{wc} is the weighted mean cosine of the error distribution,

$$\beta_{\mathrm{wc}} = \sum_{i=1}^{N}\bar{w}\left(\hat{\alpha}_i\right)\cos\left(2\delta\alpha_i\right). \tag{E.5}$$

We have assumed that the weighting scheme has successfully removed all contributions from an additive bias. From this approach we find that $\sigma_{\hat{g}_1^{(0)}} \approx \sigma_{\hat{g}_2^{(0)}} \equiv \sigma_{\hat{\boldsymbol{g}}^{(0)}}$. A similar approach can be applied to the errors on the shear estimates recovered from the first iteration simulations but with the number of galaxies being dependent on the number of galaxies in the simulations; for our analyses we simulated $N_{\mathrm{sim}} = 10^5$ galaxies as discussed in Section 4.3. The error on the first iteration of the shear estimator can then be found by looking at equation (D.2) where the error on the zeroth-order shear estimate, $\hat{g_1}^{(0)}$, is $\delta g_1^{(0)}$ (as defined in equation (4.13)), and the error on the estimate from the first-order simulations, $\hat{g}^{(1)}_{1,\mathrm{sim}}$, is $\delta g_1^{(1)}$ (as defined in equation (4.15)). Assuming that the errors on the shear estimates are Gaussian (which is expected to be true to first-order in the shear due to the central limit theorem), the error on the first-order

shear estimate is

$$\sigma^2_{\boldsymbol{g}} \approx (1 - m')^2 \, \sigma^2_{\hat{\boldsymbol{g}}^{(0)}} + \sigma^2_{\hat{\boldsymbol{g}}^{(1)}}, \tag{E.6}$$

where $\sigma^2_{\hat{\boldsymbol{g}}^{(0)}} \equiv \left\langle \delta g_1^{(0)^2} \right\rangle$ and $\sigma^2_{\hat{\boldsymbol{g}}^{(1)}} \equiv \left\langle \delta g_1^{(1)^2} \right\rangle$. In the absence of an additive bias, the multiplicative bias is effectively due to the β_c term in equation (3.50). However, when using weighted trigonometric functions $\beta_c = \beta_{\rm wc}$, such that $m' = \beta_{\rm wc} - 1$.

Appendix F

Correcting the Brown & Battye estimator

In this section, we discuss the correction to the BB estimator.

We begin by redefining the matrix $\mathbf{A}$ as

$$\mathbf{A} = \frac{2\beta_4^{\rm int}}{N} \sum_{i=1}^{N} w_i \hat{\boldsymbol{n}}_i \hat{\boldsymbol{n}}_i^T, \tag{F.1}$$

and the vector $\boldsymbol{b}$ as

$$\boldsymbol{b} = \frac{2\beta_4^{\rm int}}{N} \sum_{i=1}^{N} w_i \left(\boldsymbol{\epsilon}_i^{\rm obs} \cdot \hat{\boldsymbol{n}}_i\right) \hat{\boldsymbol{n}}_i, \tag{F.2}$$

where the definition of the vector $\hat{\boldsymbol{n}}_i$ is given in equation (5.7) and where w_i is a normalized arbitrary weight assigned to each galaxy. In the limit $N \to \infty$, the matrix $\mathbf{A}$ can be written as

$$\mathbf{A} = \beta_4^{\rm int} \begin{pmatrix} 1 - \left\langle \cos\left(4\hat{\alpha}^{\rm int}\right)\right\rangle & -\left\langle \sin\left(4\hat{\alpha}^{\rm int}\right)\right\rangle \\ -\left\langle \sin\left(4\hat{\alpha}^{\rm int}\right)\right\rangle & 1 + \left\langle \cos\left(4\hat{\alpha}^{\rm int}\right)\right\rangle \end{pmatrix}, \tag{F.3}$$

and the vector $\boldsymbol{b}$ can be written as

$$\boldsymbol{b} = \beta_4^{\rm int} \begin{pmatrix} \left\langle \epsilon_1^{\rm obs} \left[1 - \cos\left(4\hat{\alpha}^{\rm int}\right)\right]\right\rangle - \left\langle \epsilon_2^{\rm obs} \sin\left(4\hat{\alpha}^{\rm int}\right)\right\rangle \\ \left\langle \epsilon_2^{\rm obs} \left[1 + \cos\left(4\hat{\alpha}^{\rm int}\right)\right]\right\rangle - \left\langle \epsilon_1^{\rm obs} \sin\left(4\hat{\alpha}^{\rm int}\right)\right\rangle \end{pmatrix}. \tag{F.4}$$

In the presence of noise on the estimates of $\alpha^{\rm int}$, the trigonometric functions above will be biased. This bias can be corrected for by dividing the functions by the correction term $\beta_4^{\rm int}$, as defined in equation (5.14), such that the corrected matrix $\mathbf{A}$ can be written as

$$\mathbf{A} = \begin{pmatrix} \beta_4^{\rm int} - \left\langle \cos\left(4\hat{\alpha}^{\rm int}\right)\right\rangle & -\left\langle \sin\left(4\hat{\alpha}^{\rm int}\right)\right\rangle \\ -\left\langle \sin\left(4\hat{\alpha}^{\rm int}\right)\right\rangle & \beta_4^{\rm int} + \left\langle \cos\left(4\hat{\alpha}^{\rm int}\right)\right\rangle \end{pmatrix}, \tag{F.5}$$

and the corrected vector $\boldsymbol{b}$ becomes

$$\boldsymbol{b} = \begin{pmatrix} \left\langle \epsilon_1^{\rm obs} \left[\beta_4^{\rm int} - \cos\left(4\hat{\alpha}^{\rm int}\right)\right]\right\rangle - \left\langle \epsilon_2^{\rm obs} \sin\left(4\hat{\alpha}^{\rm int}\right)\right\rangle \\ \left\langle \epsilon_2^{\rm obs} \left[\beta_4^{\rm int} + \cos\left(4\hat{\alpha}^{\rm int}\right)\right]\right\rangle - \left\langle \epsilon_1^{\rm obs} \sin\left(4\hat{\alpha}^{\rm int}\right)\right\rangle \end{pmatrix}. \tag{F.6}$$

The CBB estimator can then be written more concisely by defining the matrix $\mathbf{M}_i$, where

$$\mathbf{M}_i = \begin{pmatrix} \beta_4^{\rm int} - \cos\left(4\hat{\alpha}_i^{\rm int}\right) & -\sin\left(4\hat{\alpha}_i^{\rm int}\right) \\ -\sin\left(4\hat{\alpha}_i^{\rm int}\right) & \beta_4^{\rm int} + \cos\left(4\hat{\alpha}_i^{\rm int}\right) \end{pmatrix}, \tag{F.7}$$

such that the final form of the estimator can be written as described by equations (5.22) - (5.24).

Appendix G

Details of the FAO estimator

Here we present the details of the $F_1\left(\left|\boldsymbol{\gamma}^{\mathrm{IA}}\right|\right)$ function and the bias corrections β_2^{int} and β_2^{obs}.

Following the approach outlined in Chapter 3, we can recover an estimate of $\left|\boldsymbol{\gamma}^{\mathrm{IA}}\right|$ using measurements of α^{int}, which satisfies the equation

$$F_1\left(\left|\hat{\boldsymbol{\gamma}}^{\mathrm{IA}}\right|\right) = \frac{1}{N}\sqrt{\left(\sum_{i=1}^{N}\cos\left(2\hat{\alpha}_i^{\mathrm{int}}\right)\right)^2 + \left(\sum_{i=1}^{N}\sin\left(2\hat{\alpha}_i^{\mathrm{int}}\right)\right)^2}. \tag{G.1}$$

The $F_1\left(|\boldsymbol{\gamma}|\right)$ function depends on the distribution $f\left(|\boldsymbol{\epsilon}^{\mathrm{ran}}|\right)$ and is found to be

$$\begin{aligned} F_1\left(\left|\boldsymbol{\gamma}^{\mathrm{IA}}\right|\right) =& \frac{1}{\pi}\int_0^{|\boldsymbol{\epsilon}^{\mathrm{ran}}_{\mathrm{max}}|}\int_{-\frac{\pi}{2}}^{\frac{\pi}{2}} \mathrm{d}\alpha^{\mathrm{ran}}\mathrm{d}\left|\boldsymbol{\epsilon}^{\mathrm{ran}}\right| f\left(|\boldsymbol{\epsilon}^{\mathrm{ran}}|\right) \\ & \times h_1\left(\left|\boldsymbol{\gamma}^{\mathrm{IA}}\right|, \left|\boldsymbol{\epsilon}^{\mathrm{ran}}\right|, \alpha^{\mathrm{ran}}\right), \end{aligned} \tag{G.2}$$

where the function $h_1\left(\left|\boldsymbol{\gamma}^{\mathrm{IA}}\right|, \left|\boldsymbol{\epsilon}^{\mathrm{ran}}\right|, \alpha^{\mathrm{ran}}\right)$ is given as

$$h_1\left(\left|\boldsymbol{\gamma}^{\mathrm{IA}}\right|, \left|\boldsymbol{\epsilon}^{\mathrm{ran}}\right|, \alpha^{\mathrm{ran}}\right) = \frac{\epsilon_1'^2}{\sqrt{\epsilon_1'^2 + \epsilon_2'^2}}, \tag{G.3}$$

with

$$\begin{aligned}\epsilon_1' &= \left|\boldsymbol{\gamma}^{\rm IA}\right| + |\boldsymbol{\epsilon}^{\rm ran}| \cos\left(2\alpha^{\rm ran}\right), \\ \epsilon_2' &= |\boldsymbol{\epsilon}^{\rm ran}| \sin\left(2\alpha^{\rm ran}\right).\end{aligned} \tag{G.4}$$

The forms of ϵ_1' and ϵ_2' depend on the model assumed to describe the transformation $\boldsymbol{\epsilon}^{\rm ran} \rightarrow \boldsymbol{\epsilon}^{\rm int}$. In this paper, the assumed model is given by equation (5.4).

For a non-zero measurement error on $\alpha^{\rm int}$, such that

$$\hat{\alpha}^{\rm int} = \alpha^{\rm int} + \delta\alpha^{\rm int}, \tag{G.5}$$

where $\delta\alpha^{\rm int}$ is independent of the true $\alpha^{\rm int}$, we show in Chapter 3 that estimates of $\alpha^{\rm IA}$ (equation (5.30)) remain unbiased. However, estimates of $\left|\boldsymbol{\gamma}^{\rm IA}\right|$, obtained by inverting the $F_1\left(\left|\boldsymbol{\gamma}^{\rm IA}\right|\right)$ function given in equation (G.2), become biased. The bias can be corrected for by dividing the $F_1\left(\left|\boldsymbol{\gamma}^{\rm IA}\right|\right)$ function by the correction term $\beta_2^{\rm int}$, which follows the definition given in equation (5.14):

$$F_1\left(\left|\hat{\boldsymbol{\gamma}}^{\rm IA}\right|\right) = \frac{1}{N\beta_2^{\rm int}} \sqrt{\left(\sum_{i=1}^{N} \cos\left(2\hat{\alpha}_i^{\rm int}\right)\right)^2 + \left(\sum_{i=1}^{N} \sin\left(2\hat{\alpha}_i^{\rm int}\right)\right)^2}. \tag{G.6}$$

Assuming that we are working well within the weak lensing regime, such that $\boldsymbol{\epsilon}^{\rm obs}$ can be described using equation (5.1) and ignoring measurement errors, we can express the observed ellipticity in terms of the shear and IA as

$$\boldsymbol{\epsilon}^{\rm obs} = \boldsymbol{\gamma} + \boldsymbol{\gamma}^{\rm IA} + \boldsymbol{\epsilon}^{\rm ran}. \tag{G.7}$$

Expressing the observed ellipticity in polar coordinates:

$$\begin{aligned}\epsilon_1^{\rm obs} &= \left|\boldsymbol{\epsilon}^{\rm obs}\right| \cos\left(2\alpha^{\rm obs}\right), \\ \epsilon_2^{\rm obs} &= \left|\boldsymbol{\epsilon}^{\rm obs}\right| \sin\left(2\alpha^{\rm obs}\right),\end{aligned} \tag{G.8}$$

we can follow the approach of Chapter 3 to recover estimates of the vector $\boldsymbol{\gamma} + \boldsymbol{\gamma}^{\rm IA}$ from the observed position angles. If we assume a measurement error on $\alpha^{\rm obs}$ which is independent of the true value

$$\hat{\alpha}^{\rm obs} = \alpha^{\rm obs} + \delta\alpha^{\rm obs}, \tag{G.9}$$

we can define the terms $\beta_n^{\rm obs}$ such that

$$\beta_n^{\rm obs} \equiv \left\langle \cos\left(n\delta\alpha^{\rm obs}\right)\right\rangle. \tag{G.10}$$

Upon expressing the vector $\boldsymbol{\gamma} + \boldsymbol{\gamma}^{\rm IA}$ as

$$\begin{aligned}\gamma_1 + \gamma_1^{\rm IA} &= \left|\boldsymbol{\gamma}^{\rm tot}\right| \cos\left(2\alpha^{\rm tot}\right), \\ \gamma_2 + \gamma_2^{\rm IA} &= \left|\boldsymbol{\gamma}^{\rm tot}\right| \sin\left(2\alpha^{\rm tot}\right),\end{aligned} \tag{G.11}$$

we can recover an estimate of $|\boldsymbol{\gamma}^{\rm tot}|$ which satisfies the equation

$$F_1\left(\left|\hat{\boldsymbol{\gamma}}^{\rm tot}\right|\right) = \frac{1}{N\beta_2^{\rm obs}}\sqrt{\left(\sum_{i=1}^{N}\cos\left(2\hat{\alpha}_i^{\rm obs}\right)\right)^2 + \left(\sum_{i=1}^{N}\sin\left(2\hat{\alpha}_i^{\rm obs}\right)\right)^2}. \tag{G.12}$$

The vector $\boldsymbol{\epsilon}^{\rm ran}$ given in equation (G.7) is identical to that given in equation (5.4). Therefore, the form of the $F_1\left(|\boldsymbol{\gamma}^{\rm tot}|\right)$ function given in equation (G.12) is identical to the form of the $F_1\left(\left|\boldsymbol{\gamma}^{\rm IA}\right|\right)$ function in equation (G.2) with the substitution $\left|\boldsymbol{\gamma}^{\rm IA}\right| \rightarrow |\boldsymbol{\gamma}^{\rm tot}|$. The term $\beta_2^{\rm obs}$ corrects for the bias introduced by the measurement error on $\alpha^{\rm obs}$.

References

Abazajian, K., Adelman-McCarthy, J. K., Agüeros, M. A., et al., 2003, AJ, 126, 2081, astro-ph/0305492

Ade, P. A. R., Aikin, R. W., Barkats, D., et al., 2014, Physical Review Letters, 112, 24, 241101, arXiv:1403.3985

Albrecht, A., Bernstein, G., Cahn, R., et al., 2006, ArXiv Astrophysics e-prints, arXiv:astro-ph/0609591

Allen, S. W., Evrard, A. E., Mantz, A. B., 2011, Annual Review of Astron and Astrophys, 49, 409, arXiv:1103.4829

Bacon, D. J., Refregier, A. R., Ellis, R. S., 2000, MNRAS, 318, 625, arXiv:astro-ph/0003008

Bartelmann, M., Schneider, P., 2001, Phys. Rep., 340, 291, arXiv:astro-ph/9912508

Battye, R. A., Browne, I. W. A., 2009, MNRAS, 399, 1888, arXiv:0902.1631

Battye, R. A., Browne, I. W. A., Dickinson, C., Heron, G., Maffei, B., Pourtsidou, A., 2013, MNRAS, 434, 1239, arXiv:1209.0343

Battye, R. A., Weller, J., 2003, Phys. Rev. D, 68, 8, 083506, astro-ph/0305568

Becker, M. R., Troxel, M. A., MacCrann, N., et al., 2015, ArXiv e-prints, arXiv:1507.05598

Blain, A. W., 2002, ApJL, 570, L51, astro-ph/0204138

Blandford, R. D., Saust, A. B., Brainerd, T. G., Villumsen, J. V., 1991, MNRAS, 251, 600

Brainerd, T. G., Agustsson, I., Madsen, C. A., Edmonds, J. A., 2009, ArXiv e-prints, arXiv:0904.3095

Bridle, S., Balan, S. T., Bethge, M., et al., 2010, MNRAS, 405, 2044, arXiv:0908.0945

Bridle, S., King, L., 2007, New Journal of Physics, 9, 444, arXiv:0705.0166

Bridle, S. L., Kneib, J.-P., Bardeau, S., Gull, S. F., 2002, in The Shapes of Galaxies and their Dark Halos, edited by Natarajan, P., 38–46

Brown, M. L., Bacon, D. J., Camera, S., et al., 2015, ArXiv e-prints, arXiv:1501.03828

Brown, M. L., Battye, R. A., 2011a, ApJL, 735, L23, arXiv:1101.5157

Brown, M. L., Battye, R. A., 2011b, MNRAS, 410, 2057, arXiv:1005.1926

Brown, M. L., Castro, P. G., Taylor, A. N., 2005, MNRAS, 360, 1262, arXiv:astro-ph/0410394

Brown, M. L., Taylor, A. N., Bacon, D. J., et al., 2003, MNRAS, 341, 100, arXiv:astro-ph/0210213

Brown, M. L., Taylor, A. N., Hambly, N. C., Dye, S., 2002, MNRAS, 333, 501, arXiv:astro-ph/0009499

Bull, P., Camera, S., Raccanelli, A., et al., 2015, Advancing Astrophysics with the Square Kilometre Array (AASKA14), 24, arXiv:1501.04088

Catelan, P., Kamionkowski, M., Blandford, R. D., 2001, MNRAS, 320, L7, arXiv:astro-ph/0005470

Chevallier, M., Polarski, D., 2001, International Journal of Modern Physics D, 10, 213, gr-qc/0009008

Cimatti, A., Scaramella, R., 2012, Memorie della Societa Astronomica Italiana Supplementi, 19, 314

Colless, M., Dalton, G., Maddox, S., et al., 2001, MNRAS, 328, 1039, astro-ph/0106498

Crittenden, R. G., Natarajan, P., Pen, U., Theuns, T., 2001, ApJ, 559, 552, arXiv:astro-ph/0009052

Croft, R. A. C., Metzler, C. A., 2000, ApJ, 545, 561, arXiv:astro-ph/0005384

Cunha, C., Huterer, D., Frieman, J. A., 2009, Phys. Rev. D, 80, 6, 063532, arXiv:0904.1589

Dawson, K. S., Kneib, J.-P., Percival, W. J., et al., 2015, ArXiv e-prints, arXiv:1508.04473

de Jong, J. T. A., Verdoes Kleijn, G. A., Kuijken, K. H., Valentijn, E. A., 2013, Experimental Astronomy, 35, 25, arXiv:1206.1254

D'Inverno, R., 1992, Introducing Einstein's Relativity

Dunkley, J., Hlozek, R., Sievers, J., et al., 2011, ApJ, 739, 52, arXiv:1009.0866

Dyer, C. C., Shaver, E. G., 1992, ApJL, 390, L5

Dyson, F. W., Eddington, A. S., Davidson, C., 1920, Royal Society of London Philosophical Transactions Series A, 220, 291

Eisenstein, D. J., Zehavi, I., Hogg, D. W., et al., 2005, ApJ, 633, 560, astro-ph/0501171

Erben, T., Hildebrandt, H., Miller, L., et al., 2013, MNRAS, 433, 2545, arXiv:1210.8156

Fu, L., Semboloni, E., Hoekstra, H., et al., 2008, A&A, 479, 9, arXiv:0712.0884

Giannantonio, T., Porciani, C., Carron, J., Amara, A., Pillepich, A., 2012, MNRAS, 422, 2854, arXiv:1109.0958

Guzzo, L., Pierleoni, M., Meneux, B., et al., 2008, Nature, 451, 541, arXiv:0802.1944

Haiman, Z., Mohr, J. J., Holder, G. P., 2001, ApJ, 553, 545, astro-ph/0002336

Hamilton, A. J. S., 1998, in The Evolving Universe, edited by Hamilton, D., vol. 231 of *Astrophysics and Space Science Library*, 185, astro-ph/9708102

Hartle, J. B., 2003, Gravity : an introduction to Einstein's general relativity

Heavens, A., Refregier, A., Heymans, C., 2000, MNRAS, 319, 649, arXiv:astro-ph/0005269

Herschel, W., 1786, Royal Society of London Philosophical Transactions Series I, 76, 457

Heymans, C., Brown, M., Heavens, A., Meisenheimer, K., Taylor, A., Wolf, C., 2004, MNRAS, 347, 895, arXiv:astro-ph/0310174

Heymans, C., Grocutt, E., Heavens, A., et al., 2013, MNRAS, 432, 2433, arXiv:1303.1808

Heymans, C., Van Waerbeke, L., Bacon, D., et al., 2006, MNRAS, 368, 1323, arXiv:astro-ph/0506112

Heymans, C., Van Waerbeke, L., Miller, L., et al., 2012, MNRAS, 427, 146, arXiv:1210.0032

Hinshaw, G., Larson, D., Komatsu, E., et al., 2013, ApJS, 208, 19, arXiv:1212.5226

Hirata, C. M., Mandelbaum, R., Ishak, M., et al., 2007, MNRAS, 381, 1197, arXiv:astro-ph/0701671

Hirata, C. M., Seljak, U., 2004, Phys. Rev. D, 70, 6, 063526, arXiv:astro-ph/0406275

Hivon, E., Górski, K. M., Netterfield, C. B., Crill, B. P., Prunet, S., Hansen, F., 2002, ApJ, 567, 2, arXiv:astro-ph/0105302

Hoekstra, H., Mellier, Y., van Waerbeke, L., et al., 2006, ApJ, 647, 116, arXiv:astro-ph/0511089

Hu, W., 1999, ApJL, 522, L21, astro-ph/9904153

Hubble, E., 1929, Proceedings of the National Academy of Science, 15, 168

Huff, E. M., Krause, E., Eifler, T., George, M. R., Schlegel, D., 2013, ArXiv e-prints, arXiv:1311.1489

Huterer, D., Takada, M., Bernstein, G., Jain, B., 2006, MNRAS, 366, 101, astro-ph/0506030

Jarvis, M., Sheldon, E., Zuntz, J., et al., 2015, ArXiv e-prints, arXiv:1507.05603

Jing, Y. P., 2002, MNRAS, 335, L89, arXiv:astro-ph/0206098

Joachimi, B., Mandelbaum, R., Abdalla, F. B., Bridle, S. L., 2011, A&A, 527, A26, arXiv:1008.3491

Joachimi, B., Schneider, P., 2008, A&A, 488, 829, arXiv:0804.2292

Joachimi, B., Schneider, P., 2009, A&A, 507, 105, arXiv:0905.0393

Joachimi, B., Semboloni, E., Hilbert, S., et al., 2013, MNRAS, 436, 819, arXiv:1305.5791

Kaiser, N., 1987, MNRAS, 227, 1

Kaiser, N., 1992, ApJ, 388, 272

Kaiser, N., Squires, G., 1993, ApJ, 404, 441

Kaiser, N., Squires, G., Broadhurst, T., 1995, ApJ, 449, 460, astro-ph/9411005

Kaiser, N., Wilson, G., Luppino, G. A., 2000, ArXiv Astrophysics e-prints, arXiv:astro-ph/0003338

Keisler, R., Reichardt, C. L., Aird, K. A., et al., 2011, ApJ, 743, 28, arXiv:1105.3182

Kilbinger, M., 2015, Reports on Progress in Physics, 78, 8, 086901, arXiv:1411.0115

Kilbinger, M., Fu, L., Heymans, C., et al., 2013, MNRAS, 430, 2200, arXiv:1212.3338

Kirk, D., Brown, M. L., Hoekstra, H., et al., 2015, ArXiv e-prints, arXiv:1504.05465

Kitching, T. D., Amara, A., Abdalla, F. B., Joachimi, B., Refregier, A., 2009, MNRAS, 399, 2107, arXiv:0812.1966

Kitching, T. D., Miller, L., Heymans, C. E., van Waerbeke, L., Heavens, A. F., 2008, MNRAS, 390, 149, arXiv:0802.1528

Kochanek, C. S., 1990, MNRAS, 247, 135

Komatsu, E., Smith, K. M., Dunkley, J., et al., 2011, ApJS, 192, 18, arXiv:1001.4538

Kuijken, K., 1999, A&A, 352, 355, astro-ph/9904418

Kuijken, K., Heymans, C., Hildebrandt, H., et al., 2015, MNRAS, 454, 3500, arXiv:1507.00738

Liddle, A., 2003, An Introduction to Modern Cosmology, Second Edition

Limber, D. N., 1953, ApJ, 117, 134

Linder, E. V., 2003, Physical Review Letters, 90, 9, 091301, astro-ph/0208512

Loverde, M., Afshordi, N., 2008, Phys. Rev. D, 78, 12, 123506, arXiv:0809.5112

LSST Dark Energy Science Collaboration, 2012, ArXiv e-prints, arXiv:1211.0310

Luppino, G. A., Kaiser, N., 1997, ApJ, 475, 20, astro-ph/9601194

Mackey, J., White, M., Kamionkowski, M., 2002, MNRAS, 332, 788, arXiv:astro-ph/0106364

Mandelbaum, R., Blake, C., Bridle, S., et al., 2011, MNRAS, 410, 844, arXiv:0911.5347

Mandelbaum, R., Hirata, C. M., Ishak, M., Seljak, U., Brinkmann, J., 2006, MNRAS, 367, 611, arXiv:astro-ph/0509026

Mandelbaum, R., Rowe, B., Armstrong, R., et al., 2014a, ArXiv e-prints, arXiv:1412.1825

Mandelbaum, R., Rowe, B., Bosch, J., et al., 2014b, ApJS, 212, 5, arXiv:1308.4982

Massey, R., Heymans, C., Bergé, J., et al., 2007, MNRAS, 376, 13, astro-ph/0608643

Massey, R., Hoekstra, H., Kitching, T., et al., 2013, MNRAS, 429, 661, arXiv:1210.7690

Melchior, P., Viola, M., Schäfer, B. M., Bartelmann, M., 2011, MNRAS, 412, 1552, arXiv:1008.1076

Miller, L., Heymans, C., Kitching, T. D., et al., 2013, MNRAS, 429, 2858, arXiv:1210.8201

Miller, L., Kitching, T. D., Heymans, C., Heavens, A. F., van Waerbeke, L., 2007, MNRAS, 382, 315, arXiv:0708.2340

Miralda-Escude, J., 1991, ApJ, 370, 1

Morales, M. F., 2006, ApJL, 650, L21, astro-ph/0608494

Peacock, J. A., 1999, Cosmological Physics

Peacock, J. A., Schneider, P., Efstathiou, G., et al., 2006, ESA-ESO Working Group on ”Fundamental Cosmology”, Tech. rep.

Peebles, P. J. E., 1980, The large-scale structure of the universe

Penzias, A. A., Wilson, R. W., 1965, ApJ, 142, 419

Percival, W. J., White, M., 2009, MNRAS, 393, 297, arXiv:0808.0003

Perlmutter, S., Aldering, G., Goldhaber, G., et al., 1999, ApJ, 517, 565, astro-ph/9812133

Planck Collaboration, Adam, R., Ade, P. A. R., et al., 2014, ArXiv e-prints, arXiv:1409.5738

Planck Collaboration, Ade, P. A. R., Aghanim, N., et al., 2015a, ArXiv e-prints, arXiv:1502.01589

Planck Collaboration, Ade, P. A. R., Aghanim, N., et al., 2015b, ArXiv e-prints, arXiv:1502.01597

Press, W. H., Teukolsky, S. A., Vetterling, W. T., Flannery, B. P., 1992, Numerical Recipes in C: The Art of Scientific Computing. Second Edition

Raccanelli, A., Bull, P., Camera, S., et al., 2015, Advancing Astrophysics with the Square Kilometre Array (AASKA14), 31, arXiv:1501.03821

Rapetti, D., Blake, C., Allen, S. W., Mantz, A., Parkinson, D., Beutler, F., 2013, MNRAS, 432, 973, arXiv:1205.4679

Riess, A. G., Filippenko, A. V., Challis, P., et al., 1998, AJ, 116, 1009, astro-ph/9805201

Romano, A., Fu, L., Giordano, F., et al., 2010, A&A, 514, A88, arXiv:1002.0727

Rowe, B., Jarvis, M., Mandelbaum, R., et al., 2014, ArXiv e-prints, arXiv:1407.7676

Rozo, E., Wechsler, R. H., Rykoff, E. S., et al., 2010, ApJ, 708, 645, arXiv:0902.3702

Rubin, V. C., Ford, W. K. J., . Thonnard, N., 1980, ApJ, 238, 471

Sánchez, C., Carrasco Kind, M., Lin, H., et al., 2014, MNRAS, 445, 1482, arXiv:1406.4407

Sandage, A., 1958, ApJ, 127, 513

Sargent, M. T., Carollo, C. M., Lilly, S. J., et al., 2007, ApJS, 172, 434, astro-ph/0609042

Sartoris, B., Biviano, A., Fedeli, C., et al., 2015, ArXiv e-prints, arXiv:1505.02165

Sartoris, B., Borgani, S., Rosati, P., Weller, J., 2012, MNRAS, 423, 2503, arXiv:1112.0327

Schneider, P., Seitz, C., 1995, Acta Astron., 294, 411, arXiv:astro-ph/9407032

Schrabback, T., Hartlap, J., Joachimi, B., et al., 2010, A&A, 516, A63, arXiv:0911.0053

Seitz, C., Schneider, P., 1997, A&A, 318, 687, arXiv:astro-ph/9601079

Sheldon, E. S., 2014, MNRAS, 444, L25, arXiv:1403.7669

Sifón, C., Hoekstra, H., Cacciato, M., et al., 2015, A&A, 575, A48, arXiv:1406.5196

Simon, P., 2007, A&A, 473, 711, astro-ph/0609165

Singh, S., Mandelbaum, R., More, S., 2015, MNRAS, 450, 2195, arXiv:1411.1755

Smoot, G. F., Bennett, C. L., Kogut, A., et al., 1992, ApJL, 396, L1

Springel, V., 2005, MNRAS, 364, 1105, astro-ph/0505010

Stil, J. M., Krause, M., Beck, R., Taylor, A. R., 2009, ApJ, 693, 1392, arXiv:0810.2303

Takada, M., 2010, in American Institute of Physics Conference Series, edited by Kawai, N., Nagataki, S., vol. 1279 of *American Institute of Physics Conference Series*, 120–127

The Dark Energy Survey Collaboration, 2005, ArXiv Astrophysics e-prints, astro-ph/0510346

The Dark Energy Survey Collaboration, Abbott, T., Abdalla, F. B., et al., 2015, ArXiv e-prints, arXiv:1507.05552

Troxel, M. A., Ishak, M., 2015, Phys. Rep., 558, 1, arXiv:1407.6990

Tully, R. B., Fisher, J. R., 1977, A&A, 54, 661

Van Waerbeke, L., Benjamin, J., Erben, T., et al., 2013, MNRAS, arXiv:1303.1806

Van Waerbeke, L., Mellier, Y., Erben, T., et al., 2000, A&A, 358, 30, arXiv:astro-ph/0002500

Viola, M., Kitching, T. D., Joachimi, B., 2014, MNRAS, 439, 1909, arXiv:1309.7844

Viola, M., Melchior, P., Bartelmann, M., 2011, MNRAS, 410, 2156, arXiv:1006.2470

Voigt, L. M., Bridle, S. L., 2010, MNRAS, 404, 458, arXiv:0905.4801

Walsh, D., Carswell, R. F., Weymann, R. J., 1979, Nature, 279, 381

Wang, L., Steinhardt, P. J., 1998, ApJ, 508, 483, astro-ph/9804015

Weller, J., Battye, R. A., Kneissl, R., 2002, Physical Review Letters, 88, 23, 231301,

astro-ph/0110353

White, M., 2005, Astroparticle Physics, 23, 349, arXiv:astro-ph/0502003

Wittman, D. M., Tyson, J. A., Kirkman, D., Dell'Antonio, I., Bernstein, G., 2000, Nature, 405, 143, arXiv:astro-ph/0003014

Wu, K. K. S., Lahav, O., Rees, M. J., 1999, Nature, 397, 225, astro-ph/9804062

Zuntz, J., Kacprzak, T., Voigt, L., Hirsch, M., Rowe, B., Bridle, S., 2013, MNRAS, 434, 1604, arXiv:1302.0183